

**Fundamental investigation of Zr(IV) solubility and surface processes in alkaline systems:
a combined solubility, spectroscopic and theoretical study**

Zur Erlangung des akademischen Grades eines

DOKTORS DER NATURWISSENSCHAFTEN

(Dr. rer. nat.)

von der KIT-Fakultät für Chemie und Biowissenschaften
des Karlsruher Instituts für Technologie (KIT)

in Cotutelle-de-thèse mit

L'Ecole nationale supérieure Mines-Télécom Atlantique Bretagne - Pays de la Loire
(IMT Atlantique)

genehmigte

DISSERTATION

von

M.Sc. Christian Kiefer

1. Referent: Prof. Dr. H. Geckeis
Prof. Dr. B. Grambow

Tag der mündlichen Prüfung: 11.12.2023

PhD Thesis

In joint supervision (cotutelle) by

Karlsruhe Institute of Technology (KIT)

and

L'Ecole nationale supérieure Mines-Télécom Atlantique Bretagne - Pays de la Loire (IMT Atlantique)

Ecole Doctorale N° 596

Matière, Molécules, Matériaux et Géosciences

Spécialité : Radiochimie

By

Christian KIEFER

Fundamental investigation of Zr(IV) solubility and surface processes in alkaline systems: a combined solubility, spectroscopic and theoretical study

Thesis presented and defended at: Karlsruhe Institute of Technology (KIT), Karlsruhe
11th December 2023

Research units:

Karlsruhe Institute of Technology (KIT), Department of Chemistry and Biosciences, Institute for Nuclear waste disposal (INE)

L'Ecole nationale supérieure Mines-Télécom Atlantique Bretagne - Pays de la Loire (IMT Atlantique), Laboratoire de physique subatomique et des technologies associées (Subatech)

Numéro National de Thèse (NNT): 2023IMTA0379

Jury composition:

President:	Annie POWELL	Professor, KIT, Institute for Inorganic Chemistry
Thesis directors:	Horst GECKEIS	Professor, KIT, Institute for Nuclear Waste Disposal
	Bernd GRAMBOW	Professor (Emeritus), IMT Atlantique, Subatech
Reporters:	Takayuki SASAKI	Professor, Kyoto University, Department of Nuclear Engineering
	Nina HUITTINEN	Professor, Freie Universität Berlin, Institut für Chemie und Biochemie

Acknowledgements

First of all, I would like to express my appreciation to my thesis directors, Prof. Dr. Horst Geckeis, head of the Institute for Nuclear Waste Disposal (INE) of the Karlsruhe Institute of Technology (KIT) and to Prof. Dr. Bernd Grambow, former head of Subatech laboratory, for giving me the opportunity to conduct this binational PhD in their institutes, for their various scientific ideas and their help with administrative issues.

I would like to express my greatest appreciation and gratitude to my supervisors Dr. Xavier Gaona (INE) and Dr. Tomo Susuki-Muresan (Subatech) for their great support in all parts of the work. Without their scientific ideas, their help in experimental planning and evaluations, their support in writing and their large support with administrative issues, my work would not have been possible in this way.

Furthermore, I would like to thank Dr. Dieter Schild for XPS, SEM-EDX and raman spectroscopy measurements and evaluations, Mr. Frank Geyer, Ms. Annika Fried and their team for ICP-MS measurements at INE, Ms. Karine David for HR-ICP-MS measurements and evaluations at Subatech, Ms. Stephanie Kraft and Dr. Denys Grekov for TG-DTA measurements at KIT and Subatech, respectively, Dr. Taishi Kobayashi for SAXS measurements and evaluations, Dr. Oliver Dieste Blanco for TEM measurements and evaluations, Dr. Kathy Dardenne for her help with EXAFS evaluation, Ms. Tanja Kisely for BET measurements and Prof. Dr. Monica Calatayud and Dr. Beata Taudul for their supervision and help with the DFT calculations.

In addition, I would like to thank all my colleagues at INE and Subatech. I have not only found a friendly and productive working atmosphere, but also some friends.

Last but not least, I am very thankful to my parents for their open ears and endless support all the time.

Table of Contents

Summary	1
Zusammenfassung	3
Résumé	5
1. Research objectives	11
2. Introduction	13
2.1 Origin of radioactive waste	13
2.1.1 Historical and actual nuclear energy production: German, French and international situation	13
2.2 Nuclear waste disposal	16
2.2.1 Waste types	16
2.2.2 Repository concepts	18
2.2.2.1 High-level waste (HLW)	18
2.2.2.1.1 Multi-barrier concept	18
2.2.2.1.2 Host rock systems	19
2.2.2.1.3 Actual situation of repositories for HLW	19
2.2.2.2 Intermediate-level waste (ILW)	20
2.2.3 Zirconium containing waste	20
2.3 Zirconium	20
2.3.1 Applications of zirconium and zirconium(IV) oxide	21
2.3.2 Zirconium(IV) oxide solid phases and crystal structures	23
2.3.3 Aquatic chemistry of Zr	26
2.3.3.1 Thermodynamic description of Zr(IV) in aqueous media	28
2.3.3.1.1 Thermodynamic background of solubility and hydrolysis equilibria	28
2.3.3.1.2 Specific Ion interaction Theory (SIT) model	30
2.3.3.1.3 Thermodynamic data	31
2.3.3.1.4 Thermodynamic calculations	32
2.4 Assessment of surface reaction in aqueous media by DFT modeling	36
3. Materials and Methods	39
3.1 Chemicals	39

3.2 pH measurements	40
3.3 Preparation of solid phases and samples	41
3.3.1 Precipitation of ZrO ₂ (am, hyd)	41
3.3.2 Ageing of ZrO ₂ solid phases at elevated temperatures	41
3.4 Solid phase characterization	44
3.4.1 X-ray powder diffraction (XRD)	44
3.4.2 Scanning electron microscopy with energy-dispersive X-ray spectroscopy (SEM-EDX)	44
3.4.3 Transmission electron microscopy (TEM)	45
3.4.4 Raman spectroscopy	45
3.4.5 Extended X-ray absorption fine structure (EXAFS)	45
3.4.6 Small-angle X-ray scattering (SAXS)	46
3.4.7 Thermogravimetric analysis with differential thermal analysis (TG-DTA)	46
3.4.8 Fourier-transform infrared spectroscopy (FTIR)	47
3.4.9 X-ray photoelectron spectroscopy (XPS)	47
3.4.10 Zeta potential measurements	48
3.4.11 Volumetric nitrogen sorption with the Brunauer, Emmet and Teller theory (BET)	48
3.5 Solubility experiments	49
3.5.1 Sample conditions	49
3.5.2 Determination of [Zr] by ICP-MS	51
3.6 Hydrogen-deuterium exchange experiments	51
3.7 Theoretical calculations (DFT)	52
3.7.1 Theoretical background	52
3.7.1.1 Schrödinger equation	52
3.7.1.2 Density functional theory (DFT)	53
3.7.1.2.1 Hohenberg-Kohn theorems	53
3.7.1.2.2 Kohn-Sham approach	54
3.7.1.2.3 Exchange correlation functionals	55
3.7.1.2.3.1 Local Density Approximation (LDA)	55

3.7.1.2.3.2 Generalized Gradient Approximation (GGA)	55
3.7.1.2.3.3 Hybrid functionals	56
3.7.2 Computational details	56
3.7.2.1 VASP software	56
3.7.2.2 Computational tests	57
3.7.2.2.1 Determining k points	57
3.7.2.2.2 Determining energy cut-off	58
3.7.2.2.3 Test of different functionals	58
4. Results and discussion	59
4.1 Solid phase characterization	59
4.1.1 Structure and particle size	59
4.1.1.1 X-ray powder diffraction (XRD)	59
4.1.1.2 Transmission electron microscopy (TEM)	62
4.1.1.3 Raman spectroscopy	66
4.1.1.4 Scanning electron microscopy with energy-dispersive X-ray spectroscopy (SEM-EDX)	68
4.1.1.5 Extended X-ray absorption fine structure (EXAFS)	70
4.1.1.6 Small-angle X-ray scattering (SAXS)	73
4.1.1.7 Effect of ageing on structure and particle size	75
4.1.2 Solid composition and hydration	77
4.1.2.1 Thermogravimetric analysis with differential thermal analysis (TG-TDA)	77
4.1.2.2 X-ray photoelectron spectroscopy (XPS)	83
4.1.2.3 Fourier-transform infrared spectroscopy (FTIR)	85
4.1.2.4 Hydrogen-deuterium exchange experiments	86
4.1.2.5 Effect of ageing on solid composition and hydration	94
4.1.3 Surface properties	95
4.1.3.1 Volumetric nitrogen sorption with the Brunauer, Emmet and Teller theory (BET)	95
4.1.3.2 Zeta potential	96
4.2 Solubility experiments	99

4.2.1 Solubility data of Zr(IV) in 0.5 M NaCl-NaOH	102
4.2.1.1 Calculation of solubility products for the system Zr^{4+} - Na^+ - H^+ - OH^- - Cl^- - H_2O	107
4.2.1.2 Application of the Schindler equation on the solubility data of Zr in 0.5 M NaCl-NaOH	111
4.2.2 Solubility data of Zr(IV) in 0.02 M $CaCl_2$ - $Ca(OH)_2$	113
4.2.3 Solubility data of Zr(IV) in 0.2 M $CaCl_2$ - $Ca(OH)_2$	115
4.2.3.1 Calculation of solubility products for the system Zr^{4+} - Ca^{2+} - H^+ - OH^- - Cl^- - H_2O	119
4.2.3.2 Application of the Schindler equation on the solubility data of Zr in 0.2 M $CaCl_2$ - $Ca(OH)_2$	122
4.3 DFT results	123
4.3.1 Bulk solid calculations	124
4.3.2 Cutting and optimization of surfaces	126
4.3.3 Coordination analysis of the surfaces	127
4.3.3.1 Monoclinic (-1 1 1) surface	127
4.3.3.2 Tetragonal (1 0 1) surface	128
4.3.3.3 Amorphous surface	129
4.3.4 Calculation of the surface energy	131
4.3.5 Hydration of the surfaces	132
4.3.5.1 Water adsorption on monoclinic (-1 1 1) surface	133
4.3.5.2 Water adsorption on tetragonal (1 0 1) surface	136
4.3.5.3 Water adsorption on amorphous surface	139
4.3.5.4 Evaluation of the water adsorption calculations	142
5. Summary and general discussion	145
6. Conclusion and perspectives	151
Appendix	153
List of figures	161
List of tables	163
References	165

Summary

Zirconium is an element of interest in the context of nuclear waste management. ^{93}Zr ($t_{1/2} = 1.53 \cdot 10^6$ a) is produced by nuclear fission of ^{235}U as well as by neutron activation of stable Zr in the zircaloy cladding. Zirconium forms sparingly soluble hydrous oxides, $\text{ZrO}_2(\text{am, hyd})$, which are expected to control Zr(IV) solubility over a broad range of boundary conditions of relevance in the context of nuclear waste disposal. The ageing or exposure to elevated temperatures results in the transition of amorphous $\text{ZrO}_2(\text{am, hyd})$ into the thermodynamically stable crystalline phase $\text{ZrO}_2(\text{cr})$, and thus in a decreased solubility¹⁻⁷. However, the mechanisms and kinetics of such transformations remain ill-defined.

Amorphous $\text{ZrO}_2(\text{am, hyd})$ was freshly precipitated, aged in 0.001 M NaOH or 0.2 M CaCl_2 for 4-18 months at 80°C and comprehensively investigated with solid phase characterization methods (XRD, TEM, TG-DTA, SEM-EDX, XPS, EXAFS, SAXS, FTIR, Raman spectroscopy, zeta potential and BET), undersaturation solubility experiments in alkaline (pH = 8-13.4) 0.5 M NaCl-NaOH, 0.02 / 0.2 M $\text{CaCl}_2\text{-Ca}(\text{OH})_2$ solutions and supporting theoretical calculations.

The solid phase characterization does not show changes for solid phases aged at $T = 22^\circ\text{C}$ compared to the fresh amorphous solid. For solid phases aged at $T = 80^\circ\text{C}$, XRD and TEM show increased particle size, the presence of different families of particles and higher degree of crystallinity. TG-DTA, XPS and FTIR show a decreased amount of hydration water and BET shows a lower specific surface area after ageing at $T = 80^\circ\text{C}$. These changes in the solid phases indicate that the elevated temperatures induced a transformation process from fresh amorphous to more crystalline solid phases. While the ageing time of 4 to 18 months does not show effects on the solid phase properties determined with solid phase characterization, the ageing background electrolyte triggers important differences. The ageing at $T = 80^\circ\text{C}$ in CaCl_2 solutions leads to the formation of cubic/tetragonal ZrO_2 , while in NaOH solutions the monoclinic structure is predominant. These results can be explained by either the incorporation of Ca in the crystal structure of ZrO_2 , or otherwise by the hindrance of the particle growth caused by the alteration of the surface properties (e.g., surface charge) by Ca.

Solubility experiments in 0.5 M NaCl-NaOH solutions show the highest solubility for the fresh solid phase with a solubility constant of $\log^* K_{s,0}^\circ = -4.36 \pm 0.58$. In contrast to solid phase characterization also ageing at $T = 22^\circ\text{C}$ shows effects on the solubility of the solid phases, leading to solubility constants of $\log^* K_{s,0}^\circ = -4.92 \pm 0.32$ and -4.68 ± 0.33 respectively. For solid phases aged at $T = 80^\circ\text{C}$, only a solid phase aged for 4 months in CaCl_2 shows a quite high solubility, with $\log^* K_{s,0}^\circ = -4.92 \pm 0.56$, while the other solid phases approach the solubility of crystalline ZrO_2 , $\log^* K_{s,0}^\circ = -7.00$. A decreasing solubility with ageing time and a solubility order of amorphous > cubic/tetragonal > monoclinic is observed. These results emphasize that solubility is affected by several parameters, i.e., particle size, crystal structure, presence of dopants (e.g., Ca, Y), ageing time / temperature or surface properties / energetics.

Zusammenfassung

Zirkonium ist ein Element, das im Zusammenhang mit der Entsorgung nuklearer Abfälle von Interesse ist. ^{93}Zr ($t_{1/2} = 1,53 \cdot 10^6$ a) wird durch Kernspaltung von ^{235}U sowie durch Neutronenaktivierung von stabilem Zr in der Zirkaloy-Hülle erzeugt. Es bildet schwer lösliche wasserhaltige Oxide, $\text{ZrO}_2(\text{am, hyd})$, von denen erwartet wird, dass sie die Zr(IV)-Löslichkeit über einen weiten Bereich von Randbedingungen steuern, die im Zusammenhang mit der nuklearen Entsorgung von Bedeutung sind. Die Alterung oder Exposition gegenüber erhöhten Temperaturen führt zum Übergang von amorphem $\text{ZrO}_2(\text{am, hyd})$ in die thermodynamisch stabile kristalline Phase $\text{ZrO}_2(\text{cr})$ und damit zu einer verringerten Löslichkeit ¹⁻⁷. Die Mechanismen und die Kinetik solcher Umwandlungen sind jedoch nach wie vor nicht klar definiert.

Amorphes $\text{ZrO}_2(\text{am, hyd})$ wurde frisch ausgefällt, in 0,001 M NaOH oder 0,2 M CaCl_2 Lösungen für 4-18 Monate bei 80°C gealtert und umfassend mit Festphasencharakterisierungsmethoden (XRD, TEM, TG-DTA, SEM-EDX, XPS, EXAFS, SAXS, FTIR, Raman-Spektroskopie, Zeta-Potential und BET), Löslichkeitsexperimenten bei Untersättigung in alkalischen (pH = 8-13,4), 0,5 M NaCl-NaOH, 0,02 / 0,2 M CaCl_2 - $\text{Ca}(\text{OH})_2$ Lösungen und unterstützenden theoretischen Berechnungen untersucht.

Die Festphasencharakterisierung zeigt keine Veränderungen für die bei $T = 22^\circ\text{C}$ gealterten Proben im Vergleich zum frischen amorphen Feststoff. Für Festphasen, die bei $T = 80^\circ\text{C}$ gealtert wurden, zeigen XRD und TEM eine größere Partikelgröße, das Vorhandensein verschiedener Partikelfamilien und einen höheren Kristallinitätsgrad. TG-DTA, XPS und FTIR zeigen eine verringerte Menge an Hydratationswasser und BET zeigt eine geringere spezifische Oberfläche nach der Alterung bei $T = 80^\circ\text{C}$. Diese Veränderungen in den Festphasen deuten darauf hin, dass die erhöhten Temperaturen einen Umwandlungsprozess von frischen amorphen zu kristallineren Festphasen ausgelöst haben. Während die Alterungszeit von 4 bis 18 Monaten keine Auswirkungen auf die mit der Festphasencharakterisierung ermittelten Eigenschaften zeigt, scheint der Hintergrundelektrolyt wichtige Unterschiede zu verursachen. Die Alterung bei $T = 80^\circ\text{C}$ in CaCl_2 -Lösungen führt zur Bildung von kubisch/tetragonalem ZrO_2 , während in NaOH-Lösungen die monokline Struktur vorherrscht. Diese Ergebnisse lassen sich entweder durch den Einbau von Ca in die Kristallstruktur von ZrO_2 oder durch die Behinderung des Partikelwachstums aufgrund der Veränderung der Oberflächeneigenschaften (z. B. der Oberflächenladung) durch Ca erklären.

Löslichkeitsexperimente in 0,5 M NaCl-NaOH-Lösungen zeigen die höchste Löslichkeit für die frische Festphase mit einer Löslichkeitskonstante von $\log^* K_{s,0}^\circ = -4,36 \pm 0,58$. Im Gegensatz zur Festphasencharakterisierung zeigt auch die Alterung bei $T = 22^\circ\text{C}$ Auswirkungen auf die Löslichkeit der Festphasen, was zu Löslichkeitskonstanten von $\log^* K_{s,0}^\circ = -4,92 \pm 0,32$ bzw. $-4,68 \pm 0,33$ führt. Bei den Festphasen, die bei $T = 80^\circ\text{C}$ gealtert wurden, zeigt nur eine Probe, die 4 Monate lang in CaCl_2 gealtert wurde, eine recht hohe Löslichkeit, mit $\log^* K_{s,0}^\circ = -4,92 \pm 0,56$, während die anderen Festphasen sich der Löslichkeit von kristallinem ZrO_2 annähern, $\log^* K_{s,0}^\circ = -7,00$. Die Löslichkeit nimmt mit der Alterungszeit ab, und es wird eine Löslichkeitsreihenfolge amorph > kubisch/tetragonal > monoklin beobachtet. Diese Ergebnisse machen deutlich, dass die Löslichkeit von mehreren Parametern abhängt, z. B. von der Partikelgröße, der Kristallstruktur, dem Vorhandensein von Dotierungen (z. B. Ca, Y), der Alterungszeit / Temperatur oder den Oberflächeneigenschaften / Energien.

Résumé

Le zirconium est un élément d'intérêt dans le contexte de la gestion des déchets nucléaires car il est produit par la fission de l'uranium 235 (rendement de fission : 6,3-6,4%⁸) et en raison de l'utilisation d'alliages à base de zirconium (Zircaloy) comme matériau de gainage pour le combustible nucléaire dans les réacteurs nucléaires à eau. Pendant le fonctionnement du réacteur, du zirconium radioactif est produit par activation neutronique du zirconium stable dans la gaine. Le ⁹³Zr ($t_{1/2} = 1,53 \cdot 10^6$ a) est particulièrement important en raison de sa longue demi-vie¹. Dans le contexte du retraitement du combustible usé, les gaines sont cisailées pour former des coques, puis rincées et compactées pour former des galettes qui sont placées dans des conteneurs métalliques. Il est envisagé de stocker ces colis de déchets dans un environnement cimentaire. Le scénario d'une intrusion des eaux souterraines atteignant le déchet, suivi de la formation de systèmes aqueux contenant des radionucléides doit être pris en compte dans l'évaluation de la sûreté d'un site de stockage des déchets radioactifs. Le zirconium forme des oxydes amorphes hydriques peu solubles, ZrO₂(am, hyd) (peut également être décrite comme Zr(OH)₄(am, hyd)), qui devraient contrôler la solubilité du Zr(IV) dans une large gamme de pH allant des conditions acides aux conditions hyperalcalines. La transition du ZrO₂(am, hyd) amorphe vers la phase cristalline thermodynamiquement stable ZrO₂(cr) est cinétiquement entravée et n'est généralement pas observée dans les systèmes aqueux. Des températures élevées (en fonction du type de déchets, du concept de dépôt et du système de roche hôte) affecteront la chimie dans le champ proche d'un dépôt de déchets nucléaires en cas de défaillance précoce d'un conteneur et peuvent éventuellement surmonter l'obstacle cinétique de la transformation. Le vieillissement ou l'exposition des phases solides amorphes à des températures élevées entraîne normalement une augmentation de la cristallinité (caractérisés entre autres par une taille de particule plus grande, une quantité d'hydratation plus faible, une surface plus faible) et donc une diminution de la solubilité dans les systèmes aqueux¹⁻⁷.

L'objectif principal de cette thèse est d'étudier ce processus de transformation de phase prévu. Par conséquent, du ZrO₂(am, hyd) amorphe a été fraîchement précipité comme phase solide de départ, vieilli dans plusieurs conditions à des températures élevées et étudié avec plusieurs méthodes de caractérisation de la phase solide, des expérimentations de solubilité et des calculs théoriques. La précipitation a été effectuée par titrage lent d'une solution de ZrOCl₂ 0,02 M avec une solution de NaOH 0,1 M jusqu'à un pH > 12. Le vieillissement a été effectué sous atmosphère Ar (boîte à gants) à T = 80°C (four) ou à température ambiante (T = 22°C) pendant 4 à 18 mois. Comme électrolyte de fond pendant le vieillissement, des solutions 0,001 M de NaOH et 0,2 M ou 0,02 M de CaCl₂ ajustées à pH = 11 ont été utilisées. À titre de comparaison, un échantillon a été vieilli sans ajout de phase liquide. Le solide frais, les échantillons vieillis et un solide commercial de ZrO₂ cristallin (nanoparticules) ont été analysés

par XRD, TEM, TG-DTA, SEM-EDX, XPS, EXAFS, SAXS, FTIR, spectroscopie Raman, potentiel zêta et BET afin d'obtenir des informations sur la cristallinité, la structure cristalline, la taille des particules, la structure à courte portée, la teneur en eau, la spéciation de l'oxygène, la surface spécifique et la charge de surface des échantillons afin d'évaluer la façon dont le vieillissement a transformé les phases solides. En outre, des expériences de solubilité par sous-saturation dans des solutions alcalines (pH = 8-13,4) de 0,5 M NaCl-NaOH, de 0,02 M CaCl₂-Ca(OH)₂ et de 0,2 M CaCl₂-Ca(OH)₂ ont été réalisées pour évaluer les effets du vieillissement sur la solubilité des phases solides. Pour mieux comprendre les propriétés de surface et le comportement de la solubilité, des calculs DFT ont été effectués sur l'énergie de surface et les mécanismes et énergies d'adsorption de l'eau.

La caractérisation de la phase solide par DRX (Figure 1), MET, spectroscopie Raman, SAXS, EXAFS et SEM-EDX donne un aperçu de l'impact du vieillissement à des températures élevées sur la cristallinité, la taille des particules et la croissance des particules des phases solides de ZrO₂. Ces méthodes montrent que le vieillissement à T = 80°C induit une transformation relativement rapide d'un solide amorphe fraîchement précipité vers des solides nanocristallins, accompagnée d'une augmentation de la taille des particules et de la formation de différents types de particules. Aucun changement significatif n'a été observé entre 4 et 18 mois. Contrairement au vieillissement à T = 80°C, aucun changement dans les propriétés des solides n'a été observé avec les méthodes utilisées dans cette étude pour les phases solides équilibrées à T = 22°C. Le vieillissement jusqu'à 18 mois ne montre aucun effet, ce qui indique une stabilisation de la structure cristallographique dès 4 mois.

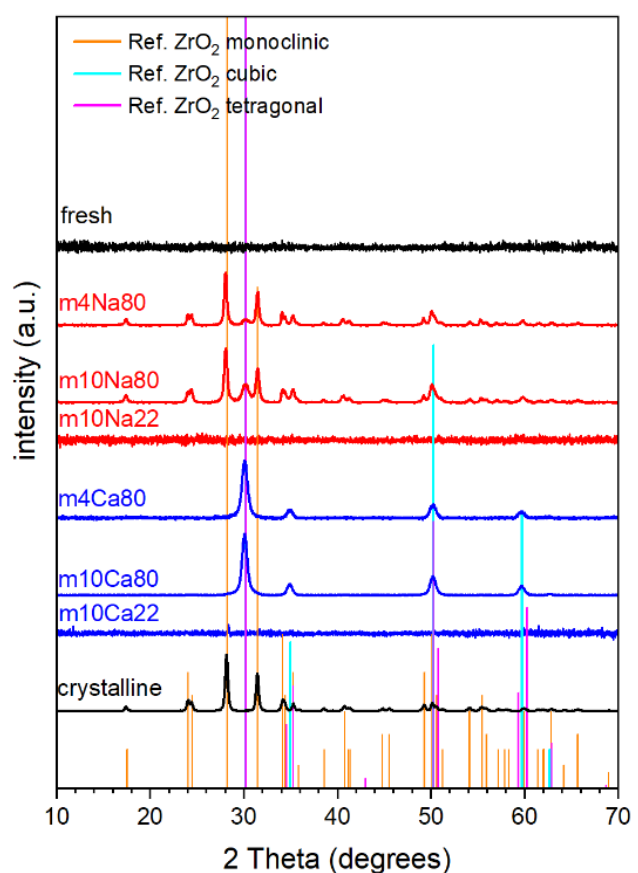


Figure 1 : Diagrammes DRX des échantillons de ZrO₂(s): rouge: phases solides vieilles dans des solutions de NaOH; bleu: phases solides vieilles dans des solutions de CaCl₂; noir: phases de ZrO₂(s) fraîchement précipitées et cristallines. Les lignes verticales indiquent les données de référence rapportées pour ZrO₂(cr) dans la base de données COD.

L'électrolyte de fond a un effet important sur les propriétés solides. Des structures cristallines cubiques/quadratiques avec une taille de particule de 11-14 nm se forment pendant le vieillissement dans les systèmes CaCl_2 , tandis que le vieillissement dans NaOH a permis d'obtenir une structure monoclinique avec une taille de particule de 23-27 nm. Une autre différence est la formation de grands bâtonnets d'une longueur allant jusqu'à 300 nm dans le cas du vieillissement dans une solution NaOH , ce qui n'est pas le cas après le vieillissement dans les solutions de CaCl_2 . Différentes options sont discutées dans la littérature comme raisons potentielles de la stabilisation de la phase cubique/quadratique en présence de Ca. Une possibilité serait l'incorporation de Ca et donc une stabilisation de la phase solide cubique/quadratique comme cela est connu pour d'autres éléments, par exemple l'yttrium⁹⁻¹¹ avec la formation d'une solution solide de $\text{Zr}_{1-x}\text{Y}_x\text{O}_2$. Le même comportement est également rapporté pour le Ca, mais dans des conditions très différentes de celles de la présente étude^{9,12,13}. Cependant, cette hypothèse serait soutenue par la présence systématique de Ca dans les échantillons vieillis en milieu CaCl_2 observée avec les mesures EDX malgré plusieurs étapes de lavage. D'autre part, les contributions plus faibles de la phase cubique/quadratique dans certains échantillons monocliniques vieillis en l'absence de Ca ne peuvent évidemment pas être expliquées par l'incorporation de Ca. Une autre hypothèse expliquant également ces résultats serait que la stabilisation des différentes structures cristallines est un effet de la surface et donc de la taille des particules. La surface spécifique des particules vieilles en présence de Ca est plus élevée parce que ces particules sont plus petites. Cela pourrait conduire à des croisements d'énergie pour la phase cristalline stabilisée^{14,15}. Les différentes structures cristallines dans les échantillons vieillis peuvent être expliquées par l'observation de gros bâtonnets (200-300 nm) et de petites particules dans les échantillons par MET. Selon les croisements d'énergies calculées, les petites particules devraient être quadratiques, tandis que pour les bâtonnets (>48 nm), les structures monocliniques devraient être préférées. Ce comportement expliquerait le caractère cubique/quadratique des échantillons vieillis dans le CaCl_2 , étant donné qu'aucune particule plus grosse n'a été observée dans ces échantillons, ainsi que le caractère monoclinique avec de faibles contributions cubiques/quadratique pour les échantillons vieillis à $T = 80^\circ\text{C}$ dans NaOH , étant donné que de gros bâtonnets et de petites particules ont été observés dans ces échantillons.

La caractérisation de la phase solide par TG-DTA, XPS et FTIR montre que le vieillissement à des températures élevées a également un impact sur la teneur en eau des solides. La transformation de solides amorphes en solides cristallins qui se produit à $T = 80^\circ\text{C}$ est liée à une réduction de la teneur en eau et à une diminution du rapport $[\text{O}]/[\text{Zr}]$. Avec la TG-DTA, la perte de poids mesurée a été attribuée à l'eau d'hydratation en supposant une stœchiométrie de $\text{ZrO}_2\text{-}n\text{H}_2\text{O}$. La figure 2 donne un aperçu de la teneur en eau des échantillons.

L'analyse par XPS montre que les solides sont décrits plus précisément comme $ZrO_x(OH)_{4-2x} \cdot nH_2O$ et que le processus de transformation conduit à une augmentation de la contribution de O^{2-} et à une diminution de la contribution de H_2O et OH^- . Cela pourrait s'expliquer par des réactions de condensation dans les solides, où 2 groupes ZrOH libèrent 1 molécule d'eau et forment une liaison Zr-O-

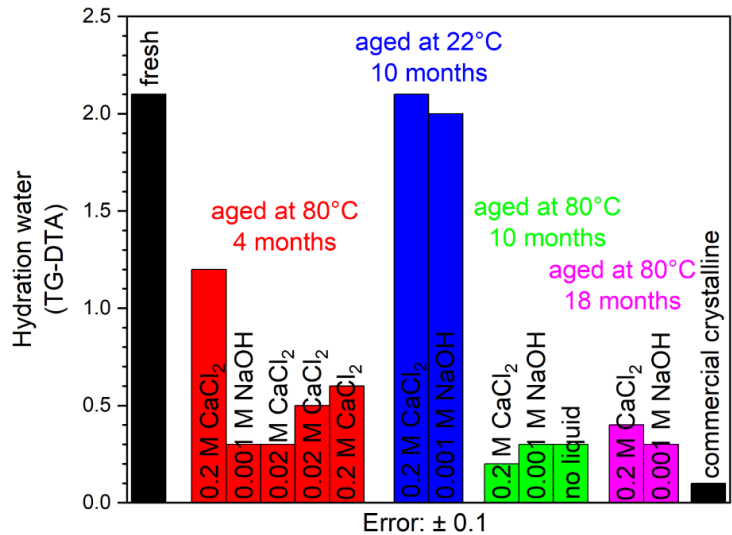


Figure 2 : Quantité d'eau d'hydratation des solides déterminée par TG-DTA en supposant une stœchiométrie également en accord avec de $ZrO_2 \cdot nH_2O$.

l'augmentation de la cristallinité et de la taille des particules observée par XRD et TEM. D'autres expériences TG-DTA indiquent que le processus de déshydratation n'est pas réversible, et donc que les liaisons Zr-O-Zr formées au cours de la transformation ne sont pas rompues si le solide est à nouveau mis en contact avec de l'eau. Les expériences d'échange isotopique avec le deutérium et l'hydrogène indiquent que la fraction de H_2O/OH^- faiblement liée à la surface des particules et échangeable diminue pour les échantillons vieillis. L'analyse de la surface spécifique de plusieurs échantillons par BET montre que la transformation des phases solides amorphes en phases plus cristallines est également liée à une diminution de la surface, ce qui est en accord avec l'augmentation observée de la taille des particules et la diminution du taux d'hydratation. Les phases solides amorphes présentent des surfaces spécifiques de plus de $250 \text{ m}^2\text{g}^{-1}$, comme prévu en raison de la petite taille des particules, tandis que les solides monocliniques présentent des valeurs de l'ordre de 20 à $40 \text{ m}^2\text{g}^{-1}$, comme prévu également en raison de la taille plus importante des particules. Les mesures du potentiel zêta indiquent que la surface des solides est chargée négativement par des groupes OH^- pendant le vieillissement dans NaOH et chargée positivement ou presque neutre dans $CaCl_2$ - $Ca(OH)_2$. Cela pourrait avoir un effet sur la formation des différents systèmes cristallins et peut-être aussi inhiber la croissance des particules en présence de Ca. Le fait que les solides vieillis en présence de Ca présentent également des potentiels zêta moins négatifs mesurés dans 1 mM NaCl-NaOH par rapport aux solides vieillis dans NaOH, soutient l'idée de l'incorporation de Ca au moins dans les couches superficielles des solides de ZrO_2 au cours du processus de vieillissement.

Contrairement à la caractérisation de la phase solide, où seuls des changements dans les propriétés solides étaient observables pour les phases solides équilibrées à $T = 80^\circ\text{C}$, mais pas

pour les phases solides équilibrées à $T = 22^\circ\text{C}$, et où aucun effet du temps de vieillissement n'est visible, les expériences de solubilité montrent des comportements différents pour les échantillons vieillis à $T = 80^\circ\text{C}$ et $T = 22^\circ\text{C}$, ainsi qu'une diminution de la solubilité avec l'augmentation du temps de vieillissement. Les données de solubilité de plusieurs phases solides dans des solutions NaCl-NaOH 0,5 M et les courbes de solubilité modélisées pour déterminer les constantes de solubilité sont présentées dans la figure 3. La solubilité la plus élevée, avec une constante de solubilité de $\log^* K_{s,0}^\circ = -4,36 \pm 0,58$, est observée pour le $\text{ZrO}_2(\text{s})$ amorphe hydraté fraîchement précipité, en accord avec les données de la littérature. Même si les phases solides vieilles à 22°C , m10Ca22 et m10Na22, ne présentent pas de différences dans le cadre de la caractérisation des phases solides, leurs constantes de solubilité diminuent à $\log^* K_{s,0}^\circ = -4,92 \pm 0,32$ et $-4,68 \pm 0,33$ respectivement, ce qui indique que le processus de maturation de la phase solide est néanmoins en cours. La solubilité des phases solides quadratiques/cubiques vieilles à 80°C en milieu CaCl_2 diminue de $\log^* K_{s,0}^\circ = -4,92 \pm 0,56$ après 4 mois vers des constantes de solubilité entre $-6,21$ et $-6,76$, où seules quelques données de concentration de Zr sont supérieures à la limite de détection.

Des solubilités encore plus faibles ont été trouvées pour les solides monocliniques, où la phase solide vieillie à 80°C pendant 4 mois présente la solubilité la plus élevée, puis diminue ensuite jusqu'à la solubilité du ZrO_2 cristallin disponible dans le commerce. Les concentrations de Zr se situent le plus souvent à la limite de détection ou en dessous de celle-ci. Ces résultats de solubilité montrent que plusieurs facteurs influencent largement la solubilité d'une phase solide. La cristallinité de la phase solide joue un rôle clé, plus la phase solide est cristalline, plus la solubilité est faible. La structure cristalline est importante, car les différentes structures présentent également des produits de solubilité différents. Les solides quadratiques/cubiques présentent une solubilité plus élevée que les solides monocliniques, mais elle reste bien inférieure à celle des solides amorphes. Cela peut s'expliquer par la stabilité thermodynamique plus élevée du ZrO_2 monoclinique, qui nécessite plus d'énergie pour se dissoudre, ou par les différentes énergies de surface, comme le montrent les calculs DFT. Un autre paramètre très important influençant la solubilité est la taille des particules ou plus précisément la surface. Une taille de particule plus faible et donc une surface plus élevée conduisent (comme l'explique l'équation de Schindler) à une réactivité plus élevée et par conséquent à une solubilité plus élevée, puisque les processus de solubilité se déroulent principalement dans les couches superficielles des phases solides. Les produits de solubilité significativement différents observés pour des phases solides ayant la même structure cristalline et la même taille de particule indiquent que la solubilité est affectée par les propriétés de surface, ce qui n'a pas été observé dans le présent travail. En résumé, la présente étude montre que le vieillissement de ZrO_2 (am, hyd, frais) fraîchement précipité à $T = 22^\circ\text{C}$ conduit à une diminution modérée de la solubilité de $\text{ZrO}_2(\text{s})$ par rapport au solide frais, bien

qu'aucune différence n'ait pu être observée par la caractérisation de la phase solide et que le vieillissement à $T = 80^\circ\text{C}$ conduit à des changements clairs dans les propriétés de la phase solide et la solubilité. Ce comportement suggère que la température élevée est suffisante pour surmonter l'obstacle cinétique et accélère le processus de transformation de la phase solide de l'amorphe au cubique/tétragonal en ZrO_2 monoclinique, qui est la structure thermodynamiquement la plus stable.

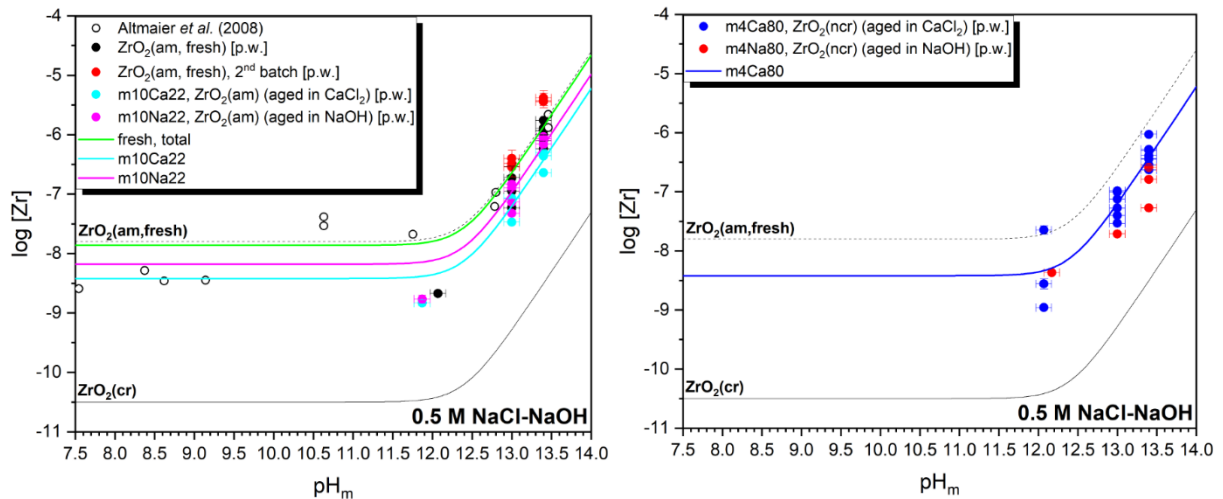


Figure 3: à gauche : données de solubilité et courbes de solubilité modélisées pour le $\text{ZrO}_2(\text{am, hyd})$ amorphe frais et les échantillons amorphes vieillis à $T = 22^\circ\text{C}$ (m10Ca22, m10Na22); à droite: données de solubilité et courbes de solubilité modélisées pour les échantillons nanocristallins vieillis à $T = 80^\circ\text{C}$ (m4Ca80, m4Na80).

Le processus s'accompagne d'une augmentation de la taille des particules, d'une diminution de la teneur en eau, d'une diminution de la surface et d'une diminution de la solubilité. Cependant, le vieillissement des échantillons en présence de Ca forme préférentiellement la phase cubique/quadratique, leur solubilité reste plus élevée et la taille de leurs particules reste plus petite par rapport au vieillissement sans Ca (dans NaOH), où les échantillons forment la phase monoclinique avec seulement de petites contributions de ZrO_2 cubique/quadratique. L'incorporation de Ca dans le solide^{9,12,13} et/ou les croisements d'énergie pour les petites particules pourraient conduire à la stabilisation de la phase solide cubique/quadratique. Outre la température de vieillissement, le temps de vieillissement a également été étudié. En ce qui concerne la caractérisation de la phase solide, la durée du vieillissement ne semble avoir que des effets mineurs. Déjà après 4 mois de vieillissement, les phases solides présentent presque la même taille de particule, la même quantité d'hydratation et la même composition solide qu'après 10 ou 18 mois de vieillissement dans le même électrolyte de base. D'autre part, le temps de vieillissement a une plus grande influence sur la solubilité des échantillons. Dans ce contexte, les échantillons vieillis pendant 4 mois présentent une solubilité nettement plus élevée que les échantillons vieillis pendant 10 ou 18 mois, où les solubilités sont proches de celles du ZrO_2 cristallin.

1. Research objectives

In order to provide a detailed and realistic picture of processes, knowledge on the behavior of relevant elements in a repository for radioactive waste over long time scales is highly desirable. Zirconium is an element of interest in this context since its isotope ^{93}Zr is produced by fission reaction of ^{235}U (yield: 6.3-6.4%⁸) and due to the use of zirconium alloys (Zircaloy) as cladding material for the nuclear fuel in water cooled reactors. During operation of the reactor, radioactive zirconium is produced by neutron activation of stable zirconium in the cladding. ^{93}Zr ($t_{1/2} = 1.53 \cdot 10^6$ a) is particularly important due to its long half-life¹.

The scenario of early canister failure and ground water intrusion followed by subsequent formation of aqueous systems with radionuclides has to be considered in the safety assessment of a potential nuclear waste disposal site. Under most conditions, the stable oxidation state of zirconium is +IV. As most other tetravalent metals, Zr(IV) has a strong tendency to hydrolyze in aqueous solutions, dominated by cationic species $\text{Zr}_x(\text{OH})_y^{4x-y}$ (with $y < 4x$) under highly acidic, neutral species $\text{Zr}(\text{OH})_4(\text{aq})$ (or analogous neutral polynuclear moieties) from acidic to alkaline and anionic hydrolysis species such as $\text{Zr}(\text{OH})_6^{-2}$ under hyperalkaline pH conditions¹⁶⁻¹⁸. Besides the strong hydrolysis, Zr(IV) forms also sparingly soluble amorphous hydrous oxides, $\text{ZrO}_2(\text{am, hyd})$, which control Zr(IV) solubility over a broad range of pH from acidic to hyperalkaline conditions. The transition of amorphous $\text{ZrO}_2(\text{am, hyd})$ into the thermodynamically stable crystalline phase $\text{ZrO}_2(\text{cr})$, is kinetically hindered and is generally not observed in aqueous systems when precipitating Zr(IV), if the hindrance is not overcome. Temperature is one of the parameters that will vary during the different phases of operation of a repository for nuclear waste. Elevated temperatures (depending upon waste type, repository concept and host-rock system) will affect chemistry in the near-field of a nuclear waste repository in the case of early canister failure. The ageing or exposure of the amorphous solid phases to elevated temperatures expectedly results in increased crystallinity (characterized among others by larger particle size, lower hydration amount, lower surface area) and thus in a decreased solubility in aqueous systems¹⁻⁷.

The main objective of this work is to investigate this expected phase transformation process of the ZrO_2 solids and its effects on the thermodynamic properties like solubility, which are very important to estimate the behavior of nuclear wastes containing Zr in the previously mentioned scenario of water contact due to canister failure. To approach this objective, an amorphous $\text{ZrO}_2(\text{am, hyd})$ starting solid phase was freshly precipitated, aged under several conditions at elevated temperatures and investigated with several solid phase characterization methods, solubility experiments and supporting theoretical calculations.

After precipitation of fresh $\text{ZrO}_2(\text{am, hyd})$, by adding NaOH to a ZrOCl_2 solution, several batches of the solid were aged under Ar atmosphere at $T = 80^\circ\text{C}$ in either 0.001 M NaOH , $0.2 \text{ M CaCl}_2\text{-Ca(OH)}_2$, $0.02 \text{ M CaCl}_2\text{-Ca(OH)}_2$ (representative of cementitious systems) solutions adjusted to $\text{pH} = 11$ or without a liquid phase for 4 to 18 months. The different aged solid phases were analyzed with various solid phase characterization methods like XRD, TEM, EXAFS, SAXS, SEM-EDX, XPS, Raman and IR spectroscopy, TG-DTA, BET and zeta potential measurements to gain information about possible changes in particle size, crystallinity, water content and surface properties of the solid phases.

Together with the changes in solid phase characteristics, also changes in solubility and thermodynamic behavior are expected. Therefore, the solubility of the solid phases in alkaline 0.5 M NaCl-NaOH , $0.2 \text{ M CaCl}_2\text{-Ca(OH)}_2$, $0.02 \text{ M CaCl}_2\text{-Ca(OH)}_2$ solutions ($8 < \text{pH} < 13.4$) was determined by ICP-MS. Solubility data were modelled based on the hydrolysis scheme (mainly NEA-TDB, Altmaier et al. for species including ternary complexes with Ca), hydrolysis constants (mainly NEA-TDB, Altmaier et al. for species including ternary complexes with Ca) and SIT coefficients (mainly Altmaier et al.) selected in the NEA-TDB zirconium database¹⁷ and by Altmaier and co-workers¹⁹. This modelling approach allows the calculation of the solubility products, $\log^*K_{s,0}^\circ$, of the solid phases synthesized in this work to assess the impact of ageing at elevated temperature, as well as their comparison with literature values.

Considering the interlink between solubility phenomena and surface processes, density functional theory (DFT) calculations were done targeting a better understanding of the surface properties, the mechanisms of addition or removal of water from surfaces and thus solubility behavior of ZrO_2 solids.

The combination of comprehensive solid phase characterization with solubility experiments of systematically aged hydrous oxides of zirconium, supported by DFT calculations is expected to provide relevant contributions to the thermodynamic description of aqueous systems containing zirconium, potentially relevant and therefore important in the context of nuclear waste disposal.

2. Introduction

2.1 Origin of radioactive waste

The main source of radioactive waste stems from the nuclear power sector, in which the heat of fission reactions (usually of ^{235}U and ^{239}Pu) is used to generate electric energy, from the front end of the cycle, covering uranium mining and milling, enrichment, fuel fabrication, to the back end, including treatment of spent fuel (e.g. reprocessing) and decommissioning ²⁰.

Besides the use for energy generation in nuclear power plants, radionuclides have several other applications in different fields for example in research, radioisotope labeling or nuclear medicine. Radionuclides or their ionizing radiation are used in medical applications for both diagnosis and therapy of various diseases like cancer ²¹. Classically, γ -emitters (e.g. $^{99\text{m}}\text{Tc}$ or ^{123}I) are preferred for diagnosis, while therapy uses β -emitters like ^{90}Y or ^{131}I , respectively ²². Positron emission tomography (PET), a technique for in vivo imaging is based on β^+ decay and uses the radionuclides ^{18}F , ^{11}C , ^{13}N and ^{15}O among others ²². More recent, so-called theranostic approaches combine diagnosis and therapy by the use of differently radiolabeled molecules or different doses of the same radionuclides ²³. However, the volumes of nuclear waste produced by medical applications are significantly lower compared to those from nuclear energy production. Furthermore, a long-term storage will not be required for this kind of waste, since the radionuclides used for medical purposes are mostly short-lived.

In addition to these civil sources of nuclear waste, also military applications as developing, producing, testing, deploying and dismantling of nuclear weapons and submarines and their legacies create a significant amount of nuclear waste ²⁴.

The use of radionuclides in the mentioned fields generates different types of nuclear waste, which needs to be treated and disposed in a safe way. Therefore, for each type of waste, different comprehensive strategies are developed in the context of nuclear waste management to avoid harmful effects for the environment.

2.1.1 Historical and actual nuclear energy production: German, French and international situation

Nuclear power plants for energy generation were established in the 1950s and their use was greatly expanded worldwide during the 1970s and 1980s due to the high energy density of nuclear fuel compared to other energy sources, the increasing total energy demand and the independence of fossil energy sources ²⁵⁻²⁷. Therefore, the evolution of the use nuclear energy proceeded similar in the industrialized countries of that time. The number of nuclear power

plants (active and under construction) and the generated electric energy of selected countries in the year 1989 is shown in Table 2.1 ^{25,27}.

However, this evolution changed in the 1990s, especially in Germany where the nuclear energy stagnated and renewable energies like wind and solar expanded ²⁵. In 2002 the construction of new nuclear power plants in Germany was prohibited and the operation time of existing power plants was limited by the nuclear phase-out decision of the German government ^{28–31}. After the reactor disaster in Fukushima, the German Bundestag decided in June 2011 with a broad majority to accelerate the phase-out from nuclear energy for commercial electricity generation by 2022. The process was recently completed in April 2023.

Most other industrialized countries decided to proceed with the use of nuclear energy and especially in Asia the amount of nuclear power plants increased largely since 1990. The number of nuclear power plants (active and under construction) and the generated electric energy of selected countries in the year 2022 is shown in Table 2.2 ^{20,25}. The biggest contrast to Germany with respect to the generation and use of nuclear energy shows France, in which 77.6% of the total electric energy in 2021 was nuclear ²⁰, so that despite the lower amount of renewable energies, also less fossil energy was used compared to Germany. The electricity mix of France (2021) is shown in Figure 2.1.

Table 2.1: number of nuclear power plants and energy generation of selected countries in 1989 ²⁷.

Country	Reactors		Generated electricity	
	operating	Under construction	GW	% of total electricity
Canada	18	4	12.2	15.6
U.S.	110	4	98.3	19.1
Germany (east)	6	5	2.1	10.9
Germany (west)	24	1	22.7	34.3
France	55	9	52.6	74.6
U.K.	39	1	11.2	21.7
China	0	3	0	0
India	7	7	1.4	1.6
Japan	39	12	29.3	27.8
South Korea	9	2	7.2	50.2
U. S. S. R.	46	26	34.2	12.3

Table 2.2: number of nuclear power plants and energy generation of selected countries in February 2022 ²⁰.

Country	Reactors		Capacity [GW]
	operating	Under construction	
Canada	19	0	13.6
U.S.	93	2	95.5
Germany	3*	0	4.1*
France	56	1	61.4
U.K.	11	2	6.8
China	54	14	50.8
India	23	6	6.9
Japan	33	2	31.7
South Korea	24	4	23.1
Russia	38	4	28.6

*meanwhile 0.

Another important difference between France, Japan, UK and most other countries in the context of nuclear energy production is the reprocessing of spent nuclear fuel. While in the other countries spent nuclear fuel is treated as waste and long-term stored, France, India, Russia, UK and Japan have regulations for reprocessing spent nuclear fuel ²⁰. During the reprocessing, fission products are removed and the recycled uranium and plutonium are used to prepare new uranium oxide (UOX) and metal oxide (MOX) fuel, which can be reused. With reprocessing, the energy generated from the original uranium can be increased by up to 22%. On the other hand the resulting used MOX fuel is more difficult to handle and the reprocessing creates additional nuclear waste streams ²⁰.

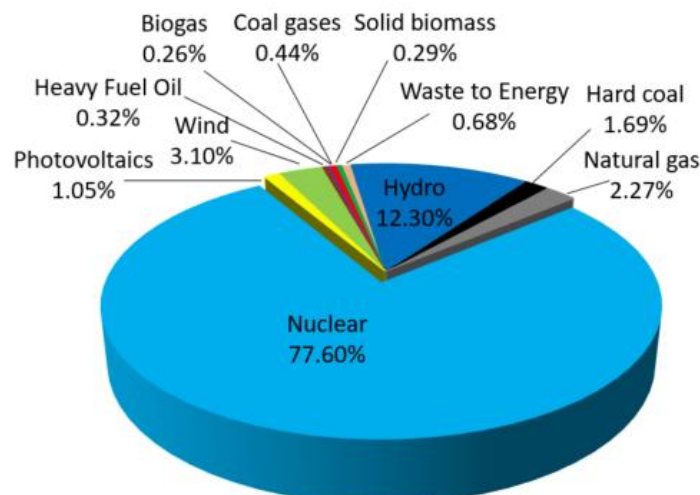


Figure 2.1: electricity mix in France (2021). Adapted from ²⁰.

Regardless of whether nuclear energy is still used or not, whether spent fuel is reprocessed or not, the management of the already produced and in the future produced nuclear waste remains a major challenge in all nuclear applications.

2.2 Nuclear waste disposal

Since the properties, the behavior and the potential dangers of nuclear waste vary strongly, a classification of the waste into different types with individual waste management concepts is necessary to ensure a reasonable and safe disposal for all nuclear wastes.

2.2.1 Waste types

The International Atomic Energy Agency (IAEA) defines 6 classes of nuclear waste according to disposal requirements depending of half-lives and activities of the waste ³². A schematic overview of the nuclear waste classes defined by the IAEA is shown in Figure 2.2.

- (1) Exempt waste (EW): waste that fulfills the regulatory control criteria for release from radiation protection purposes.
- (2) Very short-lived waste (VSLW): waste that can be released from regulatory control after storage for a limited time up to a few years. Typically composed of radionuclides with very short half-lives used for medical applications or in research.
- (3) Very low-level waste (VLLW): waste that does not fulfill the criteria for EW, but does also not need a high level of containment or isolation. Waste of this type does usually contain only a very limited amount of long-lived radionuclides and is suitable for near surface disposal with limited regulatory control.
- (4) Low-level waste (LLW): waste that may include high activities of short-lived, but only low activities of long-lived radionuclides. Waste of this type requires isolation and containment for up to a few hundred years and can be disposed in engineered near surface disposal facilities.
- (5) Intermediate-level waste (ILW): waste which cannot be stored in near surface disposal facilities because the too high activity of long-lived radionuclides requires a greater degree of containment or better isolation than near surface facilities provide. For this type of waste no or only limited precautions due to heat generation are required and the waste can be disposed in facilities with depths of tens of meters to a few hundred meters.
- (6) High-level waste (HLW): waste with such high activities that significant quantities of heat are generated by radioactive decay or with large amounts of long-lived radionuclides that have to be considered in the design of a repository. The internationally favored option for disposal of HLW is disposal in a deep geological formation hundreds of meters below the surface ³².

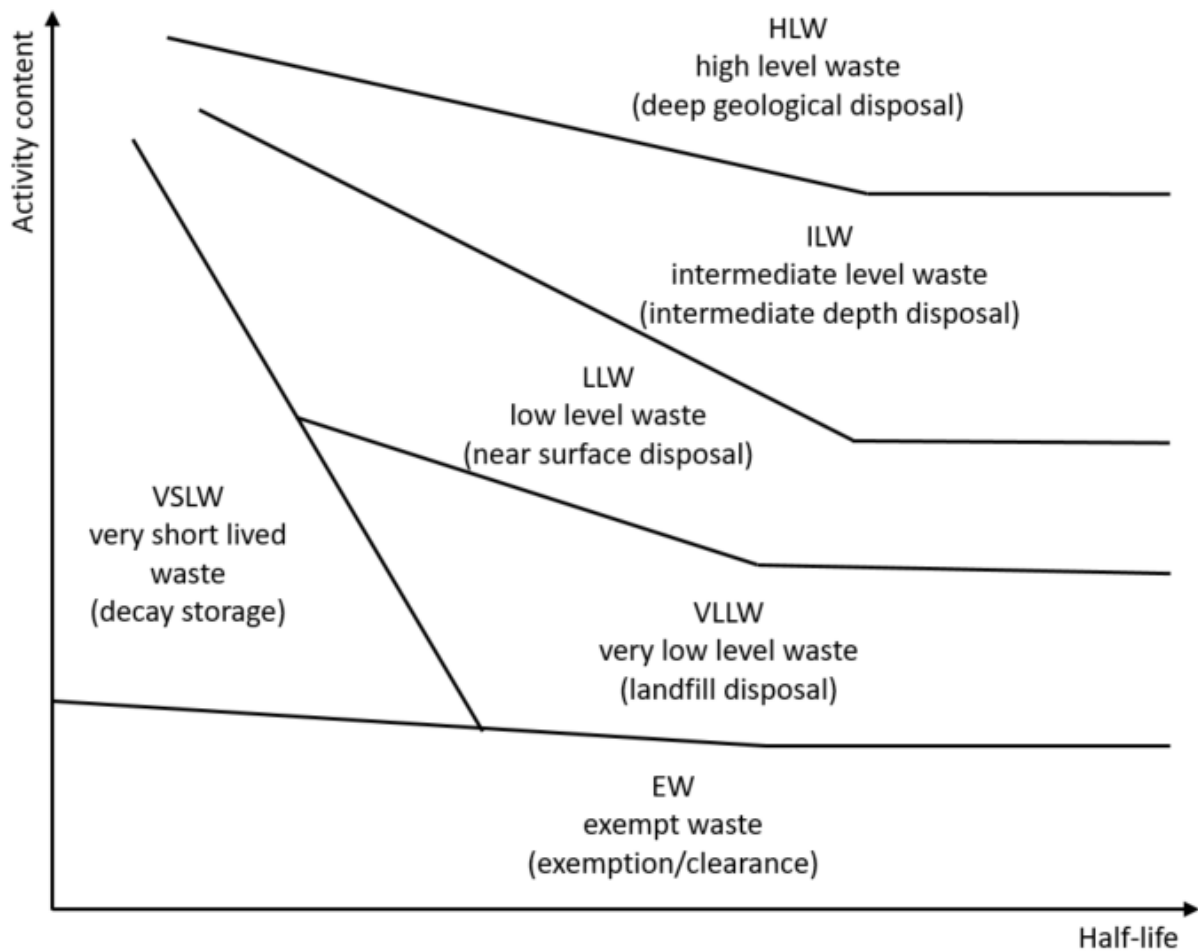


Figure 2.2: schematic overview of the nuclear waste types. Adapted from ³².

Approximately 90 % of the total volume of nuclear waste is low-level waste, which contains only 1 % of the total radioactivity. On the other hand, high-level waste accounts only for 3 % of the total volume of nuclear waste, but contains 95 % of the total activity ²⁰. The total inventory of nuclear waste in the European Union in 2013 is shown in Table 2.3.

Table 2.3: total amount of nuclear waste and spent fuel in the European Union in 2013 ²⁰.

Waste category	Total volume
VLLW	516,000 m ³
LLW	2,453,000 m ³
ILW	338,000 m ³
HLW	6,000 m ³
Spent fuel (HLW)	54,300 tons

2.2.2 Repository concepts

The repository concepts for the disposal of nuclear waste mostly depend on the waste type and the country. In the following chapters, some concepts for the disposal of high and intermediate-level wastes are introduced.

2.2.2.1 High-level waste (HLW)

The largest amount of the worldwide existing high-level waste corresponds to spent nuclear fuel (SNF), which consists of the original UO₂ matrix, fission products (¹³⁷Cs, ¹³¹I, ⁹⁹Tc, ⁹⁰Sr, ⁷⁹Se among others), transuranic elements (e.g. ²³⁹Pu, ²³⁷Np or ²⁴¹Am), which are formed by neutron capture and following β decay and activation products (⁶⁰Co, ⁶³Ni among others)³³. Due to the large heat production and the very high activity, spent nuclear fuel is stored for several years in interim storage before final disposal or reprocessing³⁴.

The internationally favored concept for final disposal of high-level waste relies on the construction of underground repositories in deep geological formations (host rocks), which have to ensure that regulatory limits are not exceeded. Depending on the composition of the waste, the final repositories have to be designed for up to one million years³⁵. Prior to storage, a manageable waste form is necessary. Therefore, the vitrification of liquid nuclear waste in borosilicate glass matrices was developed³⁶.

2.2.2.1.1 Multi-barrier concept

An integral part of the disposal concept of high-level waste relies on the concept of multiple engineered and geological barriers to hinder radionuclides to be released in the environment. A first barrier is the waste package, including the waste form (e.g. glass, the spent fuel matrix), the container, usually made out of steel, copper or corrosion-resistant alloys and overpacking. The backfilling material (e.g. swelling clay, cement, concrete, ...) is part of the engineered barriers. The host rock itself is the geological barrier in the context of the disposal in deep geological formations. As waste form, durable forms with a low release of radionuclides are preferred. Backfilling materials help to reduce the water movement through a repository after closure, by filling the remaining space and to enhance the retention of radionuclides during their transport and migration. One of these materials is bentonite (swelling clay), investigated intensively as backfilling material for heat producing wastes³⁷.

2.2.2.1.2 Host rock systems

Another very important aspect of a final repository for nuclear waste is the choice of the most suitable deep geological formation. If the requirements for host rocks regarding mechanical and thermal stability, sorption properties or thermal conductivity are taken into account, three rock types, rock salt, clay and granite, may be potential host rocks for a final high-level waste repository^{37,38}. The advantages and disadvantages of the potential host rock types are shown in Table 2.4.

Table 2.4: Main properties of the different host rock types considered for the construction of underground repositories for nuclear waste^{38,39}.

Properties\host rocks	rock salt	clay	granite
Thermal conductivity	high (+)	low (-)	intermediate (=)
Permeability	very low (+)	low (+)	high/intermediate (-)
Strength	intermediate (=)	low/intermediate (-)	high (+)
Deformation behavior	viscous (+)	plastic/brittle (=)	brittle (-)
Radionuclide solubility	high (-)	very low (+)	very low (+)
Sorption properties	low (-)	very high (+)	low/intermediate (-)
Thermal stability	high (+)	low (-)	high (+)

(+): advantage, (-): disadvantage

2.2.2.1.3 Actual situation of repositories for HLW

In most countries that produce or have produced nuclear energy, final disposal facilities for high-level waste are not yet in operation. In Finland and Sweden, granite formations are selected as host rock for high-level waste disposal facilities. In Finland, the ONKALO final repository was built and is expected to start operation in the mid-2020s^{20,40,41}. In Sweden the plans for construction of a final repository were approved by the government^{20,42}. Belgium, Switzerland and France consider clay formations a possible host rock^{43,44}. In France the decree for construction of the Cigéo repository for high- and intermediate-level waste in a clay formation, located in eastern France, bordering Meuse and Haute-Marne departments is under investigation²⁰. In Germany, the selection process for a repository site for highly radioactive waste was launched in 2017. The site selection procedure started from a "white map", i.e. all German federal states and all regions were included in the search, considering salt, claystone and granite as host rock options. A first step in the selection process was published in 2020 with the interim report on subdomains, where for 54% of the area in Germany was selected as worth to be further investigated⁴⁵.

2.2.2.2 Intermediate-level waste (ILW)

Intermediate-level waste (ILW) contains usually operational waste from nuclear power plants and research facilities, in case of reprocessing fuel cladding materials like Zircaloy and contaminated materials from dismantling reactors. In many cases, the waste is packed with cement in steel or concrete containers together with cement or grout as backfilling material ⁴⁶. In France, it is planned to dispose intermediate-level waste in a separate part of the planned Cigéo repository for high-level waste. For the final disposal of low-level and intermediate-level waste in Germany, a repository in a former iron ore mine at shaft Konrad near Salzgitter (Niedersachsen, Germany) is approved and under construction ^{34,46}. Beginning of the 2030s the storage of up to 303,000 m³ LLW and ILW is planned to start ⁴⁷.

2.2.3 Zirconium containing waste

As previously mentioned, radioactive zirconium isotopes are produced by fission reaction of ²³⁵U and by neutron capturing in the cladding material of nuclear fuel. The most relevant zirconium isotope in context nuclear waste disposal is ⁹³Zr ($t_{1/2} = 1.53 \cdot 10^6$ a) due to its long half-life ¹.

If separated from the spent nuclear fuel in reprocessing, the fuel cladding material is classified as intermediate-level waste and usually disposed in geological repositories within steel or concrete containers and with cement as backfilling material ⁴⁶.

2.3 Zirconium

Zirconium was discovered in 1789 by M. H. Klaproth in the mineral zircon, which was already known since the antiquity. The successful isolation of zirconium was achieved by J. J. Berzelius only in 1824 ⁴⁸. Zirconium is a silvery-white transition metal with an atomic number of 40 and part of the 4th group of the periodic table together with titanium, hafnium and rutherfordium. Zirconium has an atomic mass of 91.224 g mol⁻¹ and an electron configuration of [Kr]4d²5s², which explains the predominant oxidation state of zirconium as +IV. At room temperature and normal pressure, zirconium forms a hexagonal close-packed structure (α -Zr, $a = 3.233 \text{ \AA}$, $c = 5.148 \text{ \AA}$, at 298 K ⁴⁹), which transforms to a cubic body-centered structure (β -Zr, $a = 3.62 \text{ \AA}$ at 1135 K ⁵⁰) at 1135 K ⁴⁹.

Several zirconium isotopes with masses from 77 to 113 exist ⁵¹, while the naturally occurring zirconium is composed of five isotopes, the stable ⁹⁰Zr, ⁹¹Zr, ⁹²Zr, ⁹⁴Zr and the very long-lived ⁹⁶Zr. Important properties like natural abundance or half-life of the natural and the most important radioactive Zr isotopes are shown in Table 2.5.

Table 2.5: abundance, half-life and decay type of natural and the most important radioactive Zr isotopes ⁵¹.

Isotope	Natural abundance [%]	Half-life	Decay type
⁸⁹ Zr	synthetic	78.360 h	β ⁺
⁹⁰ Zr	51.45	stable	
⁹¹ Zr	11.22	stable	
⁹² Zr	17.15	stable	
⁹³ Zr	synthetic	1.53 · 10 ⁶ a	β ⁻
⁹⁴ Zr	17.38	stable*	
⁹⁵ Zr	synthetic	64.032 d	β ⁻
⁹⁶ Zr	2.80	20 · 10 ¹⁸ a	β ⁻

*predicted to undergo double beta decay, experimentally not observed.

Radioactive Zr isotopes (except the naturally occurring ⁹⁶Zr) are either created by fission reaction of ²³⁵U ¹ or due to the use of zirconium alloys as fuel cladding in nuclear power reactors, where neutron capture on stable Zr isotopes produces radioactive isotopes ⁵². In the context of nuclear waste disposal, ⁹³Zr is of particular interest due to its long half-life and high yield of 6.3-6.4% ⁸ in fission of uranium.

2.3.1 Applications of zirconium and zirconium(IV) oxide

Due to its good mechanical properties and high resistance against corrosion, zirconium and zirconium alloys are used as material to avoid corrosion in the chemical process industry ⁴⁸. The radioactive isotope ⁸⁹Zr with a half-life of 78.36 hours is an interesting nuclide for positron emission tomography (PET), since it enables imaging of long circulating probes and shows advantages in production, purity and uptake by tumor cells compared to other available isotopes as ¹²⁴I. Therefore the application of ⁸⁹Zr in PET is a promising research field ^{53,54}.

Another application of relevance is the use of zirconium alloys (Zircaloy) as fuel cladding in nuclear power reactors. Advantages of the use of zirconium alloys are the resistance to corrosion and a low neutron capture cross section ⁴⁸. A disadvantage is the formation of hydrogen due to reaction of the zirconium with water ($Zr + 2 H_2O \rightarrow ZrO_2 + 2 H_2$), leading to degradation of the fuel cladding. This corrosion process is slow under normal working conditions of a reactor, but increases rapidly, if the temperature in the reactor is increased ⁵⁵. To be useful as fuel cladding, impurities of hafnium have to be removed completely from natural Zr sources due to the much higher neutron capture cross section of Hf compared to Zr, rising difficulties in the production of zirconium alloys due to the chemically very similar behavior of Zr and Hf and their joint natural occurrence. Nevertheless, zirconium alloys are widely used as fuel cladding. An overview of the composition of the most common zirconium alloys and the reactor type in which they are used, is given in Table 2.6.

Table 2.6: Zircaloy compositions and reactor types, in which they are used as fuel cladding and as reactor components ^{48,56}.

Alloying elements [weight%]	Zircaloy-2 Fuel cladding in: SGHWR*, BWR* Reactor components in: SGHWR*, CANDU*	Zircaloy-4 Fuel cladding in: CANDU*, PWR*	ZIRLO® Fuel rods and structural components in: Light Water Reactor	M5 Fuel rods and structural components in: Light Water Reactor
Sn	1.20-1.70	1.20-1.70	1	
Nb			1	0.8-1.2
Fe	0.07-0.20	0.18-0.24	0.1	0.015-0.06
Cr	0.05-0.15	0.07-0.13		
Ni	0.03-0.08			
O	0.09-0.16	0.09-0.16	0.12	0.09-0.12
Si	0.005-0.012	0.005-0.012		
Hf	<0.01	<0.01		

*SGHWR: Steam Generating Heavy Water Reactor

BWR: Boiling Water Reactor

CANDU: CANadian Deuterium Uranium

PWR: Pressurised Water Reactor

Besides the applications of metallic zirconium, also zirconium(IV) oxides (zirconia) shows properties interesting for applications in several fields. The high mechanical strength, the fracture toughness and the good biocompatibility of zirconia are advantages over other ceramics and allows biomedical applications for example as bone fillers, as dental crowns or in arthroplasty ⁵⁷. Yttria-stabilized zirconia (see chapter 2.3.2.1) has a low electric but high ionic conductivity allowing its use in oxygen sensors to determine the air/fuel ratio in motors as well as the use in solid oxide fuel cell (SOFC). Since zirconia is a thermal and electric insulator, it is an important material for electric and mechanic components ⁵⁷.

2.3.2 Zirconium(IV) oxide solid phases and crystal structures

Due to its high charge-to-size (z/d) ratio, Zr(IV) is characterized by a strong hydrolysis and the formation of sparingly soluble hydrous oxides. Hence, the amorphous hydrous oxides of zirconium, best defined as $ZrO_x(OH)_{4-2x} \cdot zH_2O$, are expected to be the solid phases determining the aqueous chemistry of Zr(IV) at room temperature over a wide range of pH-conditions. Elevated temperatures may cause a transformation process towards thermodynamically more stable crystalline solid phases, $ZrO_2(cr)$, with expectedly lower solubility. Accordingly, the investigation of the aqueous chemistry of amorphous and crystalline zirconium oxide solid phases as well as the effects of elevated temperatures on the solid phases is necessary in the context of nuclear waste disposal^{1-7,16-18}.

Crystalline ZrO_2 is known to form three different polymorphs. The naturally occurring solid phase stable at low temperature shows a monoclinic structure with the space group $P2_1/c$. Tetragonal (space group $P4_2/nmc$) and cubic (space group $Fm\bar{3}m$) crystal structures are also observed above temperatures of $T = (1447 \pm 30)$ K and (2566 ± 8) K, respectively. At $T = (2953 \pm 15)$ K transition of the cubic phase towards liquid is observed¹⁷. The structures and some properties of the different crystal phases are shown in Figure 2.3 and Table 2.7.

Table 2.7: properties of monoclinic, tetragonal and cubic ZrO_2 .

	Monoclinic	Tetragonal	Cubic
Space group	$P2_1/c$ ¹⁷	$P4_2/nmc$ ¹⁷	$Fm\bar{3}m$ ¹⁷
Temperature range (atmosphere pressure)	< 1447 K ¹⁷	1447-2566 K ¹⁷	2566-2953 K ¹⁷
Lattice parameters			
a [Å]	5.15 ⁵⁸	3.60 ⁵⁹	5.07 ⁵⁰
b [Å]	5.21 ⁵⁸		
c [Å]	5.31 ⁵⁸	5.18 ⁵⁹	
γ [°]	99.1 ⁵⁸		
Density [g cm ⁻³]	5.82*	6.10*	6.28*/6.07**

*calculated from the lattice parameters. **Ca-stabilized zirconia⁶⁰

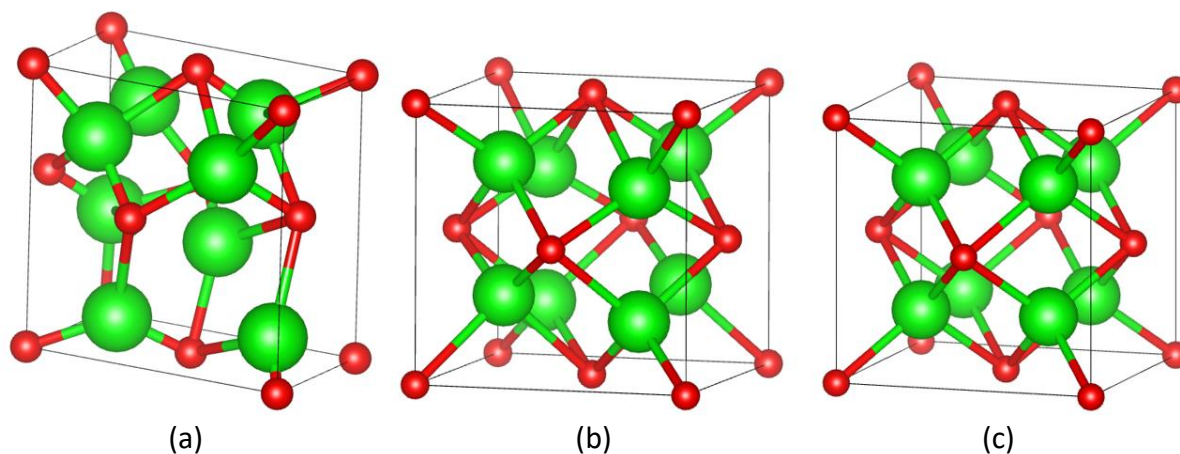


Figure 2.3: schematic structures of (a) monoclinic, (b) tetragonal and (c) cubic ZrO_2 . Adapted from ⁶¹.

While crystalline ZrO_2 solid phases are well characterized, the poorly crystalline solid phases expected to control the solubility of Zr(IV) in aqueous systems are less investigated in the literature, as well as the mechanism and kinetics for the transformation into $\text{ZrO}_2(\text{cr})$. A review on crystallization of ZrO_2 from amorphous precursors, the effects of particle size on the crystal structure, the stabilization of high temperature phases at room temperature by addition of lanthanides or calcium, the effect of temperature on amorphous ZrO_2 phases, aqueous speciation of Zr(IV) and Zr(IV) solubility is given in the following.

By thermal decomposition of amorphous precipitates, the thermodynamically metastable tetragonal or cubic solid are often stabilized instead of the most stable monoclinic solid phase. As reason for this, preordering in the amorphous solids, impurities or effects of particle size/surface area are discussed ¹⁷. Studies on the transformation mechanisms and preordering were conducted quite early. In 1935, Thomas and Owens observed an increase of pH by adding neutral salts to neutral solutions with Zr hydrosols and explained this by the possibility of exchange between hydroxide in the solid and the added anions. They also observed that basic zirconium hydrosols become more acidic with time or by heating and attributed this effect to olation and oxolation of the solids ⁶². Fryer et al. conducted microscopic studies in 1970 and observed the presence of the tetrameric $[\text{Zr}(\text{OH})_2 4\text{H}_2\text{O}]_4^{8+}$ as hydrolysis product of zirconyl chloride. Under heating they observed first the formation of two dimensional sheets based on the tetrameric species connected by double hydroxide bridges. By further heating, monoclinic ZrO_2 was created by oxolation ⁶³. In 1974, Keramidis and White performed a Raman scattering study on the crystallization and phase transformation of ZrO_2 . After dehydration by heating 1 hour at 473 K their precipitated amorphous ZrO_2 still does not show diffraction peaks measured by XRD, but Raman signals corresponding to tetragonal ZrO_2 , which the authors explained by a nanoscale preordering with a smaller periodicity than the coherence length of

x-rays. By further heating at 773 K the authors observed an abrupt crystallization of the metastable tetragonal solid with traces of monoclinic ZrO₂ (XRD and Raman) and at 1273 K a complete transformation towards the monoclinic solid ⁶⁴.

The effects of particle size and surface area on the crystal structure were studied by Pitcher et al., who investigated nanocrystalline tetragonal, monoclinic and amorphous ZrO₂ solids with different surface areas by high-temperature oxide melt solution calorimetry in order to measure surface enthalpies of the solids in 2005. This resulted in phase transition enthalpies and a stability map for ZrO₂, showing stability crossovers from monoclinic (thermodynamically most stable phase for solids with a surface area <2500 m²/mol or >48 nm particle size, respectively) to tetragonal (2500-15000 m²/mol, 9-48 nm) to amorphous (>15000 m²/mol, <9 nm) solid phases with increasing surface area, and thus decreasing particle size ¹⁴. More recently, in 2018, Sharma and co-workers proposed a new stability map for ZrO₂ calculated based on enthalpy data from previous experiments ¹⁵. These newer calculations show amorphous (<3 nm), cubic (3-6 nm), tetragonal (6-48 nm) and monoclinic (>48 nm) ZrO₂ as crystal structures as function of the particle size, thus reflecting the contribution of the surface energetics on the overall stabilization of a given structure.

Another possibility for the stabilization of the high-temperature polymorphs at lower temperatures is the addition of a few percent of lanthanide oxides ¹⁷. According to Li, Chen and Penner-Hahn, this effect is caused by the distortion of the Zr-O polyhedra by creation of vacancies or the inclusion of over or undersized cations ⁶⁵⁻⁶⁸. A similar behavior is also known for Ca, which can stabilize both the tetragonal (1-5 mol% CaO) and the cubic (>7 mol% CaO) crystal structure ⁹. The low temperature formation of calcium zirconate (CaZrO₃) and other sub-stoichiometric ternary oxides was also previously shown ^{12,13}. While CaZrO₃ is conventionally synthesized by a solid-solid reaction of ZrO₂ and CaCO₃ at temperatures higher than 1300°C, Li and co-workers were able to synthesize CaZrO₃ from molten salts out of CaCl₂, Na₂CO₃ and ZrO₂ at 700°C ¹². Sub-stoichiometric compounds as CaZr₄O₉ can be found at lower temperatures and with lower CaO mol% ¹³. Even if such high temperatures and Ca concentrations are not expected in nuclear waste repositories, the long storage time, the possible presence of Ca and the expectedly higher reactivity of amorphous hydrous zirconium oxides compared to crystalline ZrO₂ make the formation of ternary Ca-Zr-oxides possible.

Kobayashi and co-workers ^{1,69,70} investigated the effect of temperature (T = 323-363 K) on the solubility and structure of an amorphous zirconium hydrous oxide, ZrO₂(am, hyd). In 2013, they investigated the effect of equilibration of zirconium oxyhydroxide solids at 323, 343 and 363 K on the solubility and the characteristics of the solid phase. Their XRD and TEM measurements show the agglomeration and crystallization with temperature towards thermodynamic more stable solid phases, accompanied by a clear decrease of the solubility after ageing at 363 K ¹. In their study in 2015, the solubility of zirconium hydroxides and oxides

at 278, 298, 313 and 333 K after ageing at 278, 313 and 333 K was investigated. For their aged amorphous hydrous oxides, a significant decrease in solubility with increasing ageing temperature was observed, while the effect of the temperature during the solubility measurements had only a minor impact. In case of the crystalline ZrO_2 solids both, the ageing and the measurement temperature show a limited effect on the solubility⁶⁹. More recently, their study from 2019 focused more on a structural approach to understand the effect of temperature on the solubility and structure of ZrO_2 (am, hyd), investigating these solids by means of WAXS, SAXS, EXAFS and TEM techniques. The authors demonstrated that solid phases aged at $T = 298$ K contain hierarchical structures of aggregates of primary particles built of zirconium hydroxide tetramers and dimers. Investigations with solid phases aged at $T = 298, 313, 333$ and 363 K with different pHs showed that these hierarchical structures are stable up to 333 K under acidic and neutral conditions and up to 313 K under alkaline conditions. By ageing at $T = 363$ K in acidic media and ageing at $T = 333$ and 363 K under alkaline conditions the formation of crystalline solids with the previously shown effects on the solubility was observed⁷⁰.

2.3.3 Aquatic chemistry of Zr

The scenario of water intrusion and early canister failure leading to the formation of aqueous systems requires an accurate knowledge of the aquatic chemistry of radionuclides in the context of a repository for nuclear waste. The solubility and aqueous speciation of Zr(IV) was intensively investigated in the literature. However, solid phases used in these studies are often only poorly characterized, and the measurement conditions also strongly vary. This leads to a large scattering in the solubility data, which is also reflected by some discrepancies in the reported thermodynamic data, e.g., speciation models or solubility products.

Connick et al. conducted complexation experiments using the solvent extraction technique. Their experiments at 398 K in 2 M $HClO_4$ showed the predominance of equal amounts of Zr^{4+} and $ZrOH^{3+}$ under these conditions⁷¹. Peshkova and co-workers performed complexation experiments using the solvent extraction technique at 398 K in 1 M $(Na, H)ClO_4$ and were able to determine stability constants for $ZrOH^{3+}$, $Zr(OH)_2^{2+}$, $Zr(OH)_3^+$ and $Zr(OH)_4(aq)$ ⁷². Davydov and Zabrodskii studied the hydrolysis of Zr(IV) in 0.5 M $(Na, H)ClO_4$, 1.0 M $(Na, H)ClO_4$ and 0.5 M $(Na, H)NO_3$ using different techniques based on ion exchange, spectrophotometry, dialysis or centrifugation. Based on their combined experimental methods, the authors reported the stability constants for $ZrOH^{3+}$ and $Zr(OH)_2^{2+}$ ⁷³. Ekberg et al. investigated the hydrolysis of Zr(IV) in 1.0 M $(H, Na)ClO_4$ at $288, 298$ and 308 K by potentiometric methods as well as solvent extraction and solubility experiments. Their data can be explained by a speciation model divided into three main pH regions. Between $0.9 < pH < 2.0$ a combination of Zr^{4+} , $ZrOH^{3+}$,

$Zr(OH)_2^{2+}$ and $Zr(OH)_3^+$ explains the data best. The pH independent solubility at $2.9 < pH < 12.5$ is explained by the predominance of $Zr(OH)_4(aq)$. The increasing solubility with a slope of 1.9 at $pH > 13$ was interpreted to be caused by the formation of ZrO_3^{2-} or $Zr(OH)_6^{2-}$ ⁷⁴.

Based on these and various other studies the NEA-TDB (Brown et al.) selected in 2005 a hydrolysis model including Zr^{4+} , $ZrOH^{3+}$, $Zr(OH)_2^{2+}$, $Zr(OH)_3^+$, $Zr_3(OH)_4^{8+}$, $Zr_3(OH)_9^{3+}$, $Zr_4(OH)_8^{8+}$ and $Zr_4(OH)_{15}^+$ at $0.9 < pH < 2.0$, $Zr(OH)_4(aq)$ and / or polynuclear species such as $Zr_4(OH)_{16}(aq)$ for $2.9 < pH < 12.5$ and $Zr(OH)_6^{2-}$ at $pH > 12.5$ with the polynuclear species predominating at higher Zr concentrations and mononuclear species at lower Zr concentrations ¹⁷. Besides the formation of binary hydrolysis species, the strong interaction with Ca^{2+} and the consequent formation of ternary aqueous complexes Ca-Zr(IV)-OH has been described in alkaline, dilute to concentrated $CaCl_2$ solutions by Altmaier and co-workers in solubility studies of Zr(IV) at 295 K in alkaline 0.1 M to 4.5 M $CaCl_2$ solutions. The formation of the ternary complexes $Ca[Zr(OH)_6](aq)$, $Ca_2[Zr(OH)_6]^{2+}$ and $Ca_3[Zr(OH)_6]^{4+}$ was shown in presence of calcium. $Zr_n(OH)_{4n} aq$, $Zr(OH)_6^{2-}$, $Zr_3(OH)_9^{3+}$, $Ca_2[Zr(OH)_6]^{2+}$ and $Ca_3[Zr(OH)_6]^{4+}$ were determined as relevant species under the given experimental conditions ¹⁹. These aqueous complexes may play a role in brine systems with high $CaCl_2$ concentrations, but also in cementitious environments where calcium concentrations up to 20 mM are expected.

Sasaki and co-workers performed oversaturation solubility experiments of hydrous zirconium(IV) oxides ⁷⁵ delivering a solubility constant (explained on page 28 in the chapter 2.3.3.1.1) of $\log^* K_{s,0}^\circ = -0.94 \pm 0.32$ for their amorphous solid. Altmaier et al. investigated the solubility of Zr(IV) in alkaline 0.1–4.5 $CaCl_2$ and alkaline $Ca(ClO_4)_2$ solutions as well as over the entire pH range in NaCl and $CaCl_2$ solutions and evaluated a solubility products of $\log^* K_{s,0}^\circ = -4.3 \pm 0.2$ for a freshly precipitated amorphous solid which was stored for several weeks to avoid ageing effects during the experiments ¹⁹. Kobayashi and co-workers performed several undersaturation solubility studies in acidic conditions and determined solubility constants $\log^* K_{s,0}^\circ$ of -5.4 ± 0.2 , -5.7 ± 0.3 and -6.46 ± 0.1 for $Zr(OH)_4$ nano powder heated to $90^\circ C$ ¹, $Zr(OH)_4(s)$ heated to $90^\circ C$ ¹ and a crystalline phase $ZrO_2(cr)$ ⁷⁶, respectively. Zouari ⁷⁷ investigated the solubility of crystalline ZrO_2 (cubic and monoclinic) under acidic conditions and determined solubility products of $\log^* K_{s,0}^\circ = -5.8$ and -7.0 ± 0.4 for yttrium stabilized cubic and monoclinic ZrO_2 , respectively. The NEA-TDB selected $\log^* K_{s,0}^\circ = -3.24 \pm 0.1$ as solubility constant for fresh amorphous $Zr(OH)_4$ and $\log^* K_{s,0}^\circ = -7.0 \pm 1.6$ for crystalline ZrO_2 .

2.3.3.1 Thermodynamic description of Zr(IV) in aqueous media

2.3.3.1.1 Thermodynamic background of solubility and hydrolysis equilibria

In general the dissolution of a metal oxide/hydroxide in a given background electrolyte can be described as ¹⁷:



with the corresponding conditional solubility constant $K'_{s,0}$ defined by ¹⁷:

$$K'_{s,0} = [M]^a [L]^b \quad \text{and} \quad \log K'_{s,0} = a \log[M] + b \log[L] \quad (2.2)$$

where M is the metal, L is a random ligand (in the context of this work oxide/hydroxide) and a and b are their stoichiometric numbers. Square brackets indicate molar concentrations and the sub-indices “s” and “0” show that this is a solubility constant representing the equilibrium with the unhydrolyzed cation (Zr^{4+} in the current study) and no complexed species are included. The solubility constant under standard conditions ($I = 0$ (ionic strength), $T = 25^\circ\text{C}$, $P = 1$ bar) $K^\circ_{s,0}$ can be described as ¹⁷:

$$\log K^\circ_{s,0} = a \log a_M + b \log a_L \quad (2.3)$$

where a_i is the activity of the ion i defined as ¹⁷:

$$a_i = [i] \gamma_i \quad (2.4)$$

where γ_i is the activity coefficient of the ion i . The activity coefficients can be calculated with different activity models, from which the Specific Ion interaction Theory (SIT) has been favored in the current work, in line with the activity model systematically used in the NEA-TDB reviews (see page 30). Combining equations 2.2-2.4, the solubility constant under standard conditions $\log K^\circ_{s,0}$ can be expressed as ¹⁷:

$$\log K_{s,0}^{\circ} = \log K'_{s,0} + \sum \log \gamma (\text{products}) - \sum \log \gamma (\text{reactants}) \quad (2.5)$$

As described above, Zr(IV) (and tetravalent metals ions in general) tends to hydrolyze very strongly, meaning reacting with water under the formation of hydrolysis species. The general hydrolysis reaction is given by ¹⁷:



or



depending if H₂O or OH⁻ are selected as reaction partner. In a given background electrolyte concentration, the conditional hydrolysis constant $^*\beta'_{(n,m)}$ (with H⁺/H₂O) or $\beta'_{(n,m)}$ (with OH⁻) are described as ¹⁷:

$$^*\beta'_{(n,m)} = \frac{[M_n(OH)_m^{(nz-m)}][H^+]^m}{[M^{z+}]^n} \quad \text{or} \quad \beta'_{(n,m)} = \frac{[M_n(OH)_m^{(nz-m)}]}{[M^{z+}]^n[OH^-]^m} \quad (2.8)$$

respectively. Analogous to the solubility constant also the hydrolysis constant can be converted to standard conditions. For the general hydrolysis reaction, the hydrolysis constant under standard conditions $\log ^*\beta_{(n,m)}^{\circ}$ or $\log \beta_{(n,m)}^{\circ}$ can be described as ¹⁷:

$$\log ^*\beta_{(n,m)}^{\circ} = \log ^*\beta'_{(n,m)} + \log \gamma_{M_n(OH)_m^{(nz-m)}} + m \log \gamma_{H^+} - n \log \gamma_{M^{z+}} - m \log a_w \quad (2.9)$$

or

$$\log \beta_{(n,m)}^{\circ} = \log \beta'_{(n,m)} + \log \gamma_{M_n(OH)_m^{(nz-m)}} - m \log \gamma_{OH^-} - n \log \gamma_{M^{z+}} \quad (2.10)$$

2.3.3.1.2 Specific Ion interaction Theory (SIT) model

When reactions are taking place in solutions with an ionic strength (I) different than 0, corrections considering the ionic strength of the system have to be done, since the activity coefficient of the ions are affected by the other ions present in the system. Out of the various available methods to estimate the effects of ions, the specific ion interaction theory (SIT) is systematically used in this work¹⁷. In SIT, the activity coefficient γ_j of an ion j with the charge z_j in solutions can be described as:

$$\log \gamma_j = -z_j^2 D + \sum_k \varepsilon(j, k, I_m) m_k \quad (2.11)$$

where D is the Debye-Hückel term taking into account non-specific electrostatic interactions, $\varepsilon(j, k, I_m)$ the specific ion interaction coefficient between the ions j and k at a given ionic strength and m_k the molal concentration of the ion k ¹⁷. The ionic strength can be calculated with the molal concentrations m_i and the charges z_i of all ions as:

$$I_m = \frac{1}{2} \sum_i m_i z_i^2 \quad (2.12)$$

The Debye-Hückel term D is defined as:

$$D = \frac{A\sqrt{I_m}}{1+B a_j \sqrt{I_m}} \quad (2.13)$$

where $A = 0.509 \text{ kg}^{1/2} \text{ mol}^{-1/2}$ and $B a_j = 1.5 \text{ kg}^{1/2} \text{ mol}^{-1/2}$ are constants referring to standard conditions (25°C, 1 bar)¹⁷.

2.3.3.1.3 Thermodynamic data

Thermodynamic data have been used in this work for two different purposes. In a first application, existing thermodynamic constants for the solubility and hydrolysis of Zr(IV) have been used to calculate solubility curves for fresh amorphous, aged and crystalline ZrO₂ solids. Secondly, hydrolysis constants reported in the literature have been combined with experimental solubility data obtained in this work to derive the solubility constants for the solid phases prepared in this work. Solubility products, hydrolysis constants and specific ion interaction coefficients used in this work were taken from the NEA-TDB book on zirconium ¹⁷ and from Altmaier *et al.* ¹⁹, and are shown in Table 2.8 and 2.9.

Table 2.8: Equilibrium constants for Zr(IV) solubility and hydrolysis reactions.

Solubility (of Zr(OH) ₄ or ZrO ₂ + 2H ₂ O)	log* K_{s,0}^o	reference
Zr(OH) ₄ (am, hyd, fresh) + 4H ⁺ ⇌ Zr ⁴⁺ + 4H ₂ O*	-3.2 ± 0.1	Altmaier <i>et al.</i> ¹⁹ /NEA-TDB ¹⁷
Zr(OH) ₄ (am, hyd, aged) + 4H ⁺ ⇌ Zr ⁴⁺ + 4H ₂ O	-4.3 ± 0.2	Altmaier <i>et al.</i> ¹⁹
ZrO ₂ (cr) + 2H ₂ O + 4H ⁺ ⇌ Zr ⁴⁺ + 4H ₂ O	-7.0 ± 1.7	Altmaier <i>et al.</i> ¹⁹ /NEA-TDB ¹⁷
Hydrolysis	log* β_(n,m)^o	reference
Zr ⁴⁺ + H ₂ O ⇌ ZrOH ³⁺ + H ⁺	0.32 ± 0.22	NEA-TDB ¹⁷
Zr ⁴⁺ + 2H ₂ O ⇌ Zr(OH) ₂ ²⁺ + 2H ⁺	0.98 ± 1.06	NEA-TDB ¹⁷
Zr ⁴⁺ + 4H ₂ O ⇌ Zr(OH) ₄ (aq) + 4H ⁺	-3.5 ± 0.7** /2.19 ± 1.7	Altmaier <i>et al.</i> ¹⁹ / NEA-TDB ¹⁷
Zr ⁴⁺ + 6H ₂ O ⇌ Zr(OH) ₆ ²⁻ + 6H ⁺	-29.2 ± 0.3 / -29.0 ± 0.7	Altmaier <i>et al.</i> ¹⁹ / NEA-TDB ¹⁷
3Zr ⁴⁺ + 4H ₂ O ⇌ Zr ₃ (OH) ₄ ⁸⁺ + 4H ⁺	0.4 ± 0.3	NEA-TDB ¹⁷
3Zr ⁴⁺ + 9H ₂ O ⇌ Zr ₃ (OH) ₉ ³⁺ + 9H ⁺	12.19 ± 0.08	NEA-TDB ¹⁷
4Zr ⁴⁺ + 8H ₂ O ⇌ Zr ₄ (OH) ₈ ⁸⁺ + 8H ⁺	6.52 ± 0.65	NEA-TDB ¹⁷
4Zr ⁴⁺ + 15H ₂ O ⇌ Zr ₄ (OH) ₁₅ ⁺ + 15H ⁺	12.58 ± 0.24	NEA-TDB ¹⁷
Hydrolysis species in presence of Ca	log* β_(n,m)^o	reference
Zr ⁴⁺ + 6H ₂ O + Ca ²⁺ ⇌ Ca[Zr(OH) ₆](aq) + 6H ⁺	-24.6 ± 0.3	Altmaier <i>et al.</i> ¹⁹
Zr ⁴⁺ + 6H ₂ O + 2Ca ²⁺ ⇌ Ca ₂ [Zr(OH) ₆] ²⁺ + 6H ⁺	-22.6 ± 0.3	Altmaier <i>et al.</i> ¹⁹
Zr ⁴⁺ + 6H ₂ O + 3Ca ²⁺ ⇌ Ca ₃ [Zr(OH) ₆] ⁴⁺ + 6H ⁺	-23.2 ± 0.3	Altmaier <i>et al.</i> ¹⁹

*ZrO₂(am, hyd) and Zr(OH)₄(am, hyd) denote the same solid phase. **calculated value from log K_{s,4}^o = -7.8 for the reaction Zr(OH)₄(s) ⇌ Zr(OH)₄(aq) and log K_{s,0}^o = -4.3 for the reaction Zr(OH)₄(s) + 4H⁺ ⇌ Zr⁴⁺ + 4H₂O.

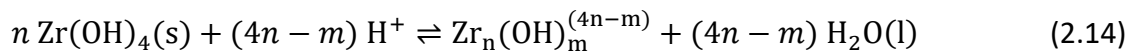
Table 2.9: Ion interaction coefficients $\epsilon(M^{n+}, X^y)$ for all aqueous species considered in the thermodynamic calculation in this work.

Species	$\epsilon(M^{n+}, Cl^-)$ [kg mol ⁻¹]	reference
H ⁺	0.12 ± 0.01	NEA-TDB ¹⁷
Ca ²⁺	0.14 ± 0.01	NEA-TDB ¹⁷
Zr ⁴⁺	0.33 ± 0.09	NEA-TDB ¹⁷
ZrOH ³⁺	0.22 ± 0.11	Altmaier <i>et al.</i> ¹⁹
Zr(OH) ₂ ²⁺	0.24 ± 0.18	Altmaier <i>et al.</i> ¹⁹
Zr(OH) ₄ aq	0	NEA-TDB ¹⁷
Zr ₃ (OH) ₄ ⁸⁺	0.33 ± 0.28	NEA-TDB ¹⁷
Zr ₃ (OH) ₉ ³⁺	0.30 ± 0.11	Altmaier <i>et al.</i> ¹⁹
Zr ₄ (OH) ₈ ⁸⁺	1.37 ± 0.40	Altmaier <i>et al.</i> ¹⁹
Zr ₄ (OH) ₁₅ ⁺	0.03 ± 0.36	Altmaier <i>et al.</i> ¹⁹
Zr(OH) ₆ ²⁻	0	Altmaier <i>et al.</i> ¹⁹
Ca[Zr(OH) ₆] aq	0	Altmaier <i>et al.</i> ¹⁹
Ca ₂ [Zr(OH) ₆] ²⁺	0.1 ± 0.1	Altmaier <i>et al.</i> ¹⁹
Ca ₃ [Zr(OH) ₆] ⁴⁺	0.40 ± 0.07	Altmaier <i>et al.</i> ¹⁹
$\epsilon(Na^+, X^y)$ [kg mol⁻¹]		
Zr(OH) ₆ ²⁻	0.04 ± 0.08	Altmaier <i>et al.</i> ¹⁹
Zr(OH) ₄ (aq)	0	NEA-TDB ¹⁷
Ca[Zr(OH) ₆](aq)	0	Altmaier <i>et al.</i> ¹⁹
$\epsilon(Ca^{2+}, X^y)$ [kg mol⁻¹]		
Zr(OH) ₆ ²⁻	0*	Altmaier <i>et al.</i> ¹⁹
Zr(OH) ₄ (aq)	0	Altmaier <i>et al.</i> ¹⁹
Ca[Zr(OH) ₆](aq)	0	Altmaier <i>et al.</i> ¹⁹

*complex formation.

2.3.3.1.4 Thermodynamic calculations

Solubility curves are calculated as addition of the concentrations of the individual hydrolysis species, considering a given solid phase, pH, temperature and background electrolyte concentration. In a first step, equations 2.1 and 2.6 were merged and adapted to the system to reach the formation reaction of each species starting with a solid phase:



The corresponding solubility constant under standard conditions $\log^* K_{S,(n,m)}^\circ$ can be calculated by addition of the solubility product $\log K_{S,0}^\circ$ of a certain solid and the hydrolysis constant $\log^* \beta_{(n,m)}^\circ$ of the species, both given in Table 2.8:

$$\log^* K_{s,(n,m)}^\circ = \log K_{s,0}^\circ + \log^* \beta_{(n,m)}^\circ \quad (2.15)$$

Since reactions do not take place under standard conditions, the use of a background electrolyte has to be included in the solubility calculation. For this, the SIT approach (see equation 2.5) was used resulting in $\log^* K'_{s,(n,m)}$, the equilibrium constant for the formation of a certain hydrolysis species under the given conditions:

$$\log^* K'_{s,(n,m)} = \log^* K_{sp}^\circ - \sum \log \gamma (\text{products}) + \sum \log \gamma (\text{reactants}) \quad (2.16)$$

Applied to the investigated system this results for each hydrolysis species in:

$$\begin{aligned} \log^* K'_{s,(n,m)} &= \log K_{s,0}^\circ \text{ (of the selected } ZrO_2 \text{ solid)} \\ &+ \log^* \beta_{(n,m)}^\circ \text{ (of the selected } Zr_n(OH)_m^{(4n-m)} \text{ hydrolysis species)} \\ &- \log \gamma_{Zr_n(OH)_m^{(4n-m)}} + (4n - m) \log \gamma_{H^+} - (4n - m) \log a_w \end{aligned} \quad (2.17)$$

where γ values can be calculated as in equation 2.11 and a_w is the activity of water taken from NEA-TDB for a given electrolyte concentration ¹⁷.

The concentration of the species is a function of pH, as H^+ is included in the formation reaction of the hydrolysis species (equation 2.14). The equilibrium constant of this reaction $\log^* K'_{s,(n,m)}$ can be either calculated as in equation 2.17 or with its original definition:

$$\log^* K'_{s,(n,m)} = \log \frac{[\text{products}]}{[\text{reactants}]} = \log \frac{[Zr_n(OH)_m^{(4n-m)}][H_2O(l)]^{(4n-m)}}{[H^+]^{(4n-m)} [Zr(OH)_4(s)]^n} \quad (2.18)$$

Under the given conditions the concentration of water and the concentration of the solid phase in aqueous solutions can be neglected, leading to:

$$\log^* K'_{s,(n,m)} = \log [Zr_n(OH)_m^{(4n-m)}] - (4n - m) \log [H^+] \quad (2.19)$$

or

$$\log\left[\text{Zr}_n(\text{OH})_m^{(4n-m)}\right] = \log^* K'_{s,(n,m)} + (4n - m) \log[\text{H}^+] \quad (2.20)$$

The total zirconium concentration $[\text{Zr}]_{\text{tot}}$ can be calculated as:

$$\log[\text{Zr}]_{\text{tot}} = \log \sum_{n,m} n \cdot \left[\text{Zr}_n(\text{OH})_m^{(4n-m)}\right] \quad (2.21)$$

where $\sum_{n,m}$ is the sum over all hydrolysis species.

An exemplary solubility curve and a species fraction diagram calculated for a fresh solid in 0.1 M NaCl solution using the data from NEA-TDB¹⁷ are shown in Figure 2.4. The same diagrams calculated for a fresh solid in 0.1 M CaCl₂ solution using the data from Altmaier et al.¹⁹ are shown in Figure 2.5.

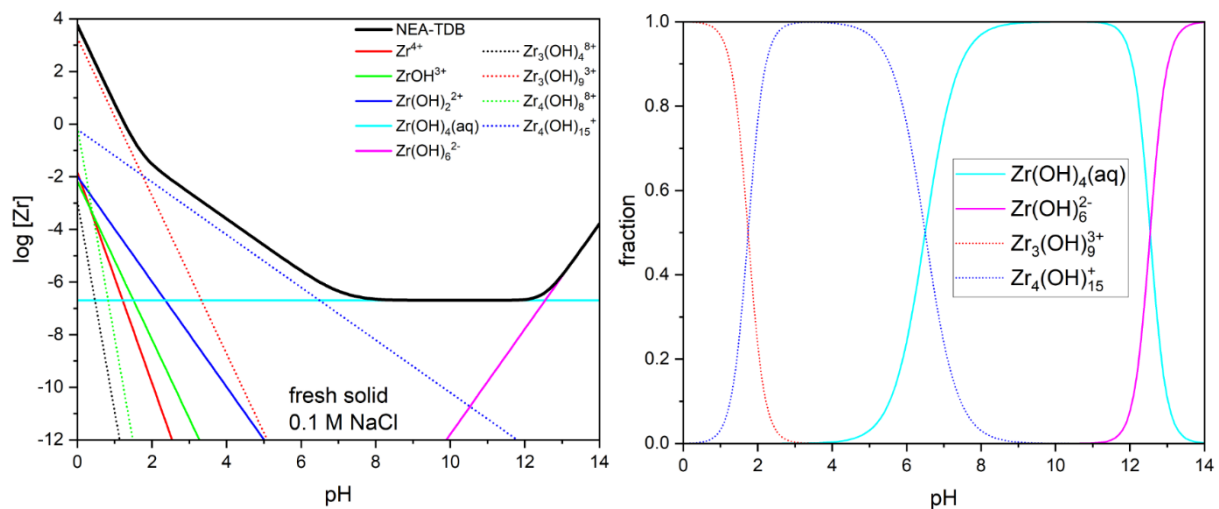


Figure 2.4: solubility curve and a species fraction diagram calculated for a fresh solid in 0.1 M NaCl using the data from NEA-TDB¹⁷.

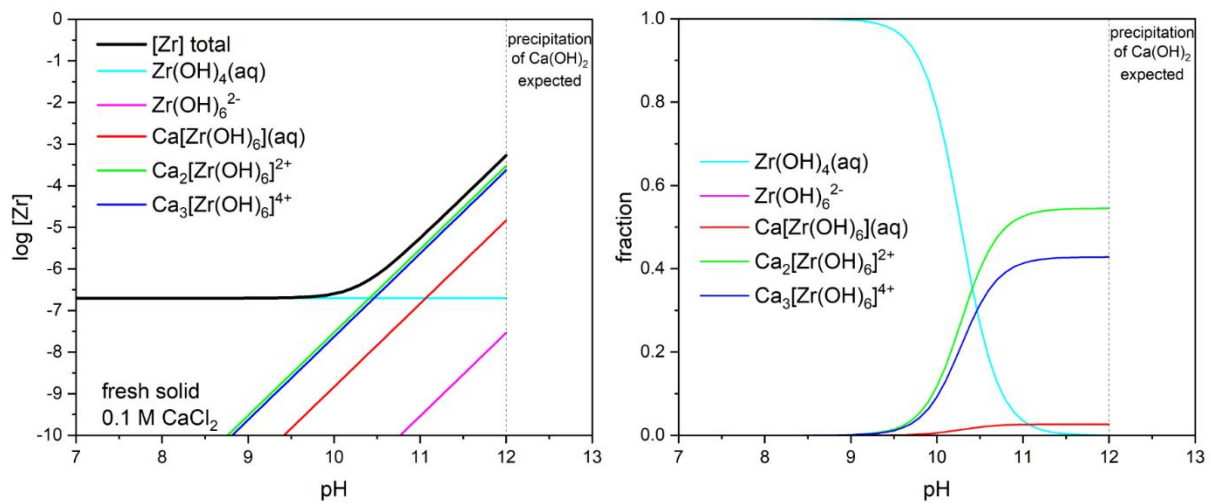


Figure 2.5: solubility curve and a species fraction diagram calculated for a fresh solid in 0.1 M $CaCl_2$ using the data from Altmaier et al. ¹⁹.

2.4 Assessment of surface reaction in aqueous media by DFT modeling

The aquatic chemistry of solid phases is also influenced by surface processes ⁷⁸, and thus investigating the mechanisms of surface reactions is important to improve the understanding of the aqueous chemistry. With theoretical calculations, such as DFT calculations, it is possible to model different surfaces and processes like adsorption or dissolution and possibly explain experimentally observed phenomena. The basic idea of DFT is to replace the complicated N-electron wave function by the simpler electron density and to determine functionals, which relate the electron density to the energy. The principles of today's DFT calculations were developed by Hohenberg, Kohn and Sham ⁷⁹.

One of the first DFT studies on zirconia was done by Jansen ⁸⁰ in 1991 investigating the electronic structures of cubic and tetragonal zirconia. The author's calculated total energies indicate a higher stability of tetragonal compared to cubic zirconia ⁸⁰. A first comprehensive study of zirconia surfaces was published by Christensen and Carter ⁸¹ in 1998. They created surfaces along lattice planes and calculated surface energies and atomic relaxations for all inequivalent lattice planes of cubic, tetragonal and monoclinic ZrO₂. Their calculations determine the ($\bar{1}11$) and the (111) surfaces as most stable for monoclinic and tetragonal zirconia, respectively and the transformation from cubic to tetragonal solids ⁸¹. However, it was shown later, that their tetragonal (111) surface indeed was a (101) surface ⁸². Haase and Sauer (1998) calculated the adsorption of sulfuric acid on zirconia surfaces and observed a base character of the pure tetragonal (101) and (001) zirconia surfaces leading to deprotonation of the acid and formation of surface hydroxyl groups and an adsorbed sulfate anion ⁸³. The adsorption of hydrogen on a tetragonal (101) surface was studied by Hofmann and co-workers in 2002 ⁸². The authors observed weak attractive interactions ($E_{\text{ads}} = -7.1 \text{ kJ mol}^{-1}$) for adding molecular H₂ above a surface Zr atom, as well as for adding dissociated hydrogen above one Zr and one O atom ($E_{\text{ads}} = -17.8 \text{ kJ mol}^{-1}$). The addition of hydrogen atoms above O ($E_{\text{ads}} = 81.0 \text{ kJ mol}^{-1}$) resulted in a repulsive interaction and a precursor structure for removing a water molecule ⁸². The surface hydration of tetragonal (101) and (001) surfaces was investigated by Iskandarova and co-workers in 2003, showing that the adsorption energy is increasing with decreasing surface coverage and that the dissociative adsorption of water is preferred especially with low surface coverage ⁸⁴. This behavior was confirmed by Korhonen, Calatayud and Krause in 2008 for the monoclinic ($\bar{1}11$) and ($\bar{1}01$) surfaces with the addition, that the adsorption energy per water molecule is decreasing with increasing surface coverage and that at higher surface coverage both, the adsorption of dissociated and molecular water is observed. The higher (more exothermic) adsorption energies for the ($\bar{1}01$) surface compared to the ($\bar{1}11$) surface is explained with the lower stability of this surface ⁸⁵. Piskorz and co-workers (2011) ⁸⁶ investigated all inequivalent surfaces in monoclinic zirconia in order

to predict the shape of monoclinic ZrO_2 nanoparticles. The calculated surface energies increase (thus the stability decreases) in the following order: $(\bar{1}11) < (111) < (\bar{1}01) < (011) < (001) < (110) < (100) < (101) < (010)$ as already observed by Christensen and Carter ⁸¹. With these values, the authors predicted a shape for nanoparticles in which only the $(\bar{1}11)$, (111) , (011) and (001) facets are exposed ⁸⁶. Water adsorption calculations on these surfaces confirm the previously mentioned characteristic of increasing dissociative adsorption with decreasing surface coverage and lower adsorption energy for more stable surfaces ⁸⁶. In 2012, Syzgantseva and co-workers ⁸⁷ calculated different types of oxygen vacancies in monoclinic $(\bar{1}11)$ and $(\bar{1}01)$ surfaces showing that monoclinic zirconia is poorly reducible, 2-fold coordinated vacancies are most stable in the $(\bar{1}11)$ surface, while 3-fold coordinated vacancies are more stable in the $(\bar{1}01)$ surface and vacancies are reactive enough to observe spontaneous dissociation of hydrogen molecules. Ricca and co-workers ⁸⁸ published a comprehensive DFT study on bulk solid phases and low-index surfaces of the different ZrO_2 polymorphs in 2015 in which various different functionals were used. All the used functionals and basis sets were able to reproduce the experimental structures with good accuracy, but as already known, an overestimation of the lattice parameters of the bulk solids is observed for HF and PBE functionals. The stability of the most abundant surfaces of the polymorphs was calculated, showing the highest stability for the cubic (111) surface, followed by the monoclinic $(\bar{1}11)$ surface and the tetragonal (101) surface ⁸⁸. Puigdollers and co-workers ⁸⁹ calculated the optimal shape of tetragonal zirconia nanoparticles $(\text{ZrO}_{2\pm x})_n$ with $n = 13$ to $n = 85$, and sizes of 0.9-1.9 nm. Partly truncated octahedral nanoparticles, exposing (101) and (001) surfaces showed the highest stability. Furthermore, they investigated oxygen vacancies on the nanoparticles, showing energies differing from the normal surfaces, indicating a higher reactivity of such nanoparticles. Very recently, Joutsuka and Tada (2023) ⁹⁰ investigated the adsorption of CO_2 on amorphous and crystalline zirconia, showing higher adsorption energies for tetragonal and monoclinic ZrO_2 compared to amorphous ZrO_2 . A model for amorphous structures was obtained by thermal annealing (molecular dynamics) starting with a cubic unit cell.

3. Materials and Methods

3.1 Chemicals

Almost all experimental steps were performed in Ar-glove boxes (< 1 ppm O₂). If the conditions for a step were different, it is explicitly mentioned. All solutions used in the experiments were prepared with purified Milli-Q water (Milli-Q academic, Millipore, 18.2 MΩ cm). Prior to use, the Milli-Q water was flushed with Ar for at least 1 hour to remove traces of CO₂. The chemicals used in the experiments are listed in Table 3.1.

Table 3.1: List of chemicals used in this study.

Name	Molecular formula	Molar mass (g mol ⁻¹)	Provider (purity)
Calcium chloride dihydrate	CaCl ₂ x2H ₂ O	147.01	Merck (p.a.)
Ethanol	CH ₃ CH ₂ OH	46.07	VWR Chemicals (99.9%)
Hydrochloric acid	HCl	36.46	Merck Titrisol
Nitric acid (60%)	HNO ₃	63.01	Merck (ultrapure)
Sodium chloride	NaCl	58.44	Merck (p.a.)
Sodium hydroxide solution	NaOH	40.00	Merck Titrisol
Zirconium dichloride oxide hydrate	ZrOCl ₂ xH ₂ O	196.15	AlfaAesar (99.99%)
Zirconium(IV) oxide	ZrO ₂	123.22	Sigma Aldrich

The buffer solutions used for the calibration of the pH electrode were provided by Merck.

3.2 pH measurements

The measurements of the pH values in aqueous solutions with ionic strength $\geq 0.1 \text{ mol kg}^{-1}$ are affected by variations in the hydrogen activity coefficient ${}^m\gamma_{H^+}$ and the liquid junction potential E_j . The real molal hydrogen concentration m_{H^+} is related to the measured pH value pH_{exp} as follows ⁹¹:

$$-\log m_{H^+} = pH_m = pH_{exp} + A_m \quad (3.1)$$

with

$$A_m = \log {}^m\gamma_{H^+} + E_j \frac{RT}{F} \ln \frac{a_2}{a_1} \quad (3.2)$$

where A_m is an empirical parameter depending on the composition and concentration test solution. R, T and F are the universal gas constant, the temperature (in Kelvin) and the Faraday constant, respectively ⁹¹. The activities a_2 and a_1 are the electrolyte activities in the measured solution and the electrode filling solution.

The pH measurements were conducted with a ROSS pH combination electrode (Thermo Scientific, OrionTM). The electrode was calibrated by measuring standard buffer solutions at pH = 2, 6, 8, and 12 at room temperature in a glove box.

3.3 Preparation of solid phases and samples

3.3.1 Precipitation of $\text{ZrO}_2(\text{am, hyd})$

In order to obtain the starting solid of the study, freshly precipitated amorphous hydrous zirconium oxide, a ≈ 0.02 M ZrOCl_2 solution was prepared. The $\text{ZrO}_2(\text{fresh, am, hyd})$ was precipitated by slow titration of the ZrOCl_2 solution with 0.1 M NaOH solution up to $\text{pH} > 12$ to ensure that the precipitation was complete. After 2-3 days, the supernatant solution was removed by centrifugation for 10-15 minutes at 4000 rpm. The remaining gel-like white precipitate was washed three times with Milli-Q water to obtain the $\text{ZrO}_2(\text{fresh, am, hyd})$ in the state of a wet paste. This procedure was repeated in several batches, each using ≈ 1 g of ZrOCl_2 corresponding to ≈ 0.6 g of dry ZrO_2 after precipitation, but the obtained amount of $\text{ZrO}_2(\text{fresh, am, hyd})$ solid phases had a significantly larger weight due to their state as wet paste.

3.3.2 Ageing of ZrO_2 solid phases at elevated temperature

To investigate the effect of ageing, the freshly precipitated $\text{ZrO}_2(\text{fresh, am, hyd})$ solid phases were equilibrated at elevated temperatures in a series of samples with different ageing times and background electrolytes in a glove box. An ageing temperature of $T = 80^\circ\text{C}$ in an oven were selected with several durations of 4, 10 and 18 months. Since a background pH of 11 was targeted, 0.001 M NaOH solution was selected as one background electrolyte and to have more representative conditions in context of nuclear waste disposal. A second series of samples was prepared in 0.2 M CaCl_2 solutions adjusted also to $\text{pH} = 11$, with the purpose of assessing the role of Ca in the ageing process. Due to significant differences regarding crystallinity and crystal structure observed between preliminary test samples with the two different background electrolytes after a shorter ageing time, samples with 0.02 M CaCl_2 solutions at $\text{pH} = 11$ were also prepared. This Ca concentration is found for instance in cementitious systems, in particular in the so-called degradation stage II, controlled by the dissolution of portlandite. Since for the samples aged in CaCl_2 media also a shift of the pH from 11 towards 7-9 during the ageing was observed, 3 more samples were prepared with regularly pH adjustment until no more pH shift was observed. For reasons of comparison, another sample was aged without a liquid phase and 2 more samples, one in 0.001 M NaOH solution and one in 0.2 M CaCl_2 solution adjusted also to $\text{pH} = 11$ were aged at $T = 22^\circ\text{C}$.

The adjustment of the 0.2 M CaCl_2 solutions to $\text{pH} = 11$ was done with a 0.2 M $\text{Ca}(\text{OH})_2$ suspension, to avoid the inclusion of further elements and to keep the ionic strength at the same level. Instead of a commercial product, $\text{Ca}(\text{OH})_2$ solid synthesized in this work was used to avoid the potential contamination with carbonates, which are often found in commercial

Ca(OH)₂. The Ca(OH)₂ was precipitated by adding NaOH solution to a 0.2 M CaCl₂ solution. The resulting precipitate was washed 2-3 times with Milli-Q water and afterwards equilibrated with 0.2 M CaCl₂ solutions to obtain alkaline \approx 0.2 M CaCl₂-Ca(OH)₂ solutions to adjust the pH of the samples with the 0.2 M CaCl₂ background electrolyte to pH = 11. To adjust the pH of the samples aged in 0.02 M CaCl₂ solutions a part of the \approx 0.2 M CaCl₂-Ca(OH)₂ solution was diluted with a factor of 10 with Milli-Q water.

Before starting the ageing, two batches (for most, but not for all samples) of the ZrO₂(fresh, am, hyd) wet paste (see 3.3.1 Precipitation of ZrO₂(am, hyd)) were merged and washed two times with the corresponding ageing background electrolyte. The wet solids, corresponding to \approx 1.2 g of dry ZrO₂ were then equilibrated in 200 ml of the corresponding background electrolyte solutions. To avoid any contaminations of CO₂(g) during the ageing at T = 80°C, the preparation of the samples was conducted under Ar atmosphere in new Teflon® vessels thoroughly cleaned with NaOH, HNO₃ and MilliQ water before use. The ageing was conducted in an oven placed inside an Ar glove box. When the targeted ageing time of a sample was reached, the sample was removed from the oven and left a few hours to cool down to room temperature under Ar atmosphere. Afterwards, the ageing background electrolyte was removed by centrifugation for 10-15 minutes at 4000 rpm (also under Ar conditions), the resulting solid was washed 3 times with Milli-Q water and stored as wet paste in order to prevent further ageing.

These aged solid phases ZrO₂(aged), the freshly precipitated solid ZrO₂(fresh, am, hyd) and a commercial crystalline solid phase ZrO₂(cr) were investigated with various solid phase characterization methods. An overview of the samples and their ageing conditions, if applying, are shown in Table 3.2.

Table 3.2: Samples and ageing conditions.

Solid phase (name)*	Ageing time (days)	Ageing background conditions	Ageing temperature (°C)
fresh	-	-	-
m4Ca80	125	0.2 M CaCl ₂ , pH = 11, pH shifted	80
m4Na80	125	0.001 M NaOH, pH = 11	80
m10Ca80	279	0.2 M CaCl ₂ , pH = 11, pH shifted	80
m10Na80	279	0.001 M NaOH, pH = 11	80
m10Ca22	279	0.2 M CaCl ₂ , pH = 11	22
m10Na22	279	0.001 M NaOH, pH = 11	22
m18Ca80	561	0.2 M CaCl ₂ , pH = 11, pH shifted	80
m18Na80	561	0.001 M NaOH, pH = 11	80
m4Ca80new	116	0.2 M CaCl ₂ , pH = 11, pH adjusted	80
m4_0.02Ca80	116	0.02 M CaCl ₂ , pH = 11, pH shifted	80
m4_0.02Ca80new	116	0.02 M CaCl ₂ , pH = 11, pH adjusted	80
m10Ca80new	329	0.2 M CaCl ₂ , pH = 11, pH adjusted	80
m10noH2O80	273	No liquid phase during ageing	80
crystalline	-	-	-

* The name of the aged samples is built by: the targeted ageing time (**m4**, **m10**, **m18** corresponding to 4, 10 and 18 months), the ageing background electrolyte (**Ca**: 0.2 M CaCl₂, pH = 11, **Na**: 0.001 M NaOH, pH = 11, **_0.02Ca**: 0.02 M CaCl₂, pH = 11, **noH2O**: no liquid phase), the ageing temperature (**80**: 80°C, **22**: room temperature) and the suffix **new** if the pH of the sample was regularly adjusted during the ageing.

3.4 Solid phase characterization

3.4.1 X-ray powder diffraction (XRD)

In order to determine the crystal structure of the samples and to obtain information about particle size and degree of crystallinity, X-ray powder diffraction (XRD) measurements were performed with a Bruker AXS D8 Advance X-ray powder diffractometer (Cu-K α radiation, LynxEye XE-T detector). The measurement angle was $2^\circ < 2\theta < 70^\circ$ with incremental steps of 0.015° and a measurement time of 0.4 seconds per step. An aliquot of approximately 1-2 mg of each solid phase was washed 3 times with 0.5 ml of ethanol to avoid possible salt contents from the matrix solutions. After the last washing step, the solid phase was re-suspended in ethanol, deposited on a sample holder and dried under Ar atmosphere.

For crystal phase identification, the diffractograms collected for the solid phases in the present work were compared with reference data reported in the Joint Committee on Powder Diffraction Standard (JCPDS) ⁹² or in the Crystallography Open Database (COD) ⁹³⁻¹⁰⁰, respectively. The Scherrer equation ¹⁰¹, which is based on the full width at half maximum (FWHM) of the diffraction peaks, was used to calculate the size of the crystal domains of the solid phases.

3.4.2 Scanning electron microscopy with energy-dispersive X-ray spectroscopy (SEM-EDX)

Usually scanning electron microscopes (SEM) are used to characterize the surface of a larger solid phase with a depth of 3-4 μm . Since the samples in the present study are of nano-particulate nature, SEM was mostly used to investigate morphology and the size of the particles. SEM is often coupled with energy dispersive X-ray spectroscopy (EDX), which allows an elemental characterization of the samples. Within this study, a Thermo Fisher Scientific UltraDry SEM with a primary electron beam energy of 30 keV equipped with a Peltier cooled, silicon drift X-ray detector was used to perform SEM-EDX measurements.

Following the same procedure as for XRD samples an aliquot of approximately 1-2 mg of each solid phase was washed 3 times with 0.5 ml of ethanol and re-suspended in ethanol after the last washing step. In this case, a few drops of this suspension were deposited on a piece of indium foil and dried under Ar atmosphere. These samples were used for XPS, SEM-EDX and Raman measurements.

3.4.3 Transmission electron microscopy (TEM)

Transmission electron microscopy (TEM) measurements provide insights on the particle size, the morphology and even the crystal phase of the solids. TEM measurements were performed at the Fusion Laboratory of the KIT-IAM institute with a FEI Tecnai G2 operating at 200kV, equipped with an insitu Gatan Tridiem Camera that provides high quality imaging and an Energy Dispersive X-ray Spectroscopy detector (EDS). Additionally, electron diffractions from the samples could be obtained and were analyzed and compared with the Process Diffraction software ¹⁰². After following the same washing procedure as in the previously mentioned methods, a few μl of the solids suspended in ethanol were deposited on a TEM grid and dried under Ar atmosphere.

3.4.4 Raman spectroscopy

As well as IR spectroscopy, also Raman spectroscopy is based on the excitation of vibrational modes and is generally used for substance identification and structural characterization. Raman measurements were done with a Bruker Senterra II Raman microscope with 532 and 785 nm lasers and a spectral resolution of 1.5 cm^{-1} . As mentioned before, the samples prepared for XPS and SEM-EDX were also used for Raman spectroscopy. The measurements took place under air conditions.

3.4.5 Extended X-ray absorption fine structure (EXAFS)

To access structural parameters as Zr-O and Zr-Zr distances and coordination numbers, extended X-ray absorption fine structure (EXAFS) measurements were performed at the INE beamline at the KIT synchrotron source (KARA) . About 10 to 15 mg of each solid phase were washed once with MilliQ water and resuspended in a small volume of MilliQ water. A few drops of the resulting suspensions were placed into gas-tight plastic cells. After drying under Ar atmosphere, the plastic cells were mounted in a sample holder and transported to the synchrotron source, where they were stored under Ar atmosphere until the measurements. The resulting EXAFS spectra were processed using Athena and Artemis software from the Demeter software package ¹⁰⁶.

3.4.6 Small-angle X-ray scattering (SAXS)

In small angle X-ray scattering (SAXS) measurements the intensity of the scattering vector q is measured to gain information about different particle families and also surface properties. The inflection points of the intensity give insights in the particle size of the samples, while the slope of the intensity can be used to characterize the surface roughness of the solids. SAXS measurements were performed at the Aichi Synchrotron Radiation Center, Japan, using a X-ray wavelength of 0.092 nm and a scattering vector q with $0.06 < q \text{ [nm}^{-1}] < 12.0$. An aliquot of each dry solid was sent to Japan after washing twice with ethanol, re-suspending in ethanol and drying under Ar atmosphere at room temperature. Small portions of the solids were loaded either in a glass capillary or in a sample cell covered by quartz glass.

3.4.7 Thermogravimetric analysis with differential thermal analysis (TG-DTA)

In the case of hydrous oxides and in the absence of other ligands (e.g. carbonate, nitrate), thermogravimetric analysis (TG) with differential thermal analysis (DTA) can provide insights on the amount of hydration water of the samples. TG-DTA analyses were done with a Netzsch STA 449C equipment and a SETARAM SETSYS Evolution device coupled with an OMNI Star Gas Analysis System. With TG the weight loss attributed to evaporation of water is measured, while DTA provides insights on the energetics of the processes occurring during the heating of the samples for example changes in the crystal structure. An aliquot of each solid was washed twice with ethanol, re-suspended in ethanol and dried under Ar atmosphere at room temperature. Typically, 10-20 mg of dry solid were analyzed up to 1200°C under Ar atmosphere with a heating rate of 10 K min⁻¹.

3.4.8 Fourier-transform infrared spectroscopy (FTIR)

Fourier transform infrared spectroscopy (FTIR) is a spectroscopic method based on the excitation of vibrational modes of chemical bonds by infrared light. It is in general used for structural characterization, identification and quantification of substances. For the samples in this study, the main focus of FTIR measurements was the characterization of the water region of the solids and to determine for some samples whether exchange between hydrogen and deuterium took place or not. The FTIR measurements were performed with a Bruker Optik Invenio R FTIR spectrometer equipped with a Platinum ATR accessory A225/QI-I single reflection diamond crystal and a DLaTGS detector with a spectral resolution of 4 cm^{-1} . A few mg of each solid were washed twice with ethanol and dried under Ar atmosphere. The dry solids were removed from the glove-box and placed on the ATR crystal. The measurements took place under air conditions. OPUS software (Bruker Optik) was used to operate the device and evaluate the data.

3.4.9 X-ray photoelectron spectroscopy (XPS)

X-ray photoelectron spectroscopy (XPS) measurements were conducted with the aim of investigating the speciation of the oxygen atoms and to have an elemental analysis of the solids. A PHI 5000 VersaProbe II (ULVAC-PHI Inc.) XPS system equipped with a scanning microprobe X-ray source (monochromatic Al K_{α} , $h\nu = 1486.7\text{ eV}$) was used. For charge compensation at isolating samples, low energy argon ions (8 eV) generated by a floating ion gun and low energy electrons (1.1 eV) generated by an electron flood gun were applied (dual beam technique). The angle between analyzer and sample surface was 45° . Survey scans were recorded with a pass energy of the analyzer of 187.85 eV. Narrow scans of the elemental lines were recorded with 23.5 eV pass energy. After taking into account sensitivity factors, the transmission function of the analyzer, asymmetry parameters of elemental lines and removal of a local Shirley background, atomic concentrations can be calculated with a relative error of $\pm (10-20)\%$ using the areas of elemental lines of the survey spectra. Gaussian curve fits to narrow scans of O 1s elemental lines were performed after Shirley background subtraction in order to determine the speciation of the oxygen atoms (O^{2-} , OH^{-} or H_2O). Data analysis was performed using ULVAC-PHI MultiPak program, version 9.9.

3.4.10 Zeta potential measurements

Zeta potential measurements were conducted with a Brookhaven Instruments NanoBrook 90Plus PALS device in order to determine the surface charge of the solid phases. For these measurements, suspensions with 0.1 g/l of each of the solid phases were prepared in either 1 mM HCl-NaCl-NaOH or in 1 mM HCl-CaCl₂-Ca(OH)₂. The pH values of the suspensions were adjusted to approximately 3.0, 4.5, 6.0, 8.0, 9.5 and 11.0 for each system. The preparation of the samples and filling into plastic cuvettes was done under Ar atmosphere, while the measurements themselves took place under air conditions.

3.4.11 Volumetric nitrogen sorption with the Brunauer, Emmet and Teller theory (BET)

The specific surface area is one of the most important properties of nanosized materials since it significantly affects their chemical and physical behavior. Volumetric gas sorption evaluated with the Brunauer, Emmet and Teller (BET) isotherm can be used to determine the specific surface area of solids and also to gain information about the porosity of the material ^{107,108}. BET measurements were done with a Quantachrome Autosorb 1 device with nitrogen as adsorbate. It was not possible to perform BET measurements with all samples, since the technique requires a relatively large amount of material (ca. 300-500 mg, depending of the surface area), which was not available for several of the investigated solid phases. The samples were dried under Ar atmosphere first for several days and afterwards outgassed for 24 hours at 60°C to avoid adsorption of water or gasses.

3.5 Solubility experiments

Most of the solid phases described in the sections 3.3.1, 3.3.2 and table 3.2 were used for the preparation of sets of samples for solubility tests from undersaturation with different pH values and background electrolytes. Small amounts of the solids (a few mg per sample), as wet paste (see end of section 3.3.2), were washed twice with the planned background electrolyte solution and were equilibrated in 10 ml of the same solution afterwards. The pH was adjusted to the target values and it was taken care that no complete dissolution of the solid took place, and that still solid phase was present in each sample. The concentration of zirconium in solution [Zr] and the pH values were checked regularly until attaining steady-state conditions, which were assumed after reaching constant [Zr] and pH measurements. Sub-sections 3.5.1 and 3.5.2 show the details of the sample compositions and the determination of the zirconium concentration, respectively.

3.5.1 Sample conditions

0.5 M NaCl-NaOH solutions, 0.2 M CaCl₂-Ca(OH)₂ solutions and 0.02 M CaCl₂-Ca(OH)₂ (representative of cementitious systems) solutions were selected as background electrolytes. For each solid phase, series of 3-6 solubility samples were prepared with pH values between 8.0 and 13.4. The details are shown in Table 3.3 and 3.4.

Table 3.3: Conditions of the solubility samples.

Solid phase*	Background electrolyte	No. of samples	pH _m range
fresh	0.5 M NaCl-NaOH	6+2**	9.0 – 13.4
	0.02 M CaCl ₂ -Ca(OH) ₂	6	8.0 – 12.5
	0.2 M CaCl ₂ -Ca(OH) ₂	5+2**	8.0 -12.0
m4Ca80	0.5 M NaCl-NaOH	6	9.0 – 13.4
	0.02 M CaCl ₂ -Ca(OH) ₂	6	8.0 – 12.5
	0.2 M CaCl ₂ -Ca(OH) ₂	5	8.0 -12.0
m4Ca80	0.5 M NaCl-NaOH	6	9.0 – 13.4
	0.02 M CaCl ₂ -Ca(OH) ₂	6	8.0 – 12.5
	0.2 M CaCl ₂ -Ca(OH) ₂	5	8.0 -12.0
m10Ca80	0.5 M NaCl-NaOH	3	12.0 – 13.4
	0.02 M CaCl ₂ -Ca(OH) ₂	3	11.0 – 12.5
	0.2 M CaCl ₂ -Ca(OH) ₂	3	10.0 – 12.0
m10Na80	0.5 M NaCl-NaOH	3	12.0 – 13.4
	0.02 M CaCl ₂ -Ca(OH) ₂	3	11.0 – 12.5
	0.2 M CaCl ₂ -Ca(OH) ₂	3	10.0 – 12.0
m10Ca22	0.5 M NaCl-NaOH	3	12.0 – 13.4
	0.02 M CaCl ₂ -Ca(OH) ₂	3	11.0 – 12.5
	0.2 M CaCl ₂ -Ca(OH) ₂	3	10.0 – 12.0

Continuation of Table 3.3.

Solid phase*	Background electrolyte	No. of samples	pH _m range
m10Na22	0.5 M NaCl-NaOH	3	12.0 – 13.4
	0.02 M CaCl ₂ -Ca(OH) ₂	3	11.0 – 12.5
	0.2 M CaCl ₂ -Ca(OH) ₂	3	10.0 – 12.0
m10noH2O80	0.5 M NaCl-NaOH	3	12.0 – 13.4
	0.02 M CaCl ₂ -Ca(OH) ₂	3	11.0 – 12.5
	0.2 M CaCl ₂ -Ca(OH) ₂	3	10.0 – 12.0
m4Ca80new	0.5 M NaCl-NaOH	3	12.0 – 13.4
	0.02 M CaCl ₂ -Ca(OH) ₂	3	11.0 – 12.5
	0.2 M CaCl ₂ -Ca(OH) ₂	3	10.0 – 12.0
m4_0.02Ca80	0.5 M NaCl-NaOH	3	12.0 – 13.4
	0.02 M CaCl ₂ -Ca(OH) ₂	3	11.0 – 12.5
	0.2 M CaCl ₂ -Ca(OH) ₂	3	10.0 – 12.0
m4_0.02Ca80new	0.5 M NaCl-NaOH	3	12.0 – 13.4
	0.02 M CaCl ₂ -Ca(OH) ₂	3	11.0 – 12.5
	0.2 M CaCl ₂ -Ca(OH) ₂	3	10.0 – 12.0
m18Ca80	0.5 M NaCl-NaOH	3+2**	9.0 – 13.4
	0.02 M CaCl ₂ -Ca(OH) ₂	3	9.0 – 12.5
	0.2 M CaCl ₂ -Ca(OH) ₂	3+2**	9.0 -12.0
m18Na80	0.5 M NaCl-NaOH	3	9.0 – 13.4
	0.02 M CaCl ₂ -Ca(OH) ₂	3	9.0 – 12.5
	0.2 M CaCl ₂ -Ca(OH) ₂	3	9.0 -12.0
m10Ca80new	0.5 M NaCl-NaOH	3	9.0 – 13.4
	0.02 M CaCl ₂ -Ca(OH) ₂	3	9.0 – 12.5
	0.2 M CaCl ₂ -Ca(OH) ₂	3	9.0 -12.0
crystalline	0.5 M NaCl-NaOH	2**	13.0 – 13.4
	0.2 M CaCl ₂ -Ca(OH) ₂	2**	11.0 – 12.0

* Explanations of the names of the solids: see table 3.2. ** Due to difficulties in measuring very low Zr concentrations of some solubility samples, for selected solid phases a set of samples was prepared in Teflon vessels to avoid any contamination by traces of Zr present in various materials.

Due to the low surface reactivity of the commercial crystalline solid ⁷⁷, several samples were prepared with different surface (of the solid) to volume (of the background electrolyte) ratios in order to reach the solubility limit in the limited time of the experiments. Values of 10⁴, 10⁵ and 10⁶ m⁻¹ were targeted as S/V in the same 3 different background electrolytes. For the calculation the specific surface area of 22 m²g⁻¹ determined with BET was used. The details of these samples are shown in Table 3.4.

Table 3.4: Conditions of the solubility samples of ZrO₂(cr) with determined S/V ratios.

m (ZrO₂) (mg)	S/V (10³ m⁻¹) actual	S/V (10³ m⁻¹) target	Background electrolyte	No. of samples	pH_m range
7 – 15	15.4 – 33.0	10	0.5 M NaCl-NaOH	3	9.0 – 13.4
9 – 20	19.8 – 44.0	10	0.02 M CaCl ₂ -Ca(OH) ₂	3	9.0 – 12.5
16 – 33	35.2 – 72.5	10	0.2 M CaCl ₂ -Ca(OH) ₂	3	9.0 – 12.0
64 – 98	140.6 – 215.4	100	0.5 M NaCl-NaOH	3	9.0 – 13.4
62 – 93	136.2 – 204.4	100	0.02 M CaCl ₂ -Ca(OH) ₂	3	9.0 – 12.5
73 – 80	160.4 – 175.8	100	0.2 M CaCl ₂ -Ca(OH) ₂	3	9.0 – 12.0
414 – 532	909.8 – 1169.1	1000	0.5 M NaCl-NaOH	3	9.0 – 13.4
399 – 460	876.8 – 1010.9	1000	0.02 M CaCl ₂ -Ca(OH) ₂	3	9.0 – 12.5
437 – 448	960.3 – 984.5	1000	0.2 M CaCl ₂ -Ca(OH) ₂	3	9.0 – 12.0

3.5.2 Determination of [Zr] by inductively coupled plasma – mass spectrometry (ICP-MS)

The zirconium concentrations [Zr] in the solubility samples were determined by inductively coupled plasma – mass spectroscopy (ICP – MS). The measurements were conducted with either a ThermoScientific iCAP TQs, a ThermoScientific ELEMENT XR ICP – MS, a Q-ICP-MS (Xseries 2, THER- MOELECTRON) or a high resolution HR-ICP-MS (ELAN 6100, Perkin Elmer) device. Due to variable background salt concentrations (NaCl or CaCl₂), different dilution factors were applied and led to detection limits between $\approx 10^{-7}$ and 10^{-10} M.

Before the measurements, a phase separation step was conducted in order to separate colloids and suspended particles. An aliquot of the supernatant of each solubility sample was centrifuged (13500 rpm) in 3 kD filters (Nanosep[®] centrifuge tubes, Pall Life Sciences). After the phase separation a dilution with factors of 1:5 to 1:10⁵ was applied depending on the background electrolyte concentration and the expected zirconium concentration.

3.6 Hydrogen deuterium exchange experiments

In order to gain information about possibly different types of hydration water, exchangeability of hydration water and reversibility of hydration and dehydration H-D exchange experiments were conducted. Aliquots of some solids (fresh, m18Ca80, m18Na80, m10Ca80new, crystalline) as wet pastes (see 3.3.2) were dried under vacuum and afterwards re-equilibrated in pure D₂O (SigmaAldrich, 99.9 atom% D). After several days, this procedure was repeated 3 times to make sure that most exchangeable H atoms are substituted by D. After a final drying step, the samples were analyzed by FTIR and TG coupled with mass spectroscopy. The samples were kept under Ar atmosphere as long as possible, but the measurement took place under air conditions.

3.7 Theoretical calculations (DFT)

3.7.1 Theoretical background

3.7.1.1 Schrödinger equation

A quantum mechanical system is described by the wave function $\Psi_i(x_i, R_i)$ given by the time independent Schrödinger equation:

$$\hat{H}\Psi_i(x_i, R_i) = E_i\Psi_i(x_i, R_i) \quad (3.3)$$

where \hat{H} is the Hamiltonian operator representing the total energy of a system. Ψ_i is the wave function of the i 'th state of the system. R_i and x_i represent the combined spatial and spin coordinates of the nuclei and electrons, respectively. E_i is the energy of the state described by Ψ_i ⁷⁹. The Hamilton operator is a differential operator containing the kinetic energy of the electrons ($T_e(r)$) and nuclei ($T_N(R)$), as well as attractive ($V_{Ne}(r)$) and repulsive ($V_{NN}(R)$ and $V_{ee}(r)$) electrostatic interactions between the electrons and nuclei:

$$\hat{H} = T_e(r) + T_N(R) + V_{Ne}(r) + V_{ee}(r) + V_{NN}(R) \quad (3.4)$$

$$\hat{H} = -\frac{1}{2}\sum_{i=1}^N \nabla_i^2 - \frac{1}{2}\sum_{A=1}^M \frac{1}{M_A} \nabla_A^2 - \sum_{i=1}^N \sum_{A=1}^M \frac{Z_A}{r_{iA}} + \sum_{i=1}^N \sum_{j>i}^N \frac{1}{r_{ij}} + \sum_{A=1}^M \sum_{B>A}^M \frac{Z_A Z_B}{R_{AB}} \quad (3.5)$$

where i and j denote the N electrons and A and B the M nuclei. R and r are the distances between the particles, ∇^2 is the Laplacian operator defined as sum of differential operators and Z the charge of the nuclei. With several approximations like the Born-Oppenheimer approximation, considering the electrons as moving in a field of fixed nuclei (due to the much higher speed of electrons compared to nuclei), the kinetic energy of the nuclei gets zero and the potential energy due to nucleus-nucleus repulsions constant, so that the Hamiltonian can be reduced to the so called electronic Hamiltonian \hat{H}_{elec} containing only the electronic parts $T_e(r)$, $V_{Ne}(r)$ and $V_{ee}(r)$ ⁷⁹.

To solve the Schrödinger equation, it is necessary to first set up the specific Hamiltonian operator for the system and secondly to find the eigenfunctions Ψ_i and the corresponding eigenvalues E_i of \hat{H} . Unfortunately, no strategy for solving the Schrödinger equation (except few simple cases) is known. A well-known solution of this problem is the variational principle starting with a certain wave function Ψ_i and the corresponding $E_i > E_0$ searching for wave functions with lower energy until the changes in energy are so small that a good approximation of the ground state Ψ_0 with the corresponding energy E_0 is reached ⁷⁹.

3.7.1.2 Density functional theory (DFT)

The theoretical calculations in the context of this thesis were done with density functional theory (DFT). The basic idea of DFT is to replace the complicated N-electron wave function by the simpler electron density and to determine functionals, which relate the electron density to the energy. The principles of today's DFT calculations were developed by Hohenberg, Kohn and Sham ⁷⁹.

3.7.1.2.1 Hohenberg-Kohn theorems

In their first theorem, Hohenberg and Kohn ¹⁰⁹ proved that the electron density uniquely determines the Hamiltonian and therefore the total energy and all other properties of a system by:

$$E_0[\rho_0] = \int \rho_0(\vec{r}) V_{Ne} d\vec{r} + F_{HK}[\rho_0] \quad (3.6)$$

where $E_0[\rho_0]$ is the ground state energy, ρ_0 the ground state electron density, $\int \rho_0(\vec{r}) V_{Ne} d\vec{r}$ the system depending potential energy due to nuclei-electron attraction and $F_{HK}[\rho_0]$ the Hohenberg-Kohn functional, which can be described independently of the system as:

$$F_{HK}[\rho] = T[\rho] + E_{ee}[\rho] \quad (3.7)$$

where $T[\rho]$ and $E_{ee}[\rho]$ are the functionals for the kinetic energy and the electron-electron interactions, respectively.

Their second theorem is a proof of the variational principle showing that the functional $F_{\text{HK}}[\rho]$, which delivers the ground state energy, only delivers the lowest energy, if the input density is the ground state density, since each density defines its own Hamiltonian and thus its own wave function, so that the ground state wave function is only reached using the ground state density:

$$\langle \tilde{\Psi} | \hat{H} | \tilde{\Psi} \rangle = T[\tilde{\rho}] + V_{\text{ee}}[\tilde{\rho}] + \int \tilde{\rho}(\vec{r}) V_{\text{ext}} d\vec{r} = E[\tilde{\rho}] \geq E_0[\rho_0] = \langle \Psi_0 | \hat{H} | \Psi_0 \rangle \quad (3.8)$$

3.7.1.2.2 Kohn-Sham approach

The remaining problem for calculations is that neither the functional for the kinetic energy nor for the electron-electron interactions are known. In order to simplify this problem Kohn and Sham¹¹⁰ proposed to treat systems as independent electrons instead of interacting electrons, so that a large part of the kinetic energy can be calculated exactly and only a rather small contribution is not covered. The functional can be described as:

$$F[\rho(\vec{r})] = T_S[\rho(\vec{r})] + J[\rho(\vec{r})] + E_{\text{XC}}[\rho(\vec{r})] \quad (3.9)$$

where $T_S[\rho(\vec{r})]$ is the kinetic energy of the electrons without interaction, $J[\rho(\vec{r})]$ the classical Coulomb interaction and $E_{\text{XC}}[\rho(\vec{r})]$ the exchange-correlation energy containing the difference between $T_S[\rho(\vec{r})]$ and the true kinetic energy as well as electron-electron interactions which are not covered by the Coulomb interactions.

Therefore, the main objective of DFT calculations is to find functionals, which approximate the exchange-correlation energy in the most accurate way. For this purpose several types of functionals were developed. The basis of most current functionals is the local density approximation (LDA) based on the uniform electron gas. Since LDA functionals fail in chemical applications they were developed into generalized gradient approximation functionals (GGA) and hybrid functionals⁷⁹.

3.7.1.2.3 Exchange correlation functionals

3.7.1.2.3.1 Local Density Approximation (LDA)

The main idea of LDA is to treat the system like a hypothetical uniform electron gas with N electrons in the volume V . While N and V approach infinity, the electron density $N/V = \rho$ remains spatially constant. This approach delivers a good physical model for metals, but is far from a realistic model of atoms or molecules. The uniform electron gas is still largely used in DFT, because it is the only system for which the exchange and correlation energy functionals are known exactly or with very high accuracy. The energy for exchange and correlation in this model is given by:

$$E_{XC}^{LDA}[\rho] = \int \rho(\vec{r}) \varepsilon_{XC}(\rho(\vec{r})) d\vec{r} \quad (3.10)$$

where $\varepsilon_{XC}(\rho(\vec{r}))$ is the exchange-correlation energy per particle ⁷⁹.

3.7.1.2.3.2 Generalized Gradient Approximation (GGA)

Due to the not sufficient accuracy of LDA for computational chemistry, the LDA approach was extended by including the gradient of the charge density $\nabla\rho(\vec{r})$ to account for the non-homogeneity of the electron density. With some small adaptations, the energy for exchange and correlation can be expressed as:

$$E_{XC}^{LDA}[\rho] = \int f(\rho(\vec{r}), \nabla\rho(\vec{r})) d\vec{r} \quad (3.11)$$

where f is a function of the electron density and its gradient ⁷⁹. With this method, most of the commonly used functionals as the PW91 (Perdew and Wang ¹¹¹) or the PBE (Perdew, Burke and Ernzerhof ¹¹²) functional were developed. It is necessary to note, that functionals of the previously mentioned types do not take into account dispersion forces occurring in systems containing hydrogen, correctly. Therefore, optimized versions like the optPBE ¹¹³ functional or corrections like the D3 ¹¹⁴ dispersion correction were developed.

3.7.1.2.3.3 Hybrid functionals

A more recent approach to improve the performance of the functionals is the use of so-called DFT/HF hybrid functionals, which contain density functionals for the exchange as well as the exact Hartree-Fock exchanges. Commonly used functionals are B3LYP¹¹⁵ (Becke's three parameters exchange functional combined with the Lee-Yang-Parr correlation functional) or PBE0¹¹⁶ (PBE functional contain 25% of HF exchange) functionals. For the calculation in this work, no hybrid functionals were used.

3.7.2 Computational details

3.7.2.1 VASP software

The Vienna Ab initio Simulation Package (VASP)^{117–120} is a software package prepared to perform quantum mechanical calculations based on DFT in solid-state physics. Since VASP is adapted to periodic systems by the creation of unit cells, which are repeated infinitely often in all three dimensions, it is suitable for zirconium dioxide solid phases and surfaces. VASP calculations require several input files and produce some output files. An overview on these files and the calculation procedure is given in the following.

Input files:

INCAR: tells VASP what to do / specifies the parameters of the calculation (what type of calculation is done, which functionals are used, maximum number of iterations, convergence criteria)

KPOINTS: specifies the Bloch vectors / points where the calculation is done (automatic file prepared by M. Calatayud, only one parameter to change, defines how dense the mesh of k-points is).

POSCAR: contains structure data, starting point of the calculation (lattice parameters of the unit cell, positions of each atom).

POTCAR: contains pseudopotentials and all other relevant information of each type of atoms. Projector Augmented Wave (PAW) potentials with 4, 6 and 1 valence electron for Zr, O and H were used.

Job-file: specifies the computational settings (how many nodes/cores are used, time limit, maximum memory used, maximum cpu used).

Possible ends of calculations:

1. Energy converges
 - Reasonable results
 - Unexpected/chemically senseless results
2. Calculation is aborted (due to server issues)
3. Time limit is reached before convergence criteria are reached
4. Iterations limit is reached before convergence criteria or time limit are reached

Output files:

OUTCAR: main output file that contains all information (calculation parameters and results).

CONTCAR: corresponding to POSCAR file, contains same structural parameters of the last geometry calculated (optimized one if the calculation converged correctly).

OSZICAR: shows data of each iteration (total energy of electronic/ionic loops).

log file: shows the reason for the end (convergence, error, iterations, time).

3.7.2.2 Computational tests

Several tests had to be done before to find out the optimal settings for the calculations, which were kept over all calculations.

3.7.2.2.1 Determining k points

To determine the optimal k points value, which specifies the Bloch vectors, test calculations were done. A ZrO₂ structure was optimized with different k values (Figure 3.1) to see at which value the energy converges to have correct calculations and a k value as low as possible to reduce computational efforts. An automatic mesh creation with k = 30 was selected (distance between k-points in the reciprocal space $\sim 0.033 \text{ \AA}^{-1}$).

3.7.2.2.2 Determining energy cut-off

To determine the optimal energy cut off, test calculations were done. A monoclinic ZrO_2 structure was optimized with different energy cut offs (Figure 3.1) to see at which value the energy converges to have correct calculations and to reduce computational efforts. An energy cutoff of 400eV was selected, which is a good compromise between energy and time.

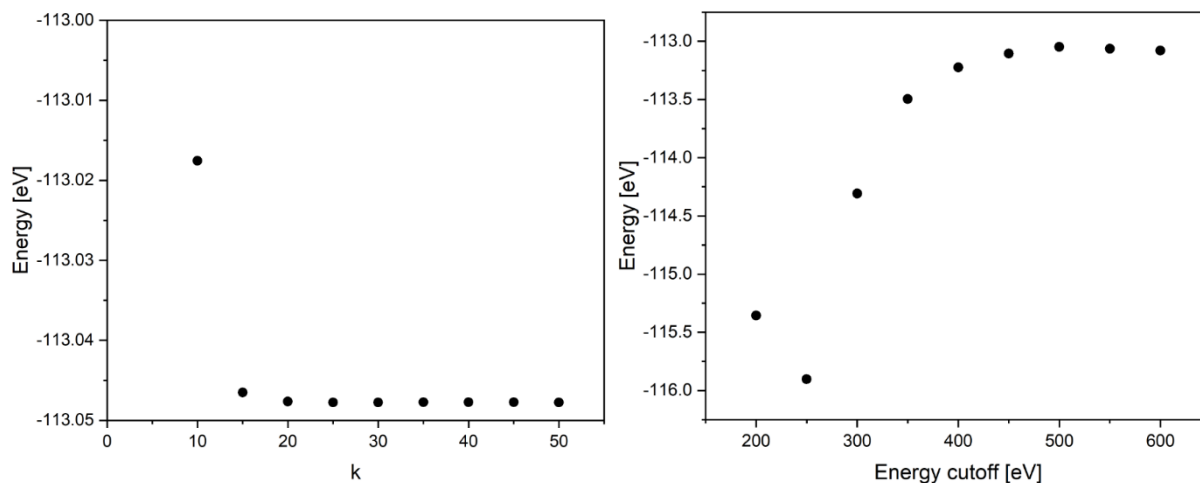


Figure 3.1: k points and energy cutoff convergence tests.

3.7.2.2.3 Test of different functionals

A set of different functionals, PBE, PBE with D3 correction, optPBE and PBE with D3 correction and optPBE were tested. For this purpose, monoclinic, tetragonal and amorphous bulk structures were optimized with the different combinations of functionals (see Table 4.14). The PBE functional with D3 correction was selected since the calculated parameters like lattice parameters of the unit cells approached the literature values best.

4. Results and discussion

4.1 Solid phase characterization

4.1.1 Structure and particle size

4.1.1.1 X-ray powder diffraction (XRD)

XRD was measured in order to determine the crystal structure of the samples and to obtain information about the particle size and degree of crystallinity. The XRD patterns of the samples are shown in Figure 4.1 and 4.2. The diffractogram of the freshly precipitated $\text{ZrO}_2(\text{am, hyd, fresh})$ is characterized by the lack of any reflection, which underpins the X-ray amorphous character of the material. Similarly, solids aged for 10 months at $T = 22^\circ\text{C}$ (m10Na22, m10Ca22) do not present any XRD reflections. However, after 4 to 18 months of equilibration time at $T = 80^\circ\text{C}$, the aged solid phases show broad but well-defined XRD patterns in agreement with references for monoclinic, tetragonal or cubic $\text{ZrO}_2(\text{cr})$ available in the COD database⁹³⁻¹⁰⁰. The solid phases aged in NaOH (m4Na80, m10Na80, m18Na80, Figure 4.1, red diffractograms) solutions, aged without liquid phase (m10noH2O80, Figure 4.1, black) and the commercial crystalline solid phase (Figure 4.1 and 4.2, black) show main reflections at $2\theta = 24.2, 28.1, 31.5, 34.2, 35.3$ and 50.1° agreeing well with reference pattern of monoclinic ZrO_2 (Figure 4.1 and 4.2, orange)⁹³⁻¹⁰⁰. A reflection at $2\theta = 30.2^\circ$, also present in some of these diffractograms indicates a small contribution of the cubic/tetragonal structure⁹³⁻¹⁰⁰. The results are in good agreement with previous observations by Kobayashi and co-workers, who reported the predominance of amorphous solids for samples aged at up to $T = 40^\circ\text{C}$ (Figure 4.1 and 4.2, green) and crystalline samples with broad reflections after ageing under at least $T = 60^\circ\text{C}$ (Figure 4.1 and 4.2, green)⁷⁰. In contrast to the crystal structures identified in systems aged in NaOH solutions, the samples aged in presence of Ca (m4Ca80, m4Ca80new, m4_002Ca80, m4_002Ca80new, m10Ca80, m18Ca80, Figure 4.2, blue) show XRD patterns with main reflections at $2\theta = 30.1, 34.9, 50.2$ and 59.7° , in perfect agreement with reference patterns reported for cubic (Figure 4.1 and 4.2, cyan) and tetragonal (Figure 4.1 and 4.2, magenta) $\text{ZrO}_2(\text{cr})$ structures. The coherence length of the crystal domains was determined by Scherrer analysis¹⁰¹, resulting in 23-27 nm for all monoclinic solids and 11-14 nm for all cubic/tetragonal solids. No significant differences depending on the ageing time, 4, 10 or 18 months, were observed. The coherence length of the crystal domains determined for the commercial $\text{ZrO}_2(\text{cr})$ (monoclinic) was 27 nm. The marking of a pattern with a * indicates that two small reflexes, which were also present in a blank measurement and thus do not correspond to the sample, are present between $2\theta = 42^\circ$ and 44° .

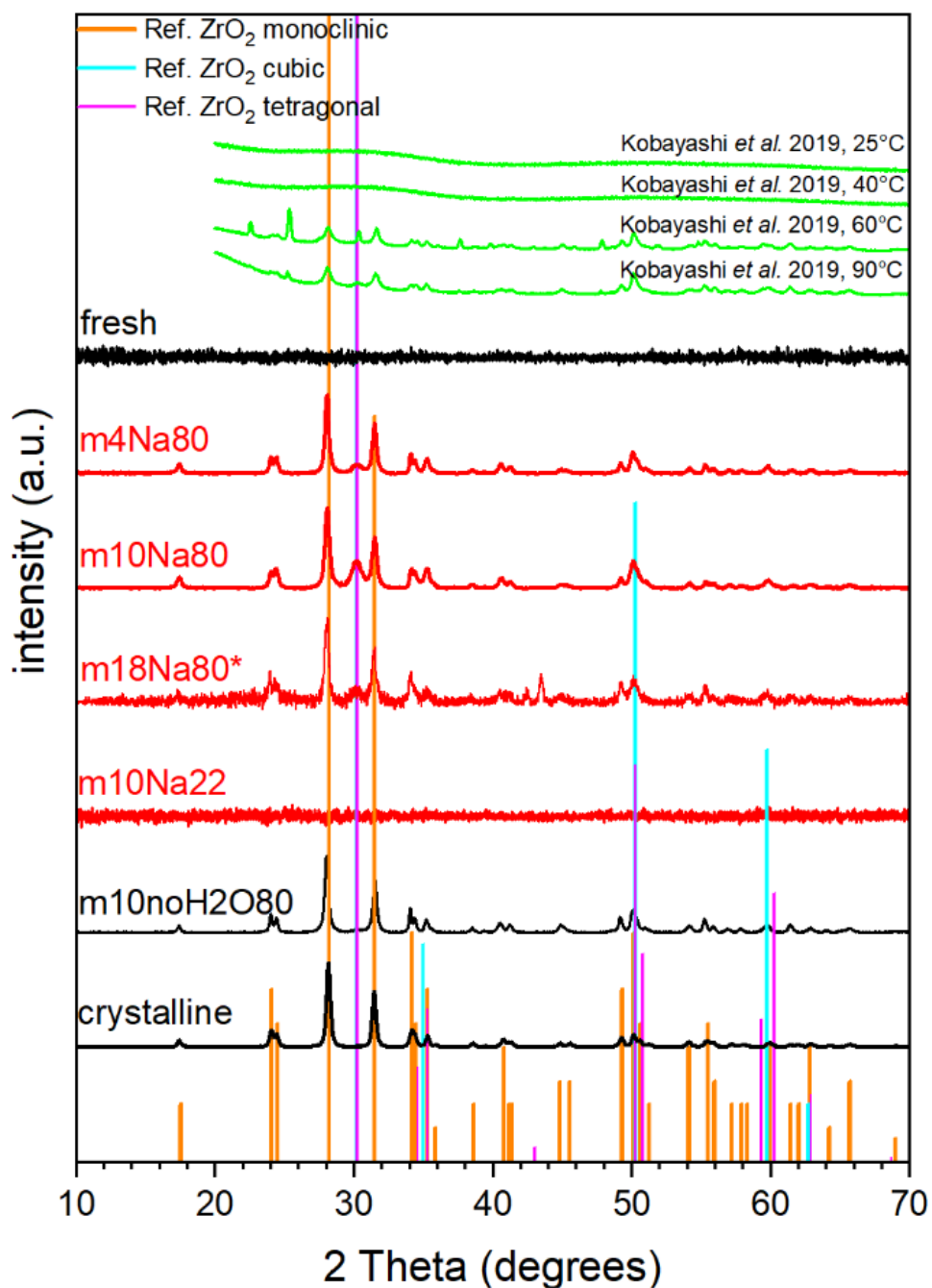


Figure 4.1: XRD patterns of ZrO₂(s) samples: red: solid phases aged in NaOH solutions; black: freshly precipitated, aged without liquid phase and crystalline ZrO₂(s) phases; green: diffractograms reported by Kobayashi *et al.*⁷⁰. Vertical lines indicate reference data reported for ZrO₂(cr) in the COD database^{93–100}: ZrO₂ monoclinic (COD ID: 1528984), ZrO₂ tetragonal (COD ID: 1539831), ZrO₂ cubic (COD ID: 5000038).

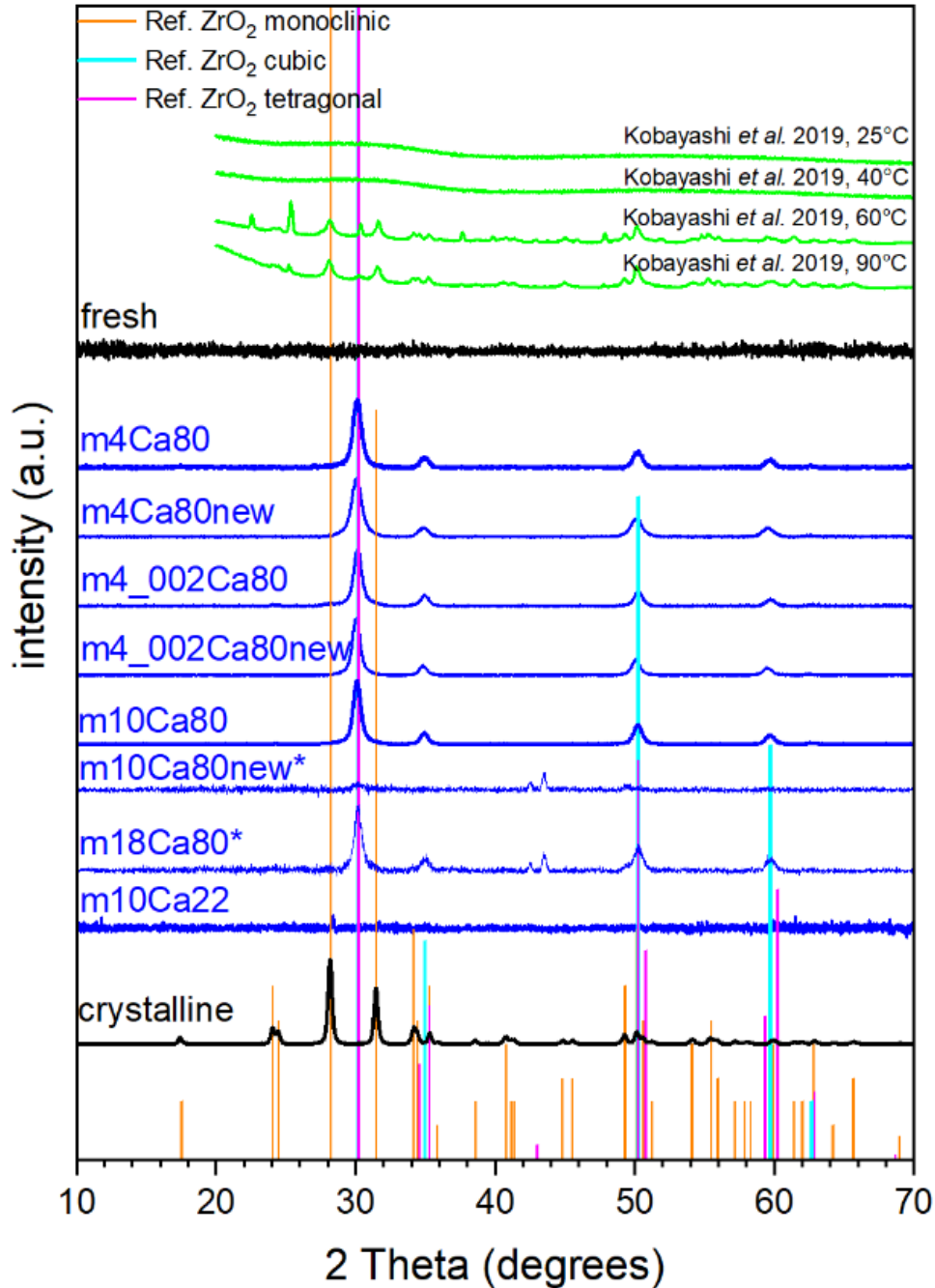


Figure 4.2: XRD patterns of $\text{ZrO}_2(\text{s})$ samples: blue: solid phases aged in CaCl_2 solutions; black: freshly precipitated and crystalline $\text{ZrO}_2(\text{s})$ phases; green: diffractograms reported by Kobayashi *et al.* ⁷⁰. Vertical lines indicate reference data reported for $\text{ZrO}_2(\text{cr})$ in the COD database ^{93–100}: ZrO_2 monoclinic (COD ID: 1528984), ZrO_2 tetragonal (COD ID: 1539831), ZrO_2 cubic (COD ID: 5000038).

It is important to note that the crystallization in the cubic/tetragonal structure occurs both in solutions containing 0.2 and 0.02 M Ca, indicating that even the lower Ca concentrations expected in cementitious systems (0.02 M as defined by equilibrium with portlandite at pH = 12.5) prevent (i) the crystallization in the form of the monoclinic ZrO_2 structure and (ii) the growth of the ZrO_2 particles to the size achieved in Ca-free systems.

4.1.1.2 Transmission electron microscopy (TEM)

Transmission electron microscopy (TEM) was conducted in order to gain more information about the morphology and the particle size of the solid phases. Electron diffraction delivers information about crystallinity and crystal structure of the samples. Selected TEM and electron diffraction images of the samples are shown in Figures 4.3-4.5.

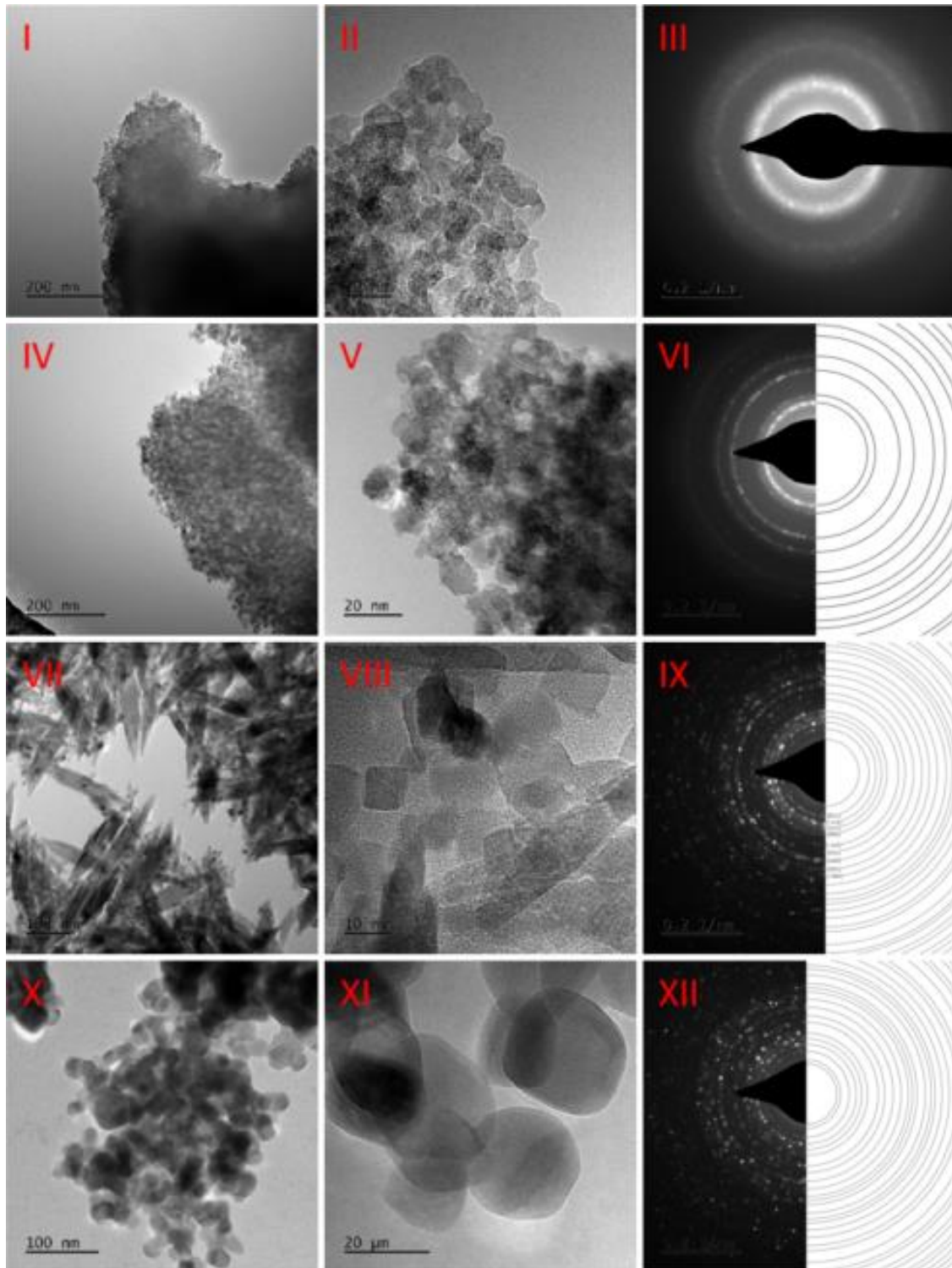


Figure 4.3: TEM images and electron diffraction of: fresh (I, II, III), m4Ca80 (IV, V, VI), m4Na80 (VII, VIII, IX) and commercial crystalline ZrO_2 (X, XI, XII) samples.

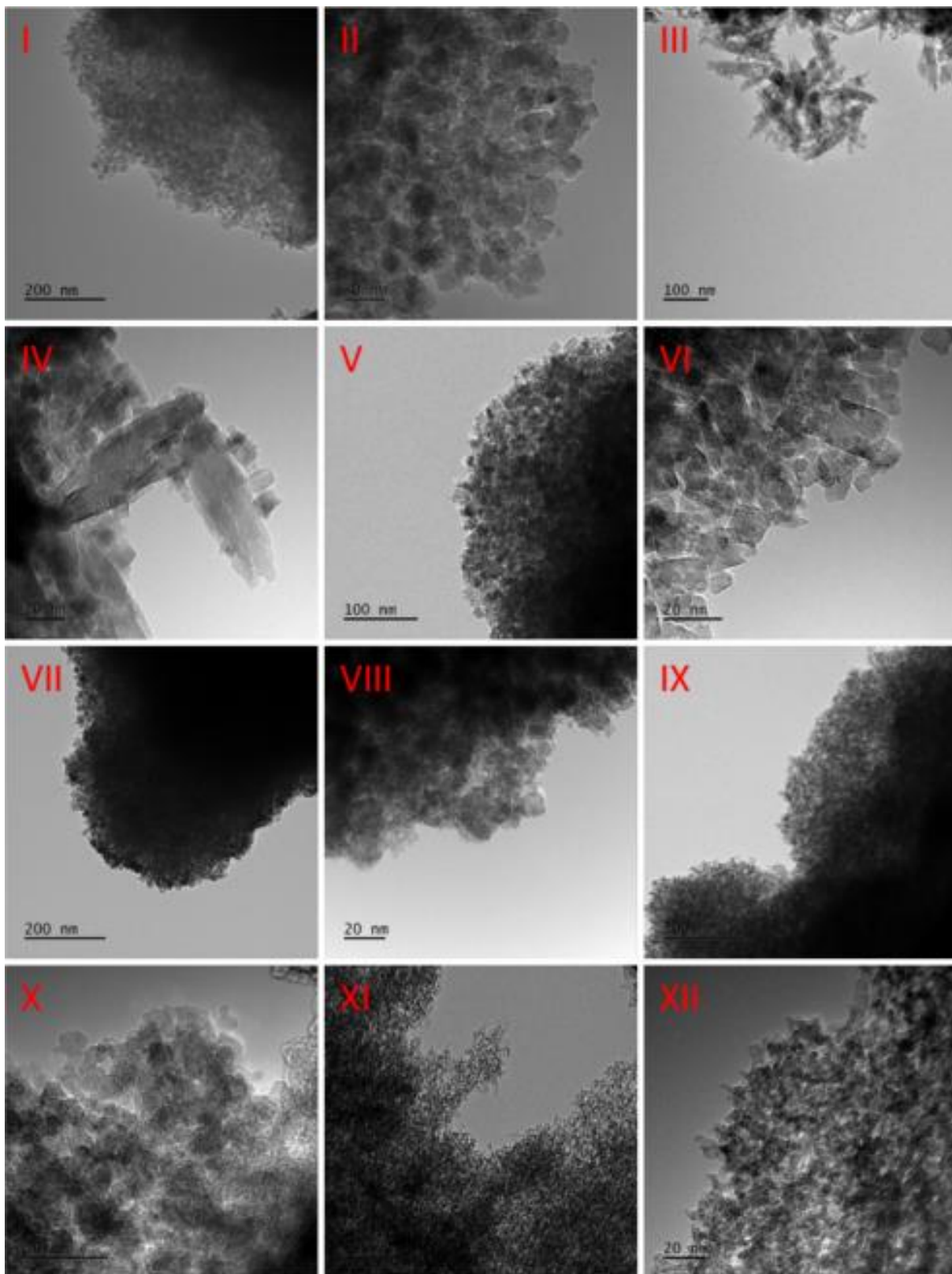


Figure 4.4: TEM images of: m10Ca80 (I, II), m10Na80 (III, IV), m4_002Ca80 (V, VI), m4_002Ca80new (VII, VIII), m4Ca80new (IX, X) and m10Ca22 (XI, XII) samples.

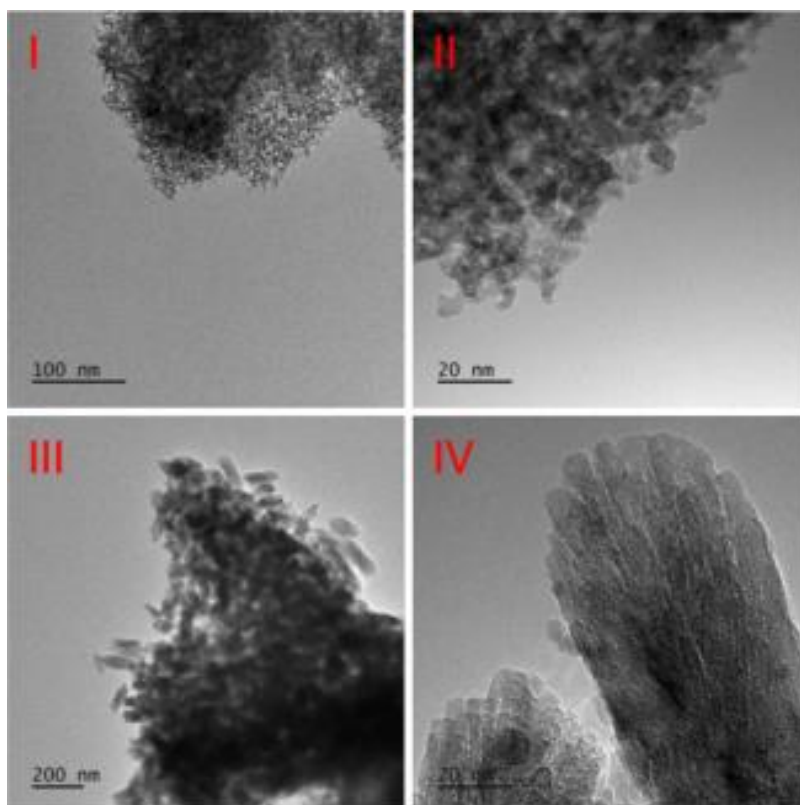


Figure 4.5: TEM images of: m10Na22 (I, II) and m10noH2O80 (III, IV), samples.

TEM images of the fresh solid (Figure 4.3 I-III) show that the sample is not crystalline, but that some ordering is present. The solid consists of primary particles which are homogeneous in size and shape with diameters of 3.6 ± 0.8 nm. The electron diffraction (Figure 4.3 III) shows (compared to the other samples) only very weak signals compatible with cubic/tetragonal ZrO_2 indicating a rather amorphous or nanocrystalline character of the solid phase. The solid phases aged at $80^\circ C$ in $CaCl_2$ media, m4Ca80 (Figure 4.3 IV-VI), m10Ca80 (Figure 4.4 I+II), m4_002Ca80 (Figure 4.4 V+VI), m4_002Ca80new (Figure 4.4 VII+VIII) and m4Ca80new (Figure 4.4 IX+X) show aggregation and two families of particles, primary particles with a size of 1-3 nm and secondary particles with a size of 10-20 nm. Similar to XRD also electron diffraction of these samples shows signals clearly corresponding to cubic/tetragonal ZrO_2 . In contrast, the solid phases aged at $80^\circ C$ in 0.001 M NaOH, m4Na80 (Figure 4.3 VII-IX) and m10Na80 (Figure 4.4 III+IV) show three families of particles, primary particles with a size of around 3 nm, secondary particles with a size of around 10 nm and large rods with a length of up to 300 nm. The electron diffraction shows large contributions of monoclinic and small contributions of cubic/tetragonal ZrO_2 which are also observed by XRD. The solid phase aged without liquid phase, m10noH2O80 (Figure 4.5 III+IV) shows large agglomerated particles with a size up to 200 nm and electron diffraction corresponding to large contributions of monoclinic and small contributions of cubic/ tetragonal ZrO_2 . The solid phases aged at $T = 22^\circ C$ in 0.2 M $CaCl_2$, m10Ca22 (Figure 4.4 XI+XII) and 0.001 M NaOH, m10Na22 (Figure 4.5 I+II) show an amorphous

character, with traces of the cubic/tetragonal structure in the case of ageing in presence of Ca. The commercial crystalline solid phase (Figure 4.3 X-XII) consists of homogenous spherical particles with a size of 21.1 ± 9.5 nm and completely monoclinic electron diffractions.

The TEM results discussed in this section qualitatively agree with those presented in subchapter 4.1.1.1 (XRD), however showing that all samples are characterized by a distribution of particles with different morphologies and sizes. This aspect will be further tackled in the discussion of the solubility data, acknowledging that the more soluble solid phases (expectedly with smaller particle size / less crystalline) are those expected to control the solubility in systems where different solid phases are co-existing. At the same time, mass transfer from the more soluble to the less soluble solid phase by dissolution and precipitation is expected. The less soluble phase is expectedly oversaturated, whereas the more soluble phase is saturated and/or undersaturated.

4.1.1.3 Raman spectroscopy

Raman spectra (Figure 4.6) of the solid phases are also strongly affected by the different crystal systems of the samples. The solids with predominant monoclinic structure, according to XRD and TEM, show well defined peaks compared with literature in Table 4.1. An intense duplet around 180 and 190 cm^{-1} , several peaks between 300 and 380 cm^{-1} , a strong signal at 476 cm^{-1} and less defined peaks between 540 and 640 cm^{-1} are in good agreement with literature, where strong signals at 180, 192 and 476 cm^{-1} , as well as several weaker signals at 300 – 380 cm^{-1} , 500 – 560 cm^{-1} and 620 – 640 cm^{-1} are reported for monoclinic ZrO_2 ^{64,121,122}. The tetragonal /cubic (XRD, TEM) solids and the amorphous solids aged at $T = 22^\circ\text{C}$ show less defined spectra. A broad signal around 140 cm^{-1} , a strong signal around 440 - 450 cm^{-1} and a signal around 667 cm^{-1} are only in moderate agreement with literature values reported at 148 cm^{-1} ^{64,122}, 263 cm^{-1} ⁶⁴/269 cm^{-1} ¹²², 476 cm^{-1} ⁶⁴/462 cm^{-1} ¹²² and 646 cm^{-1} ¹²² for tetragonal ZrO_2 . The less defined, but observable signals of the amorphous samples aged at $T = 22^\circ\text{C}$ at the same wavenumbers as for tetragonal/cubic solids supports the observation of weak tetragonal/cubic electron diffraction signals by TEM, indicating a possible pre-ordering in these amorphous solids. Differences in the quality of the spectra for the samples aged in NaOH and CaCl_2 solutions are possibly related to the larger particles observed in the former system (as well as for the crystalline solid), as opposed to samples aged in the presence of Ca.

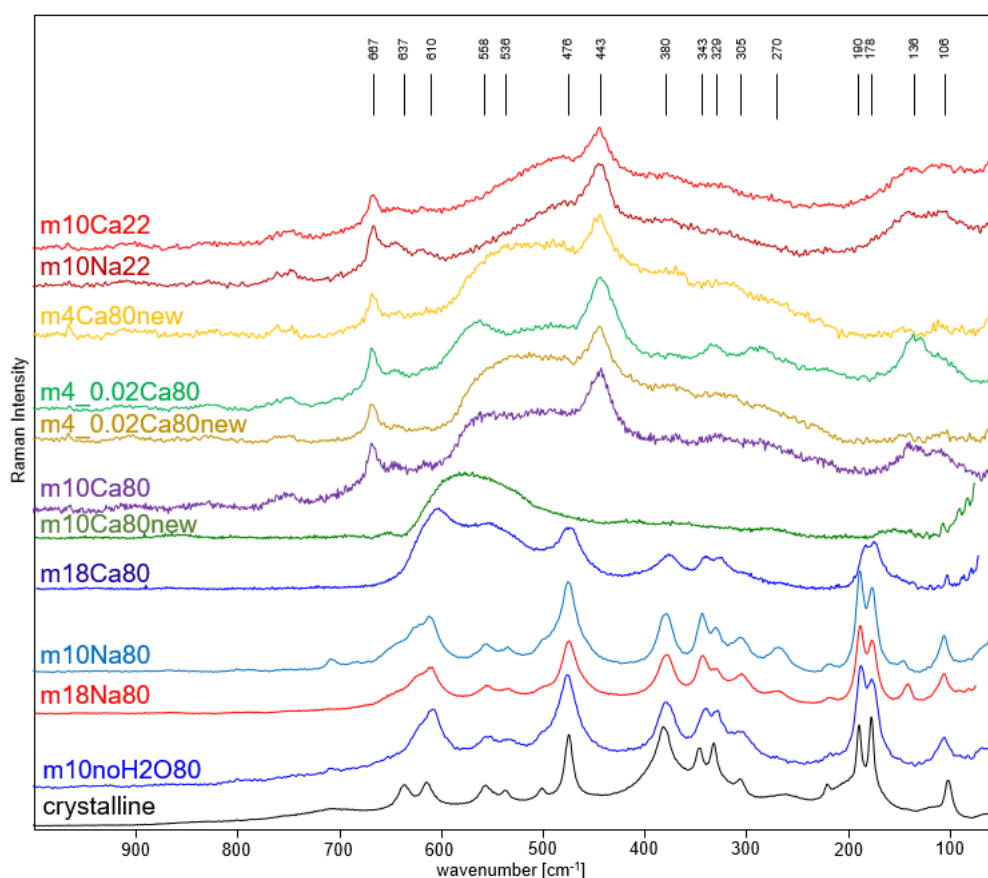


Figure 4.6: Raman spectra of the $\text{ZrO}_2(\text{s})$ solid phases.

Table 4.1: Raman signals compared to literature.

Solid phase		Raman signals [cm⁻¹]						
Keramidas et al. ⁶⁴								
amorphous		(148)			(263)		(476)	
tetragonal		148	(180+192)	(224)	263	(308-383)	476	(500-560) (620-640)
monoclinic	103		180+192	224		308-383	476	500-560 620-640
Bouvier et al. ¹¹⁹								
tetragonal		150	(177-188)		260	(320)	460	650
monoclinic			180		260	300-380	440-500	650
Garg et al. ¹²²								
tetragonal		148			269	317	462	646
monoclinic		148	180+192					
Present work								
m10Ca22							443	667
m10Na22							443	667
m4Ca80new							443	(500-560) 667
m4_002Ca80		100-180					443	560 667
m4_002Ca80new							443	(500-560) 667
m18Ca80			160-200			330-340	476	520-580 610
m10Na80	106	(150)	178+190		(270)	300-380	476	(536+558) 610
m18Na80	106	(150)	178+190		(270)	300-380	476	(536+558) 610
m10noH2O80	106		178+190			300-380	476	(536+558) 610
crystalline	106		178+190			300-380	476	(536+558) 610+637

4.1.1.4 Scanning electron microscopy with energy-dispersive X-ray spectroscopy (SEM-EDX)

SEM images of the $ZrO_2(s)$ solid phase were taken in order to investigate the morphology and particle size of the samples. EDX delivers information about the sample composition. SEM images are shown in Figure 4.7 and EDX data in Table 4.2.

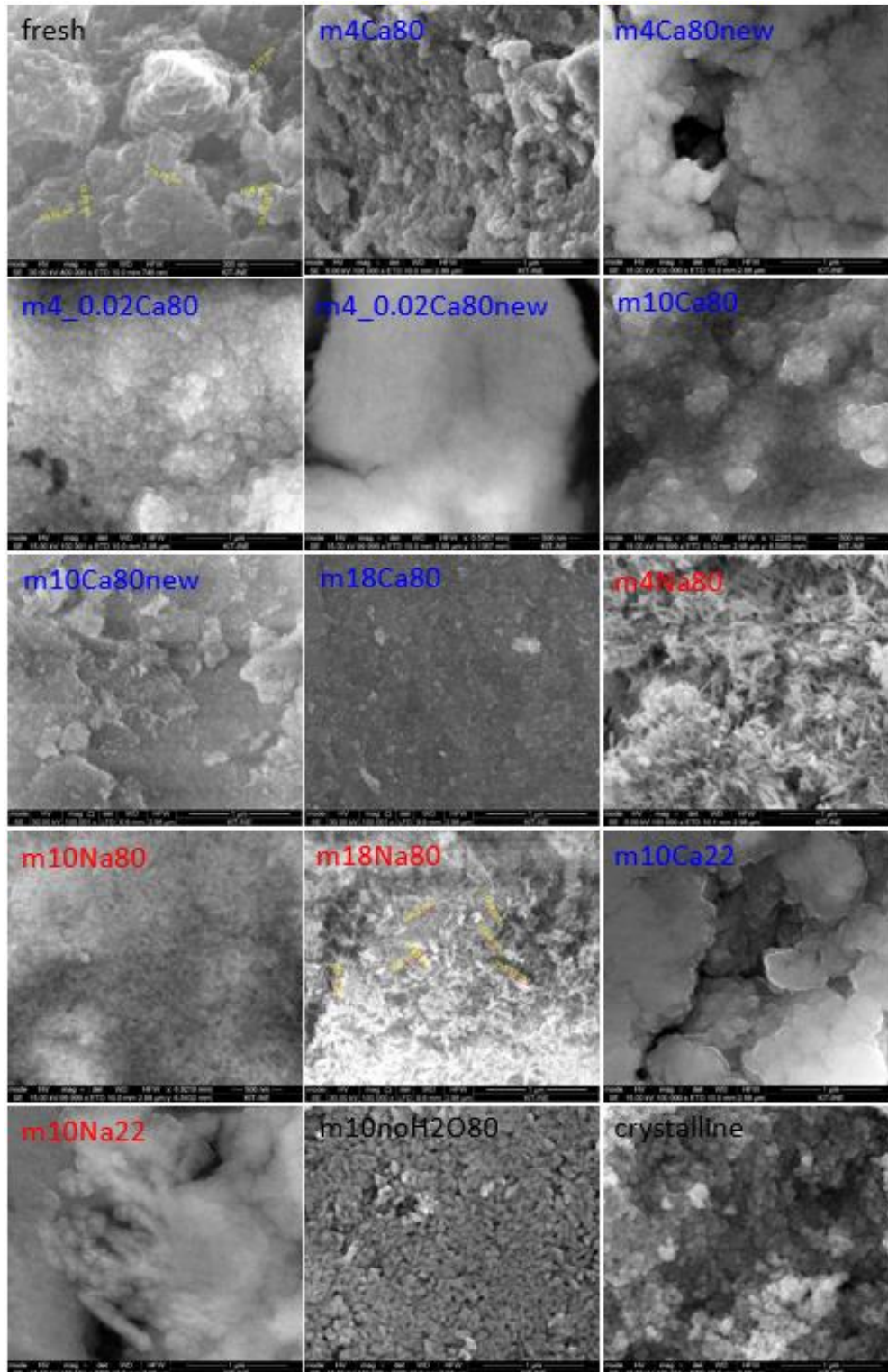


Figure 4.7: SEM images of the $ZrO_2(s)$ solid phases.

Table 4.2: weight (w%) and atomic (a%) percentages of Zr, O, Ca and Cl for the solid phases by EDX.

Solid phase	Zr		O		Ca		Cl		[O]/[Zr]	[Zr]/[Ca]
	w%	a%	w%	a%	w%	a%	w%	a%	EDX	EDX
fresh	53.0	16.5	31.0	55.0					3.3	
	±2.9	±2.7	±0.9	±4.8					±0.8	
m10Ca22	52.5	16.8	29.7	54.2	5.0	3.6	1.4	1.1	3.2	4.7 ±0.4
	±1.0	±0.3	±0.9	±1.7	±0.3	±0.2	±0.2	±0.2	±0.2	
m10Na22	58.5	19.5	27.6	52.4					2.7	
	±1.2	±0.4	±1.0	±1.8					±0.1	
m4Ca80	49.6	15.7	32.8	59.3	6.5	4.7	1.8	1.4	3.8	3.3 ±0.9
	±2.4	±2.3	±0.9	±4.8	±0.2	±0.4	±0.2	±0.4	±0.9	
m4Ca80new	58.3	21.0	25.3	51.9	8.1	6.6			2.5	3.2 ±0.2
	±1.1	±0.4	±1.0	±2.1	±0.4	±0.3			±0.1	
m4_002Ca80	66.1	25.4	22.5	49.3	2.9	2.5			1.9	10.2 ±1.6
	±1.2	±0.5	±1.0	±2.1	±0.3	±0.3			±0.1	
m4_002Ca80new	59.8	21.5	24.3	49.8	7.0	5.7			2.3	3.8 ±0.3
	±1.2	±0.4	±1.0	±2.1	±0.4	±0.4			±0.1	
m10Ca80	62.5	22.5	24.2	49.7	3.5	2.8			2.2	8.0 ±1.6
	±1.4	±0.5	±1.3	±2.6	±0.4	±0.4			±0.2	
m10Ca80new*	56.8	19.9	33.9	67.8	6.1	4.9	0.1	0.1	3.4	4.1 ±0.3
	±1.2	±0.4	±1.0	±1.9	±0.4	±0.3	±0.1	±0.1	±0.2	
m18Ca80*	64.6	24.7	28.5	62.2	2.8	2.4			2.5	10.3 ±2.3
	±1.1	±0.4	±0.8	±1.7	±0.5	±0.4			±0.1	
m4Na80	62.4	22.7	28.6	59.4					2.6	
	±2.0	±2.2	±0.6	±3.6					±0.4	
m10Na80	69.7	27.3	22.3	49.8					1.8	
	±1.0	±0.4	±0.7	±1.6					±0.1	
m18Na80*	67.3	25.9	29.2	64.0					2.5	
	±1.3	±0.5	±1.0	±2.1					±0.1	
m10noH2O80	71.3	29.2	23.3	54.3					1.9	
	±1.2	±0.5	±1.0	±2.3					±0.1	
crystalline	72.6	30.2	21.2	50.2					1.7	
	±1.4	±0.6	±1.1	±2.6					±0.1	

The total a% and m% are different from each other and different from 100% because of the carbon coating of the samples.

* prepared at a different time, significantly lower amount of carbon (carbon-coating) influences the values.

The SEM images show that the particles consist of large irregular aggregates of smaller particles. As with TEM the most remarkable observation from the SEM images is the presence of larger rods up to 200-300 nm for samples aged in 0.001 M NaOH solutions (m4Na80, m10Na80, m18Na80) and the sample aged without liquid phase (m10noH2O80). While the SEM images do not contain further information compared to TEM, the EDX measurements

may provide insights in the solid phase composition and thus also structure. EDX measurements summarized in Table 4.2 confirm the systematic presence of Ca in all solids aged in CaCl_2 , both at $T = 22$ and 80°C . This observation, in connection with the lower presence /absence of chloride, supports that Ca is not only remaining from insufficient washing, but is incorporated in the structure of $\text{ZrO}_2(\text{s})$ with Zr : Ca ratios of 3.2 to 10.3. Table 4.2 reflects also greater $[\text{O}]/[\text{Zr}]$ ratios for $\text{ZrO}_2(\text{am, hyd, fresh})$, as well as for solid phases aged at $T = 22^\circ\text{C}$. This observation supports the greater content of OH / H_2O in amorphous samples, as opposed to the lower $[\text{O}]/[\text{Zr}]$ ratios observed for the more crystalline samples, approaching a ratio of 2. In qualitative terms, solid phases aged at $T = 80^\circ\text{C}$ in NaOH solutions show smaller $[\text{O}]/[\text{Zr}]$ ratios than those aged at the same temperature in $\text{CaCl}_2\text{-Ca}(\text{OH})_2$ solutions. This correlates well with the larger crystal domains quantified for the former.

4.1.1.5 Extended X-ray absorption fine structure (EXAFS)

The evaluation of the EXAFS spectra with Athena and Artemis software is shown in Figure 4.8 and Table 4.3. The EXAFS analysis of the solids also reflects a different degree of crystallization. While all samples show a large Zr-O backscattering signal, important differences in the intensity of the Zr-Zr backscattering signals were observed. In the case of the amorphous solids, a Zr-Zr backscattering signal with only a small intensity is found. In agreement with the previously shown results, the samples aged at $T = 80^\circ\text{C}$ show higher Zr-Zr signals compared to the amorphous solids reflecting their higher order / crystallinity. The largest Zr-Zr backscattering signal was observed for the solid aged without liquid phase and the commercial crystalline solid indicating the most crystalline character of these samples. These qualitative observations are in line with the fitting approach and the resulting parameters. While it was possible to obtain fits with sufficient quality with only one oxygen and one zirconium shell in the case of the amorphous/rather amorphous solid phases, more shells were required for satisfying fits of the data of the more crystalline samples. The data of samples with tetragonal character (XRD) were fitted using two oxygen shells with identical coordination number, as expected for the tetragonal structure, a double oxygen scattering and one zirconium shell. For the monoclinic solid phases (XRD) two or three oxygen and two or three zirconium shells were used, partially with fixed coordination numbers to the expected values to obtain useful fits. The fresh solid phase shows a lower Zr-Zr coordination (4.35) compared to the solids aged at $T = 22^\circ\text{C}$ (10.60 and 11.74), in terms of the Zr-O coordination (7.54-8.92) and the distances of the shells (2.16 Å for Zr-O and 3.44-3.47 Å for Zr-Zr) no significant differences were observed. The tetragonal solid phases show similar EXAFS profiles with total oxygen coordination numbers of 6.72-8.42 at distances of 2.09-2.11 Å and 2.22-2.24 Å as well as Zr-Zr coordination numbers of 9.19-11.99 at 3.49-3.53 Å. Since for amorphous, tetragonal and monoclinic and within the monoclinic samples different approaches for fitting were used, it is not possible to

compare the results between these different groups quantitatively. In the case of the monoclinic samples a splitting of the Zr-Zr signal into a large part with smaller Zr-Zr distance and a smaller contribution with larger Zr-Zr distance is observed in agreement with crystallographic data (7 Zr-Zr distances: 3.34-3.59 Å, 5 Zr-Zr distances: 3.92-4.54 Å)⁶⁵ of monoclinic ZrO₂. This explains why at least two Zr shells are required to fit these data. In the case of the tetragonal solids, the Zr-Zr distances are very similar (crystallographic data: 4x 3.64 Å and 8x 3.68 Å)⁶⁵, so that only one Zr-Zr backscattering signal is observed.

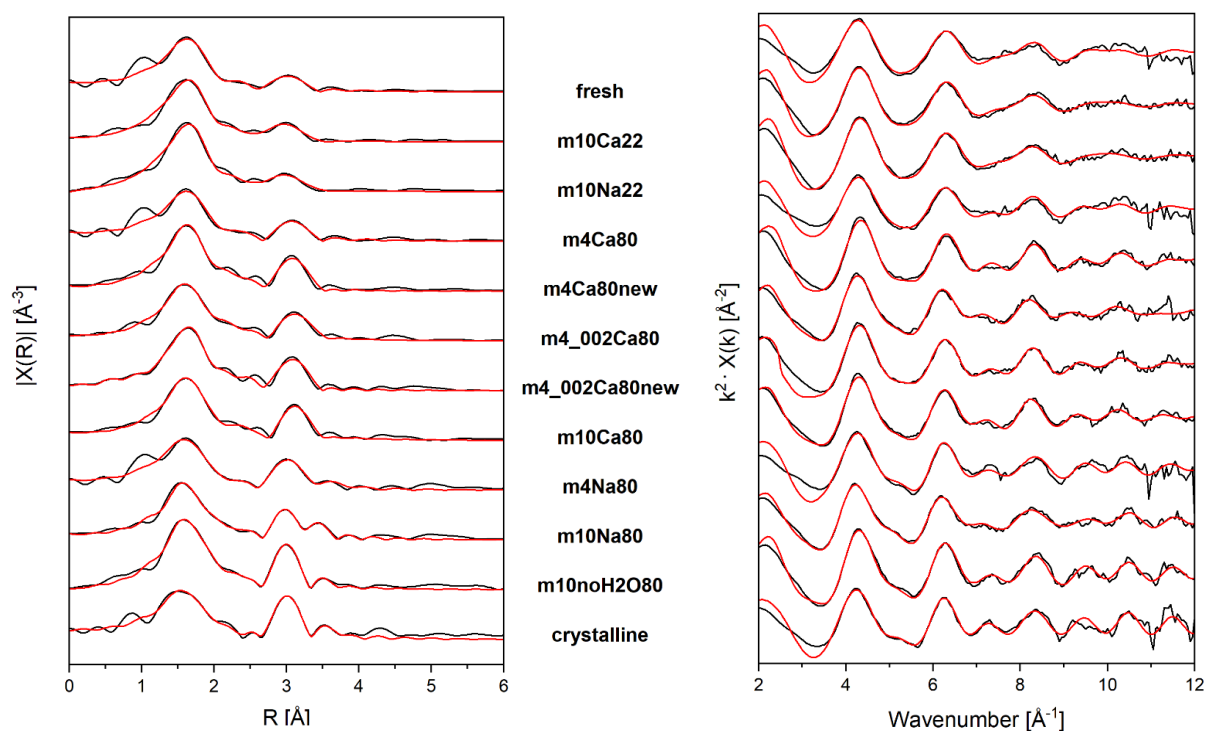


Figure 4.8: Fourier transform EXAFS spectra of the ZrO₂(s) samples in R and k space.

Table 4.3: EXAFS fit data for the solid phases.

Solid phase	Path	N	R (Å)	σ^2	ΔE_0	R
fresh	Zr-O	7.54	2.16	0.009	-3.70	0.009
	Zr-Zr	4.35	3.44	0.013		
m10Ca22	Zr-O	8.74	2.16	0.011	-3.25	0.019
	Zr-Zr	10.60	3.45	0.020		
m10Na22	Zr-O	8.92	2.16	0.010	-2.02	0.018
	Zr-Zr	11.74	3.47	0.022		
m4Ca80	Zr-O	7.20	2.15	0.009	-3.68	0.026
	Zr-Zr	4.64	3.47	0.011		
m4Ca80new	Zr-O1	4.21**	2.11	0.004	-0.42	0.023
	Zr-O2	4.21**	2.24	0.007		
	Zr-Zr	9.26	3.49	0.013		
	Zr-O-O	24.00*	3.45	0.011		

Table 4.3 (continuation): EXAFS fit data for the solid phases.

Solid phase	Path	N	R (Å)	σ^2	ΔE_0	R
m4_0.02Ca80	Zr-O1	3.39**	2.09	0.001	-2.77	0.014
	Zr-O2	3.39**	2.24	0.002		
	Zr-Zr	11.99	3.53	0.016		
	Zr-O-O	24.00*	3.44	0.004		
m4_0.02Ca80new	Zr-O1	3.36**	2.10	0.001	-1.89	0.021
	Zr-O2	3.36**	2.24	0.002		
	Zr-Zr	9.19	3.49	0.013		
	Zr-O-O	24.00*	3.43	0.004		
m10Ca80	Zr-O1	3.62**	2.09	0.002	-2.43	0.018
	Zr-O2	3.62**	2.22	0.002		
	Zr-Zr	9.95	3.51	0.013		
	Zr-O-O	24.00*	3.43	0.005		
m4Na80	Zr-O1	8.85	2.15	0.012	-4.88	0.010
	Zr-O2	4.00*	3.64	0.013		
	Zr-Zr1	6.33	3.45	0.010		
	Zr-Zr2	4.00*	4.02	0.012		
m10Na80	Zr-O1	2.25	2.07	0.000	-2.94	0.010
	Zr-O2	4.50	2.21	0.005		
	Zr-O3	4.00*	3.69	0.016		
	Zr-Zr1	8.03	3.48	0.009		
	Zr-Zr2	4.90	3.63	0.007		
m10noH2O80	Zr-O1	3.90**	2.09	0.002	-1.42	0.007
	Zr-O2	3.90**	2.23	0.002		
	Zr-O3	4.00*	3.63	0.026		
	Zr-Zr1	9.62	3.47	0.008		
	Zr-Zr2	4.33	3.66	0.007		
crystalline	Zr-O1	2.00*	2.06	0.002	-3.22	0.012
	Zr-O2	5.89	2.21	0.008		
	Zr-O3	4.00*	3.61	0.005		
	Zr-Zr1	4.14	3.46	0.005		
	Zr-Zr2	1.00*	3.65	0.001		
	Zr-Zr3	4.00*	4.00	0.015		

Coordination numbers (N), bond distances (R (Å)), Debye-Waller factors (σ^2), shift in energy from calculated Fermi level (ΔE_0) and 'goodness of fit' factor (R).

* N fixed to expected value, ** N(Zr-O1) forced to be equal to N(Zr-O2) as expected for tetragonal structure.

4.1.1.6 Small-angle X-ray scattering (SAXS)

SAXS measurements provide information on particle sizes and families, but additionally about some surface properties. The observed inflection points (Figure 4.9) in the intensity of the scattering vector q suggest the presence of small primary particles with a size of a few nm and larger aggregates of secondary particles. In the case of solids aged at $T = 80^\circ\text{C}$ in NaOH (m10Na80), three inflection points corresponding to 3 families of particles with different particle sizes were observed as also shown by TEM. In contrast, the solids aged in CaCl_2 (m10Ca80), the solid aged without liquid phase (m10noH2O80), the crystalline solid (crystalline) and the amorphous solids (fresh) show only two inflection points corresponding to 2 families of particles as also observed by TEM. The inflection point at $q = 0.15 \text{ nm}^{-1}$ was not observed in the SAXS profile of the solids aged in CaCl_2 (m10Ca80), while it was observed for other solid phases. Considering that the monoclinic phase is not observed in the solids aged in CaCl_2 (m10Ca80) (see Figure 4.2), the largest particles corresponding to $q = 0.15 \text{ nm}^{-1}$ are likely to exhibit monoclinic structure. Then, the secondary particle with the size of 10 nm corresponding to $q = 0.4 \text{ nm}^{-1}$ observed in m10Na80 and m10Ca80 would exhibit tetragonal and/or cubic phase. This behaviour is in agreement with previous studies of Pitcher et al.¹⁴ and Sharma et al.¹⁵ showing stability crossovers for the different crystal structures depending on particle size/surface area.

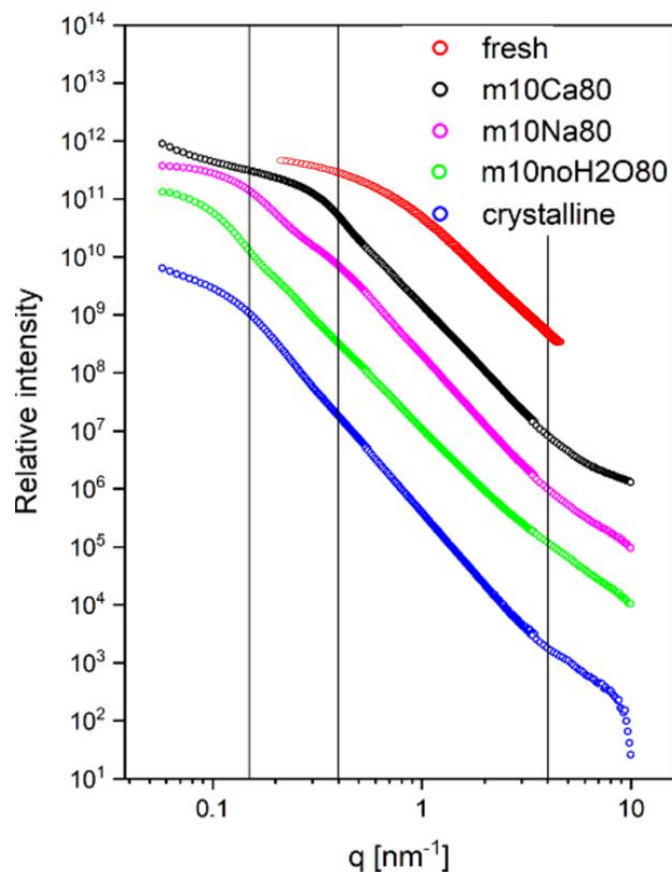


Figure 4.9: SAXS measurements of selected solid phases.

The slope of the intensity of the scattering vector q in the Porod region gives information about the surface roughness of the solids. The slope of 4 after the inflection points at $q = 4 \text{ nm}^{-1}$ and 0.15 nm^{-1} observed in the case of the samples aged at $T = 80^\circ\text{C}$ in NaOH and the solid aged without liquid phase indicates a smooth surface of secondary particle. For the samples aged at $T = 80^\circ\text{C}$ in CaCl_2 the slope is slightly smaller than 4 indicating still a rather smooth surface, though less than in NaOH systems. In the case of the fresh solid and the amorphous solids aged at $T = 22^\circ\text{C}$ slopes close to 3 were observed and correspond to a rough surface. Correlations between crystallinity and surface roughness were previously reported for ceramic thin films and glazes^{123–126}. In contrast to the increasing smoothness by ageing in the present study, in these studies crystallization in amorphous thin layers by annealing generally leads to increasing roughness. This behaviour, which at first glance appears to be contradictory may be explained by the different crystallization methods since annealing of fixed amorphous layers leads to rapid and thus to inhomogeneous crystallization, while the hydrothermal approach in the present study causes continuous condensation and crystallization processes with long-term effects on bulk solid phases and their surfaces.

Kobayashi and co-workers^{70,127} performed similar experiments with amorphous $\text{ZrO}_2(\text{s})$ precipitates aged at room temperature or elevated temperatures up to 90°C . As in the present work, they also observed primary particles with a size of several nanometers, which build larger aggregates for solid phases aged at low temperatures. For solid phases aged at 90°C ($\text{pH} = 2.7$) and $>60^\circ\text{C}$ ($\text{pH} = 12.2$) a lower amount of aggregates and the formation of crystallized particles with a size of 25 nm was observed accompanied by appearance of diffraction peaks corresponding to monoclinic ZrO_2 in wide-angle X-ray scattering (WAXS) measurements^{70,127}.

4.1.1.7 Effect of ageing on structure and particle size

The solid phase characterization with XRD, TEM, electron diffraction, Raman spectroscopy, SAXS, EXAFS and SEM-EDX gives insights on the impact of ageing at elevated temperatures on the crystallinity, particle size and particle growth of the ZrO₂ solid phases. These methods show that the ageing at T = 80°C induces a transformation from a freshly precipitated amorphous solid towards nano-crystalline solids, accompanied with an increasing particle size and the formation of different types of particles.

In contrast to ageing at T = 80°C, no changes in the solid properties were observable with the methods used within this study for solid phases equilibrated at T = 22°C. Variations in the ageing time (4, 10 or 18 months) do not promote evident changes in the structure of the solid phase, indicating the stabilization of larger ZrO₂ particles with defined crystallographic structure already after 4 months. Contrary to the ageing time, the background electrolyte used during the ageing shows a large effect on the solid properties.

Ageing at T = 80°C in either NaOH or CaCl₂ systems shows an increasing particle size and crystallinity and the formation of different types of particles. A very significant effect of the background electrolyte used during ageing is the stabilization of the cubic/tetragonal crystal structure with a particle size of 11-14 nm in CaCl₂ systems, while the ageing in NaOH systems results in the monoclinic structure with a particle size of 23-27 nm. A further difference is the formation of very large rods (up to 300 nm length) in the case of NaOH ageing background which is not present after ageing in CaCl₂ solutions.

As reason for the stabilization of the different crystal phase in presence of Ca, different options are discussed in the literature. One possibility is the incorporation of Ca and thus a stabilization of the cubic/tetragonal solid phase as known for other elements, e.g. Y⁹⁻¹¹ with the formation of a solid solution of Zr_{1-x}Y_xO₂. The same behavior is also reported for Ca, but under conditions that are very different from the conditions in the present study^{9,12,13}. However, this hypothesis would be supported by the systematic presence of Ca in the samples aged in CaCl₂ media observed with EDX measurements despite several washing steps. On the other hand, the smaller contributions of the cubic/tetragonal phase in some monoclinic samples aged in absence of Ca can obviously not be explained by incorporation of Ca.

Another hypothesis explaining also these results would be, that the stabilization of different crystal structures is an effect of specific surface area and thus of particle size. The higher specific surface area of the smaller particles in presence of Ca could lead to energy crossovers for the stabilized crystal phase^{14,15}. The different crystal structures in the aged samples can be explained by the observation of large rods (200-300+ nm) and small particles in the samples with TEM. Following the reported energy crossovers, the small particles should be tetragonal, while for the rods (>48 nm) the monoclinic structures should be preferred. This behavior

would explain the cubic/tetragonal character of the samples aged in CaCl_2 , since in these samples no larger particles were observed. The monoclinic character with small contributions of cubic/tetragonal for the samples aged at $T = 80^\circ\text{C}$ in NaOH can also be explained, since large rods and small particles were observed in these samples.

4.1.2 Solid composition and hydration

4.1.2.1 Thermogravimetric analysis with differential thermal analysis (TG-TDA)

In addition to particle growth and increase of crystallinity during the transformation process from amorphous towards more crystalline solid phases, a decrease in the amount of hydration waters due to condensation reactions in the $ZrO_2(s)$ solid phases is expected. Therefore, TG-DTA measurements were performed to determine the amount of hydration water of the solid phases. The main quantitative outcome evaluated from the TG-DTA data is the total weight loss measured up to 1200 °C, which is assigned to the number of hydration waters in the investigated hydrous oxides with the assumed stoichiometry $ZrO_2 \cdot nH_2O$. The real stoichiometry of the solids can be described more accurately as $ZrO_x(OH)_{4-2x} \cdot zH_2O$. The TG-DTA results of the solids are shown in Figures A.1 to A.7 in the appendix. An overview of all solids is given in Table 4.4 and Figure 4.10.

Table 4.4: weight loss of the samples determined with TG and calculated amount of hydration water assuming $ZrO_2 \cdot nH_2O$ as stoichiometry.

Solid phase	Weight loss (%)	Hydration water per Zr
fresh	23.6 ± 0.5	2.1 ± 0.1
m10Ca22	23.7 ± 0.5	2.1 ± 0.1
m10Na22	22.9 ± 0.5	2.0 ± 0.1
m4Ca80	15.2 ± 0.5	1.2 ± 0.1
m4Ca80new	8.4 ± 0.5	0.6 ± 0.1
m4_0.02Ca80	4.9 ± 0.5	0.3 ± 0.1
m4_0.02Ca80new	6.5 ± 0.5	0.5 ± 0.1
m10Ca80	2.7 ± 0.5	0.2 ± 0.1
m18Ca80	5.5 ± 0.5	0.4 ± 0.1
m4Na80	4.7 ± 0.5	0.3 ± 0.1
m10Na80	4.3 ± 0.5	0.3 ± 0.1
m18Na80	4.0 ± 0.5	0.3 ± 0.1
m10noH2O80	4.3 ± 0.5	0.3 ± 0.1
crystalline	1.3 ± 0.5	0.1 ± 0.1

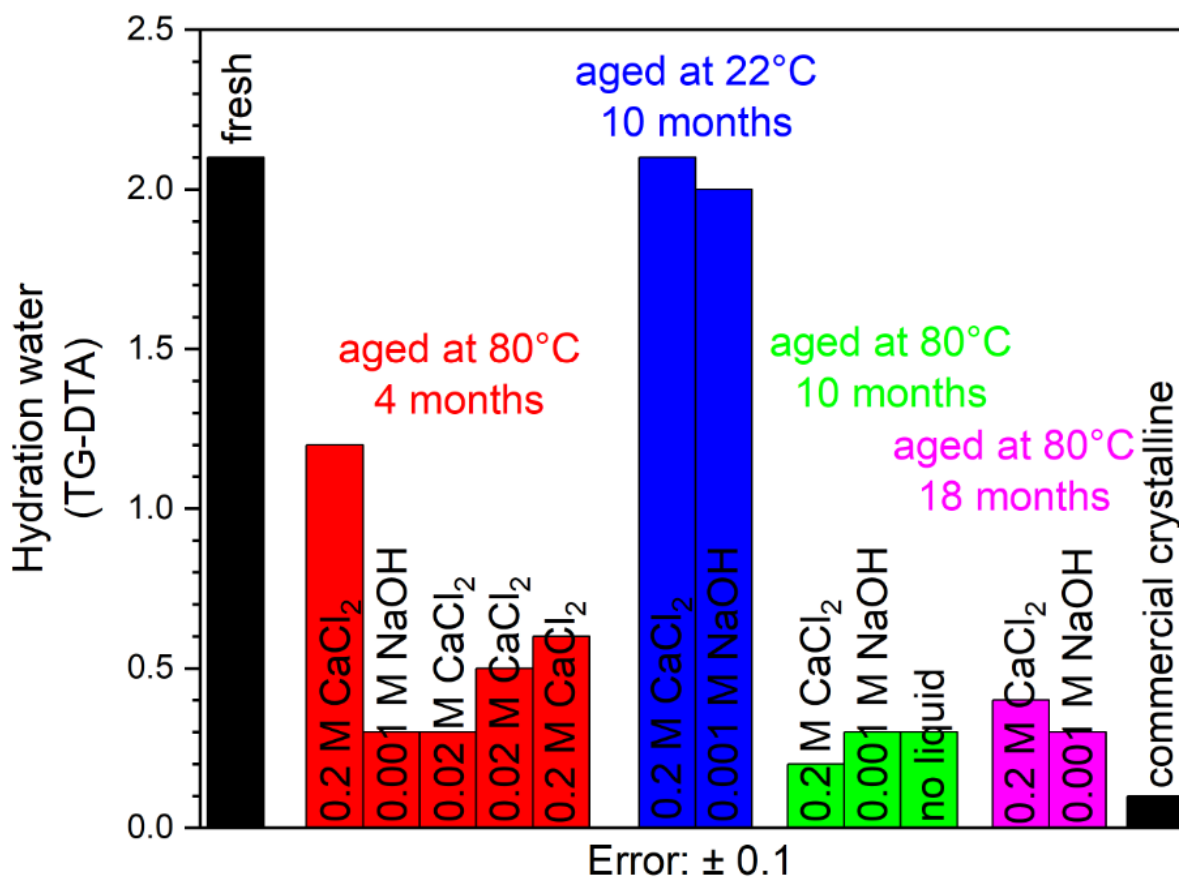


Figure 4.10: Amount of hydration water n of the solids determined by TG-DTA assuming a stoichiometry of $ZrO_2 \cdot nH_2O$.

The main weight loss, determined with TG, takes place from room temperature (RT) up to 400 °C and can be divided into two parts, RT to 200 °C and 200 °C to 400 °C. Over 400 °C only very small weight losses are observed. The weight loss below 200 °C is more pronounced, especially in the case of amorphous solid phases and can be assigned to desorption of physically bound water¹²⁸. The weight losses above 200°C may correspond to the removal of surface hydroxides by condensation reactions¹²⁸ or strongly bound water molecules. The DTA data show that the removal of water is an endothermic process, as expected. Furthermore, DTA data of amorphous solid phases (fresh, m10Ca22 and m10Na22) show exothermic peaks, without weight loss in TG, between 430 °C and 500 °C, which probably correspond to crystallization of the metastable tetragonal solid phase. A transformation of the amorphous and tetragonal/cubic solids towards the monoclinic phase was not observable with TG-TDA, either because it is a continuous process with low energy¹²⁸ or because this transformation does not take place during such a short measurement. The results clearly show a significantly larger amount of hydration waters in the freshly precipitated solid and the solids aged at $T = 22$ °C ($n = 2.0 - 2.1$) compared to the solid phases aged at $T = 80$ °C ($n = 0.4 \pm 0.2$), indicating that elevated temperatures of 80 °C are high enough to enable an endothermic dehydration

process, taking place during the ageing. In average, the amount of water in the solids aged for 10 months is only slightly lower compared to solids aged for 4 months, showing that most of the transformation process occurs during the first 4 months of ageing at elevated temperatures. In order to investigate the reversibility of this dehydration process, a fraction of the freshly precipitated solid phase was divided into three parts. Instead of directly measuring TG-DTA, the first part was rehydrated in H₂O for 24 hours, the second part was heated to 200 °C for 2 hours and rehydrated in H₂O for 24 hours and the third part was heated to 400 °C for 2 hours and rehydrated in H₂O for 24 hours. Afterwards the solids were washed, dried under reduced pressure and investigated by TG-DTA, the results are shown in Figures 4.11 and 4.12.

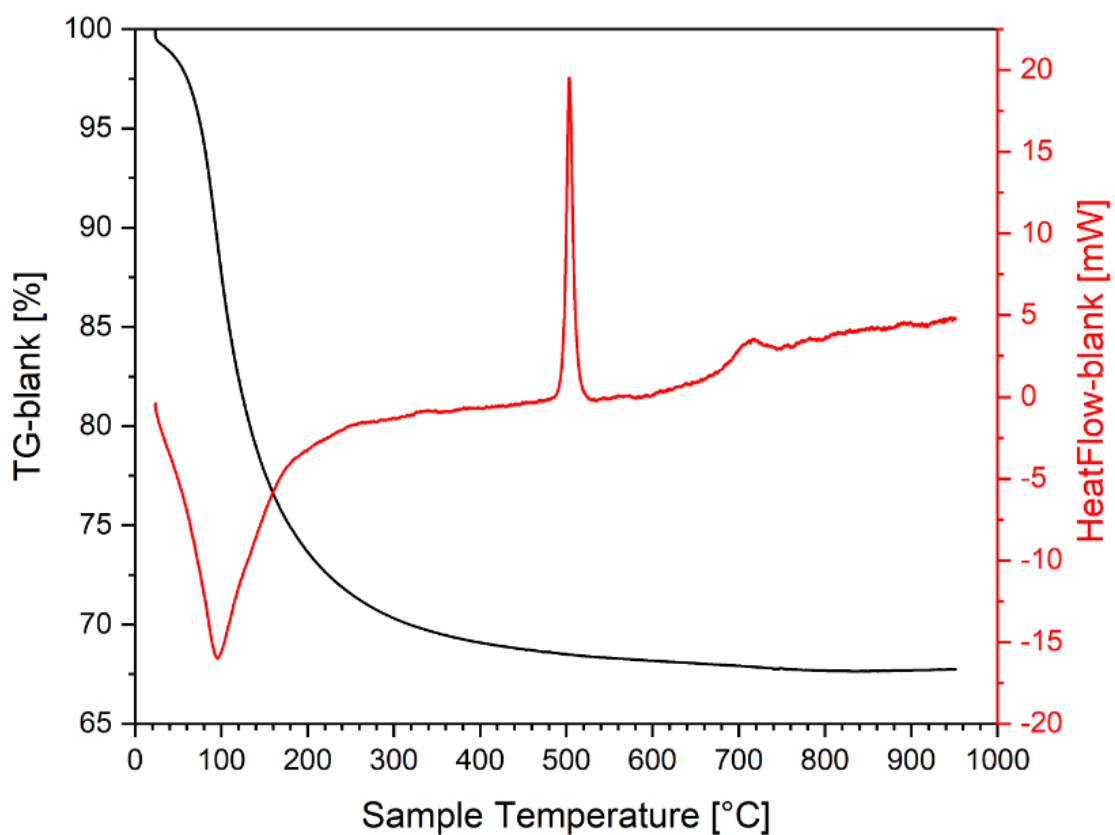


Figure 4.11: TG-DTA results of the fresh rehydrated solid without heating.

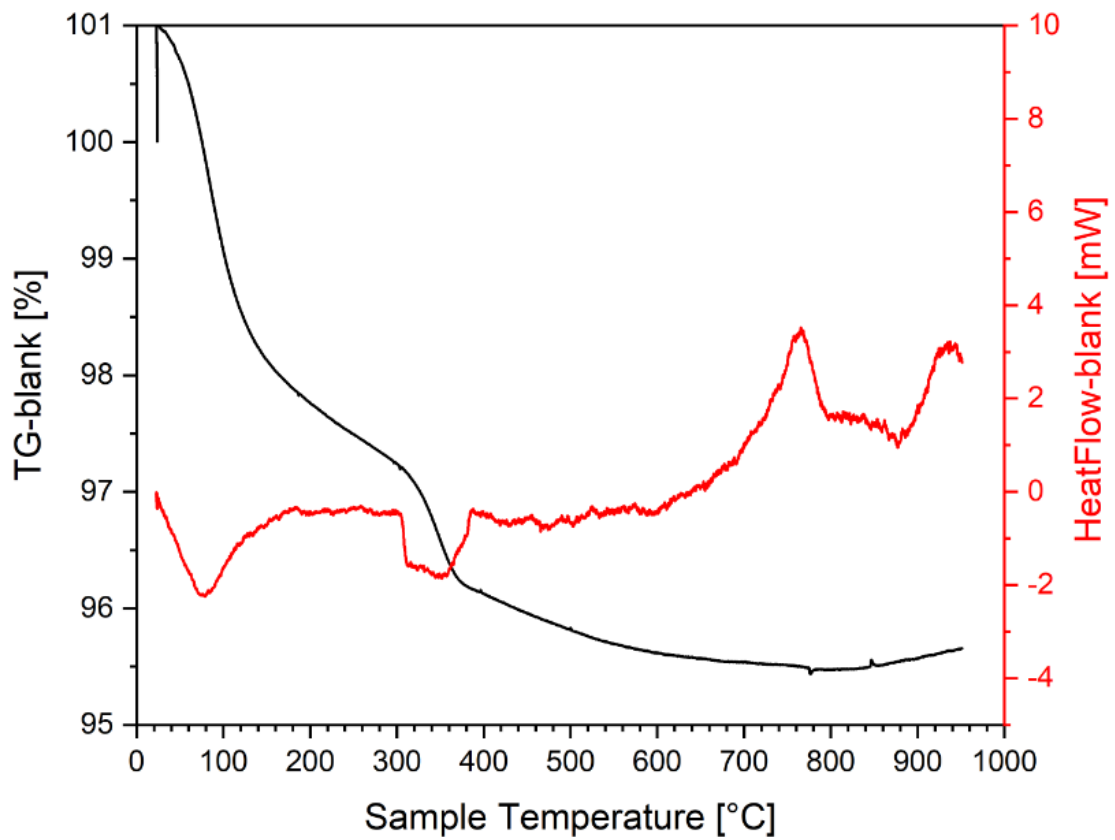
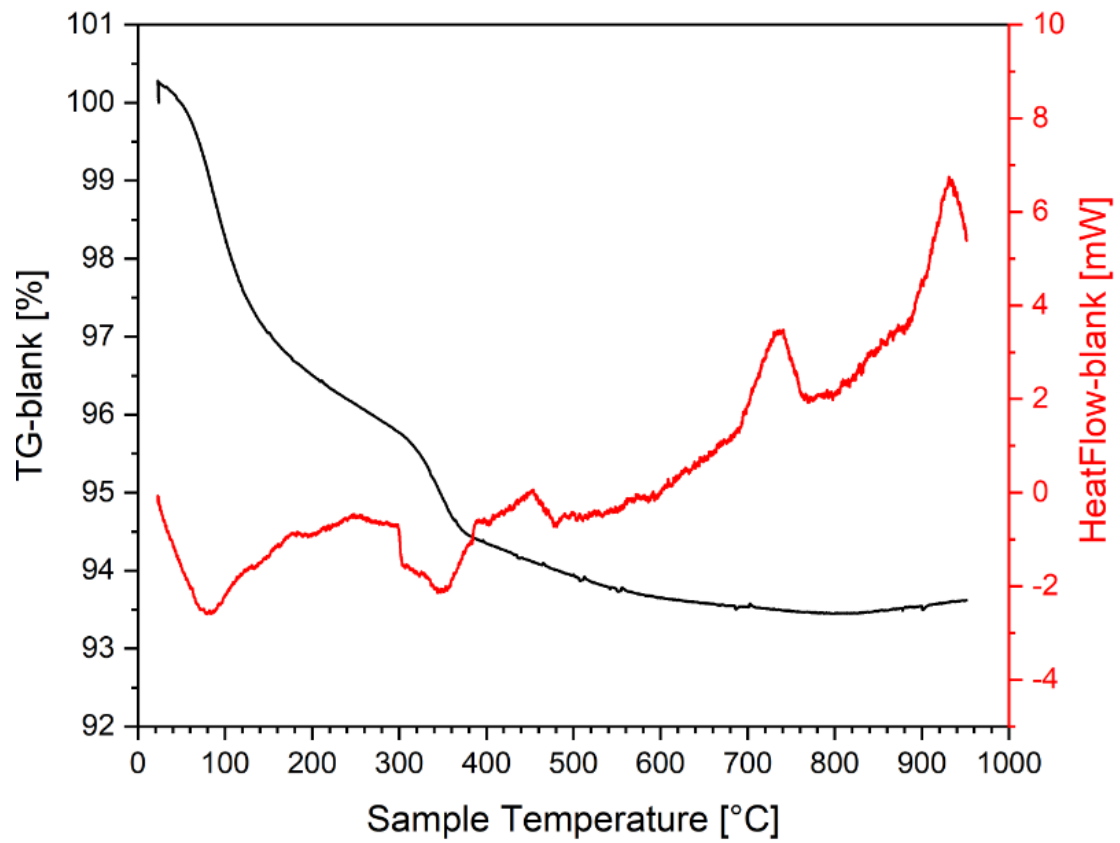


Figure 4.12: TG-DTA results of the fresh rehydrated solid with heating to 200°C (above) and 400°C (below) for 2 hours.

The determined weight losses and corresponding amounts of hydration water are shown in Table 4.5. The unheated fresh rehydrated solid shows an even higher amount of hydration water as the originally freshly precipitated solid, which may be explained by the different drying conditions and TG devices. The weight losses of the heated rehydrated solids are much lower and in the same range as the aged solids, indicating that the transformation process is irreversible. Since the dehydration is endothermic ¹²⁸ and thus a rehydration should be exothermic, this irreversibility is surprising at the first moment, but may be explained with the DTA signals. The unheated fresh rehydrated solid, as well as other amorphous solids, shows an exothermic DTA signal around 500 °C corresponding probably to crystallization of the metastable tetragonal solid phase, which is not observed in the heated rehydrated solid phases, indicating that these solids are already crystallized. This assumption was confirmed with XRD measurements (Figure 4.13) which show reflexes corresponding to cubic/tetragonal ZrO₂ and particle sizes of 12-13 nm, determined by Scherrer analysis, for the heated rehydrated solids. These results show that the dehydration occurring during heating/ageing at elevated temperatures is connected with irreversible structural changes in the solid phases, like particle growth and crystallization. Note further that the size of 12-13 nm is again connected to a cubic/tetragonal crystal structure, as occurred in the samples aged at T = 80 °C in CaCl₂ systems. This observation supports again the interlink between the particle size and the crystal structure, as previously discussed (in terms of surface area, instead of particle size) by Pitcher and co-workers ¹⁴ and Sharma and co-workers ¹⁵.

Table 4.5: weight loss, amount of hydration water, crystal structure and particle size of the rehydrated solid phases.

Solid	Weight loss	Hydration water	Structure	Size
Fresh, rehydrated	32.5 %	3.3	amorphous	-
Fresh, 200°C, rehydrated	6.5 %	0.5	Tetragonal/cubic	12-13 nm
Fresh, 400°C, rehydrated	4.5 %	0.3	Tetragonal/cubic	12-13 nm

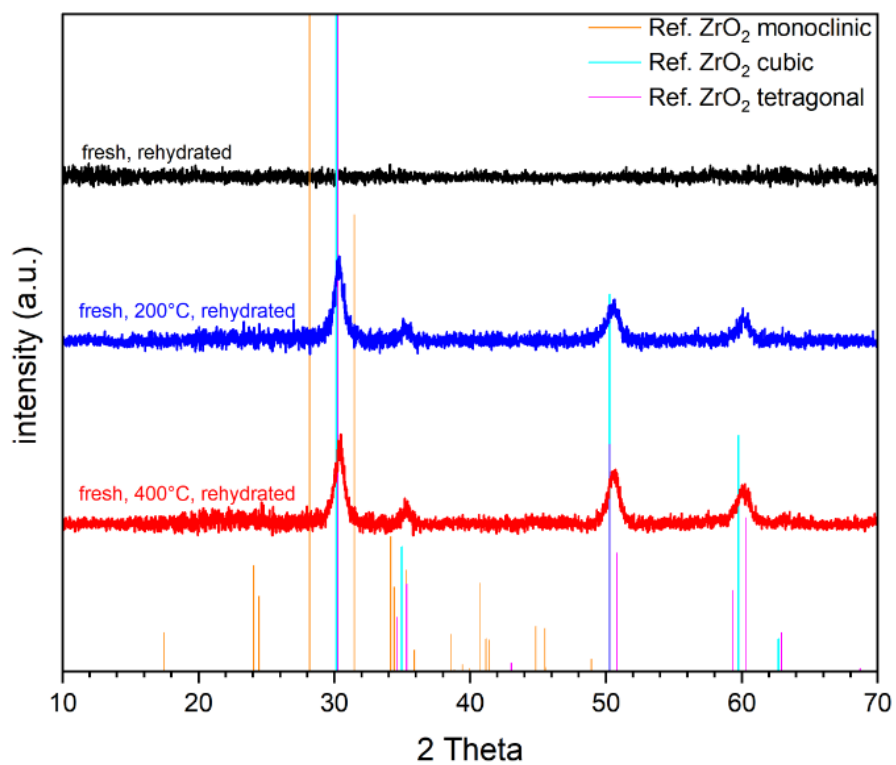


Figure 4.13: XRD patterns of the rehydrated solids. Vertical lines indicate reference data reported for ZrO₂(cr) in the COD database^{93–100}: ZrO₂ monoclinic (COD ID: 1528984), ZrO₂ tetragonal (COD ID: 1539831), ZrO₂ cubic (COD ID: 5000038).

4.1.2.2 X-ray photoelectron spectroscopy (XPS)

X-ray photoelectron spectroscopy (XPS) measurements were conducted in order to determine the elemental composition of the $ZrO_2(s)$ solid phases and especially to evaluate oxygen speciation, by fitting contributions of O^{2-} , OH and H_2O to the narrow scan of the O 1s signal. Figure 4.14 shows an exemplary survey spectrum of one of the solids, the O 1s narrow scans of all solids and an example how the O^{2-} , OH and H_2O contributions are calculated. The resulting contributions and a [O]/[Zr] ratio calculated for all solids from the intensities of Zr and O signals are summarized in Table 4.6. The amorphous solids show higher contributions of OH and H_2O , but lower amounts of O^{2-} compared to solid phases aged at 80 °C. The commercial crystalline solid shows the highest amount of O^{2-} and the lowest contribution of OH and H_2O . This is also reflected in the [O]/[Zr] ratio, which is above 3.0 for the amorphous solids and around 2.5 for the monoclinic solid phases (aged in 0.001 M NaOH and commercial crystalline). This behavior is consistent with the previous observations of dehydration and particle growth during the ageing at 80 °C, since in the dehydration process water molecules and surface hydroxides are removed. The [O]/[Zr] ratios of all solids are significantly higher compared to the ideal value of 2 in $ZrO_2(cr)$, indicating still the presence of surface hydroxide or hydrate groups. Comparing the [O]/[Zr] ratios determined by XPS with those from SEM-EDX and TG-DTA a qualitative agreement is observed, since all three methods deliver higher ratios for the amorphous solids and lower ones for the aged solids. For amorphous samples the values from XPS and EDX are similar, while TG shows higher ratios. In the case of aged samples the XPS and TG values are similar and higher compared to the ratios determined by EDX.

Table 4.6: O^{2-} , OH and H_2O contributions and [O]/[Zr] ratio, determined with XPS, relative errors $\pm(10-20)\%$.

Solid	O^{2-} (%)	OH (%)	H_2O (%)	[O]/[Zr]	[O]/[Zr]	[O]/[Zr]
				XPS	EDX	TG-DTA
fresh	58.1		41.9	3.20	3.3±0.8	4.1±0.1
m10Ca22	52.4	40.8	6.9	3.34	3.2±0.2	4.1±0.1
m10Na22	56.1	37.2	6.7	3.11	2.7±0.1	4.0±0.1
m4Ca80	67.3		32.7	2.92	3.8±0.9	3.2±0.1
m4Ca80new	68.0	25.7	6.2	3.01	2.5±0.1	2.6±0.1
m4_0.02Ca80	78.5	18.6	3.0	2.60	1.9±0.1	2.3±0.1
m4_0.02Ca80new	71.7	22.9	5.5	2.97	2.3±0.1	2.5±0.1
m10Ca80	77.6	19.0	3.4	2.70	2.2±0.2	2.2±0.1
m10Ca80new	63.6	30.8	5.6	3.21	3.4±0.2	
m18Ca80	70.4	22.3	7.3	2.68	2.5±0.1	2.4±0.1
m4Na80	72.9		27.1	2.49	2.6±0.4	2.3±0.1
m10Na80	75.1	19.7	5.2	2.48	1.8±0.1	2.3±0.1
m18Na80	74.1	20.3	5.7	2.39	2.5±0.1	2.3±0.1
m10noH2O80	71.0	20.6	8.4	2.46	1.9±0.1	2.3±0.1
crystalline	83.3	13.2	3.5	2.50	1.7±0.1	2.1±0.1

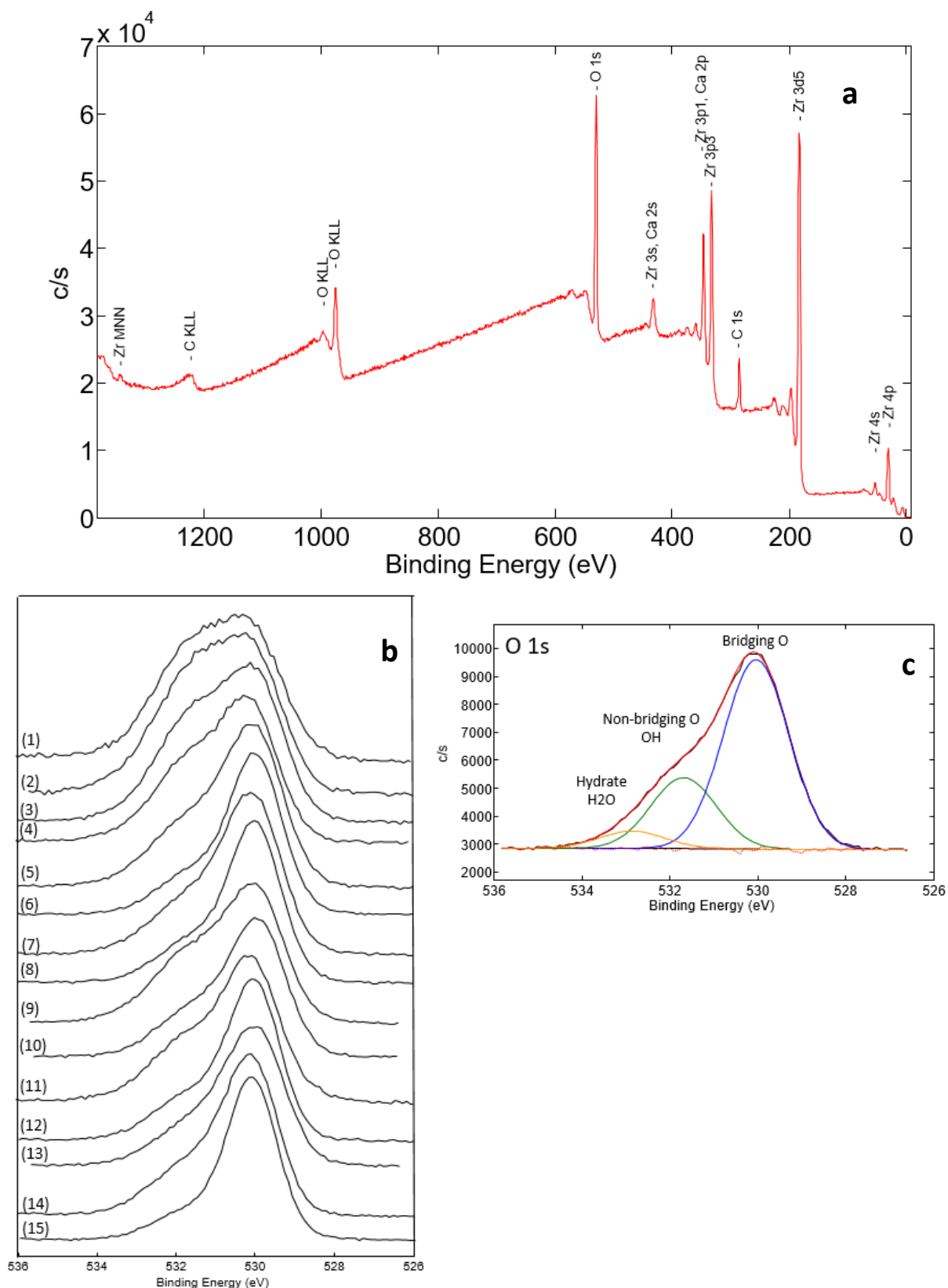


Figure 4.14: a) complete XPS spectrum of one solid, b) narrow scan of the O 1s signal of all ZrO_2 solids: (1) fresh, (2) m10Ca22, (3) m10Na22, (4) m4Ca80, (5) m4Ca80new, (6) m4_002Ca80, (7) m4_0.02Ca80new, (8) m10Ca80, (9) m10Ca80new, (10) m18Ca80, (11) m4Na80, (12) m10Na80, (13) m18Na80, (14) m10noH2O80, (15) commercial crystalline and c) an exemplary fit showing how the contributions of O^{2-} , OH and H_2O are calculated.

4.1.2.3 Fourier-transform infrared spectroscopy (FTIR)

The FTIR spectra of the fresh, aged and commercial crystalline $\text{ZrO}_2(\text{s})$ are shown in Figure 4.15. Most of the signals cannot be assigned to ZrO_2 , but to adventitiously adsorbed CO_2 and ethanol. Signals approximately at 700 cm^{-1} , $2300\text{--}2400\text{ cm}^{-1}$, 3600 cm^{-1} and 3700 cm^{-1} correspond to carbon dioxide ¹²⁹, which was present due to measurements under air conditions. Signals at 900 cm^{-1} , 1050 cm^{-1} , 1250 cm^{-1} , 1400 cm^{-1} , $2850\text{--}3000\text{ cm}^{-1}$ and 3650 cm^{-1} can be explained by ethanol ¹²⁹ which was used for washing the solids before the measurement. The signals between 1300 cm^{-1} and 1700 cm^{-1} , which are more pronounced in the case of amorphous solids may correspond to previously observed signals at approximately 1340 cm^{-1} and 1630 cm^{-1} for amorphous ZrO_2 nanoparticles ^{130,131}. Signals at 3680 cm^{-1} and 3780 cm^{-1} are also known for ZrO_2 ¹³² and may correspond to the small signals observed at $3650\text{--}3750\text{ cm}^{-1}$. The largest signals are observed in the water region ($2500\text{--}3800\text{ cm}^{-1}$) corresponding to hydroxides in the solid phases. Thus, FTIR qualitatively confirms the TG-DTA and XPS results, showing much larger signals in the water region for amorphous solid phases due to the higher amount of hydration water and hydroxides compared to the more crystalline samples. A quantitative confirmation of the TG-DTA and XPS results could not be achieved by FTIR.

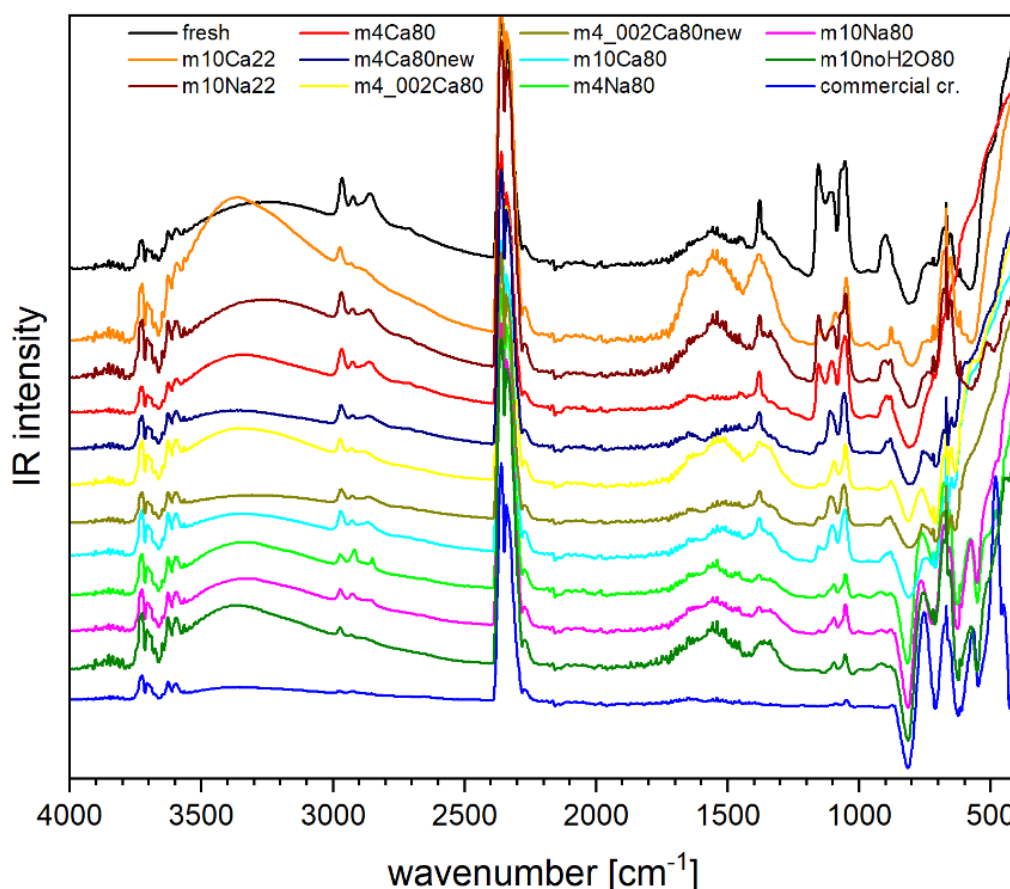


Figure 4.15: FTIR spectra of the fresh, aged and crystalline solid phases investigated in this work.

4.1.2.4 Hydrogen-deuterium exchange experiments

To gain information about possibly different types of hydration water, exchangeability of hydration water and reversibility of hydration and dehydration, hydrogen-deuterium exchange experiments were conducted as explained in chapter 3.6. The samples, a freshly precipitated solid, a commercial crystalline solid and three long-term aged solids, were analyzed by FTIR and TG-DTA coupled with mass spectroscopy. The TG-DTA and TG-MS data are shown in Figures 4.16 to 4.20, respectively. The FTIR spectra of selected samples are shown in Figure 4.21. In the case of the fresh solid, TG-DTA shows the same properties before and after H-D exchange, a large weight loss between room temperature and 200 °C, as well as an exothermic DTA peak corresponding to crystallization. The TG-DTA of the aged solids (m10Ca80new, m18Ca80, m18Na80) with weight losses of 5 to 9 % are in agreement with the other aged samples. The high weight loss of the commercial crystalline solid may be explained by insufficient drying. FTIR of the fresh solid shows a shift of the signal in the water region (2500-3800 cm⁻¹) towards 1700-2700 cm⁻¹ indicating that an exchange between hydrogen and deuterium took place and that the fresh solid contains OD instead of OH groups after the exchange. In the case of the other solids, FTIR indicates a partial (m10Ca80new, m18Na80, crystalline) or negligible (m18Ca80) exchange. These results were not confirmed with the mass spectroscopy results. The heating of the samples results expectedly in the removal of gaseous H₂O, HDO and D₂O, depending of the sample composition after exchange. Due to the signal distribution for pure D₂O, HDO and pure H₂O¹³³, signals at masses of 16 (O), 17 (OH), 18 (H₂O, OD), 19 (HDO) and 20 (D₂O) were expected. The area of the signals at masses of 17, 18, 19 and 20 were calculated by integration of the peaks to receive the relative intensities of each mass signal. The relative amounts of H₂O, HDO and D₂O and thus the relative amounts of H and D can be calculated out of the measured intensity distribution with the help of the signal distribution for pure D₂O, HDO and pure H₂O¹³³. First, the amount of D₂O was calculated from the signal at m = 20. The signal at m = 19 was used to calculate the amount of HDO and finally the amount of H₂O can be either calculated from the signal at m = 18 or m = 17. The peak areas, relative intensities and relative amounts of H₂O, HDO and D₂O as well as the H/D ratios are shown in Table 4.7. In contrast to FTIR the mass spectroscopy still shows the predominance of H over D with H/D ratios of approximately 2 (fresh) and 6 to 36 for the long term aged solids. This high contribution of H observed with TG-MS compared to the FTIR measurements may be explained by measurement conditions of the TG-DTA coupled with mass spectroscopy, if somehow humidity is introduced to the samples during the measurement. Since even the mass spectroscopy for pure D₂O showed a large contribution of hydrogen, the FTIR data seem more reliable in this context. Even if the TG-DTA-MS and FTIR measurements are affected by incomplete drying or adsorption of humidity, these measurements show that the H-D exchange is clearly reduced for the samples aged at 80°C compared to fresh samples.

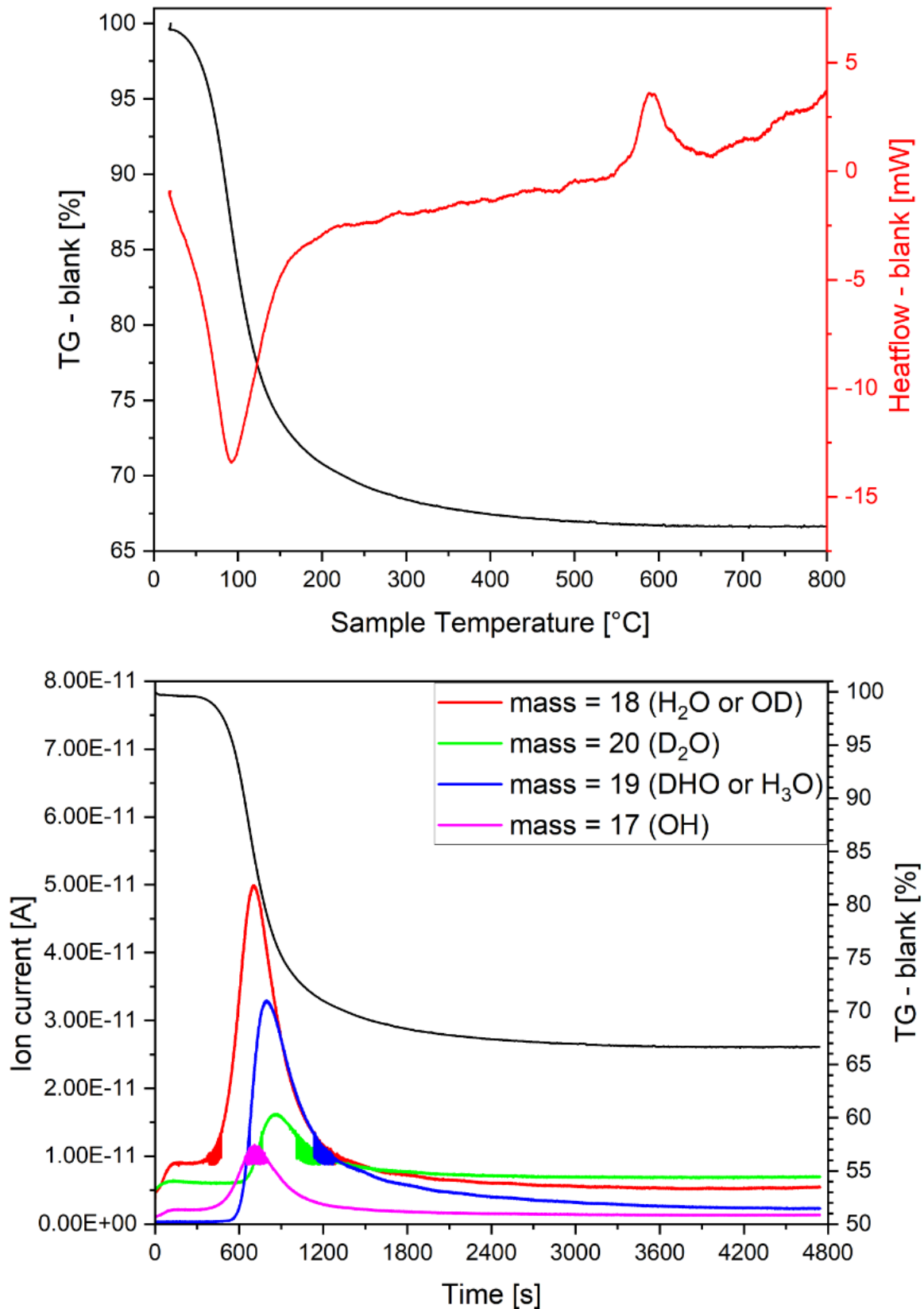


Figure 4.16: TG-DTA and TG-MS results for a freshly precipitated $ZrO_2(s)$ after exchange with D_2O .

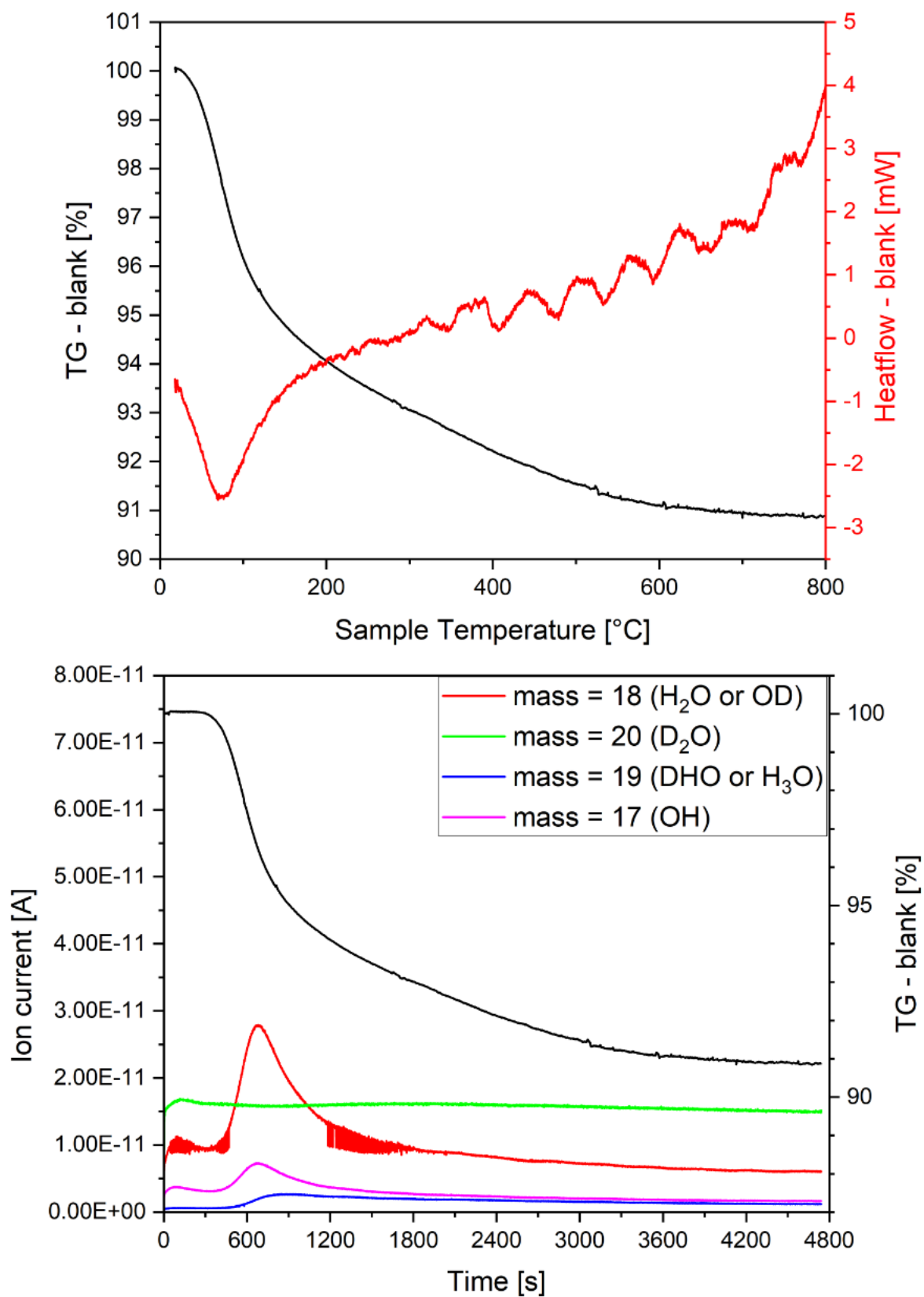


Figure 4.17: TG-DTA and TG-MS results for m10Ca80new after exchange with D₂O.

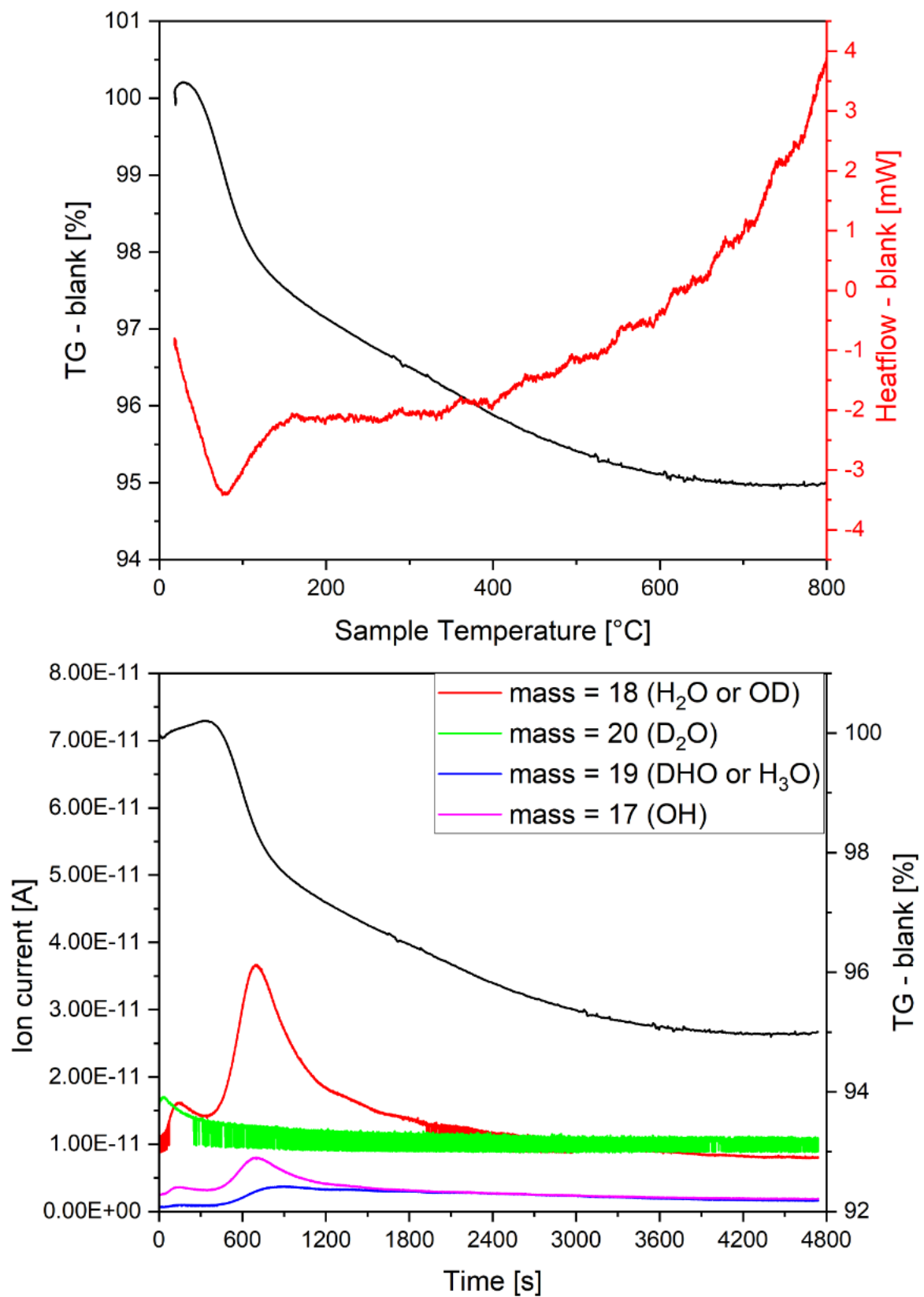


Figure 4.18: TG-DTA and TG-MS results for m18Ca80 after exchange with D₂O.

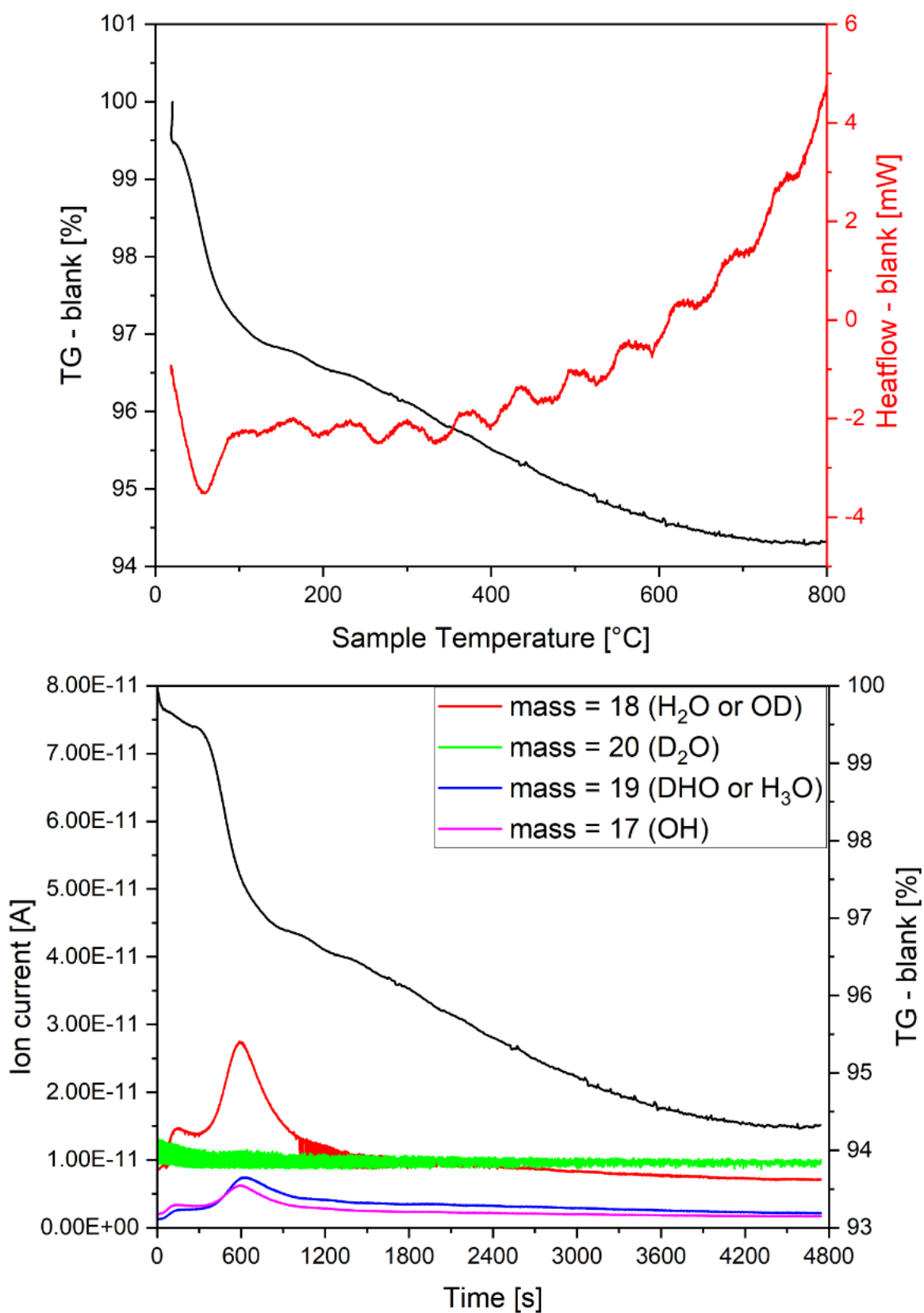


Figure 4.19: TG-DTA and TG-MS results for m18Na80 after exchange with D₂O.

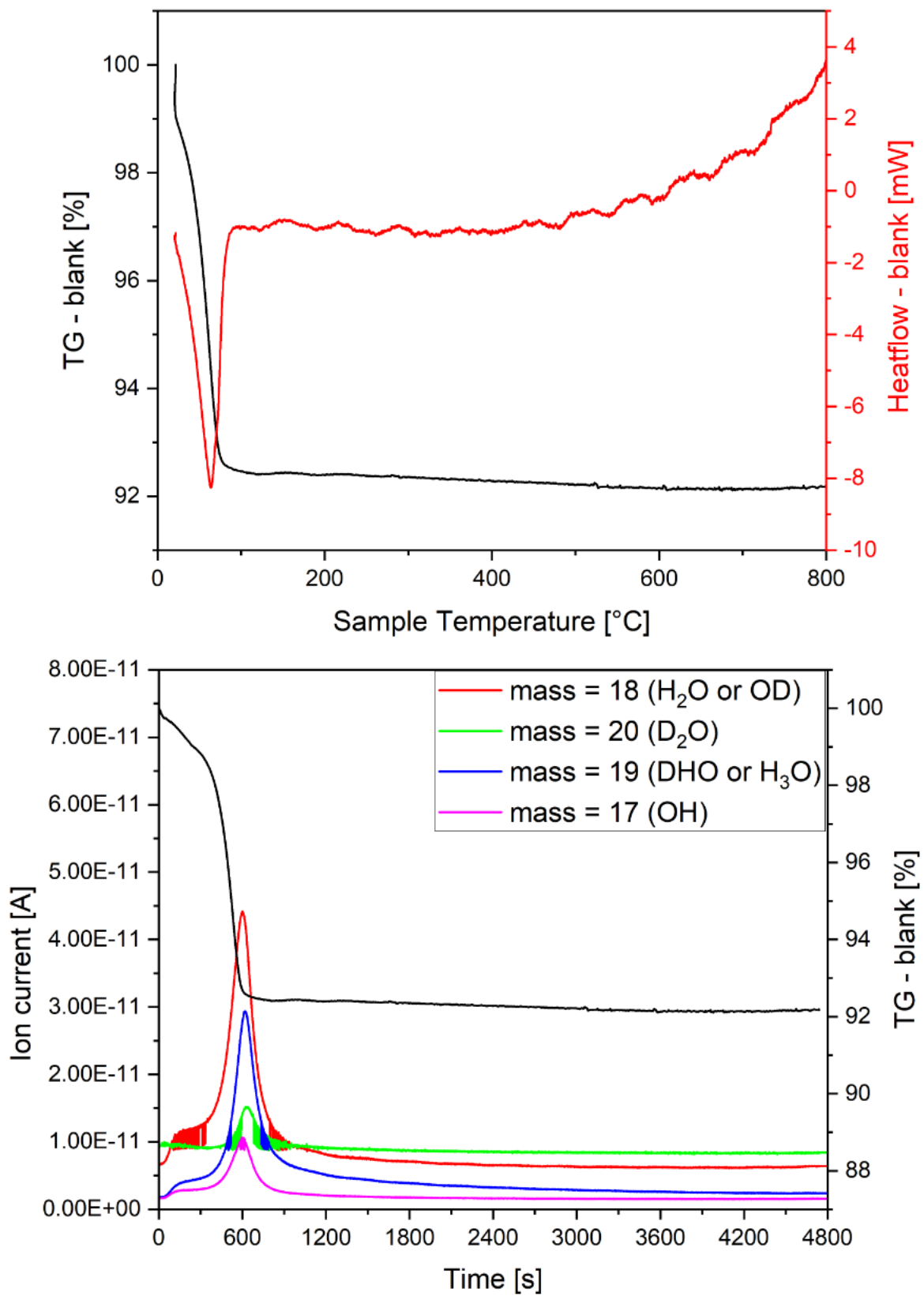


Figure 4.20: TG-DTA and TG-MS results for commercial crystalline ZrO_2 after exchange with D_2O .

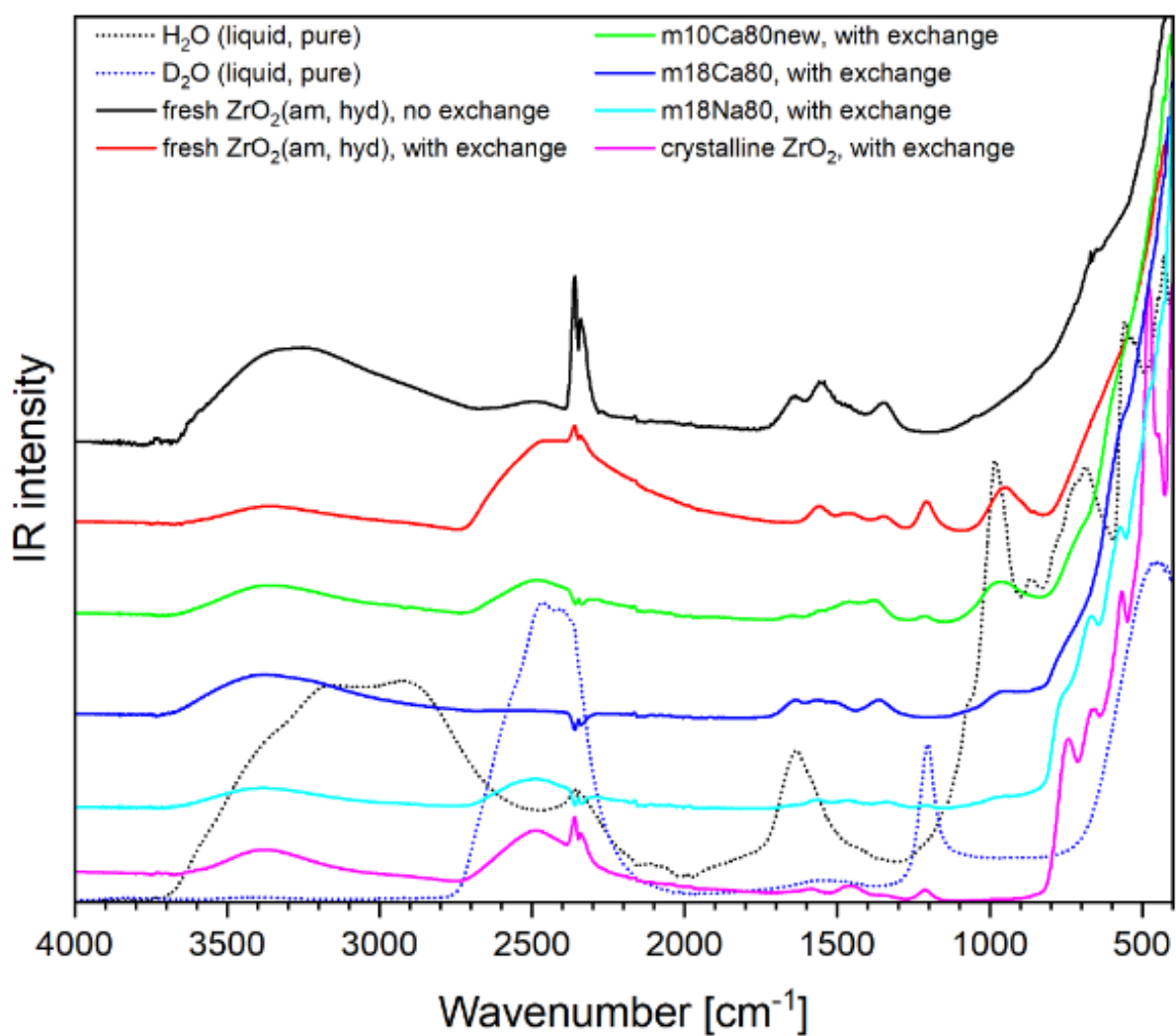


Figure 4.21: FTIR spectra of solid phases after exchange with D₂O. Note that the doublet between 2300 and 2400 cm⁻¹ is caused by CO₂ and varies due to background subtraction and measurement conditions.

Table 4.7: integrated mass spectroscopy signals and calculated D-H ratios for the solid phases after H-D exchange.

Signal distribution ¹³³	H₂O	HDO	D₂O		
Mass = 16	0.0161	0.017	0.0170		
17	0.1852	0.056			
18	0.7988	0.126	0.1803		
19		0.801			
20			0.8027		
Fresh ZrO₂(s)	Peak area (10⁻⁹ As = nC)	Relative intensity	Relative ratios		
			D₂O	HDO	H₂O^a
Mass = 17	3.16	0.10	0.12	0.42	0.49
18	14.2	0.47			H₂O^b
19	10.2	0.34	H/D^a	H/D^b	0.43
20	2.88	0.09	2.1	2.0	
m10Ca80new	Peak area (10⁻⁹ As = nC)	Relative intensity	Relative ratios		
			D₂O	HDO	H₂O^a
Mass = 17	1.39	0.18	0.00	0.05	0.97
18	6.13	0.78			H₂O^b
19	0.34	0.04	H/D^a	H/D^b	0.94
20	0.00	0.00	37.3	36.2	
m18Ca80	Peak area (10⁻⁹ As = nC)	Relative intensity	Relative ratios		
			D₂O	HDO	H₂O^a
Mass = 17	2.23	0.16	0.00	0.12	0.92
18	10.5	0.75			H₂O^b
19	1.31	0.09	H/D^a	H/D^b	0.82
20	0.00	0.00	16.8	15.1	
m18Na80	Peak area (10⁻⁹ As = nC)	Relative intensity	Relative ratios		
			D₂O	HDO	H₂O^a
Mass = 17	0.98	0.14	0.01	0.27	0.75
18	4.33	0.63			H₂O^b
19	1.50	0.22	H/D^a	H/D^b	0.69
20	0.04	0.01	6.2	5.7	
Commercial crystalline ZrO₂	Peak area (10⁻⁹ As = nC)	Relative intensity	Relative ratios		
			D₂O	HDO	H₂O^a
Mass = 17	1.59	0.10	0.06	0.41	0.56
18	8.04	0.51			H₂O^b
19	5.18	0.33	H/D^a	H/D^b	0.42
20	0.80	0.05	2.8	2.3	

^a determined with the signal at mass = 18, ^b determined with the signal at mass = 17

4.1.2.5 Effect of ageing on solid composition and hydration

The solid phase characterization with TG-DTA, XPS and FTIR shows that the ageing at elevated temperatures has also an impact on the water content of the solids. The transformation from amorphous to crystalline solids occurring at $T = 80\text{ }^{\circ}\text{C}$ is connected with a reduction of water content and a decreasing $[\text{O}]/[\text{Zr}]$ ratio. XPS analysis shows that the solids are described more accurately as $\text{ZrO}_x(\text{OH})_{4-2x}\cdot n\text{H}_2\text{O}$ and that the transformation process leads to an increase of O^{2-} contribution and a decrease of H_2O and OH^- contributions. This could be explained by condensation reactions at the surface of the solids, where 2 ZrOH groups at the surface release 1 water molecule and form a Zr-O-Zr bond. The growth of the particle results also in a decrease of the surface, accordingly decreasing the amount of physically bound water, as confirmed by TG-DTA. This behavior is schematically shown in Figure 4.22 and is also in agreement with the increasing crystallinity and particle size observed with XRD and TEM. Further TG-DTA experiments indicate that the dehydration process is not reversible, thus that the Zr-O-Zr bonds formed during the transformation are not broken again, if the solid is contacted again with water. The isotope exchange experiments with deuterium and hydrogen indicate that at least loosely bound $\text{H}_2\text{O}/\text{OH}$ at the particle surfaces is exchangeable, but also the presence of hydrogen atoms which do not undergo H-D exchange.

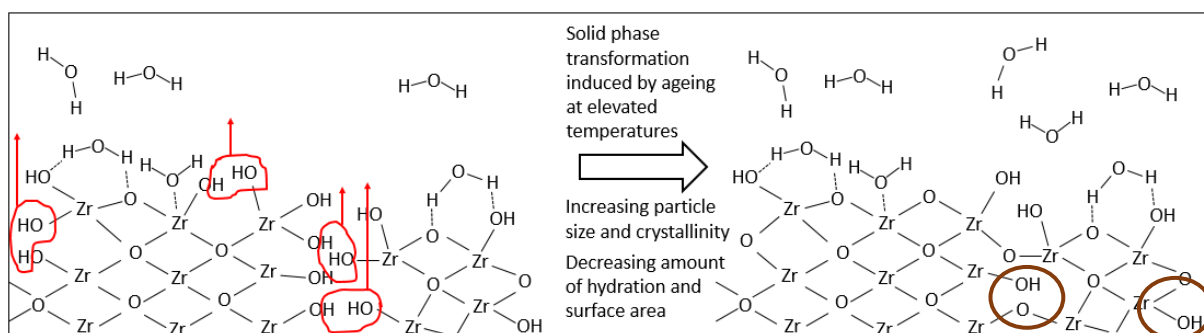


Figure 4.22: scheme of condensation reactions occurring during the ageing of the solid phases.

4.1.3 Surface properties

4.1.3.1 Volumetric nitrogen sorption with the Brunauer, Emmet and Teller theory (BET) and estimation of the surface area

Since BET measurements require a relatively large amount of substance, up to 1 g depending on the surface area, this technique was only applied to those samples for which sufficient material was available. Besides the direct measurement of the surface area by BET, estimations can be performed based on the density and the particle size of the solids and assuming homogenous spherical particles. The measured specific surface areas and the estimated values are shown in Table 4.8. The amorphous samples (m10Ca22 and m10Na22) show as expected very high surface areas of 257 and 390 m²/g due to their small particle size. In agreement with the larger particle size determined by other methods, the m10noH2O80 and crystalline samples show smaller surface areas of 37 and 24 m²/g. For the m4Ca80 sample (aged in CaCl₂) only a qualitative agreement (i.e. greater surface area than more crystalline phases and smaller surface area than amorphous phases) is obtained, the measured value (199 m²/g) is significantly higher compared to the estimated value of 70-89 m²/g. This could be explained by the presence of a fraction of amorphous ZrO₂, in addition to the tetragonal/cubic phase observed by XRD. Note that the sample m4Ca80 was identified by TG-DTA as the Ca-sample with the largest H₂O content (see Table 4.4), which again would support a larger contribution of amorphous phase in this specific sample.

Table 4.8: measured and estimated specific surface areas of the solid phases.

BET measurements		Estimations			
Solid phase	Specific surface area (m ² /g)	Solid phases	Particle size (nm)	Density (g/cm ³)	Specific surface area (m ² /g)
m10Na22	390	amorphous ^a	<4	5.0 ^d	>300
m10Ca22	257	tetragonal ^b	11-14	6.10 ⁵⁹	70-89
m4Ca80	199	monoclinic ^c	23-27	5.82 ⁵⁸	39-46
m10noH2O80	37				
crystalline	24				

^a fresh, m10Ca22, m10Na22

^b m4Ca80, m4Ca80new, m4_002Ca80, m4_002Ca80new, m10Ca80, m10Ca80new, m18Ca80

^c m4Na80, m10Na80, m18Na80, m10noH2O80, crystalline

^d estimated based on weight loss (TG) / modelled structure (DFT)

4.1.3.2 Zeta potential

Zeta potential measurements were conducted with suspensions containing 0.1 g/l of selected solid phases in either 1 mM HCl-NaCl-NaOH or in 1 mM HCl-CaCl₂-Ca(OH)₂ adjusted to pH values of approximately 3.0, 4.5, 6.0, 8.0, 9.5 and 11.0 for each system (see Figures 4.23 to 4.25). The measurements in 1 mM HCl-NaCl-NaOH systems show the point of zero charge of the solids, which is for all measured solids in slightly acidic conditions (pH 5-6) and in agreement with the majority of the literature values¹³⁴, although the reported values are strongly affected by the measurement conditions and the solid phases. Measurements of the zeta potential done in suspensions containing CaCl₂ show mostly positive potentials, significantly higher compared to measurements in suspensions containing NaOH and therefore no points of zero charge. This observation can be explained by the sorption of Ca²⁺ on the negatively charged surfaces forming above the point of zero charge. This provides evidence on the different surface properties of ZrO₂ induced by the different ageing solutions considered in this work, i.e. NaOH or CaCl₂-Ca(OH)₂. Moreover, it can be hypothesized that the sorption of Ca on the surface of ZrO₂ might be a first step towards its incorporation into the ZrO₂ structure. Further experimental or theoretical evidence is required to confirm this hypothesis.

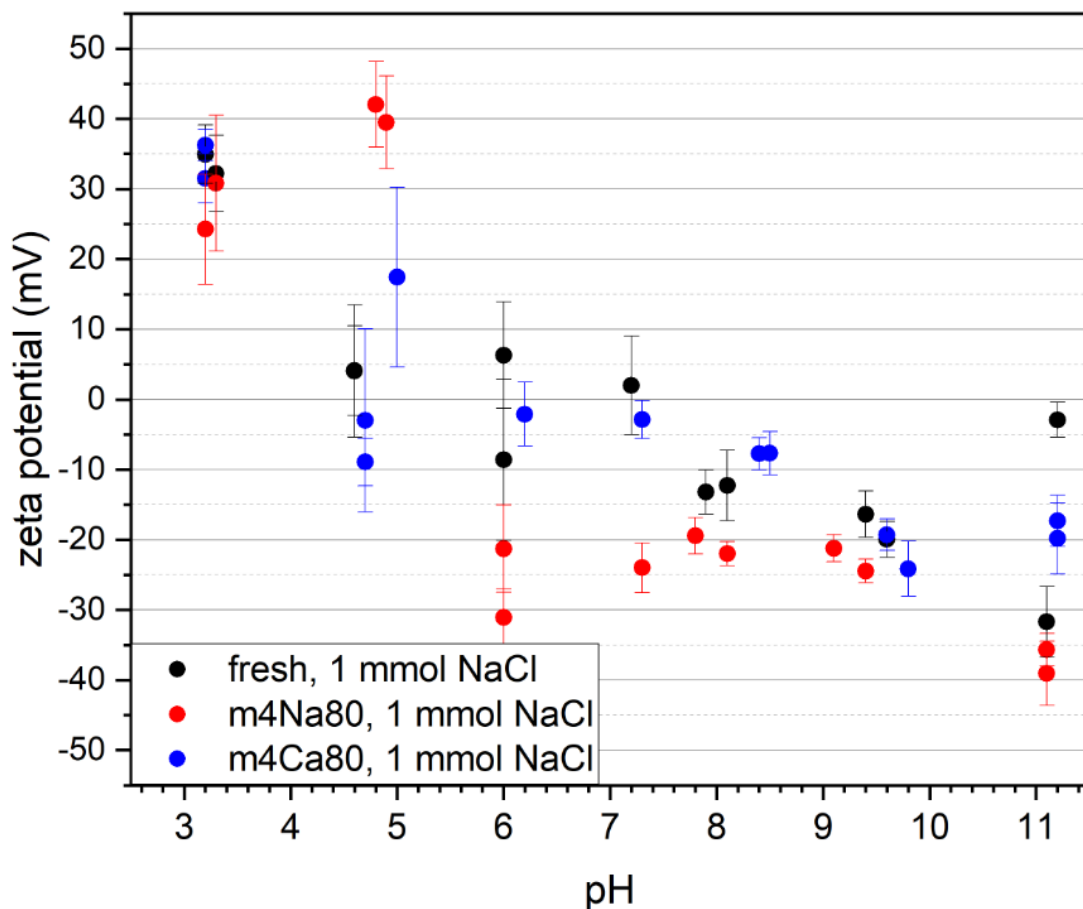


Figure 4.23: zeta potentials of fresh, m4Ca80 and m4Na80 ZrO₂ solid phases in NaCl solutions.

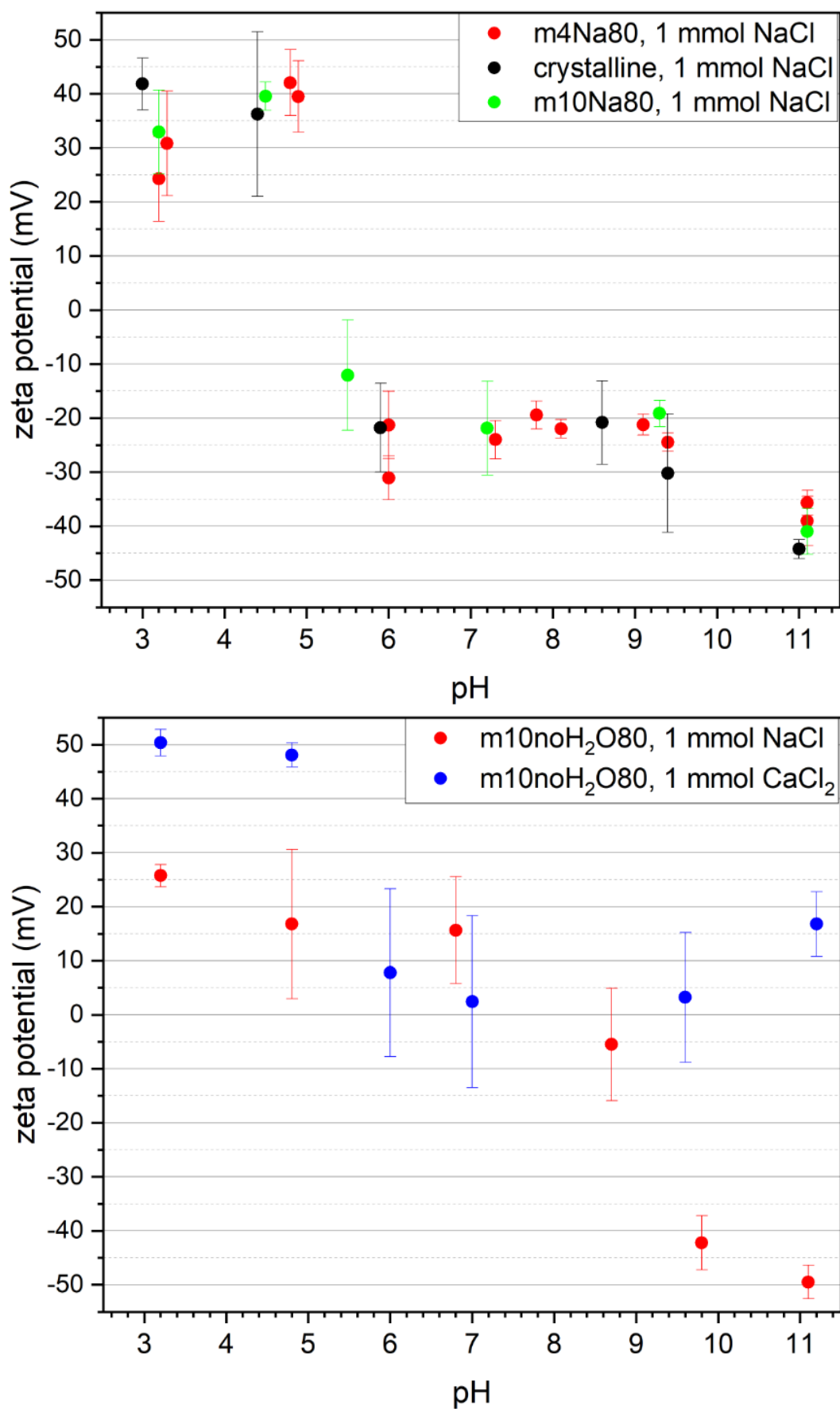


Figure 4.24: zeta potentials of monoclinic solid phases: aged in NaOH (m4Na80 and m10Na80), aged without liquid phase- and commercial crystalline in NaCl and CaCl₂ solutions.

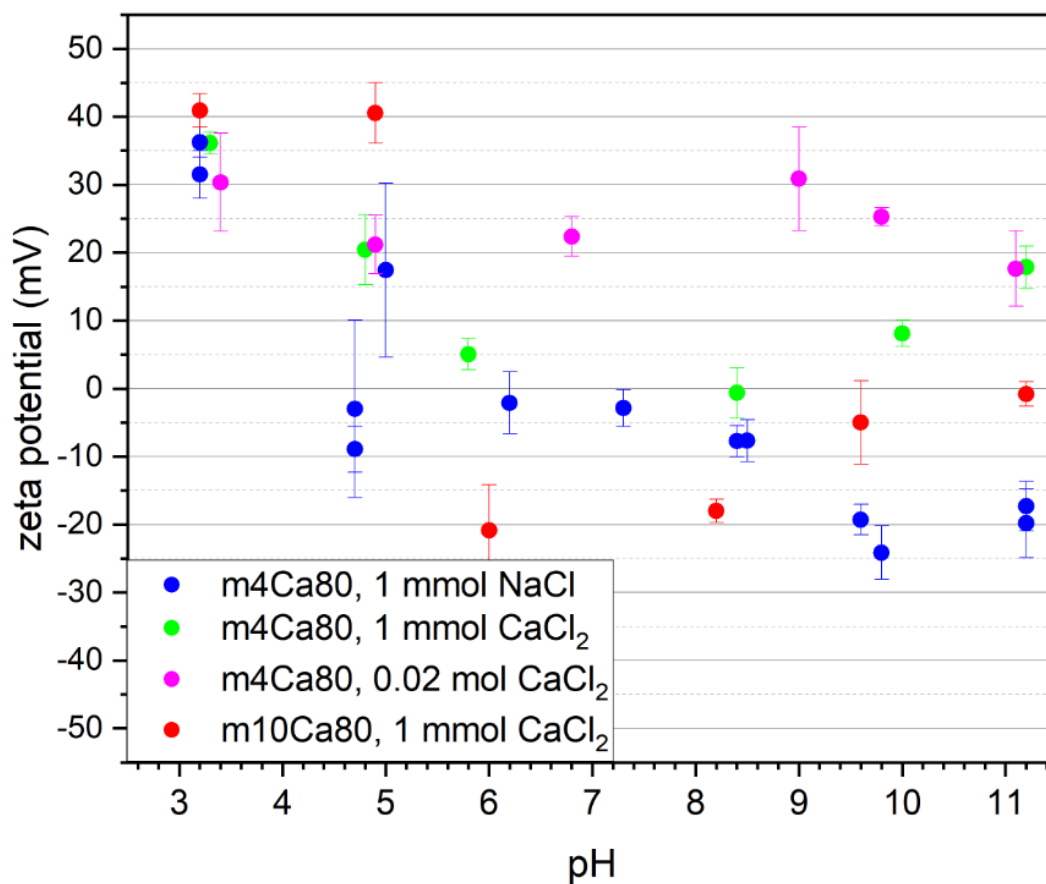


Figure 4.25: zeta potentials of tetragonal solid phases aged in CaCl₂ solutions (m4Ca80 and m10Ca80) in NaCl and CaCl₂ solutions.

4.2 Solubility experiments

In order to investigate the effects of the ageing and according solid phase transformations on the solubility of the solid phases, undersaturation solubility experiments were performed in 0.5 M NaCl-NaOH, 0.2 M CaCl₂-Ca(OH)₂ and 0.02 M CaCl₂-Ca(OH)₂ solutions.

The experimental solubility data were modelled in order to determine solubility constants ($\log^* K_{s,0}^\circ$) for the solid phases. In this context, solubility curves were calculated as shown in the equations 2.17 to 2.21 in chapter 2.3.3.1.4. For each measured solubility sample, its own solubility curve and thus solubility constant was calculated by setting the calculated zirconium concentration $[Zr]_{tot}$ (equation 2.21) equal to the measured zirconium concentration $[Zr]_m$. The hydrolysis constants ($\log^* \beta_{(n,m)}^\circ$) were kept constant (as selected in chapter 2.3.3.1.3), so that only the solubility constant ($\log^* K_{s,0}^\circ$) was varied to match the measured and calculated zirconium concentrations as shown below:

$$\begin{aligned} \log[Zr]_m &= \log[Zr]_{tot} = \log \sum_{n,m} n \cdot 10^{\log[Zr_n(OH)_m^{(4n-m)}]} & (4.1) \\ &= \log \sum_{n,m} n \cdot 10^{\log^* K_{sp}^\circ - (4n-m) \text{pH}} \\ &= \log \sum_{n,m} n \cdot 10^{n \log^* K_{s,0}^\circ + \log^* \beta_{(n,m)}^\circ - \log \gamma_{Zr_n(OH)_m^{(4n-m)}} + (4n-m) \log \gamma_{H^+} - (4n-m) \log a_w - (4n-m) \text{pH}} \end{aligned}$$

The solubility constants of each sample of a solid phase in a given background electrolyte were then averaged to reach a solubility product for the solid phase in the specific background electrolyte. The variance $V(\log^* K_{s,0}^\circ)$ and the standard deviation $\sigma(\log^* K_{s,0}^\circ)$ were calculated to evaluate the quality of the determined solubility constant as follows:

$$V(\log^* K_{s,0}^\circ) = \frac{1}{n} \sum_i^n (\log^* K_{s,0}^\circ(i) - \log^* K_{s,0}^\circ(avg))^2 \quad (4.2)$$

where n is the number of samples, $\log^* K_{s,0}^\circ(i)$ the solubility constant of the sample i and $\log^* K_{s,0}^\circ(avg)$ the averaged constant of all n samples. The standard deviation is given by:

$$\sigma(\log^* K_{s,0}^\circ) = \sqrt{V(\log^* K_{s,0}^\circ)} \quad (4.3)$$

The differences in the solubility of different metal oxide solid phases are often attributed to the particle size/surface area^{6,135}. The Schindler equation correlates the Gibbs energy of formation $\Delta_f G_m^\circ$ of crystalline and amorphous solids with a surface contribution^{135,136} as follows:

$$\Delta_f G_m^\circ(\text{ZrO}_2(\text{am/col})) = \Delta_f G_m^\circ(\text{ZrO}_2(\text{cr})) + \frac{2}{3}\gamma S \quad (4.4)$$

where S is the molar surface (depending from the particle size) and γ the mean free surface energy per unit surface area of liquid-solid interface. S is defined as:

$$S = \frac{M\alpha}{\rho d} \quad (4.5)$$

where M is the molecular mass, α is a geometrical factor with $\alpha \approx 6$ for spherical particles, ρ is the density of the solid and d is the particle size. Following the approach of Schindler, γ can be estimated by^{135,136}:

$$\gamma = -\frac{3RT \ln K_{sp}^\circ(S \rightarrow 0)}{2N_A \sum 4\pi r_i^2} \quad (4.6)$$

where R is the universal gas constant ($R = 8.314 \text{ J K}^{-1} \text{ mol}^{-1}$), T is the temperature in Kelvin, $\ln K_{sp}^\circ(S \rightarrow 0)$ is the solubility product of $\text{ZrO}_2(\text{cr})$ ($\log K_{sp}^\circ = -63$ for monoclinic ZrO_2 ¹⁷, since the reaction $\text{ZrO}_2(\text{cr}) + 2\text{H}_2\text{O} \rightleftharpoons \text{Zr}^{4+} + 4\text{OH}^-$ is required instead of $\text{ZrO}_2(\text{cr}) + 2\text{H}_2\text{O} + 4\text{H}^+ \rightleftharpoons \text{Zr}^{4+} + 4\text{H}_2\text{O}$ with $\log^* K_{sp}^\circ = -7$), N_A is the Avogadro constant ($N_A = 6.022 \cdot 10^{23} \text{ mol}^{-1}$) and r_i are the ionic radii $r_{\text{Zr}^{4+}} = 0.084 \text{ nm}$ ¹⁷ and $r_{\text{O}^{2-}} = 0.140 \text{ nm}$ ¹³⁵ of Zr^{4+} and O^{2-} . With this approach, $\gamma = 1.54 \text{ J m}^{-2}$ is determined, which agrees with theoretical and experimental values given in the literature⁸⁸. Together with the known data for $\text{ZrO}_2(\text{cr})$ ($\Delta_f G_m^\circ = -1042.7 \text{ kJ mol}^{-1}$ ¹⁷, $M(\text{ZrO}_2) = 123.22 \text{ g mol}^{-1}$ and $\rho = 5.82 \text{ g cm}^{-3}$ for the monoclinic solid⁵⁸) the dependence of $\Delta_f G_m^\circ$ on the particle size can be expressed as:

$$\Delta_f G_m^\circ(\text{ZrO}_2, \text{ particle size } d) = \left(-1042.7 + \frac{130.0}{d(\text{nm})} \right) \frac{\text{kJ}}{\text{mol}} \quad (4.7)$$

To compare this model predictions of the Schindler equation with the experimentally measured solubility products and particle sizes the Gibbs energies of the investigated solid phases have to be determined, which is possible with the following equations:

$$\ln K_{sp}^{\circ} = -\frac{\Delta_R G_m(T)}{RT} \quad (4.8)$$

$$\Delta_R G_m(T) = \sum \Delta_f G_m(\text{Products}) - \sum \Delta_f G_m(\text{Reactants}) \quad (4.9)$$

Considering $ZrO_2(s) + 4H^+ \rightleftharpoons Zr^{4+} + 2H_2O$ as reaction for the determination of the Gibbs energy, the latter one can be expressed as:

$$\Delta_f G_m^{\circ}(ZrO_2(s)) = RT \ln {}^*K_{s,0}^{\circ} + \Delta_f G_m(Zr^{4+}) + 2\Delta_f G_m(H_2O) - 4\Delta_f G_m(H^+) \quad (4.10)$$

Thereby, ${}^*K_{s,0}^{\circ}$ are the solubility constants calculated with the previously explained modelling approach (chapter 4.2, page 99). The $\Delta_f G_m$ values of Zr^{4+} , H_2O and H^+ were taken from NEA-TDB ¹⁷.

4.2.1 Solubility data of Zr(IV) in 0.5 M NaCl-NaOH

Figures 4.26 to 4.28 show the experimentally measured solubility data of several $ZrO_2(s)$ solid phases in 0.5 M NaCl-NaOH solutions as well as experimental data reported in the literature (Altmaier et al. ¹⁹) and solubility curves calculated for amorphous and crystalline solids using thermodynamic data selected in the NEA-TDB ¹⁷ and Altmaier et al. ¹⁹ as summarized in Tables 2.8 and 2.9. The numerical values of the measured solubility data and their relative errors are shown in Table 4.9.

Table 4.9: numerical values of the measured Zr concentration in 0.5 M NaCl-NaOH background electrolyte.

Solid phase	log[Zr]	Analytical error (%)	log[Zr]	Analytical error (%)	log[Zr]	Analytical error (%)
pH fresh	12.1±0.1		13.0±0.1		13.4±0.1	
	-8.67	2.61	-6.53	0.66	-5.89	1.44
			-6.73	1.02	-5.76	0.90
			-7.23	0.80	-6.10	1.86
			-6.95	1.80	-5.93	0.94
			-6.54	32.00	-6.24	1.90
			-6.49	17.00	-6.00	1.20
			-6.40	26.50	-6.11	0.70
					-5.44	14.00
					-5.42	25.10
				-5.38	24.60	
pH m10Ca22	11.9±0.1		13.0±0.1		13.4±0.1	
	-8.83	10.60	-7.47	1.80	-6.35	2.36
			-7.08	1.30	-6.64	1.60
			-7.07	2.32	-6.36	2.00
					-6.30	1.73
pH m10Na22	11.9±0.1		13.0±0.1		13.4±0.1	
	-8.77	14.80	-7.14	0.72	-6.03	0.75
			-7.32	0.60	-6.16	0.90
			-6.90	1.80	-6.10	1.60
			-6.83	1.91	-6.07	0.75
pH m4Ca80	12.1±0.1		13.0±0.1		13.4±0.1	
	-7.65	15.10	-7.12	1.05	-6.03	1.39
	-8.56	17.9	-7.53	2.00	-6.39	0.61
	-8.96	4.64	-7.28	1.10	-6.63	3.59
			-7.40	1.20	-6.44	1.01
			-7.01	1.90	-6.55	1.90
			-6.98	1.42	-6.39	1.10
					-6.45	0.90
				-6.28	1.30	
				-6.30	0.75	

Table 4.9 (continuation): numerical values of the measured Zr concentration in 0.5 M NaCl-NaOH background electrolyte.

Solid phase	log[Zr]	Analytical error (%)	log[Zr]	Analytical error (%)	log[Zr]	Analytical error (%)
pH	12.2±0.1		13.0±0.1		13.4±0.1	
m4Na80	-8.37	1.50	-7.71	1.30	-6.79	2.02
			-6.59	2.10	-7.27	1.48
pH	11.9±0.1		13.0±0.1		13.4±0.1	
m4Ca80new	-8.78	10.50	-8.52	5.60	-7.78	3.70
			-9.72	4.41	-7.86	1.27
pH	11.9±0.1		13.0±0.1		13.4±0.1	
m4_002Ca80	-8.31	7.90	-9.20	22.50	-8.38	5.90
	-8.34	1.81			-9.18	10.51
pH			13.0±0.1		13.4±0.1	
m4_002Ca80new			-8.78	19.40	-7.92	3.30
					-8.04	3.58
pH	11.9±0.1		13.0±0.1		13.4±0.1	
m10Ca80	-8.62	11.30	-9.08	8.90	-8.11	6.50
					-8.36	3.79
pH			13.0±0.1			
m10Na80			-7.16	0.93		
pH			13.0±0.1		13.4±0.1	
m10noH2O80			-8.39	197.12	-8.22	5.70
					-8.49	3.65
pH			13.0±0.1		13.4±0.1	
m18Ca80			-8.53	15.80	-7.67	
					-7.72	13.9
pH					13.4±0.1	
crystalline					-8.42	20

The measured solubility data of the freshly precipitated $ZrO_2(am, hyd, fresh)$ (Figure 4.26) agree well with the data of Altmaier et al.¹⁹ even though it was not possible to determine zirconium concentration of samples with $pH < 11.8$ in 0.5 M NaCl-NaOH. Samples below this pH were usually very close to or on the same level as the background zirconium concentration measured in blank samples. Due to the dilutions required to decrease the background electrolyte concentration before ICP-MS measurements sample concentrations below 10^{-9} mol/l could not be determined in most measurements. Data points with values below 10^{-9} mol/l come from measurement series in which it was possible to decrease the background zirconium concentration.

As expected, the solid phases aged at $T = 80$ °C for 4 months in NaOH (m4Na80) and $CaCl_2$ (m4Ca80) (Figure 4.27, lower part) show significantly lower solubilities compared to the fresh solid, which is correlated with the differences observed by solid phase characterization.

On the other hand, solid phases aged at $T = 22\text{ }^{\circ}\text{C}$, m10Ca22 and m10Na22 (Figure 4.27, upper part) also show lower solubilities compared to the fresh solid, even though these solid phases showed also an amorphous character in the XRD characterization. This points out to a possible alteration of the surface properties, which may affect the solubility of the solid phases, but was not detected by the used bulk characterization techniques. In similar terms although referring to crystalline phases, a solubility control by only one monolayer was proposed by Grambow et al.⁷⁸ for metal oxide phases.

Significantly lower Zr concentrations were determined for solid samples aged for 10 months at $T = 80\text{ }^{\circ}\text{C}$ and several samples aged for 4 months at $T = 80\text{ }^{\circ}\text{C}$. Due to the lower solubilities, in some cases close to the background Zr concentration, only a limited number of solubility controlled Zr concentrations were determined for these systems. For m18Ca80 and the commercial crystalline sample only concentrations of a limited number of samples (the ones prepared in Teflon vessels, see chapter 3.5.1) could be measured due to their low solubility. Solubility data of the samples m10Ca80, m4Ca80new, m4_002Ca80, m4_002Ca80new and m10noH2O80 and for m18Ca80 and the crystalline solid phase are shown in Figure 4.28.

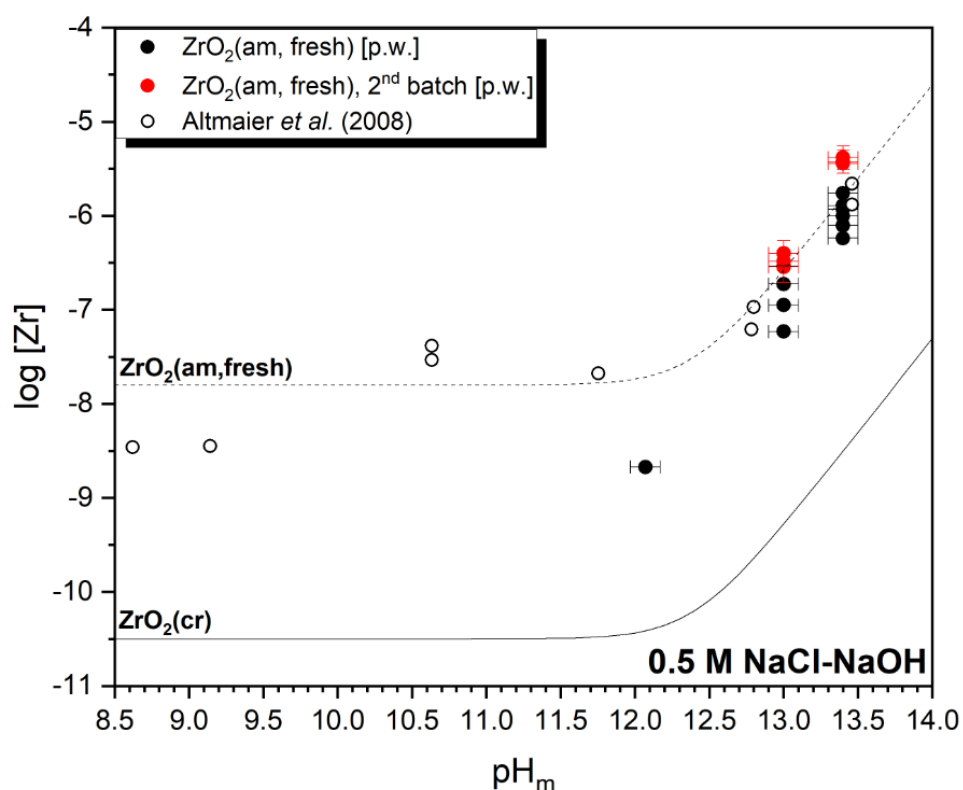


Figure 4.26: Solubility data of freshly precipitated $\text{ZrO}_2(\text{am, hyd, fresh})$ of the present work compared to data from Altmaier et al.¹⁹, including also expected solubility curves for amorphous and crystalline solid phases based on data of NEA-TDB¹⁷ and Altmaier et al.¹⁹, respectively.

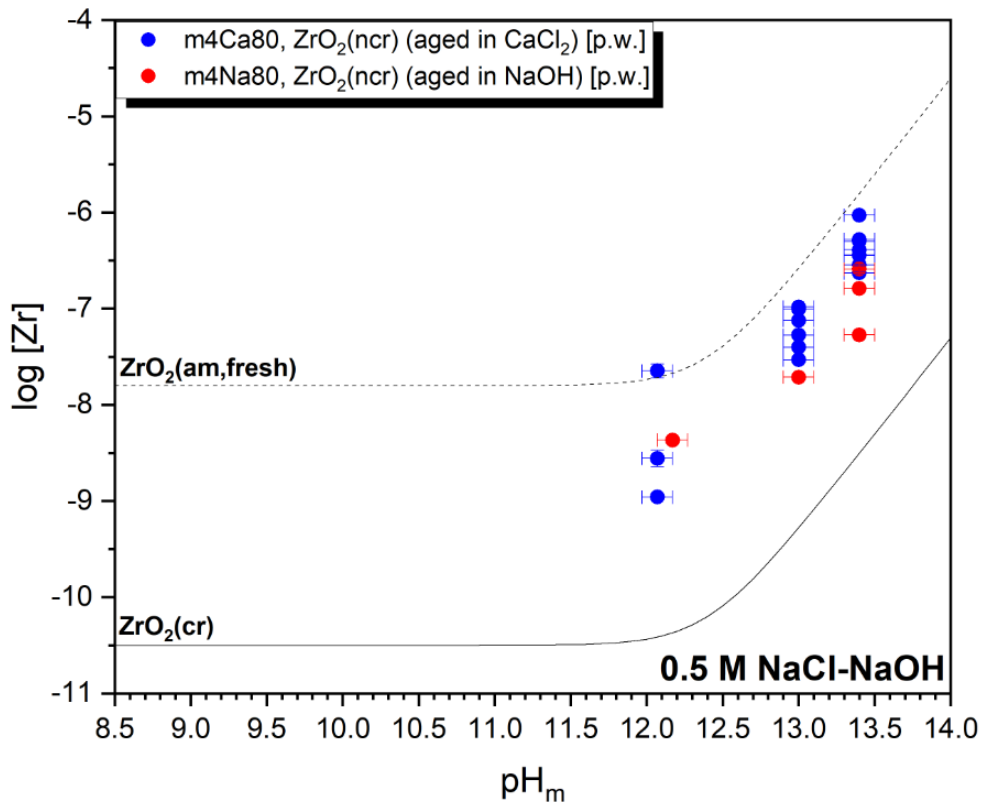
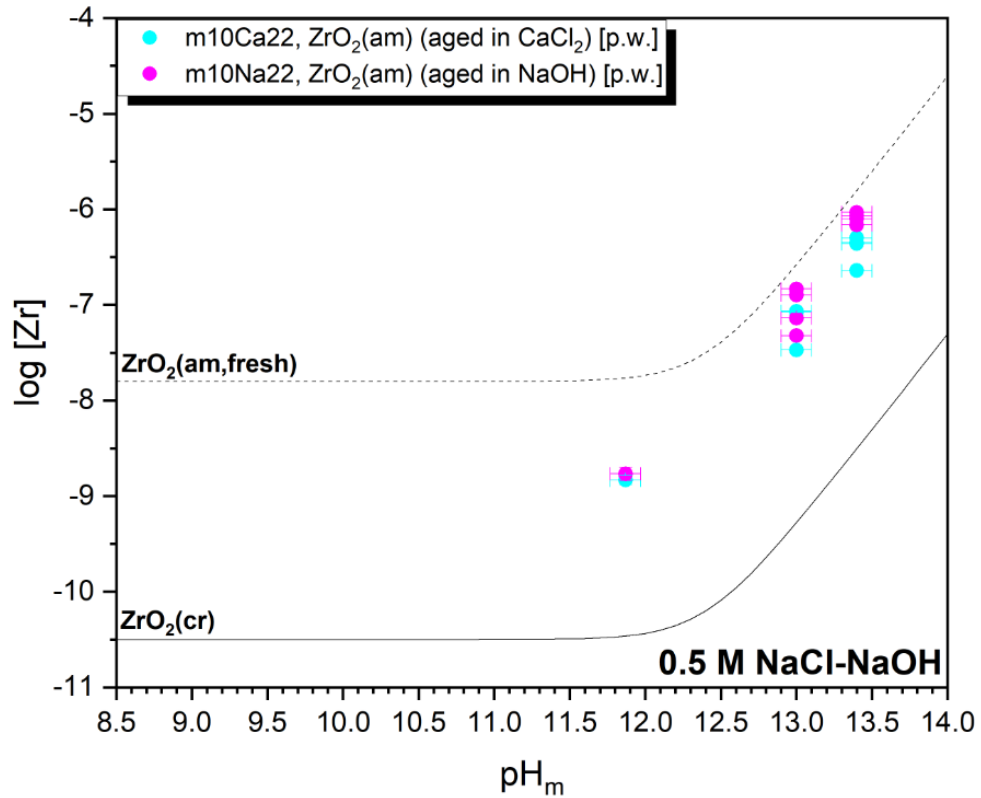


Figure 4.27: Solubility data of the aged solid phases m10Ca22 and m10Na22 (above) as well as m4Ca80 and m4Na80 (below), including also expected solubility curves for amorphous and crystalline solid phases based on data of NEA-TDB¹⁷ and Altmaier et al.¹⁹, respectively.

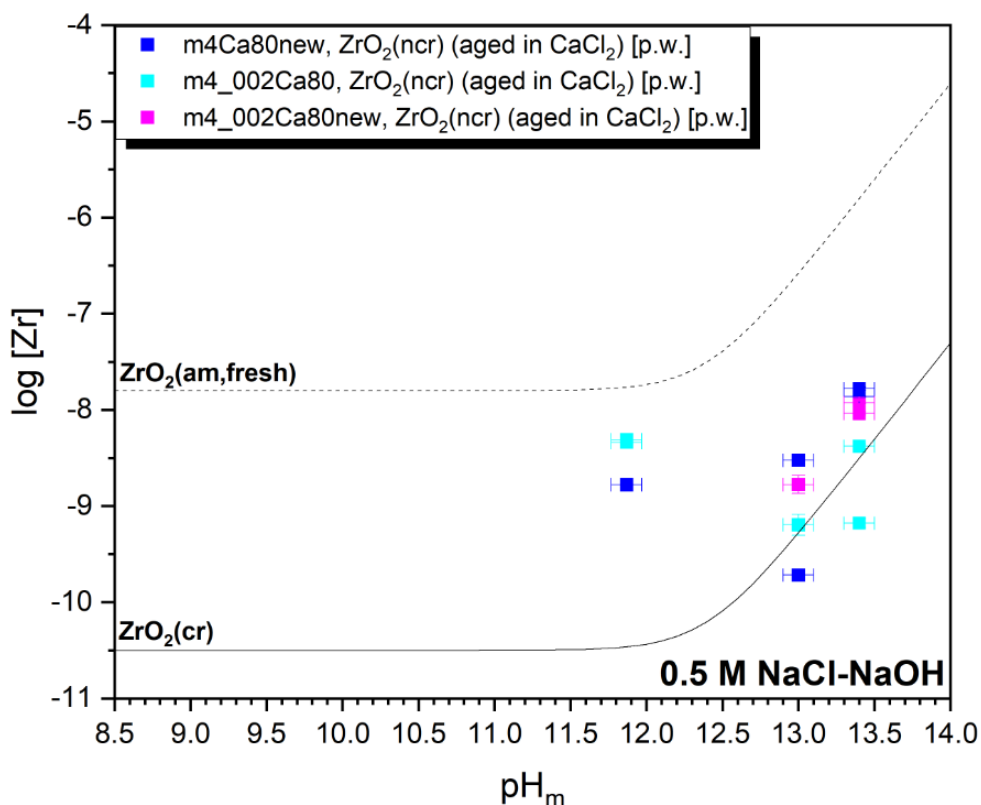
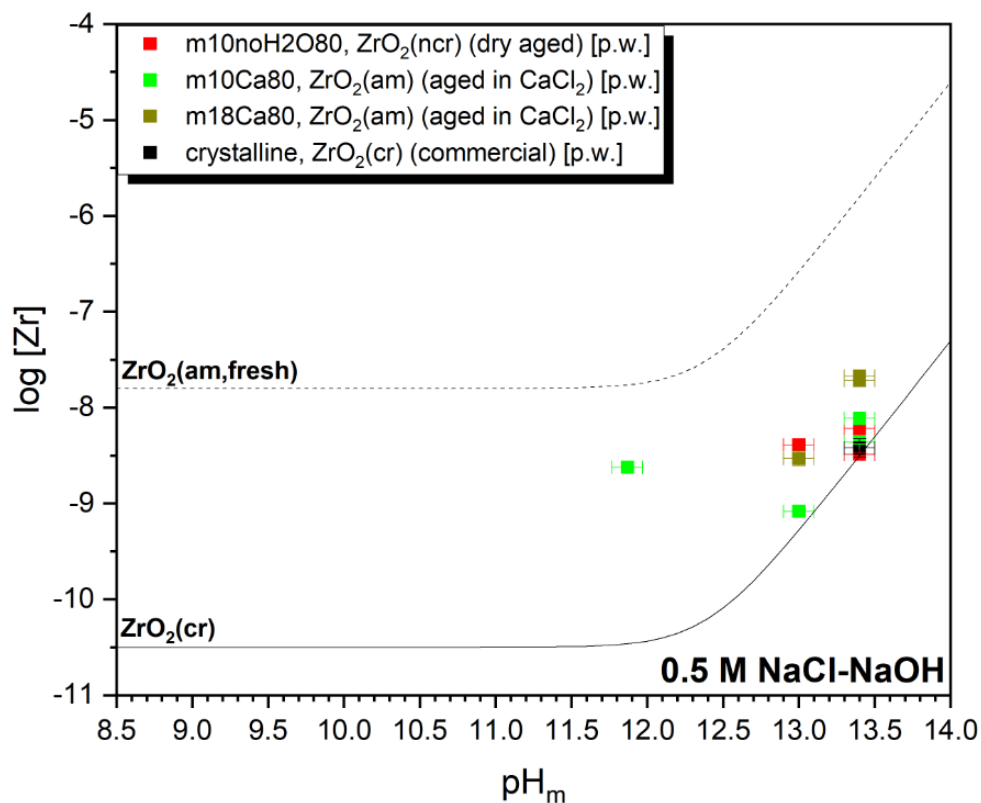


Figure 4.28: Solubility data of the long-term aged solid phases m10noH2O80, m10Ca80, m18Ca80 and commercial crystalline (above) as well as further samples aged in $CaCl_2$ background m4Ca80new, m4_002Ca80 and m4_002Ca80new (below), including also expected solubility curves for amorphous and crystalline solid phases based on data of NEA-TDB¹⁷ and Altmaier et al.¹⁹, respectively.

4.2.1.1 Calculation of solubility products for the system $\text{Zr}^{4+}\text{-Na}^+\text{-H}^+\text{-OH}^-\text{-Cl}^-\text{-H}_2\text{O}$

Figures 4.29 and 4.30 show the solubility data of the $\text{ZrO}_2(\text{s})$ solid phases in 0.5 M NaCl-NaOH together with modelled solubility curves of selected solid phases as described in chapter 4.2. The modelling approach was only followed for the fresh, m10Ca22, m10Na22 and m4Ca80 samples, since sufficient solubility data were available. For the other solid phases, the amount of measured data was too small (see Table 4.9) and the amount of samples at the same level as blank measurements was too high to evaluate a meaningful solubility constant. Note however that several of the samples aged at $T = 80^\circ\text{C}$ for 4 months, and most of the samples aged at $T = 80^\circ\text{C}$ for 10 and 18 months approach the solubility of $\text{ZrO}_2(\text{cr})$. Although the solubility product of these solid phases was not quantified in this work, they are expectedly lower than those summarized in Table 4.10 for fresh, m10Ca22, m10Na22 and m4Ca80 samples.

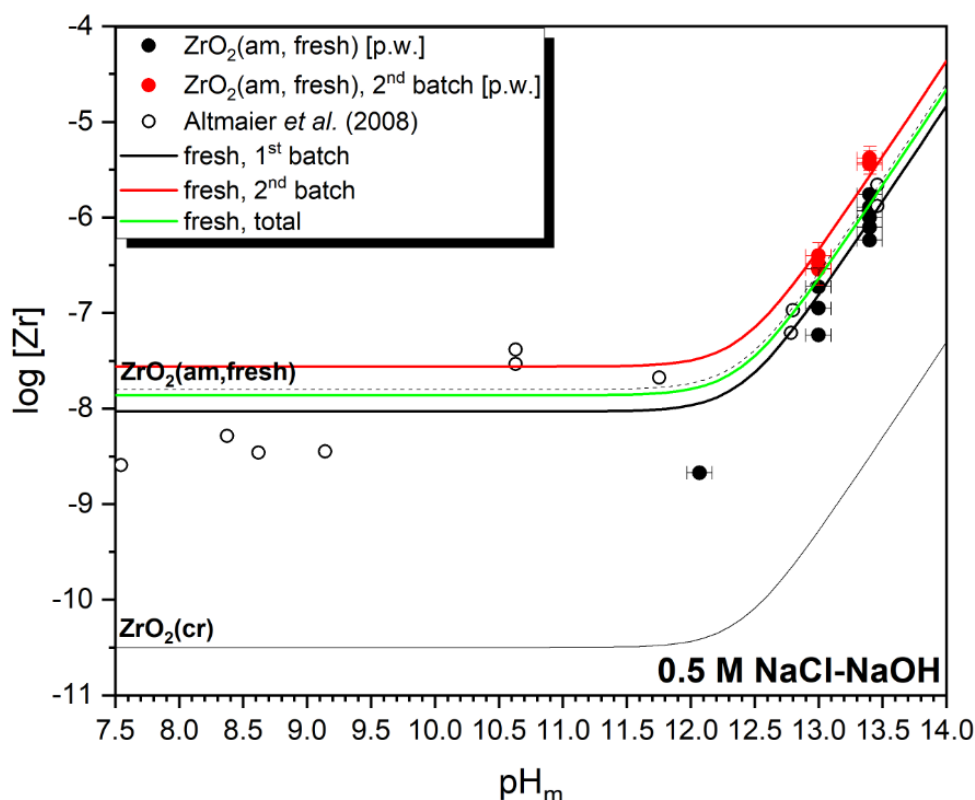


Figure 4.29: Solubility data and modelled solubility curves of the freshly precipitated $\text{ZrO}_2(\text{am, hyd, fresh})$ of the present work compared to data from Altmaier et al. ¹⁹, including also expected solubility curves for amorphous and crystalline solid phases based on data of NEA-TDB ¹⁷ and Altmaier et al. ¹⁹, respectively.

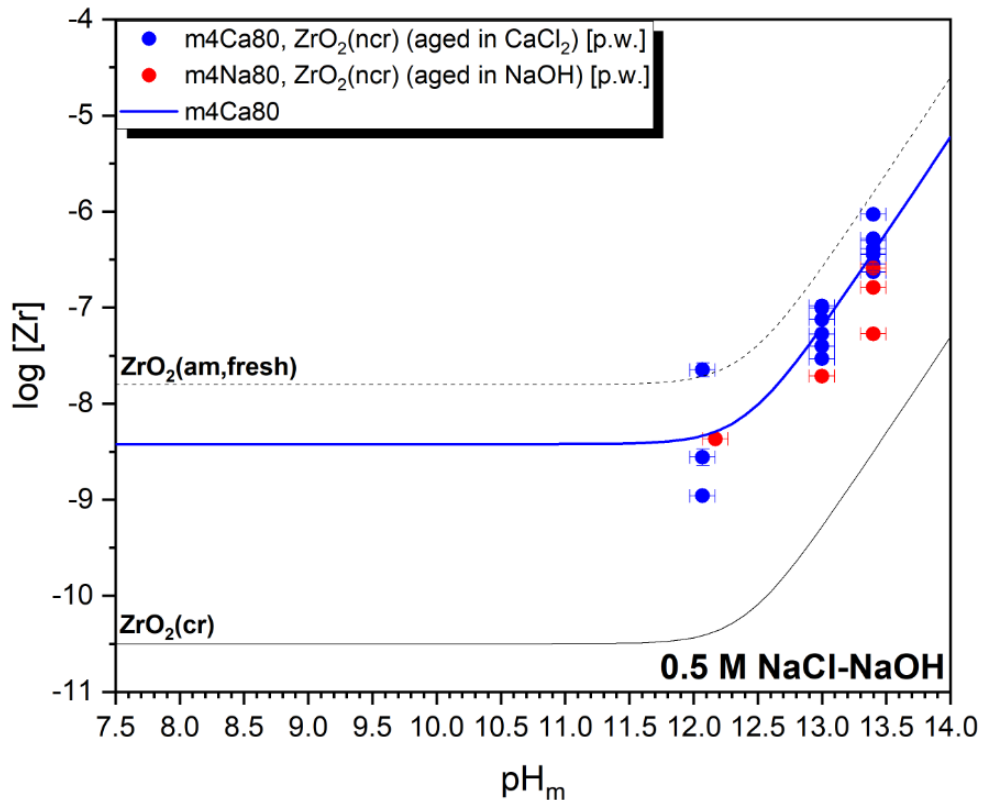
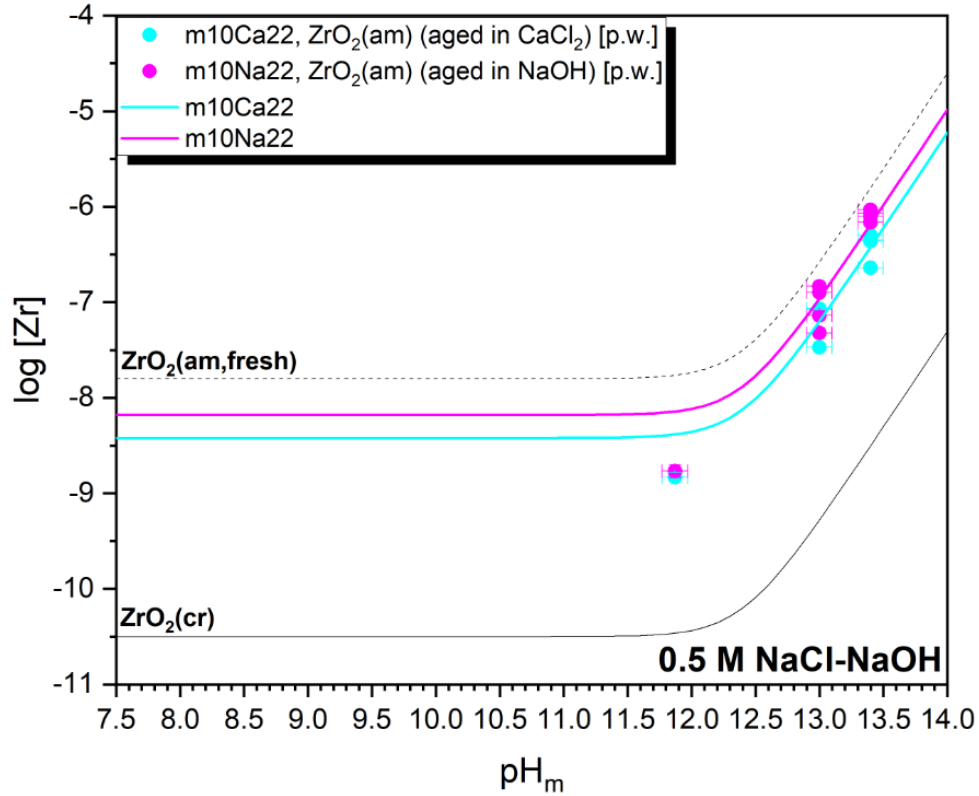


Figure 4.30: Solubility data and modelled solubility curves of the aged solid phases m10Ca22 and m10Na22 (above) as well as m4Ca80 and m4Na80 (below), including also expected solubility curves for amorphous and crystalline solid phases based on data of NEA-TDB¹⁷ and Altmaier et al.¹⁹, respectively.

Table 4.10: Solubility constants for $\text{ZrO}_2(\text{s})$ solid phases determined in the present work based on experimental data in 0.5 M NaCl-NaOH systems, or otherwise reported in the literature. The $\log^* K_{\text{s},0}^\circ$ values correspond to the reaction: $\text{ZrO}_2(\text{s}) + 2\text{H}_2\text{O} + 4\text{H}^+ \rightleftharpoons \text{Zr}^{4+} + 4\text{H}_2\text{O}$. Uncertainties are calculated as 2σ , as described in chapter 4.2.

Solid phase	$\log^* K_{\text{s},0}^\circ$	Source
$\text{ZrO}_2(\text{am, hyd, fresh})$, amorphous	-4.53 ± 0.40	Present work
$\text{ZrO}_2(\text{am, hyd, fresh})$, 2 nd batch	-4.06 ± 0.30	Present work
$\text{ZrO}_2(\text{am, hyd, fresh})$, total	-4.36 ± 0.58	Present work
m4Ca80, cubic/tetragonal	-4.92 ± 0.56	Present work
m10Ca22, amorphous	-4.92 ± 0.32	Present work
m10Na22, amorphous	-4.68 ± 0.33	Present work
$\text{ZrO}_2 \cdot x\text{H}_2\text{O}(\text{aged})$	-4.3 ± 0.2	Altmaier et al. ¹⁹
$\text{Zr}(\text{OH})_4(\text{am})$	-0.94 ± 0.32	Sasaki et al. ⁷⁵
$\text{Zr}(\text{OH})_4(\text{s})$, heated at 90 °C	-5.7 ± 0.3	Kobayashi et al. ¹
$\text{Zr}(\text{OH})_4(\text{np})$, heated at 90 °C	-5.4 ± 0.2	Kobayashi et al. ¹
$\text{ZrO}_2(\text{cr})$	-6.46 ± 0.1	Kobayashi et al. ⁷⁶
$\text{ZrO}_2(\text{cubic})$, yttrium stabilized	-5.8	Zouari ⁷⁷
$\text{ZrO}_2(\text{monoclinic})$	-7.0 ± 0.4	Zouari ⁷⁷
$\text{ZrO}_2(\text{am, fresh})$	-3.24 ± 0.1	NEA-TDB ¹⁷
$\text{ZrO}_2(\text{monoclinic})$	-7.0 ± 1.6	NEA-TDB ¹⁷

In the case of the freshly precipitated $\text{ZrO}_2(\text{am, hyd, fresh})$ solid phase, two batches with different solubilities were measured. For the first batch (with more samples/data) the modelled solubility constant was $\log^* K_{\text{s},0}^\circ = -4.53 \pm 0.40$, for the second one $\log^* K_{\text{s},0}^\circ = -4.06 \pm 0.30$. The combination of both batches resulted in $\log^* K_{\text{s},0}^\circ = -4.36 \pm 0.58$ (see Figure 4.29) for the freshly precipitated $\text{ZrO}_2(\text{am, hyd, fresh})$ solid phase, which is in good agreement with the value of Altmaier et al. ¹⁹, $\log^* K_{\text{s},0}^\circ = -4.3 \pm 0.2$ for an amorphous precipitate (referred as “ $\text{ZrO}_2 \cdot x\text{H}_2\text{O}(\text{aged})$ ” in their publication) which was stored for several weeks prior to the solubility experiments, to avoid ageing effects during the measurements ¹⁹. The similarity between these solids is not surprising since their approach for the solid phase precipitation, slow addition of 0.1 M NaOH to 0.02 M $\text{ZrOCl}_2 \cdot x\text{H}_2\text{O}$ solutions ¹⁹ was also followed in this work and the sample in the present work rested also for several days prior to the beginning of the solubility experiments. The significant difference to the value determined by Sasaki et al. ⁷⁵, $\log^* K_{\text{s},0}^\circ = -0.94 \pm 0.32$, and the value selected in NEA-TDB ¹⁷, $\log^* K_{\text{s},0}^\circ = -3.24 \pm 0.1$, may be explained by the different solid phase preparation or the different time between precipitation and solubility experiments. The comparison of the solubility data determined by Altmaier et al. in acidic conditions (with a similar solid phase as the one in this work) with data reported by Sasaki et al. (see Figure 2 in Altmaier et al.) clearly shows the higher solubility determined by the Japanese team, which is consistently reflected in the significantly higher value of $\log^* K_{\text{s},0}^\circ$.

In general, samples aged at $T = 80\text{ }^{\circ}\text{C}$ show significantly lower solubilities, approaching the solubility reported in the literature for the crystalline solid^{17,76,77}. This agrees well with the solid phase characterization results shown in the previous chapters and supports the idea of a solid phase transformation induced by the ageing at elevated temperatures. The determined solubility products for the m4Ca80 solid ($\log^* K_{s,0}^{\circ} = -4.92 \pm 0.56$) shows in comparison to the samples aged under the same conditions for 10 and 18 months, that the longer ageing time results in a decreased solubility, which is in apparent disagreement with the similar solid characteristics as determined by the different methods considered in this work. This seeming contradiction could be reconciled assuming a solubility control by only one monolayer of the solid phase, which cannot be probed with the bulk oriented methods considered in this work. A similar concept was previously proposed by Grambow et al.⁷⁸ for crystalline metal oxides.

Finally, the solubility data of the solid phases aged at room temperature, m10Ca22 and m10Na22, are between the fresh solid and the solids aged at $T = 80\text{ }^{\circ}\text{C}$. The solubility products of $\log^* K_{s,0}^{\circ} = -4.92 \pm 0.32$ and -4.68 ± 0.33 respectively, indicate that also at room temperature transformation processes in the solid phase take place, even if these are not visible by bulk characterization techniques. This can be taken as indication that even a small degree of “ripening” of the amorphous solid (or even only the surface layer) may have a significant impact on solubility.

In general, the fresh solid phase shows the highest solubility, followed by the other amorphous solids and finally by the more crystalline solids aged at elevated temperatures. Comparing the different ageing times under the same conditions, longer ageing leads to a decreasing solubility. Comparing the crystal structure of the solids with same ageing times, amorphous solids have a higher solubility as cubic/tetragonal solids and monoclinic solids showed the lowest solubility, which was also reported previously^{17,77}.

4.2.1.2 Application of the Schindler equation on the solubility data of Zr in 0.5 M NaCl-NaOH

As described in chapter 4.2 the Schindler equation ¹³⁶ relates the particle size/surface area to the Gibbs energy and thus the solubility of a solid phase. The evaluation of the samples in the present work is shown in Figure 4.31.

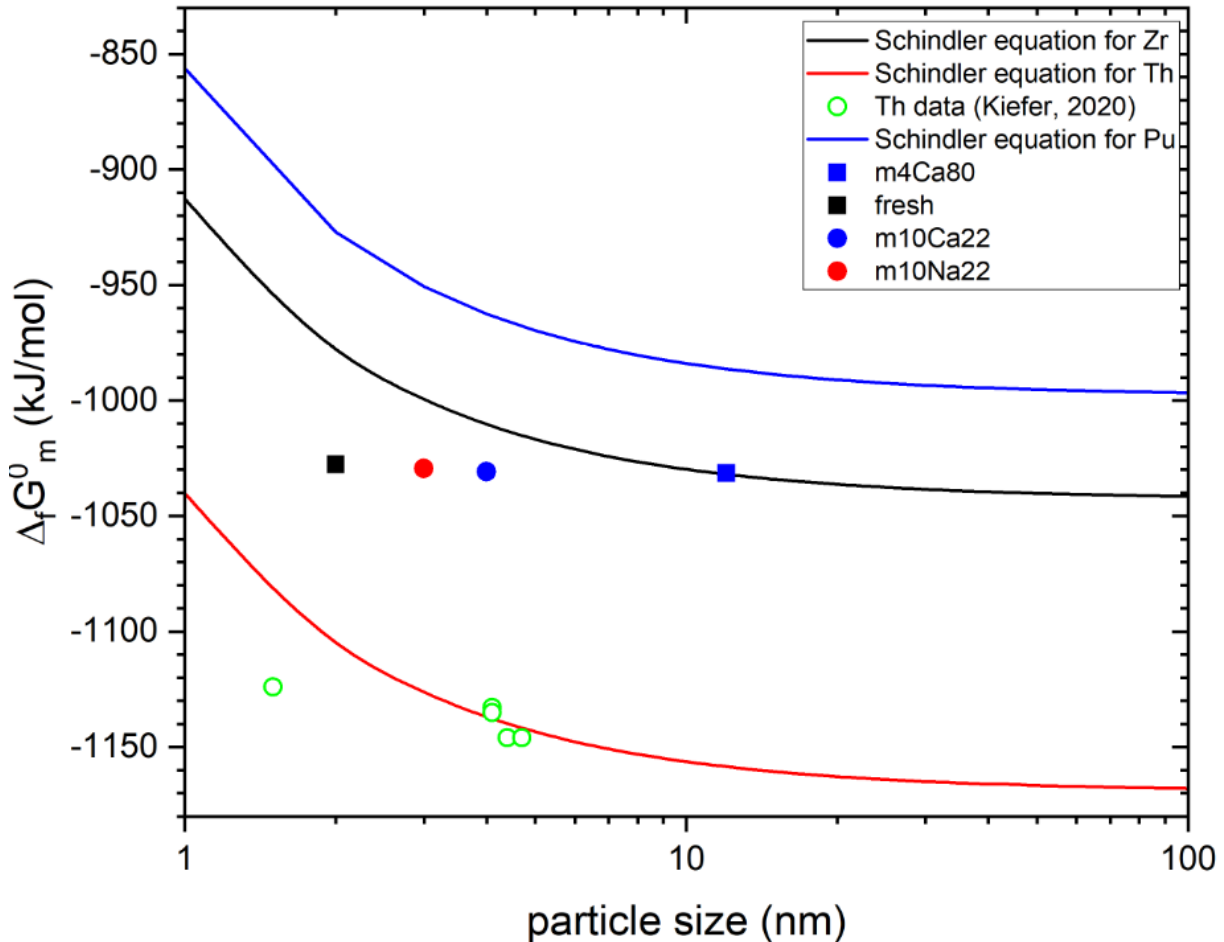


Figure 4.31: Application of the Schindler equation on the $ZrO_2(s)$ system calculated using the approach described in Neck et al. ¹³⁵. For comparison also Th and Pu curves and Th data from my master thesis ¹³⁷ and the corresponding publication ¹³⁸ are included. The $\Delta_f G_m^\circ$ values of the experimental data were calculated from the solubility constants as described in chapter 4.2. The particle size of the samples was taken from the XRD and TEM results or estimated from the surface area (BET) in the case of m10Ca22 and m10Na22.

With the previously explained way to estimate the surface tension γ , the Schindler equation overestimates the effect of decreasing particle size on the solubility. This behavior was also observed previously in the case of thorium. Reasons for this may be aggregates which hide the real particle size of the solids or effects which are not taken into account in the estimation of γ by the Schindler equation.

4.2.2 Solubility data of Zr(IV) in 0.02 M CaCl₂-Ca(OH)₂

Figure 4.32 shows the experimentally measured solubility data of several ZrO₂(s) solid phases in 0.02 M CaCl₂-Ca(OH)₂ solutions as well as expected solubility curves for amorphous and crystalline solids. The data for the calculation of the solubility curve of crystalline ZrO₂ were taken from NEA-TDB¹⁷, the data for the fresh solid from Altmaier et al.¹⁹. The numerical values of the measured solubility data and their relative errors are shown in Table 4.11.

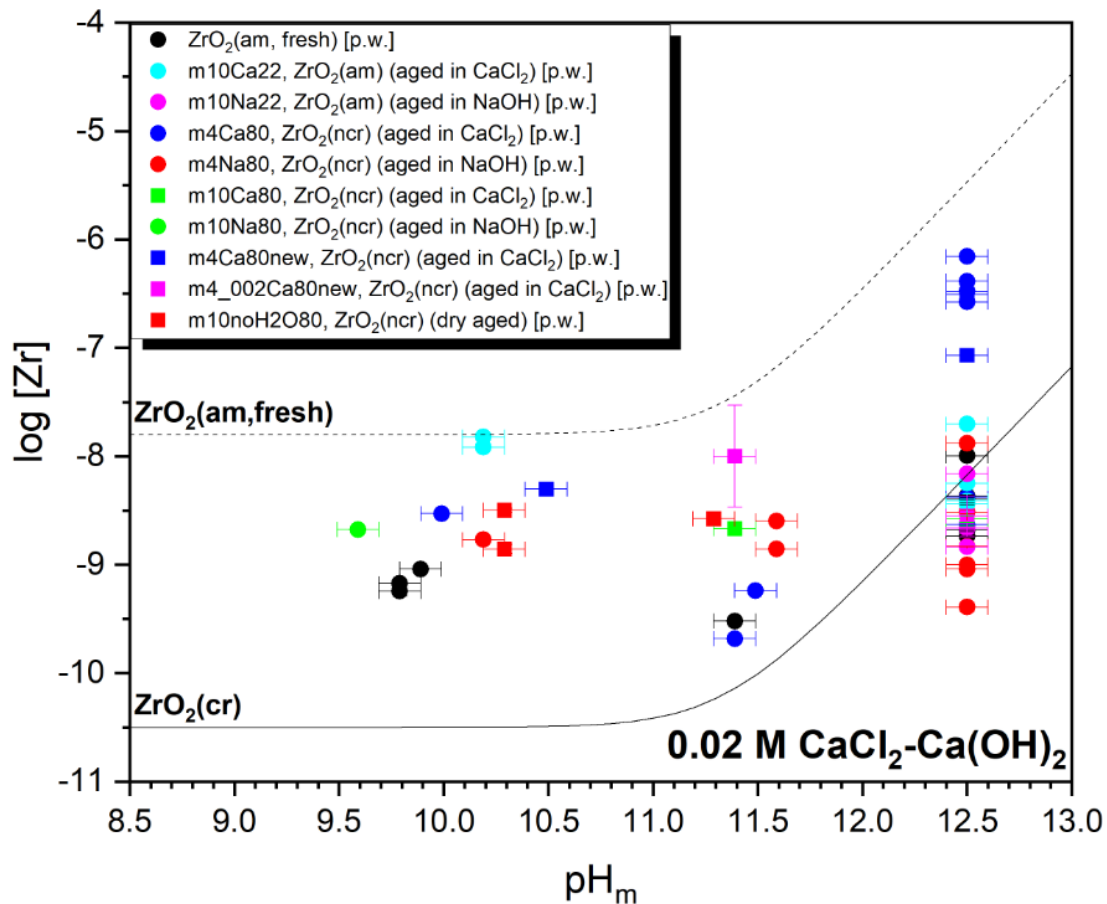


Figure 4.32: Solubility data of several solid phases, including also expected solubility curves for amorphous and crystalline solid phases based on data of NEA-TDB¹⁷ and Altmaier et al.¹⁹, respectively.

In the case of the solubility samples with 0.02 M CaCl₂-Ca(OH)₂ solutions as background electrolyte, most Zr concentrations were close to or at the detection limit. The reasons for this behavior could be the more difficult measurement conditions leading to higher scattering in the sample concentrations and higher blank measurements or that the expected increase in the Zr solubility at higher pH values was not as pronounced as calculated. Therefore, at some point solubility experiments in 0.02 M CaCl₂-Ca(OH)₂ solutions were reduced and the further evaluation was disregarded.

Table 4.11: numerical values of the measured Zr concentration in 0.02 M CaCl₂-Ca(OH)₂ background electrolyte.

Solid phase	log[Zr]	Analytical error (%)	log[Zr]	Analytical error (%)	log[Zr]	Analytical error (%)
pH fresh	9.8±0.1		11.4±0.1		12.5±0.1	
	-9.24	10.00	-9.52	3.73	-8.40	1.03
	-9.17	2.76			-8.00	1.05
	9.9±0.1				-8.74	0.81
	-9.04	1.62			-8.68	2.10
				-8.37	2.30	
				-8.44	1.96	
pH m10Ca22	10.2±0.1				12.5±0.1	
	-7.92	4.90			-7.70	1.61
	-7.82	2.99			-8.25	0.70
					-8.44	4.90
				-8.41	3.08	
pH m10Na22					12.5±0.1	
					-8.16	1.45
					-8.84	4.00
				-8.66	10.10	
pH m4Ca80	10.0±0.1		11.4±0.1		12.5±0.1	
	-8.53	0.81	-9.68	3.01	-6.39	3.96
			11.5±0.1		-8.63	1.23
			-9.24	0.85	-8.38	1.70
					-6.48	12.50
					-6.16	4.20
				-6.58	0.95	
pH m4Na80	10.2±0.1		11.6±0.1		12.5±0.1	
	-8.77	0.97	-8.60	0.85	-9.00	5.04
			-8.86	1.10	-7.88	1.20
					-8.83	1.93
					-9.04	0.60
					-9.39	9.10
				-8.52	3.89	
pH m4Ca80new	10.5±0.1				12.5±0.1	
	-8.30	2.85			-6.51	12.30
				-7.07	11.99	
pH m4_002Ca80new			11.4±0.1		12.5±0.1	
			-8.00	195.29	-8.55	54.00
pH m10Ca80			11.4±0.1		12.5±0.1	
			-8.67	5.00	-8.58	6.67
pH m10Na80	9.6±0.1					
	-8.68	6.48				
pH m10noH2O80	10.3±0.1		11.3±0.1			
	-8.86	9.10	-8.58	4.58		
	-8.50	3.94				

4.2.3 Solubility data of Zr(IV) in 0.2 M CaCl₂-Ca(OH)₂

Figures 4.33 to 4.35 show the experimentally measured solubility data of several ZrO₂(s) solid phases in 0.2 M CaCl₂-Ca(OH)₂ solutions as well as expected solubility curves for amorphous and crystalline solids and literature data. The data for the calculation of the solubility curve of crystalline ZrO₂ were taken from NEA-TDB ¹⁷, the data for the fresh solid and the literature values from Altmaier et al. ¹⁹. The numerical values of the measured solubility data and their relative errors are shown in Table 4.12.

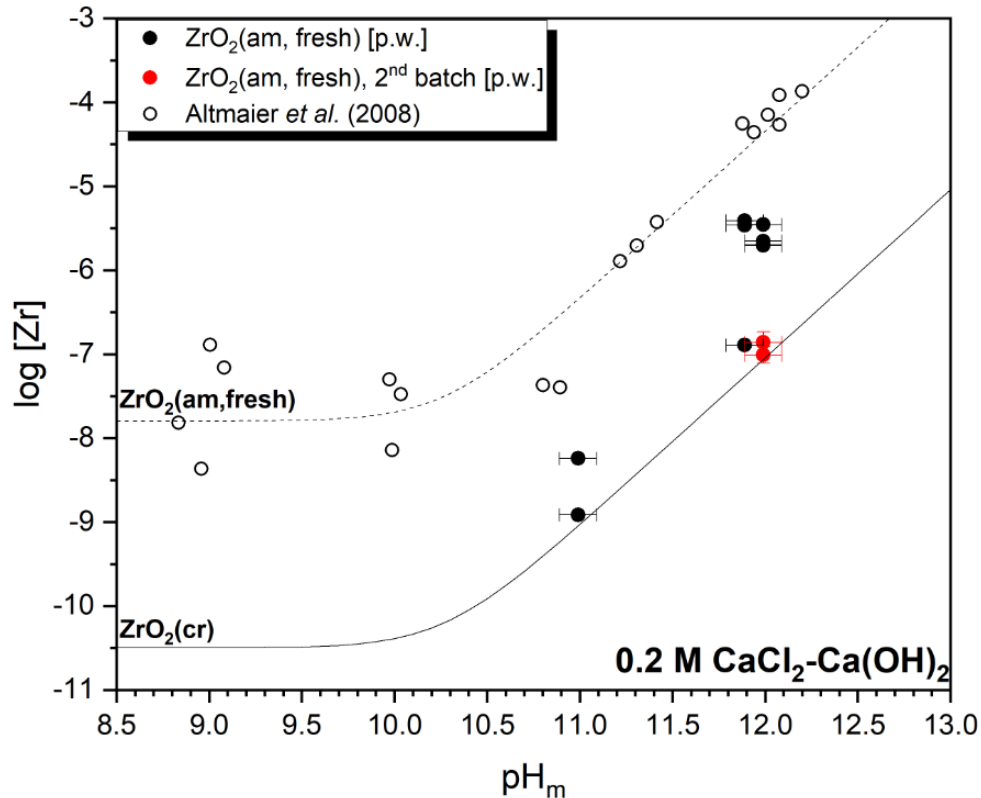


Figure 4.33: Solubility data of freshly precipitated ZrO₂(am, hyd, fresh) of the present work compared to data from Altmaier et al. ¹⁹, including also expected solubility curves for amorphous and crystalline solid phases based on data of NEA-TDB ¹⁷ and Altmaier et al. ¹⁹, respectively.

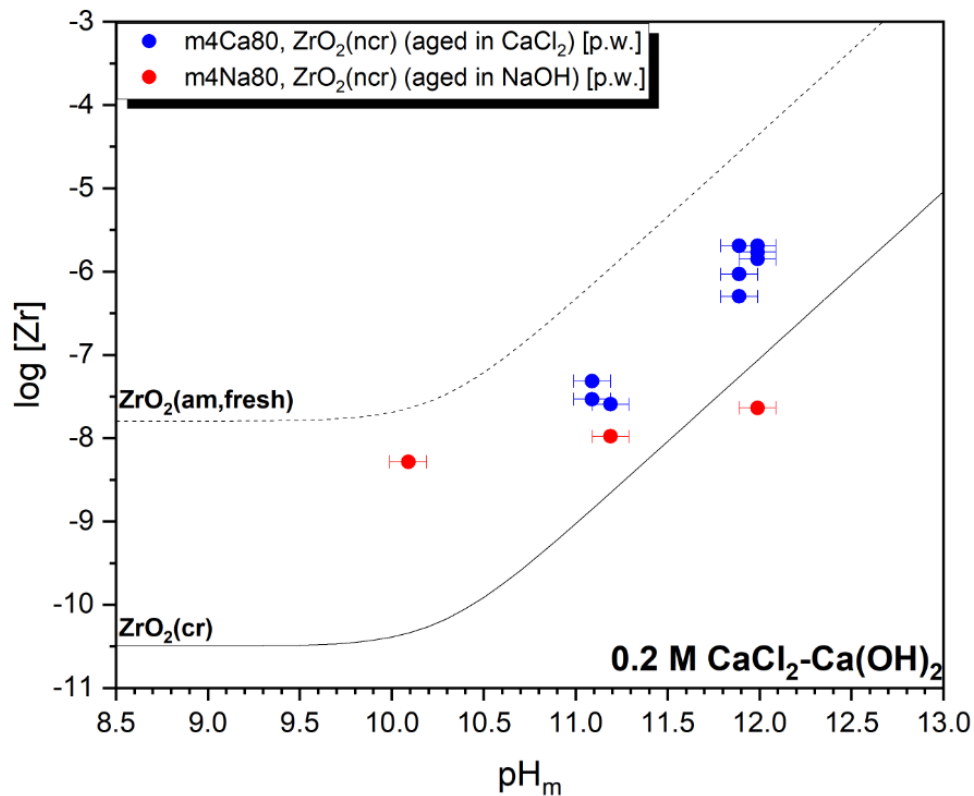
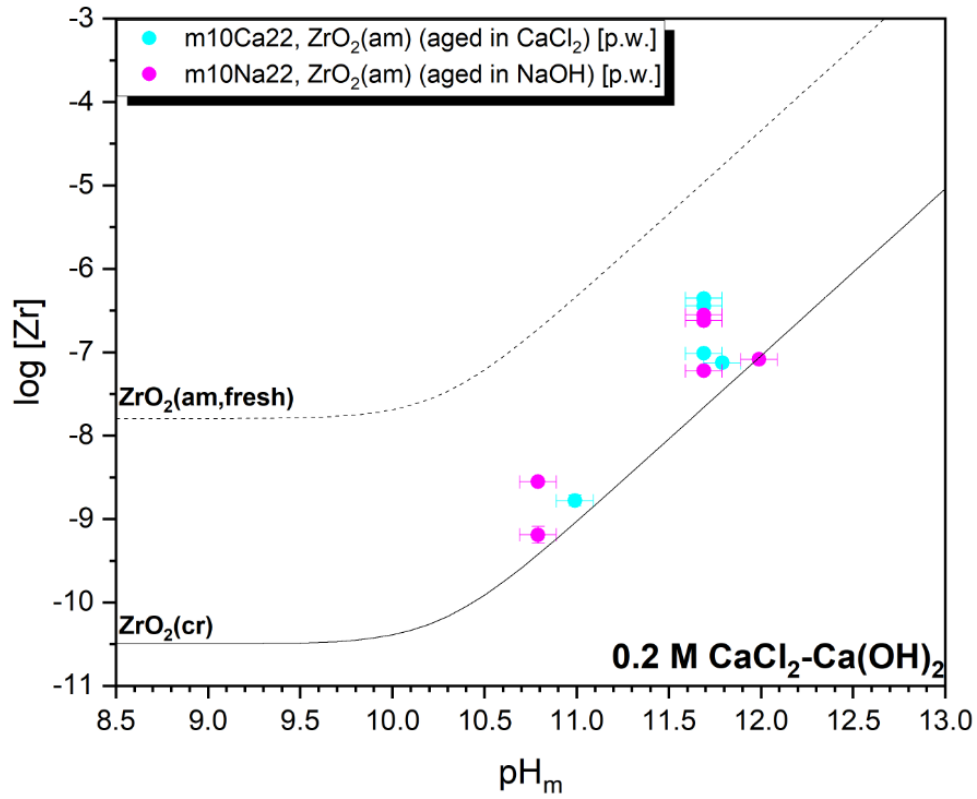


Figure 4.34: Solubility data of the aged solid phases m10Ca22 and m10Na22 (above) as well as m4Ca80 and m4Na80 (below), including also expected solubility curves for amorphous and crystalline solid phases based on data of NEA-TDB¹⁷ and Altmaier et al.¹⁹, respectively.

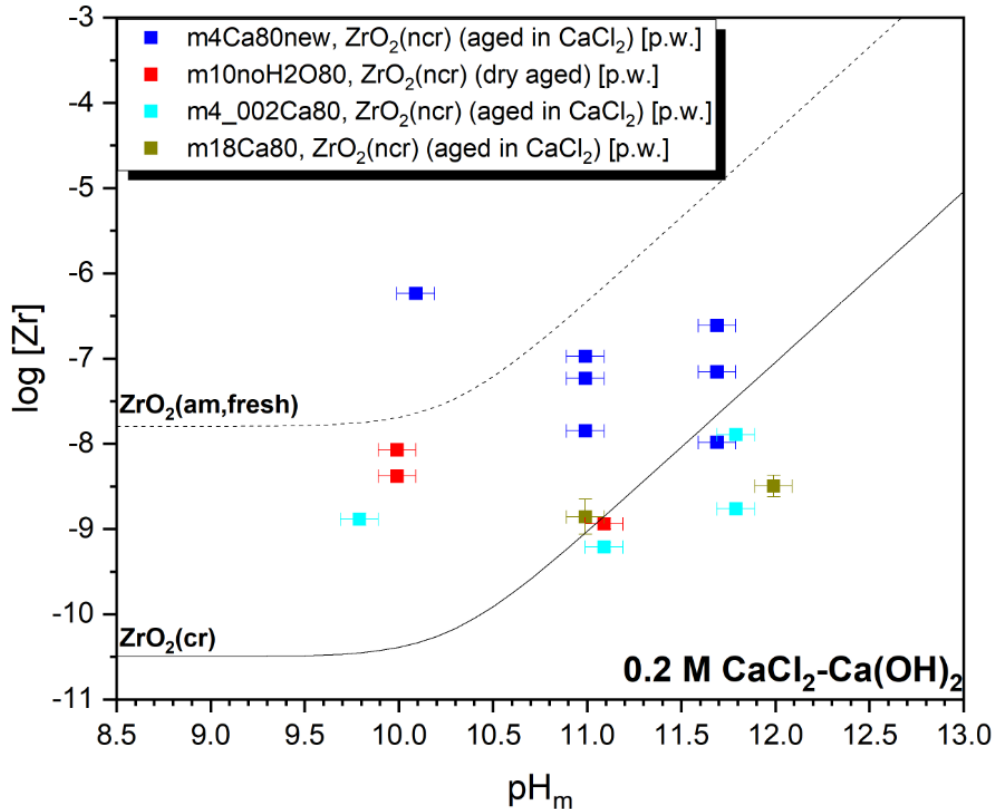


Figure 4.35: Solubility data of the aged solid phases $m4Ca80new$, $m10noH2O80$, $m4_002Ca80$ and $m18Ca80$, including also expected solubility curves for amorphous and crystalline solid phases based on data of NEA-TDB¹⁷ and Altmaier et al.¹⁹, respectively.

The measured concentrations of the samples of the freshly precipitated $ZrO_2(am, hyd, fresh)$ (Figure 4.33) are unexpected low, around 2 order of magnitude lower compared to measurements of Altmaier et al.¹⁹, and show a larger scattering as observed in the $NaCl\text{-}NaOH$ system. The reasons for this behavior remain unclear. In the case of the solid aged at $80^\circ C$ for 4 months in $CaCl_2$ ($m4Ca80$) the scattering in the data is much lower and the concentrations are in the expected range between the calculated solubility curves for fresh and crystalline solid phases. In the case of $m4Na80$ and several other solids ($m4Ca80new$, $m10noH2O80$, $m4_002Ca80$ and $m18Ca80$) the measured concentrations look almost randomly distributed and do not show the expected increase with a slope of 2 in high pH regions due to the formation of $Zr(OH)_6^{2-}$ and subsequently the complexes $Ca[Zr(OH)_6]_{aq}$, $Ca_2[Zr(OH)_6]^{2+}$ and $Ca_3[Zr(OH)_6]^{4+}$. This increase is again observed in the samples aged at $T = 22^\circ C$ ($m10Ca22$ and $m10Na22$), which show lower solubilities as expected from their amorphous character. Finally, for the other solid phases ($m4_002Ca80new$, $m10Ca80$, $m10Ca80new$, $m10Na80$, $m18Na80$ and the commercial crystalline solid) no concentrations could be determined.

Table 4.12: numerical values of the measured Zr concentration in 0.2 M CaCl₂-Ca(OH)₂ background electrolyte.

Solid phase	log[Zr]	Analytical error (%)	log[Zr]	Analytical error (%)	log[Zr]	Analytical error (%)
pH fresh	11.0±0.1		11.9±0.1		12.0±0.1	
	-8.24	2.81	-5.46	0.52	-5.71	0.76
	-8.91	2.64	-6.89	2.00	-5.70	1.78
			-5.41	0.60	-5.65	1.40
					-5.46	0.40
					-7.01	20.00
				-6.86	25.00	
pH m10Ca22	11.0±0.1		11.7±0.1		11.8±0.1	
	-8.78	14.20	-7.01	1.20	-7.13	1.30
			-6.45	2.30		
			-6.36	1.02		
pH m10Na22	10.8±0.1		11.7±0.1		12.0±0.1	
	-9.19	21.10	-7.22	1.70	-7.09	1.60
	-8.55	6.94	-6.62	2.40		
			-6.55	0.39		
pH m4Ca80	11.1±0.1		11.9±0.1		12.0±0.1	
	-7.53	2.56	-6.30	0.27	-5.77	0.27
	-7.32	7.70	-6.03	2.44	-5.85	1.30
	11.2±0.1		-5.69	0.60	-5.69	0.10
	-7.60	0.81				
pH m4Na80	10.1±0.1		11.2±0.1		12.0±0.1	
	-8.29	1.09	-7.98	1.70	-7.64	1.41
pH m4Ca80new	10.1±0.1		11.0±0.1		11.7±0.1	
	-6.24	5.10	-6.97	8.90	-7.98	6.90
			-7.23	11.50	-6.61	12.90
		-7.85	6.22	-7.16	1.01	
pH m4_002Ca80	9.6±0.1		11.1±0.1		11.8±0.1	
	-8.89	15.20	-9.21	10.50	-8.76	8.10
					-7.89	1.52
pH m10noH2O80	10.0±0.1		11.1±0.1			
	-8.38	8.00	-8.94	13.40		
	-8.07	2.84				
pH m18Ca80			11.0±0.1		12.0±0.1	
			-8.86	37.60	-8.50	25.1

4.2.3.1 Calculation of solubility products for the system $\text{Zr}^{4+}\text{-Ca}^{2+}\text{-H}^+\text{-OH}^-\text{-Cl}^-\text{-H}_2\text{O}$

Figures 4.36 and 4.37 show the solubility data of the $\text{ZrO}_2(\text{s})$ solid phases in 0.2 M $\text{CaCl}_2\text{-Ca(OH)}_2$ together with modelled solubility curves as described in chapter 4.2. The determined solubility constants are shown in Table 4.13.

In the case of the fresh solid phase and the two solid phases (m10Ca22 and m10Na22) aged at $T = 22^\circ\text{C}$, the modelled solubility constants $\log^* K_{s,0}^\circ = -6.04 \pm 1.38$, -6.26 ± 0.87 and -6.41 ± 0.85 , respectively, are significantly lower as expected and also observed for the same solids in 0.5 M NaCl-NaOH . Only the solubility constant determined for m4Ca80, $\log^* K_{s,0}^\circ = -5.74 \pm 0.38$, is in the expected range.

The modelling approach was only followed for the fresh, m10Ca22, m10Na22 and m4Ca80 samples, since sufficient solubility data were available. For the other solid phases the amount of measured data was too small (see Table 4.12) and the amount of samples at the same level as blank measurements was too high to evaluate a meaningful solubility constant. The determined solubility constants for the fresh $\text{ZrO}_2(\text{am, hyd})$, m10Ca22, m10Na22 and m4Ca80 are shown in Table 4.13 together with literature values.

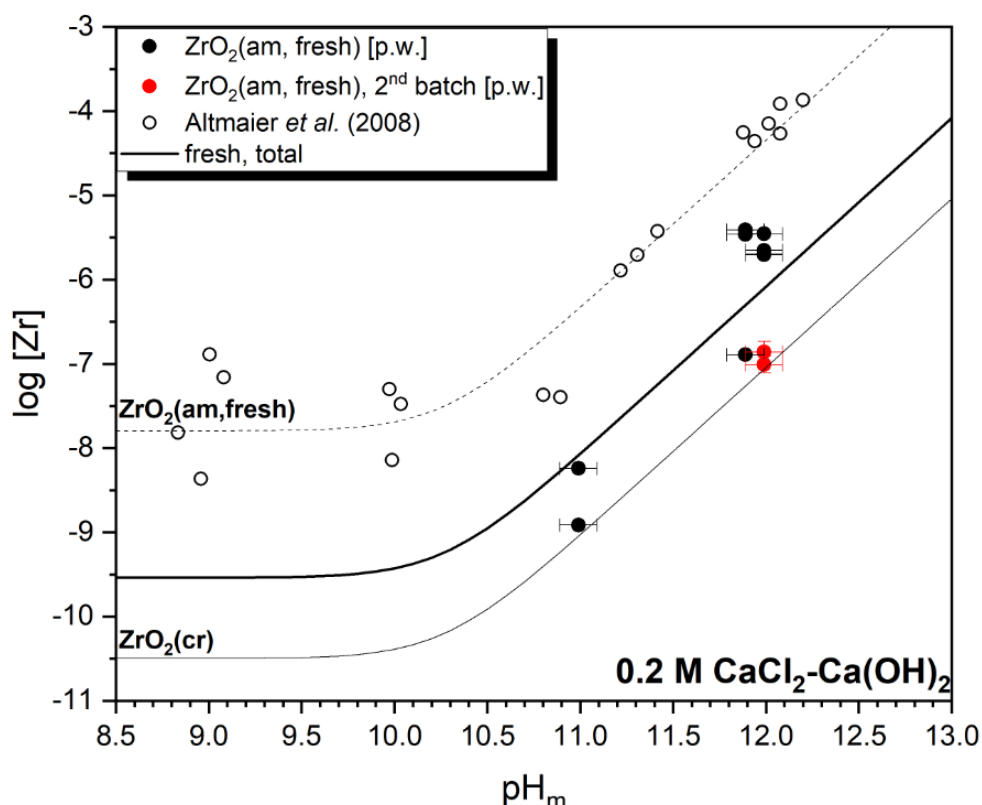


Figure 4.36: Solubility data and modelled solubility curve of the freshly precipitated $\text{ZrO}_2(\text{am, hyd, fresh})$ of the present work compared to data from Altmaier et al.¹⁹, including also expected solubility curves for amorphous and crystalline solid phases based on data of NEA-TDB¹⁷ and Altmaier et al.¹⁹, respectively.

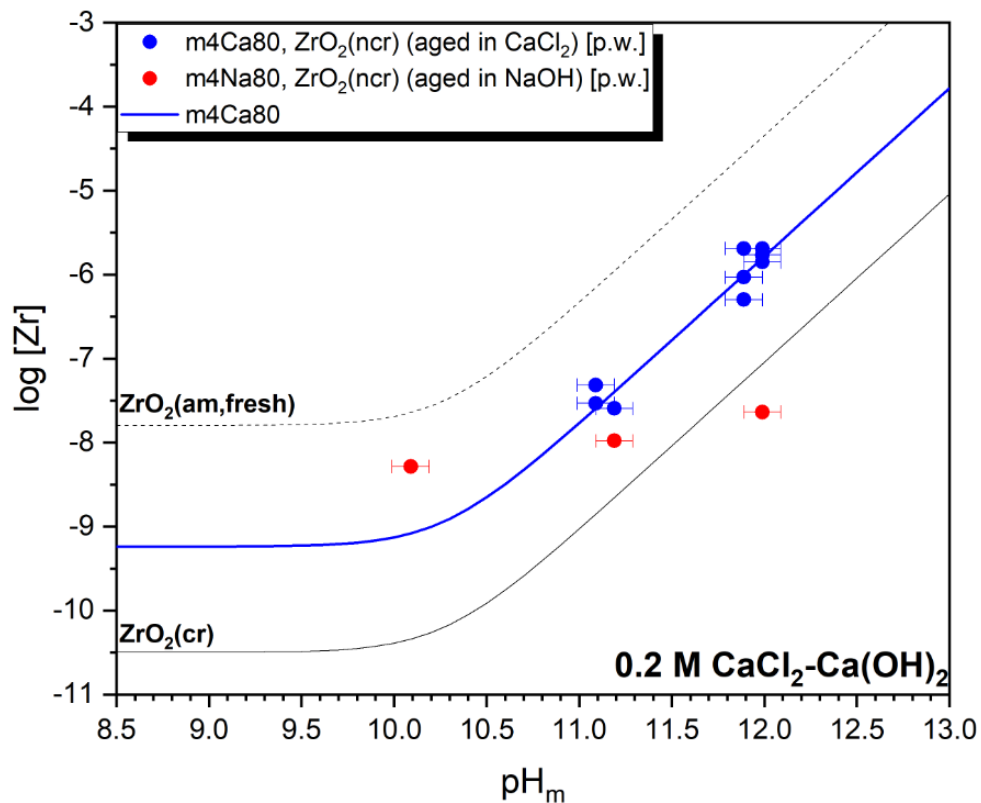
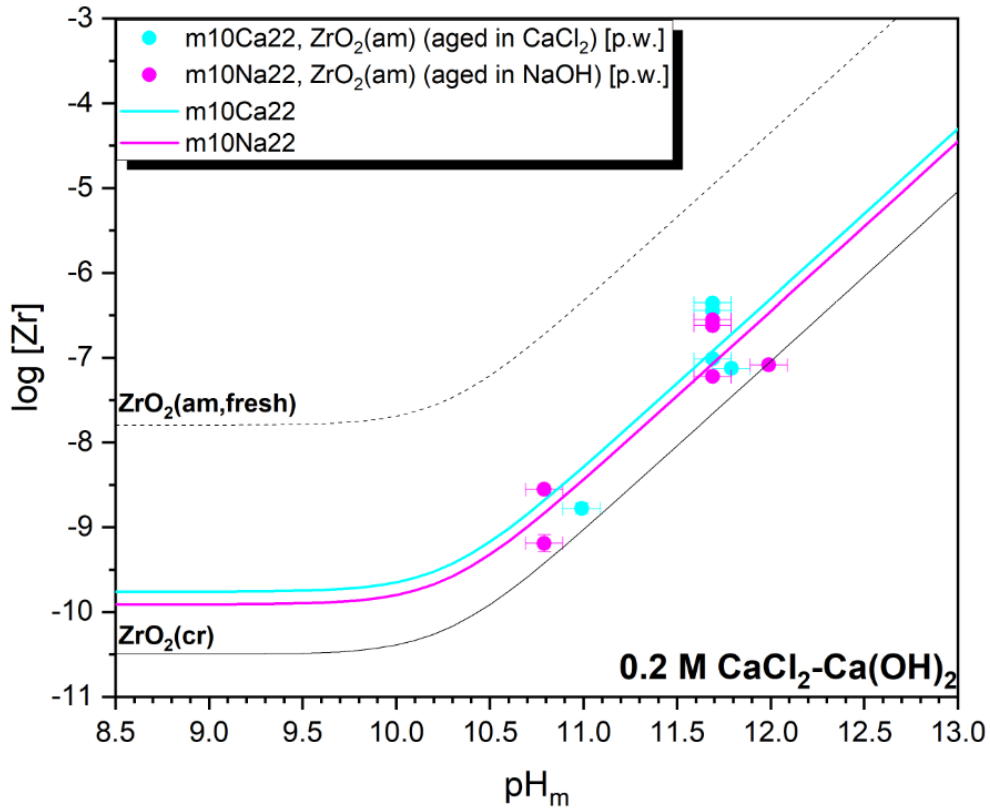


Figure 4.37: Solubility data and modelled solubility curves of the aged solid phases m10Ca22 and m10Na22 (above) as well as m4Ca80 and m4Na80 (below), including also expected solubility curves for amorphous and crystalline solid phases based on data of NEA-TDB¹⁷ and Altmaier et al.¹⁹, respectively.

Table 4.13: Solubility constants for ZrO₂(s) solid phases from the present work or literature. The log* K_{s,0}^o values correspond to the reaction: ZrO₂(s) + 2H₂O + 4H⁺ ⇌ Zr⁴⁺ + 4H₂O. The given errors are 2σ, calculated as described in chapter 4.2.

Solid phase	log* K _{s,0} ^o	Source
Present work in 0.2 M CaCl ₂ -Ca(OH) ₂		
ZrO ₂ (am, hyd, fresh), amorphous	-6.04 ± 1.38	Present work
m4Ca80, cubic/tetragonal	-5.74 ± 0.38	Present work
m10Ca22, amorphous	-6.26 ± 0.87	Present work
m10Na22, amorphous	-6.41 ± 0.85	Present work
Present work in 0.5 M NaCl-NaOH		
ZrO ₂ (am, hyd, fresh), amorphous	-4.53 ± 0.40	Present work
ZrO ₂ (am, hyd, fresh), 2 nd batch	-4.06 ± 0.30	Present work
ZrO ₂ (am, hyd, fresh), total	-4.36 ± 0.58	Present work
m4Ca80, cubic/tetragonal	-4.92 ± 0.56	Present work
m10Ca22, amorphous	-4.92 ± 0.32	Present work
m10Na22, amorphous	-4.68 ± 0.33	Present work
Literature		
ZrO ₂ ·xH ₂ O(aged)	-4.3 ± 0.2	Altmaier et al. ¹⁹
Zr(OH) ₄ (am)	-0.94 ± 0.32	Sasaki et al. ⁷⁵
Zr(OH) ₄ (s), heated at 90 °C	-5.7 ± 0.3	Kobayashi et al. ¹
Zr(OH) ₄ (np), heated at 90 °C	-5.4 ± 0.2	Kobayashi et al. ¹
ZrO ₂ (cr)	-6.46 ± 0.1	Kobayashi et al. ⁷⁶
ZrO ₂ (cubic), yttrium stabilized	-5.8	Zouari ⁷⁷
ZrO ₂ (monoclinic)	-7.0 ± 0.4	Zouari ⁷⁷
ZrO ₂ (am, fresh)	-3.24 ± 0.1	NEA-TDB ¹⁷
ZrO ₂ (monoclinic)	-7.0 ± 1.6	NEA-TDB ¹⁷

4.2.3.2 Application of the Schindler equation on the solubility of Zr in 0.2 M CaCl₂-Ca(OH)₂

Due to the lower solubilities observed for the smaller amorphous particles also the evaluation with the Schindler equation does not work as well as for the NaCl-NaOH system. Nevertheless, the evaluation of the samples in the present work is shown in Figure 4.38. Adjustment of the γ value to the samples would in this case deliver a physically senseless negative value for γ .

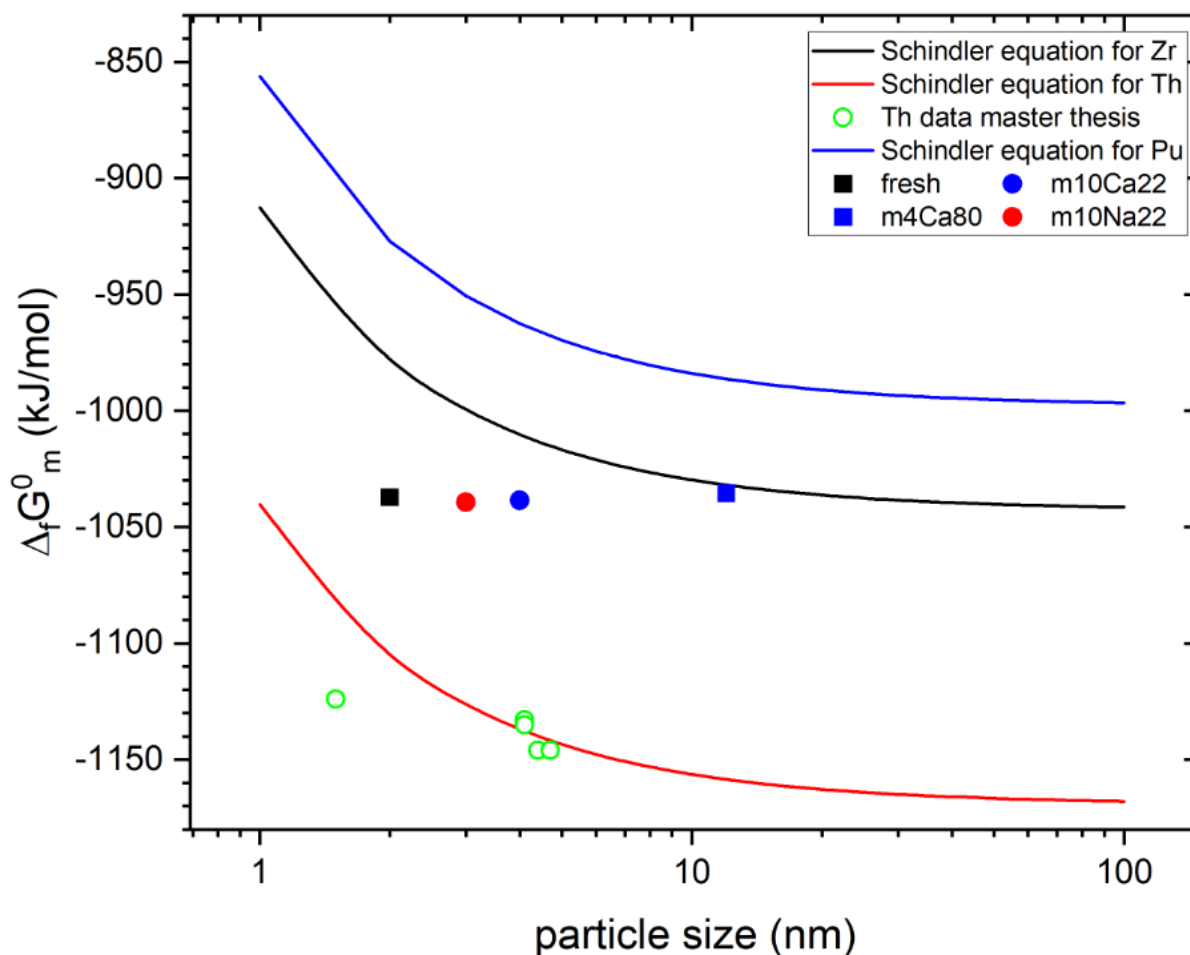


Figure 4.38: Application of the Schindler equation on the ZrO₂(s) system calculated in the same way as Neck et al.¹³⁵. For comparison also Th and Pu curves and Th data are included. The $\Delta_f G_m^\circ$ values of the experimental data were calculated from the solubility constants as described in chapter 4.2. The particle size of the samples was taken from the XRD and TEM results or estimated from the surface area (BET) in the case of m10Ca22 and m10Na22.

4.3 DFT results

The main goal of the DFT calculations was to better understand the effect of crystallinity and different crystal structures on the hydration behavior of the solid phases in order to be able to better explain the observed solubility phenomena. The strategy of the DFT calculation was therefore to use 3 polymorphs (monoclinic, tetragonal and amorphous) and compute their surface interaction with water molecules. For this purpose, the most stable termination for each bulk solid was modelled first in vacuum, then in interaction with different numbers of water molecules to consider different water coverages. The expected main results were the geometrical distortions upon water adsorption, the role of water coverage and the determination of accurate energetics/electronic structures of the surfaces of the different solid phases. In the DFT calculations in the context of this work several approximations were done. Firstly, the calculations were static (0 K, no dynamic effects). To be still representative several adsorption sites and modes (molecular or dissociative) were considered. Secondly, the surfaces were modelled in vacuum and only the most stable terminations without any defects were used. Several water molecules were included to simulate a surface under aqueous conditions instead of vacuum, to be more representative of real systems, even if a full hydration is not modelled in this way. It is also expected that in real systems not only the most stable surfaces are present, but also more reactive surfaces and defective sites at which solubility certainly will start, but these are much more complex to model and out of the scope of the present work.

The following steps as schematically shown in Figure 4.39 were done in the context of this study. Firstly, the calculations were started with a set of solid phase structures for bulk monoclinic, tetragonal and amorphous ZrO_2 . The amorphous structure was created ad hoc by M. Calatayud based on the work of Zhao and co-workers¹³⁹ with simulated annealing molecular dynamics. These bulk solid phases were optimized in two steps, first a volume relaxation, subsequently an atomic position relaxation. The resulting optimized structures (monoclinic, tetragonal and amorphous, Figure 4.40 and Table 4.14) were used to create surfaces. For this purpose the structures were cut along the most stable lattice planes i.e. (-111) for monoclinic and (101) for tetragonal, as shown in Figure 4.41). In the case of the amorphous solid, a vacuum layer was added on top of the slab to create a surface and a short dynamics was run then quenched. The resulting slabs were optimized with an atomic positions relaxation. After optimization, the surface energy was calculated (Table 4.16) and the coordination of the surface atoms was compared with the bulk solids (Figure 4.42-4.44). In the next step, several water molecules (as H_2O or dissociated as OH^- and H^+) were added to the surface, systematically testing different sites on the surface. The optimal positions of the water molecules (Figures 4.45-4.47) were determined by calculating the water adsorption

energy of each tested position (Tables 4.17-4.19), to gain information about the surface structural modification and reactivity towards hydration.

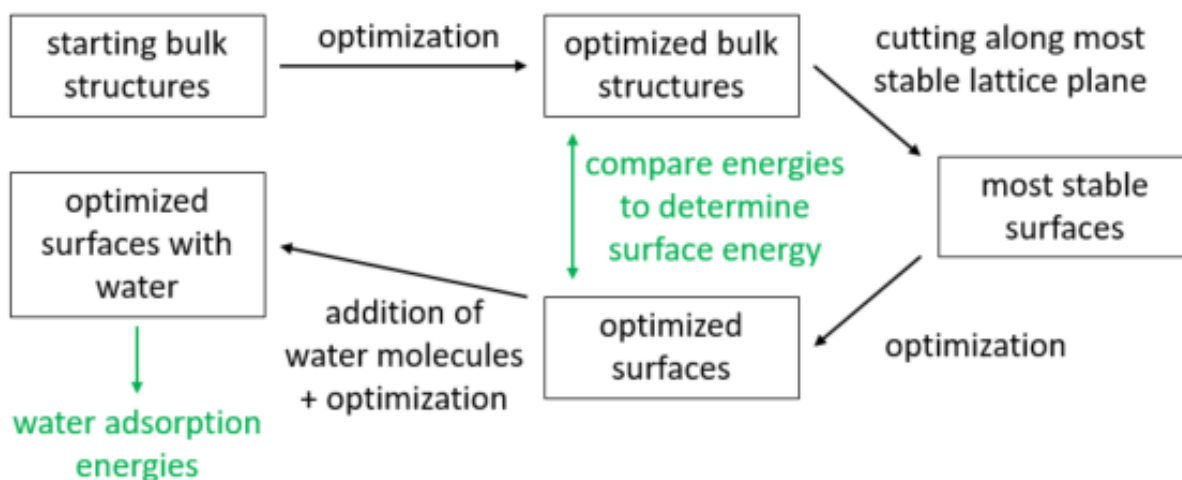


Figure 4.39: schematic overview on the DFT calculations.

4.3.1 Bulk solid calculations

The calculation of the bulk solids was done in two steps, in the first step a volume relaxation of the unit cell was done, in the second step an atomic position optimization of all the atoms in a unit cell. The results of the bulk optimization are shown in Figure 4.40 and Table 4.14. To model a unit cell of an amorphous structure, the approach of Zhao and co-workers¹³⁹ was followed, a cubic starting structure was heated up and quenched with molecular dynamics calculations. In the case of monoclinic and tetragonal ZrO_2 , structures corresponding to $P2_1/c$ and $P4_2/nmc$ space groups were used, respectively. Starting structures for the three solid phases were provided by M. Calatayud. The parameters of the optimized solid phases are in agreement with previous calculations, knowing that the lattice parameters are overestimated with this type of functionals.

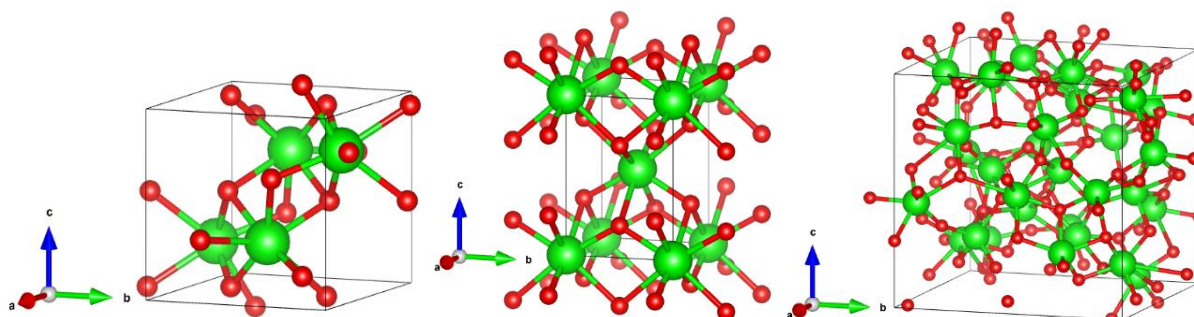


Figure 4.40: optimized unit cells of monoclinic (left), tetragonal (middle) and amorphous (right) ZrO_2 .

Table 4.14: Structural parameters of the optimized bulk solids.

	Method/ functionals	Energy (eV)	E/ZrO ₂ (eV)	Lattice parameters (Å)			γ (°)
				a	b	c	
Monoclinic							
Literature	Rietveld ⁵⁸			5.15	5.21	5.31	99.1
	Neutron diffr. ¹⁴⁰			5.15	5.21	5.32	99.2
	PBE0 ⁸⁸			5.18	5.26	5.30	99.1
Present work	PBE	-112.758	-28.190	5.26	5.35	5.42	99.0
	PBE+D3	-115.298	-28.825	5.25	5.33	5.40	99.0
	optPBE	-90.516	-22.629	5.27	5.35	5.42	99.0
	optPBE+PBE+D3	-95.076	-23.769	5.26	5.35	5.42	99.0
Tetragonal							
Literature	Powder diffr. ¹⁴¹			a		c	
	Rietveld ⁵⁹			3.59		5.18	
	PBE0 ⁸⁸			3.60		5.18	
Present work	PBE	-56.779	-28.389	3.61		5.20	
	PBE+D3	-57.841	-28.920	3.65		5.28	
	optPBE	-46.531	-23.265	3.66		5.30	
	optPBE+PBE+D3	-47.956	-23.978	3.66		5.30	
Amorphous							
Present work	PBE	-894.565	-27.955	a			
	PBE+D3	-909.579	-28.424	11.08			
	optPBE	-727.554	-22.736	11.03			
	optPBE+PBE+D3	-748.332	-23.385	11.04			

4.3.2 Cutting and optimization of surfaces

The most stable surfaces of monoclinic and tetragonal ZrO_2 are the $(-1\ 1\ 1)$ and $(1\ 0\ 1)$ lattice planes, respectively^{81,82,88}. Such surfaces can be created by cutting a bulk solid along these lattice planes. Optimized bulk unit cells, where the lattice planes are marked, as well as unit cells of the slabs after cutting along these lattice planes are shown in Figure 4.41. With this method surfaces of the corresponding lattice planes, infinite in x and y direction, with a vacuum of at least 20 Å above the surface in z direction to avoid interactions between the surface and the bottom layer of the next unit cell, are created. In the case of the amorphous solid, a surface was created by adding a vacuum layer on top of the unit cell. Since the first two top and bottom layers are affected by the surface creation and optimization, sizes of 6 to 8 Zr layers were selected for the slabs of the monoclinic and tetragonal structures, in order to keep a bulk-like part in the middle of the structure. Another atomic position relaxation was done to optimize the surfaces.

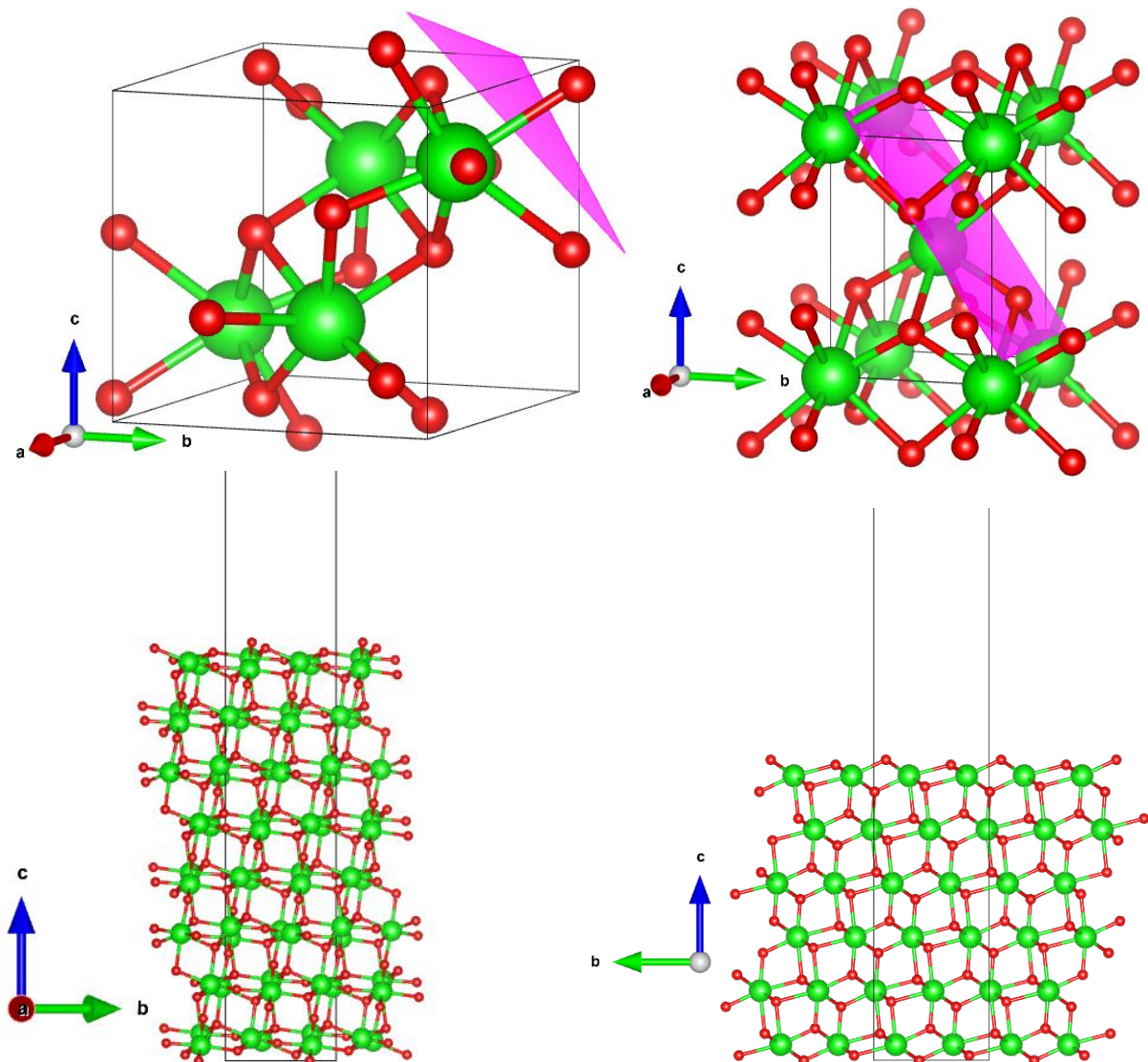


Figure 4.41: top: optimized unit cells, bottom: side view of the slabs after cutting, left: monoclinic $(-1\ 1\ 1)$, right: tetragonal $(1\ 0\ 1)$.

4.3.3 Coordination analysis of the surfaces

By creating the surface, a reduction of the atomic coordination number (CN) is expected and observed. A high surface stability is usually correlated with higher atomic coordination whereas high reactivity is expected for low-coordinated atoms.

4.3.3.1 Monoclinic (-1 1 1) surface

Figure 4.42 displays the surface atomic sites for the monoclinic (-1 1 1) surface and Table 4.15 summarizes the CN values obtained after optimization. The stoichiometric, regular surface shows two coordination numbers for zirconium atoms, 3 sites with CN 6 and one with CN 7, with average Zr-O distances of 2.15-2.19 and 2.22 Å respectively. Out of the 8 different oxygen sites, one shows only a coordination with 2 Zr atoms, five oxygen atoms show CN 3 and two coordinate with 4 Zr atoms. Compared to the bulk, this represents a decrease in CN, as in the bulk Zr is 7-fold and oxygen 3- and 4-fold. Regarding the Zr-O distances only smaller differences are observed.

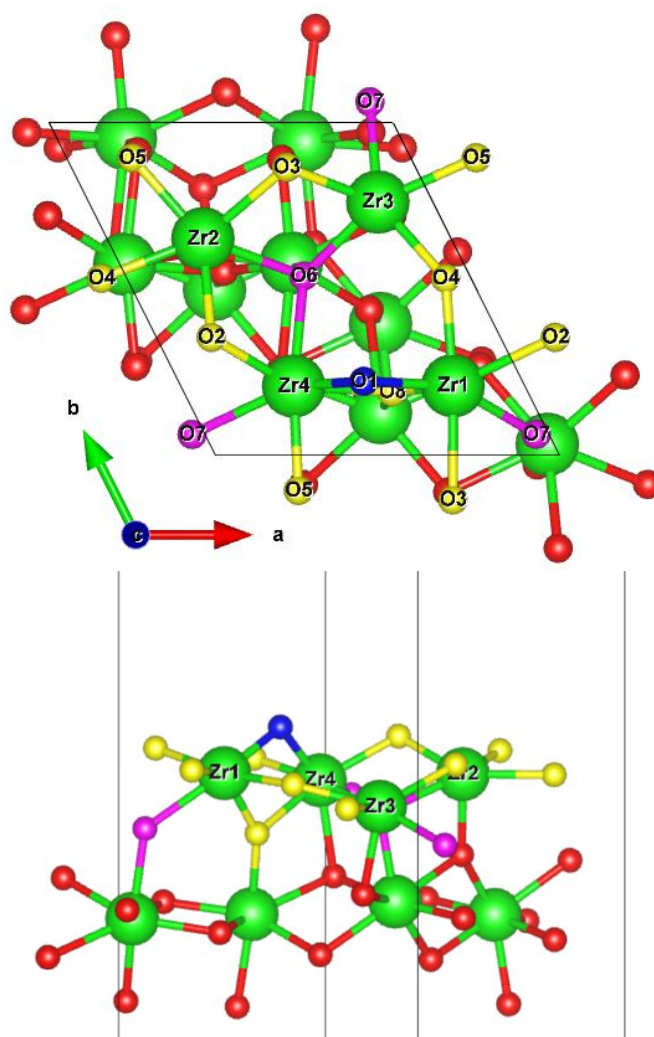


Figure 4.42: Surface coordination of the monoclinic (-1 1 1) surface after optimization (top view: above, side view: below).

4.3.3.2 Tetragonal (1 0 1) surface

The surface atomic sites of the tetragonal (1 0 1) surface are shown Figure 4.43. The corresponding coordination numbers after optimization are also summarized in Table 4.15. For zirconium atoms only 7-fold oxygen coordination is observed, with average Zr-O distances of 2.25 Å. Half of oxygen atoms show a coordination 3 Zr atoms with a distance of 2.26-2.27 Å, the other half has a CN of 4 and Zr-O distances of 2.22-2.24 Å. Compared to the bulk, this represents a decrease in CN, as in the bulk Zr atoms are 8-fold and all oxygen atoms are 4-fold coordinated. Regarding the Zr-O distances only smaller differences are observed.

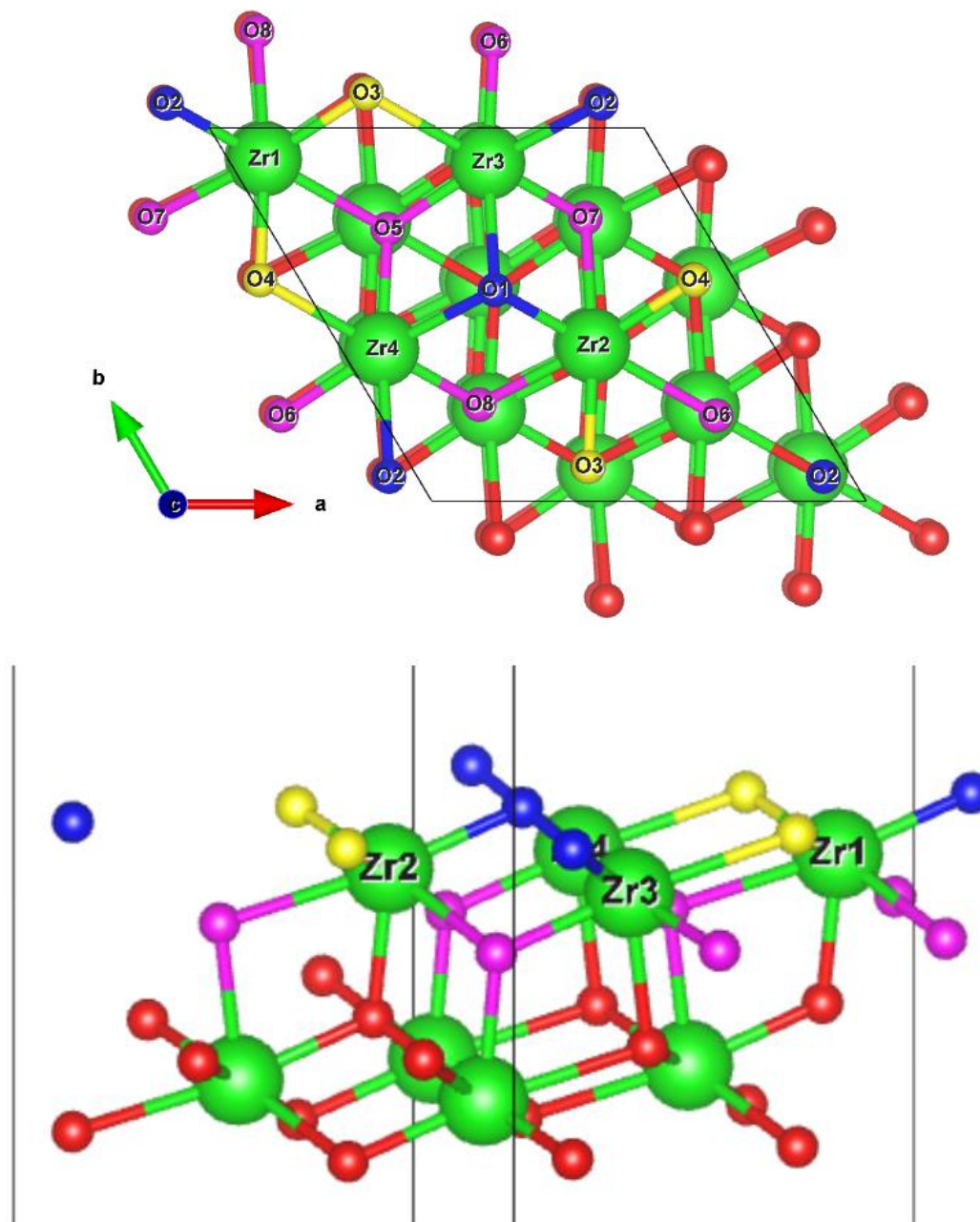


Figure 4.43: Surface coordination of the tetragonal (1 0 1) surface after optimization (top view: above, side view: below).

4.3.3.3 Amorphous surface

In the case of the amorphous bulk and surface, the range of coordination numbers is larger compared to the other solids. For Zr atoms, coordination numbers of 4 to 8 are observed, for oxygen 2 to 4. The surface is shown in Figure 4.44, the corresponding coordination numbers after optimization are also in Table 4.15. Comparing the surface and the bulk solid, the average coordination numbers are smaller for the surface, Zr coordinates to 6.19 and 5.84 O atoms, respectively and oxygen to 3.09 and 2.92 Zr atoms. The average distance of 2.15 Å is also smaller for the surface compared to the bulk (2.18 Å).

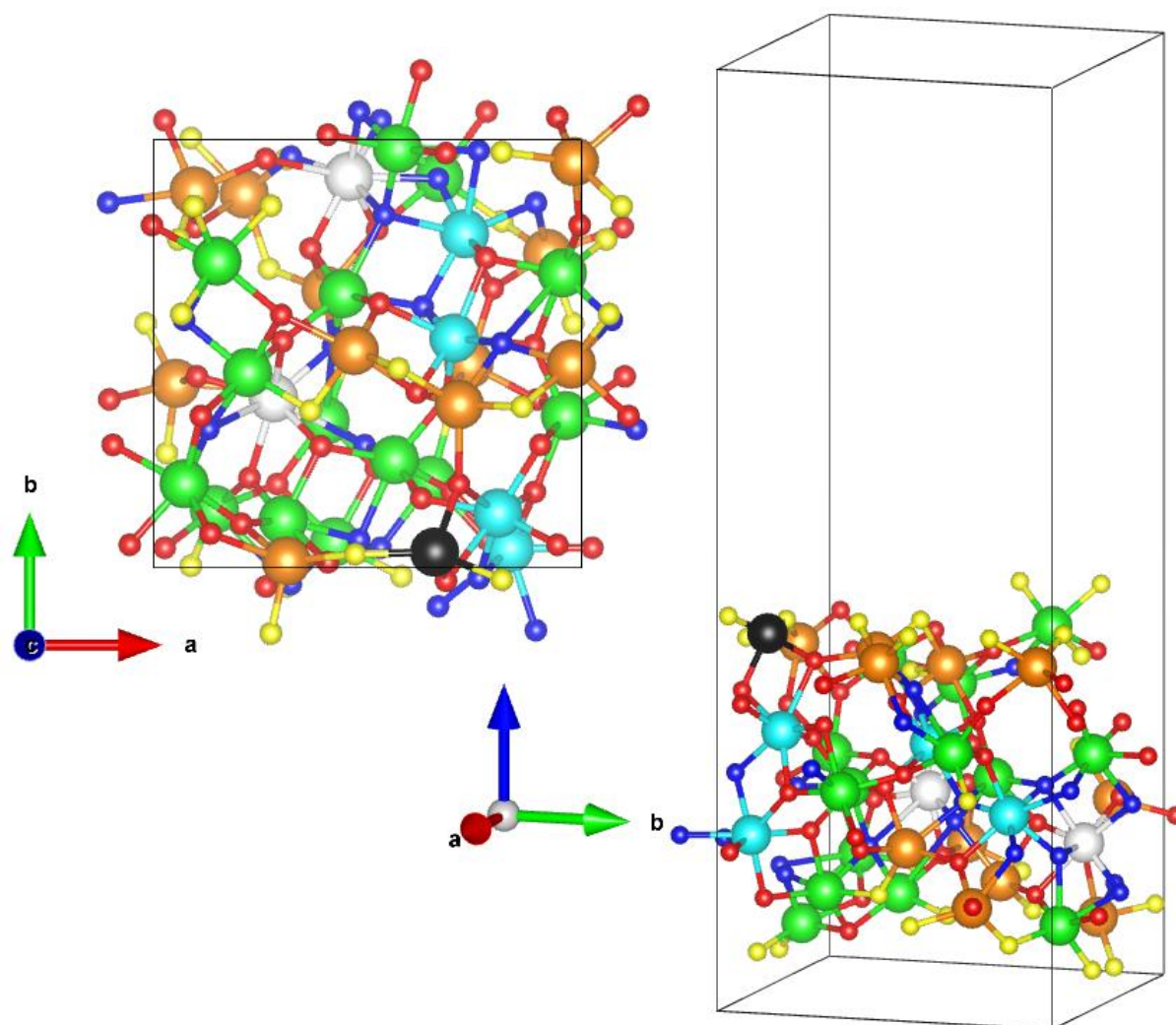


Figure 4.44: Surface coordination of the amorphous surface after optimization (top view: left, side view: right).

Table 4.15: Coordination numbers of the bulk solids and the optimized surfaces.

Atom	Coordination	Average distances
Monoclinic bulk		
Zr	7 O atoms	2.18-2.19 Å
O (50%)	3 Zr atoms	2.11-2.13 Å
O (50%)	4 Zr atoms	2.23 Å
Monoclinic (-1 1 1) surface (Figure 4.42)		
Zr1	6 O atoms	2.19 Å
Zr2	6 O atoms	2.18 Å
Zr3	6 O atoms	2.15 Å
Zr4	7 O atoms	2.22 Å
O1 (blue)	2 Zr atoms	
O2, O3, O4, O5, O8 (yellow)	3 Zr atoms	
O6, O7 (magenta)	4 Zr atoms	
Tetragonal bulk		
Zr	8 O atoms	4x 2.10 Å, 4x 2.42 Å
O	4 Zr atoms	2x 2.10 Å, 2x 2.42 Å
Tetragonal (1 0 1) surface (Figure 4.43)		
Zr1-Zr4	7 O atoms	2.25 Å
O1, O2 (blue)	3 Zr atoms	2.27 Å
O3, O4 (yellow)	3 Zr atoms	2.26 Å
O5-O8 (magenta)	4 Zr atoms	2.22-2.24 Å
Amorphous bulk		
6x Zr	5 O atoms	
15x Zr	6 O atoms	
10x Zr	7 O atoms	
1x Zr	8 O atoms	
Average	6.19 O atoms	2.18 Å
10x O	2 Zr atoms	
38x O	3 Zr atoms	
16x O	4 Zr atoms	
Average	3.09 Zr atoms	2.18 Å
Amorphous surface (Figure 4.44)		
1x Zr (black)	4 O atoms	
11x Zr (orange)	5 O atoms	
14x Zr (green)	6 O atoms	
4x Zr (cyan)	7 O atoms	
2x Zr (white)	8 O atoms	
Average	5.84 O atoms	2.15 Å
18x O (yellow)	2 Zr atoms	
33x O (red)	3 Zr atoms	
13x O (blue)	4 Zr atoms	
Average	2.92 Zr atoms	2.15 Å

Comparing the three surfaces shows the highest average coordination numbers for the tetragonal (1 0 1) surface with zirconium coordinated by 7 oxygen atoms and oxygen coordinated by 3 or 4 (50 % each) Zr atoms, followed by the monoclinic (-1 1 1) surface (coordination numbers 6.25 and 3.125) and the amorphous surface (coordination numbers 5.84 and 2.92). These average coordination numbers and also the lowest coordination numbers which are found in the surfaces (Zr: 7, 6 and 4, O: 3, 2 and 2 for tetragonal, monoclinic and amorphous respectively), indicate a lowest stability and thus highest reactivity for the amorphous surface followed by the monoclinic and finally the tetragonal one.

4.3.4 Calculation of the surface energy

The surface energy is very important parameter to evaluate the reactivity of a surface. Optimized bulk solid and surface structures enable the calculation of the surface energy E_{surf} (energy/area) by:

$$E_{\text{surf}} = \frac{E_{\text{slab}} - nE_{\text{bulk}}}{2A} \quad (4.11)$$

where E_{slab} is the total energy of the slab, E_{bulk} the total energy of a unit cell of the bulk solid, n a factor to have equal numbers of Zr in the bulk and the slab and A the area of the surface in the slab. The factor of 2 is included, because two surfaces, one in the top layers and one at the bottom are created in each slab (visible in previous Figures). The surface energies calculated for the structures in the present work as well as some theoretical and experimental literature values are shown in Table 4.16. The calculated results of 1.098 J/m² for the monoclinic and 1.348 J/m² for the tetragonal surface are in general in agreement with the literature, but varying because of the different functionals that were used. The unrealistic surface energy calculated for the amorphous solid may be explained by the different method to create the surface as described in previous chapters. In contrast to the coordination analysis, the higher calculated surface energy of the tetragonal solid compared to the monoclinic one, indicates that the monoclinic surface is more stable and thus less reactive.

Table 4.16: Surface energies calculated for the different surfaces.

Surface energy (J/m ²)	Monoclinic (-1 1 1)	Tetragonal (1 0 1)	Amorphous
Present work	1.098*	1.348	-0.345
PBE0/Zr ^{ECP} -O ^{ECP} ⁸⁸	1.482	1.512	
LDA/PAW ^{81,88}	1.246	1.239	
PBE/PAW ^{83,85,88}	1.224	1.090	
PW91/PAW ^{82,86,88}	1.340	1.107	
LDA/PW ^{84,88}		1.316	
PBEsol ⁷⁷	1.10		
Experimental ⁸⁸		1.428**	
Experimental ⁸⁸		1.927**	

*Symmetry was removed in the calculation of the monoclinic bulk, since the structure seemed to be understabilized. The same change had no effect on the other bulk and surface calculations. ** Mix of surfaces, not only (1 0 1).

4.3.5 Hydration of the surfaces

In order to gain more information about the surfaces reactivity and their hydration behavior, the adsorption of water was studied on the selected slab models. For this purpose water, in different content, in molecular form (m) as H₂O or dissociated (d) as OH and H, were systematically added at different sites of the surfaces. The adsorption energy E_{ads} was then calculated by:

$$E_{ads} = \frac{E_{slab+H_2O} - E_{slab} - nE_{H_2O}}{n} \quad (4.12)$$

where E_{slab+H_2O} is the total energy of the slab with n adsorbed water, E_{slab} is the total energy of the slab without water, E_{H_2O} the energy of a water molecule in gas phase (-14.225 eV) and n the number of adsorbed water molecules.

The procedure consists of adding first one water molecule on different sites and evaluating the adsorption energy. Then the most stable structure is used and a second molecule is added exploring the available sites, then a third and finally a fourth molecule. In the following, each surface is described separately and Section 4.3.5.4 compares the results for the three structures.

4.3.5.1 Water adsorption on monoclinic (-1 1 1) surface

Figure 4.45 shows the monoclinic (-1 1 1) surface with 1-4 water added molecular or dissociated on different sites of the surface. The adsorption energy for each of these structures was calculated by optimizing them and the structure with the lowest total energy, caused by the highest (exothermic) adsorption energy was selected to continue. The determined adsorption energies are shown in Table 4.17.

Table 4.17: water adsorption energies and positions on the monoclinic (-1 1 1) surface.

1 st water		2 nd water	
Position	E _{ads} [eV]	Position	E _{ads} [eV]
1. Zr1, O1, O2 (m)	-0.900	1. Zr2, O2, O3 (m)	-1.111
2. Zr1, O1, O2 (m)	-0.963	2. Zr2, O4, O5 (m)	-1.103
3. Zr2, O2, O4, O5 (m)	-1.057	3. Zr3, O3, O4 (m)	-1.311
4. Zr2, O2, O3 (m)	-1.147	4. Zr4, O1, O2 (m)	-1.343
5. Zr3, O4, O5 (m)	-0.766	5. Zr4, O49 (m)	-1.330
6. Zr4, O1, O2 (m)	-0.830	6. Zr2O2, O3 (d)	-1.049
7. Zr1O1, O2 (d)	-0.830	7. Zr2O3, O5 (d)	-1.143
8. Zr1O2, O1 (d)	-1.298	8. Zr3O4, O3 (d)	-1.228
9. Zr2O4, O3 (d)	-1.138	9. Zr3O49, O4 (d)	-1.070
10. Zr2O4, O2 (d)	-0.656	10. Zr4O49, O2 (d)	-1.328
11. Zr3O4O5, O3 (d)	-1.023	11. Zr4O49, O1 (d)	-1.328
12. Zr3O3, O4 (d)	-0.733	12. Zr4O1, O2 (d)	-1.345
13. Zr4O1, O2 (d)	-0.833	13. Zr4O2, O1 (d)	-0.822
14. Zr4O2, O1 (d)	-1.225		
3 rd water		4 th water	
Position	E _{ads} [eV]	Position	E _{ads} [eV]
1. Zr2, O3 (m)	-1.214	1. Zr1, O49 (m)	-1.157
2. Zr2, O4, O5 (m)	0.026*	2. Zr4, O49, O50 (m)	-1.126
3. Zr4, O1, O2 (m)	-1.136	3. Zr2O6, O2 (d)	-1.138
4. Zr4, O50 (m)	-1.179	4. Zr4O49, O2 (d)	-1.131
5. Zr2O2, O3 (d)	-1.241	5. Zr3O6, O4 (d)	-0.997
6. Zr2O5, O3 (d)	-1.140		
7. Zr2O3, O5 (d)	-1.094		
8. Zr4O2, O1 (d)	-1.136		
9. Zr4O50, O1 (d)	-1.162		
10. Zr4O49, O2 (d)	-1.038		

*In structure 2, Zr2 was hydrated and almost ejected from the surface (1 Zr-O bond to the solid left). This behavior might be interesting for the dissolution of the solid phase, but due to the significantly higher energy, this structure was not taken into account for the adsorption calculations.

The optimization after adding the first water molecule leads in most cases only to small shifts of the water molecules. In general, the structures with dissociated water are more stable compared to ones with molecular water, even if in some cases recombination to H₂O or dissociation into H and OH was observed during the optimization. The structure with the lowest energy (Figure 4.45 (II)), adding OH on Zr1 and H on O1 (position 8), was selected to continue. The adsorption energy of this structure was -1.298 eV.

The addition of the second water molecule in the dissociated form resulted in half of the tested positions in a recombination of H₂O. The energies of the structures keeping dissociated water were higher (less exothermic) indicating that the second water is more stable in the molecular form. Adding water (dissociated and molecular form) on Zr4 was unstable, a movement towards Zr3 was observed. The structures with the lowest energy, positions 4, 5, 10, 11 and 12 delivered very similar, almost identical structures after optimization, so that position 12 (Figure 4.45 (III)) with a adsorption energy of -1.345 eV was selected to continue.

The 3rd water was added in several positions on the two remaining Zr atoms without water, Zr2 and Zr4. The addition at Zr4 leads in 4 of 5 tested positions to an ejection of a water molecule from the surface. For structures with water addition on Zr2 only small shifts to optimize H bonds were observed. The energy difference between addition of molecular and dissociated water on Zr2 was very small, position 5 (OH on Zr2 and H on O3, Figure 4.45 (IV)) with -1.241 eV was selected to continue.

Five different structures for the addition of a 4th water were tested, in four of these a molecular water was removed from the surface. The fifth structure formed a bridging H₂O between Zr3 and Zr4 during optimization (Figure 4.45 (VI)), which was not observed for any other calculation. The energy of this structure was higher compared to the very similar energy of the other four structures (the one with the lowest energy is shown in Figure 4.45 (V)), indicating that a 4th water molecule will not rest on the surface. The most interesting structures are shown in Figure 4.45.

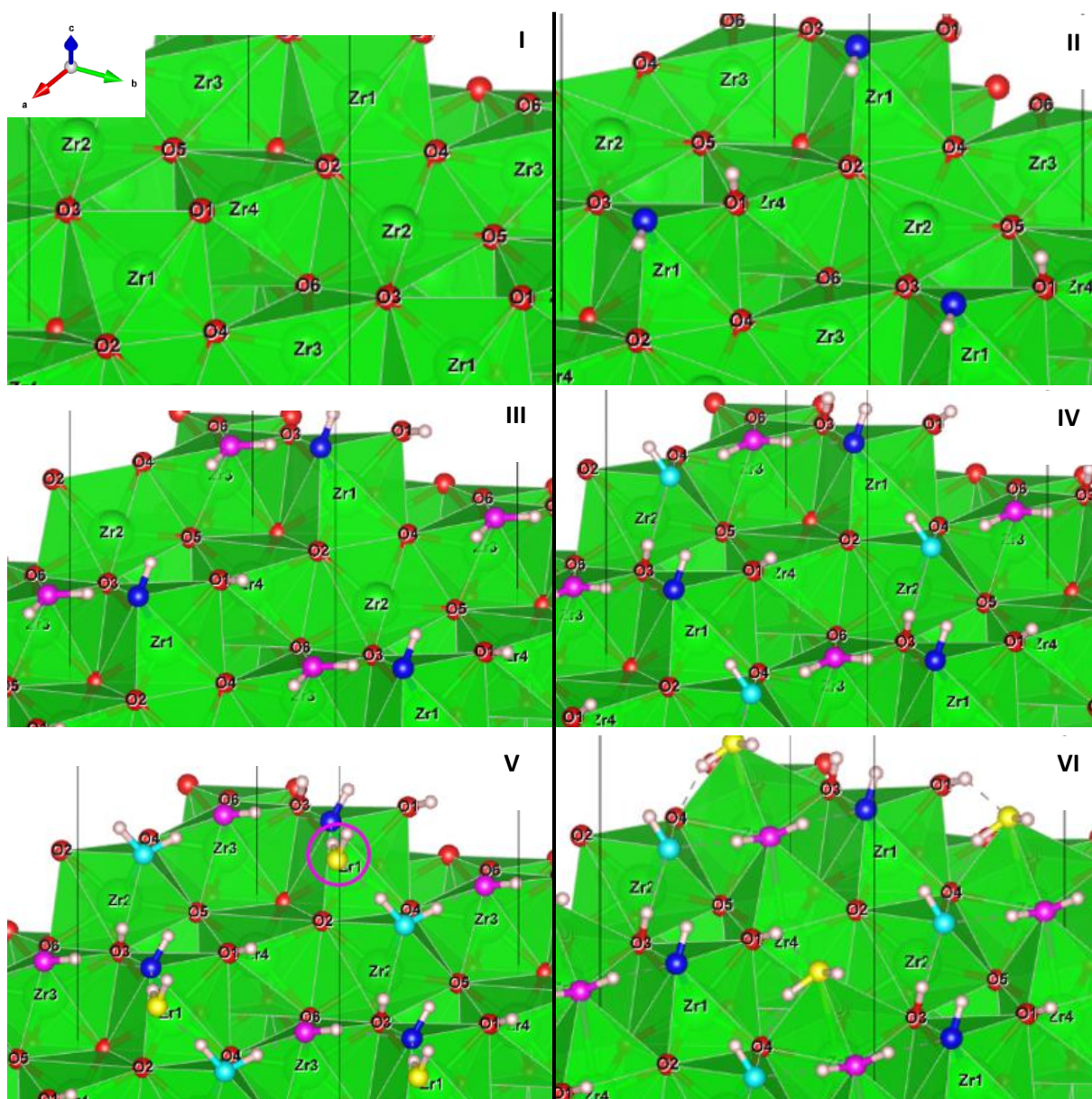


Figure 4.45: optimized monoclinic $(-1\ 1\ 1)$ surface with (I): 0 water molecules, (II): 1 water molecule, (III): 2 water molecules, (IV): 3 water molecules, (V): 4 water molecules (1 ejected from the surface, marked with magenta circle), (VI): 4 water molecules adsorbed on the surface. Color code (for Figure 4.46-4.48): green: Zr atoms and Zr-O polyhedron, red: oxygen atoms from ZrO_2 , white: hydrogen atoms, blue: O atom of 1st water, magenta: O atom of 2nd water, cyan: O atom of 3rd water, yellow: O atom of 4th water.

4.3.5.2 Water adsorption on tetragonal (1 0 1) surface

For the tetragonal (1 0 1) surface the same procedure as for the monoclinic surface was followed. The results are shown in Table 4.18 and Figure 4.46.

Table 4.18: water adsorption energies and positions on the tetragonal (1 0 1) surface.

1 st water		2 nd water	
Position*	E _{ads} [eV]	Position	E _{ads} [eV]
1. Zr1, O2, O3 (m)	-1.561	1. Zr1, O3, O4 (m)	-1.383
2. Zr1, O3, O4 (m)	-1.048	2. Zr2, O3, O4 (m)	-1.403
3. Zr3, O1, O2 (m)	-1.332	3. Zr2, O3, O1 (m)	-1.408
4. Zr3, O2, O3 (m)	-1.683	4. Zr3, O2, O3 (m)	-1.451
5. Zr1O2, O3 (d)	-1.492	5. Zr3, O1, O2 (m)	-1.248
6. Zr1O3, O2 (d)	-1.517	6. Zr1O3, O4 (d)	-1.121
7. Zr1O3, O4 (d)	-1.461	7. Zr1O3, O2 (d)	-1.368
8. Zr3O3, O1 (d)	-1.679	8. Zr1O2, O3 (d)	-1.223
9. Zr3O1, O2 (d)	-1.710	9. Zr2O1, O3 (d)	-1.407
10. Zr3O1, O3 (d)	-1.584	10. Zr2O4, O3 (d)	-1.409
		11. Zr3O1, O2 (d)	-1.383
		12. Zr3O3, O2 (d)	-1.387
3 rd water		4 th water	
Position	E _{ads} [eV]	Position	E _{ads} [eV]
1. Zr1, O2, O3 (m)	-1.469	1. Zr1, O2 (m)	-1.253
2. Zr1, O2, O4 (m)	-1.469	2. Zr2, O4 (m)	-0.542
3. Zr3, O1, O3 (m)	-1.297	3. Zr3, O2 (m)	-1.178
4. Zr3, O2 (m)	-1.291	4. Zr4, O4 (m)	-1.328
5. Zr2, O4 (m)	-1.469	5. Zr3O2, O3 (d)	-1.145
6. Zr1O2, O3 (d)	-1.400	6. Zr3O3, O2 (d)	-1.253
7. Zr1O3, O4 (d)	-1.231	7. Zr1O51, O2 (d)	-1.062
8. Zr3O2, O3 (d)	-1.256	8. Zr4O4, O2 (d)	-1.351
9. Zr3O1, O2 (d)	-1.297	9. Zr2O1, O4 (d)	-1.259
10. Zr2O50, O4 (d)	-1.469		
11. Zr1O3, O2 (d)	-1.337		

*To reach a surface with 4 Zr sites, the original surface was duplicated, so that Zr1 and Zr2 are identical, as well as Zr3 and Zr4. After the addition of the first water molecule, this was repealed due to the shift occurring during the corresponding optimization.

The first water was added as H₂O molecule or as dissociated OH and H on different positions on the surface. The optimization and adsorption energy calculations showed the higher stability of structures, in which the water was added on Zr3 site. Furthermore, a dissociation of molecular H₂O into OH and H was observed in half of the structures with addition of molecular H₂O, as well as a lower energy for the structures with OH and H. The lowest energies were reached for structures 4, 8 and 9, where the optimized structures were almost identical with OH on Zr4, H on O1 and a broken Zr-O bond between Zr4 and O1. Out of these, position 9 (Figure 4.46 (II)) with $E_{\text{ads}} = -1.710$ eV was selected to continue.

The addition of a second water leads to two concurring structures. The structure with the lowest energy was reached by addition of molecular H₂O on the Zr3 site (Figure 4.46 (III)). The optimization of this structure, led only to small shifts of the atoms to optimize H bonds. On the other hand, the positions 2, 3, 9 and 10 delivered a second structure with OH on Zr2, H on O3 (dissociation of H₂O for positions 2 and 3) and a broken Zr-O bond between Zr2 and O3 with an only very slightly higher energy. Since four different starting positions delivered this structure, position 10 (Figure 4.46 (IV)) ($E_{\text{ads}} = -1.409$ eV) was used to continue.

For the addition of the 3rd water several positions on Zr1, Zr2 and Zr3 were tested with molecular and dissociated water. The optimizations of the different structures showed recombination of OH and H to H₂O, indicating that molecular water is more stable and movements of water from Zr2 to Zr1, showing that Zr1 is to best position to add water. The positions 1, 2, 5 and 10 reached the lowest energy and showed very similar structures with a molecular water at Zr1, position 1 (Figure 4.46 (V)) was used to add the next water. The adsorption energy of this structure was -1.469 eV.

Adding a 4th water on the surface led in most cases to the ejection of 1 water molecule from the surface, only 2 structures showed a molecular water on Zr3. If water was added as OH and H, H₂O was rebuild. The lower energy, when water is removed from the surface, indicates that a 4th water molecule will not rest on the surface. One structure with the 4th water on Zr3 and one with H₂O removed from the surface are shown in Figure 4.46 (VI) and Figure 4.46 (VII), respectively.

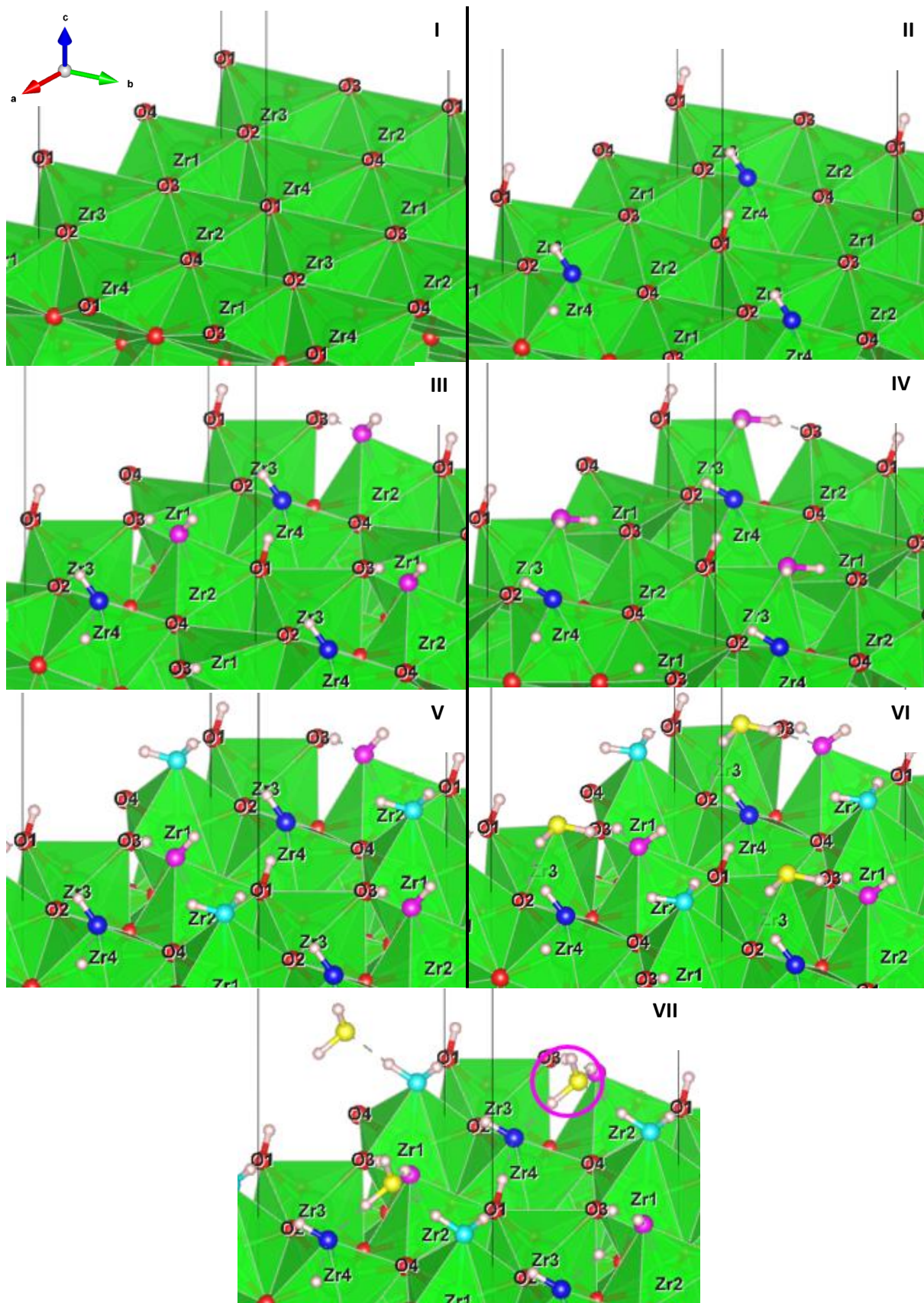


Figure 4.46: optimized tetragonal (1 0 1) surface with (I): 0 water molecules, (II): 1 water molecule, (III)+(IV): 2 water molecules, (V): 3 water molecules, (VI): 4 water molecules adsorbed on the surface, (VII): 4 water molecules (1 ejected from the surface, marked with magenta circle).

4.3.5.3 Water adsorption on amorphous surface

In the case of the amorphous surface, the procedure was less systematic, since the surface was less regular and larger compared to the other solids. Due to the less dense structure, also the intrusion of water into deeper layer may occur. Therefore, only a set of calculations with water addition at different sites of the surface was done, but in contrast to the other solids, it cannot be excluded that important sites for water addition were overseen. The results are shown in Table 4.19 and Figure 4.47.

Table 4.19: water adsorption energies and positions on the amorphous surface.

1 st water		2 nd water	
Position	E _{ads} [eV]	Position	E _{ads} [eV]
1. Zr1, O28, O25 (m)	-1.038	1. Zr1, O65 (m)	-1.444
2. Zr16, O46, O47 (m)	-1.185	2. Zr1, O28, O25 (m)	-1.444
3. Zr31, O47, O19 (m)	-0.488	3. Zr24, O25, O50 (m)	-1.407
4. Zr17, O19, O34, O16, O39 (m)	-0.822	4. Zr16, O65 (m)	-1.268
5. Zr5, O28, O34, O50 (m)	-0.813	5. Zr16, O46, O47 (m)	-1.208
6. Zr24, O25, O50 (m)	-0.968	6. Zr31, O47, O19 (m)	-1.134
7. Zr30, O46 (m)	-0.712	7. Zr17, O19, O34, O16, o39 (m)	-1.409
8. Zr28 (m)	-0.711	8. Zr5, O28, O34, O50 (m)	-1.358
9. Zr1O28, O25 (d)	-1.413	9. Zr30, O46 (m)	-1.631
10. Zr16O47, O46 (d)	-1.922	10. Zr1O25, O65 (d)	-1.442
11. Zr31OQ47, O19 (d)	-0.815	11. Zr24O50, O25 (d)	-1.557
12. Zr17O16O39, O19, O34 (d)	-1.080	12. Zr30O16, O46 (d)	-1.631
13. Zr5O34O28, O50 (d)	-1.402	13. Zr16O47, O46 (d)	-1.188
14. Zr24O50, O25 (d)	-0.597	14. Zr16O46, O47 (d)	-1.045
15. Zr30O16, O46 (d)	-0.882	15. Zr17O16, O34 (d)	-1.505
16. Zr28O16, O54 (d)	-0.712	16. Zr5O28, O34 (d)	-1.407
3 rd water		4 th water	
Position	E _{ads} [eV]	Position	E _{ads} [eV]
1. Zr1, O28, O25, O66 (m)	-1.539	1. Zr24, O6, O25, O50 (m)	-1.461
2. Zr24, O6, O25, O50 (m)	-1.539	2. Zr17, O19, O34, O16, O39 (m)	-1.438
3. Zr17, O19, O34, O16, O39 (m)	-1.417	3. Zr5, O28, O34, O50 (m)	-1.395
4. Zr5, O28, O34, O50 (m)	-1.354	4. Zr13, O50, O54 (m)	-1.444
5. Zr13, O50, O54 (m)	-1.390	5. Zr31, O47, O19 (m)	-1.196
6. Zr31, O47, O19 (m)	-1.322	6. Zr24O6, O25 (d)	-1.428
7. Zr1O66, O28 (d)	-1.632	7. Zr17O16, O34 (d)	-1.517
8. Zr24O6, O25 (d)	-1.609	8. Zr5O28O34, O50 (d)	-1.339
9. Zr17O16, O34 (d)	-1.536	9. Zr13O38, O50 (d)	-1.358
10. Zr5O28O34, O50 (d)	-1.421		
11. Zr13O38, O50 (d)	-1.479		

The adsorption energy of the 1st water was strongly influenced by the selected Zr site and generally the addition of OH and H delivered more stable structures compared to the addition of H₂O. In the most stable structure (Figure 4.47 (II)), H was added on O46 and OH on Zr16, but formed another Zr-O bond with Zr1. The adsorption energy of this structure was -1.922 eV.

The calculations with a 2nd water showed again a strong influence of the selected Zr site, but this time the higher stability for molecular H₂O, but the energy differences between the structures were significantly smaller compared to the 1st water. The lowest energy of -1.631 eV and thus the most stable structure was reached by adding molecular H₂O on Zr30 (Figure 4.47 (III)).

The most stable way to add a 3rd water was reached, when OH was added on Zr1 and H on O28 (Figure 4.47 (IV)), but the energy differences were relatively small for all structures.

Also for the addition of the 4th water molecule, the energy differences were small and the calculations focused on the optimization of the O-Zr-O angles and the H bonds. The most stable structure (Figure 4.47 (V)) was created by addition of OH on Zr17 and H on O34. Due to the larger unit cell and the less dense structure further water molecules could be added in this amorphous structure.

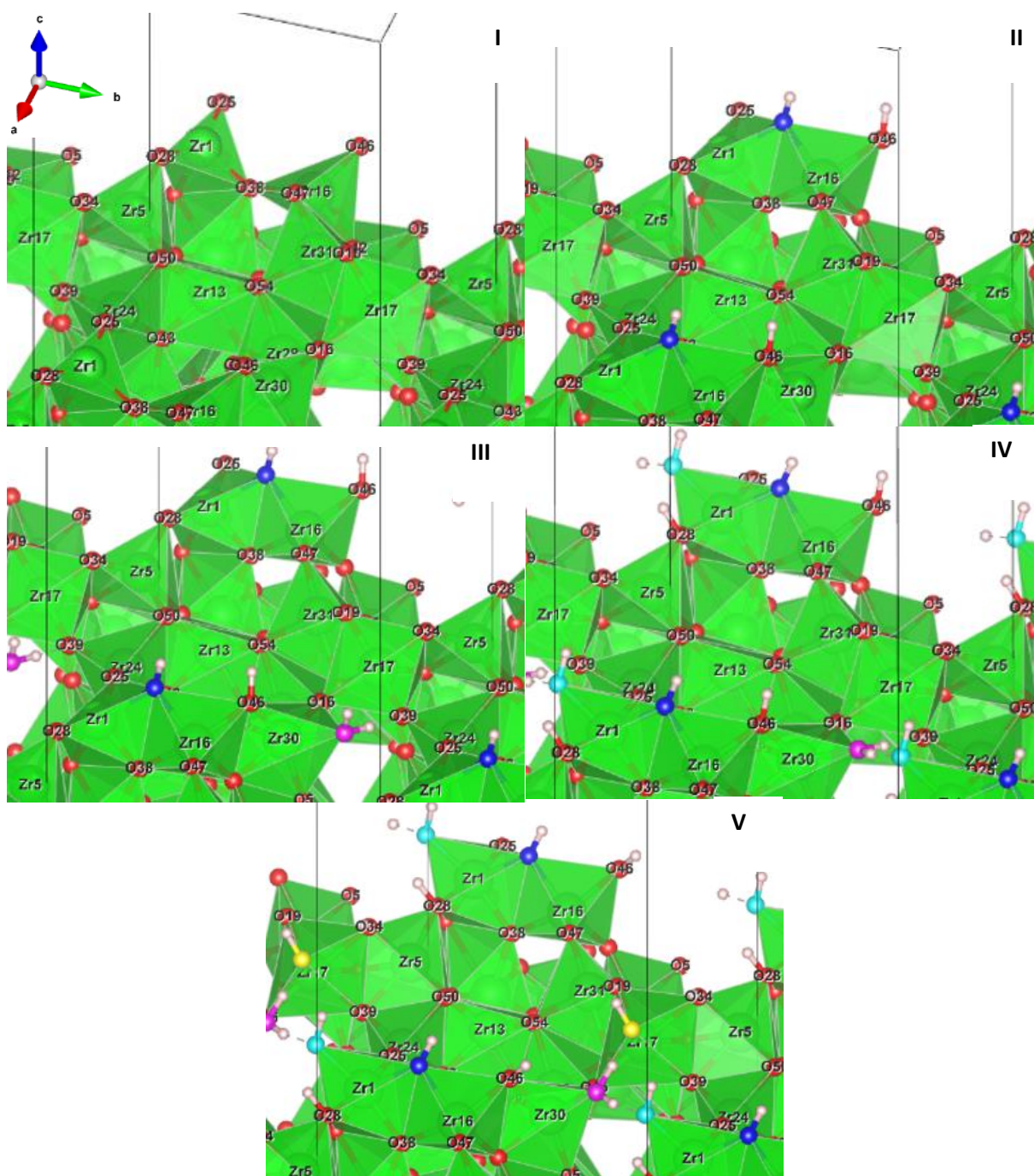


Figure 4.47: optimized amorphous surface with (I): 0 water molecules, (II): 1 water molecule, (III): 2 water molecules, (IV): 3 water molecules, (V): 4 water molecules adsorbed on the surface.

4.3.5.4 Evaluation of the water adsorption calculations

In all three cases only small distortions of the surface are observed. The water adsorption energies show in general the most exothermic values for the addition of a 1st water molecule and less but still exothermic values for the addition of further water molecules. This can be explained by the coverage of the most reactive surface sites with the first water molecules. The comparison between the different surfaces (Figure 4.48), monoclinic (-1 1 1), tetragonal (1 0 1) and amorphous shows the most exothermic adsorption energies for the amorphous surface, followed by the tetragonal and the monoclinic surfaces, meaning a less stable thus more reactive surface, and a higher affinity to water adsorption in the case of amorphous. This agrees well with the experimental observations of a higher water content and higher solubility of amorphous ZrO₂ solids. In this context, it is necessary to mention that the addition of 4 water molecules corresponds already to a surface coverage of $\theta = 1.0$ (4 water on 4 surface Zr atoms) for the monoclinic and tetragonal surfaces, while the coverage of the amorphous surface is difficult to define due to the unordered structure. A comparison with literature values is shown in Table 4.20. The values are in the same range and show the same trends as the literature, but vary from previous values. A reason for this could be the different functionals used for the calculations or also differences in the model structures regarding layer thickness or structure size.

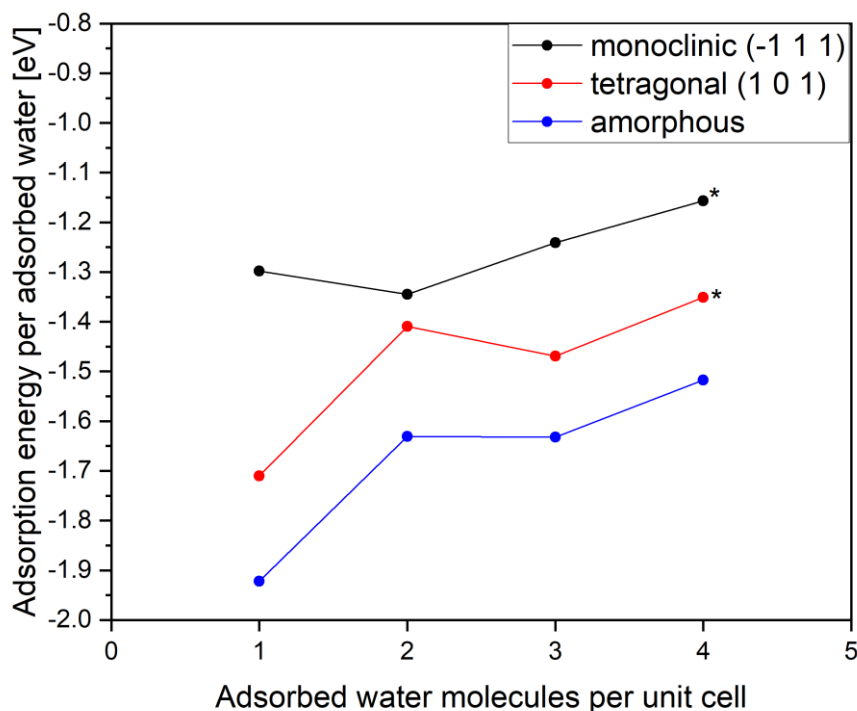


Figure 4.48: water adsorption energies on monoclinic (-1 1 1), tetragonal (1 0 1) and amorphous ZrO₂ surfaces. *marks structures with water that is not adsorbed to a surface Zr atom, but still connected to the surface by H bonds.

Table 4.20: water adsorption energies (eV per adsorbed water molecule) for different surfaces.

	surface	E_{ads} 1 st water	E_{ads} 2 nd water	E_{ads} 3 rd water	E_{ads} 4 th water
Present work	m (-1 1 1)	-1.30	-1.34	-1.24	-1.16
Present work	t (1 0 1)	-1.71	-1.41	-1.47	-1.35
Present work	am*	-1.92	-1.63	-1.63	-1.52
85	m (-1 1 1)	-1.20	-1.05	-0.93	-0.83
86	m (-1 1 1)	-1.10	-1.13	-0.93	-0.85
77	m (-1 1 1)*	-1.63	-1.47	-1.38	-1.51

* the addition of 4 water molecules does not correspond to a full coverage of the surface due to the size of the unit cell.

As well as with the coordination analysis and the calculated surface energy, also with the water adsorption behavior the reactivity of the different surfaces can be estimated. In this case the highest reactivity / affinity to water is expected for the amorphous surface, followed by the tetragonal and finally the monoclinic one.

5. Summary and general discussion

The aim of the present study was to investigate the effects of ageing on amorphous hydrous zirconium oxides. For this purpose amorphous hydrous $\text{ZrO}_2(\text{s})$ was precipitated and several batches were aged for 4 to 18 months at $T = 80^\circ\text{C}$ and $T = 22^\circ\text{C}$ in 0.001 M NaOH, 0.2 M $\text{CaCl}_2\text{-Ca(OH)}_2$ and 0.02 M $\text{CaCl}_2\text{-Ca(OH)}_2$ solutions and afterwards investigated by solid phase characterization methods and solubility experiments with thermodynamic evaluation and supplemented by theoretical calculations. The solid phase characterization with XRD, TEM, electron diffraction, Raman spectroscopy, SAXS, EXAFS and SEM-EDX gives insights on the impact of ageing at elevated temperatures on the crystallinity, particle size and particle growth of the ZrO_2 solid phases. These methods show that the ageing at $T = 80^\circ\text{C}$ induces a transformation from a freshly precipitated amorphous solid towards nano-crystalline solids, accompanied with an increasing particle size and the formation of different types of particles. The solid phase characterization with TG-DTA, XPS and FTIR shows that the ageing at elevated temperatures has also an impact on the water content of the solids. The transformation from amorphous to crystalline solids occurring at $T = 80^\circ\text{C}$ is connected with a reduction of water content and a decreasing $[\text{O}]/[\text{Zr}]$ ratio. XPS analysis shows that the solids are described more accurately as $\text{ZrO}_x(\text{OH})_{4-2x}\cdot n\text{H}_2\text{O}$ and that the transformation process leads to an increase of O^{2-} contribution and a decrease of H_2O , OH^- contribution. The analysis of the specific surface area of several samples by BET shows that the transformation of the solid phases from amorphous to more crystalline phases is also connected with a decrease in surface area, which is in agreement with the observed increase in particle size and the decrease in hydration content. Zeta potential measurements indicate, that the surface of the solids is negatively charged by deprotonated $-\text{OH}$ groups during the ageing in NaOH and positively charged or near neutral in $\text{CaCl}_2\text{-Ca(OH)}_2$. According to these solid phase characterization results, the investigated solids can be divided in several groups with similar solid properties as shown in Figure 5.1.

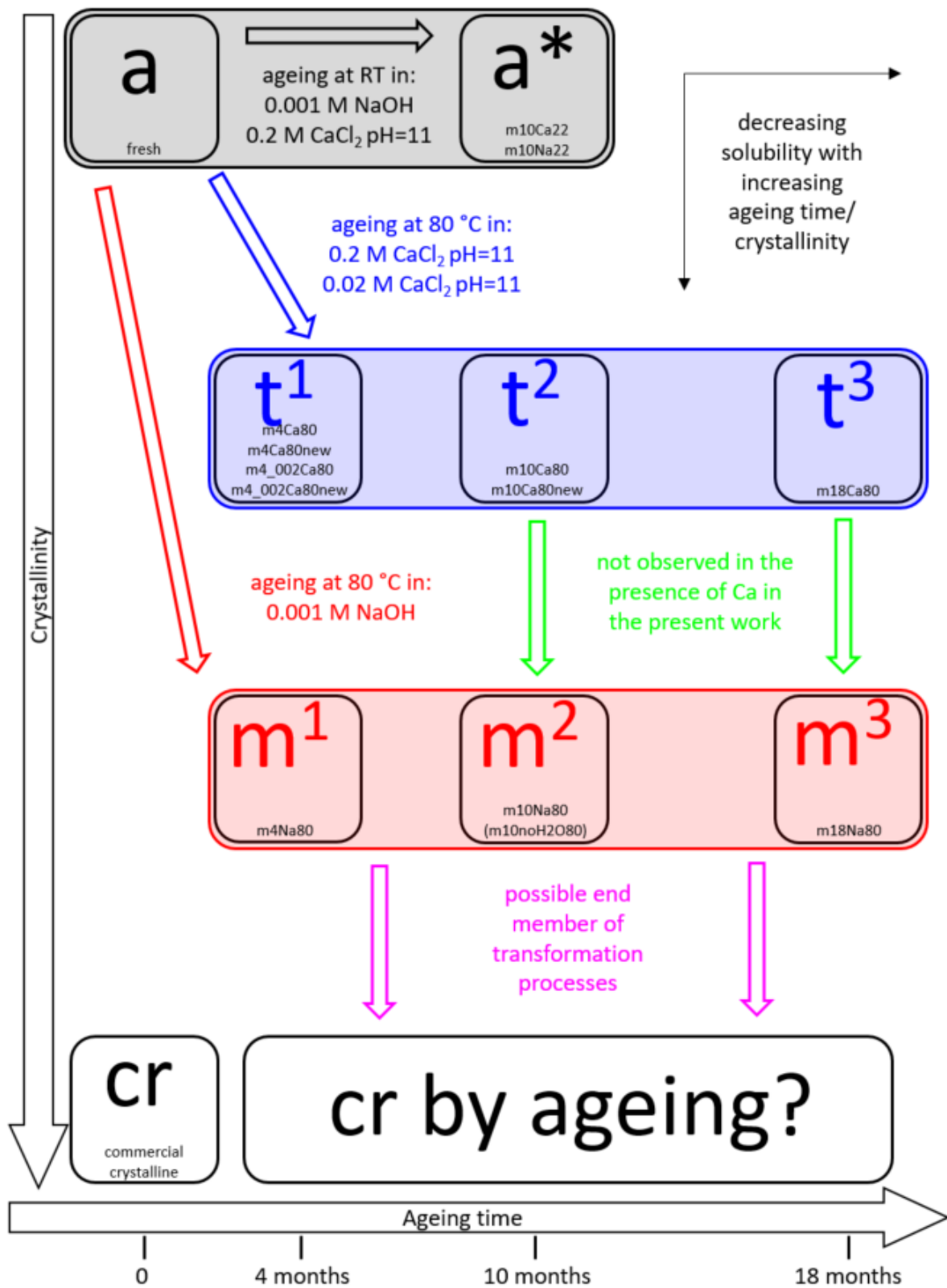


Figure 5.1: Schematic classification of the investigated solid phases according to the solid phase characterization results.

The first group (group a) contains the amorphous solid phases (fresh, m10Ca22, m10Na22) which show similar solid phase characteristics. The absence of reflexes in the diffractograms of these solids confirms their amorphous character. Large aggregates and small primary particles (few nm) are observed with TEM and SAXS measurements. The latter also indicate a rough surface of the particles. TG-DTA determines the hydration water content of the solids to be 2.0-2.1 assuming a stoichiometry of $ZrO_2 \cdot nH_2O$. The measured (BET) or estimated (based on the particle size) surface areas are in the range of $250+ \text{ m}^2\text{g}^{-1}$. Details of group a solid phases are summarized in Figure 5.2.

The ageing at $T = 80^\circ\text{C}$ in 0.2 M and 0.02 M CaCl_2 solutions leads to a transformation into several tetragonal/cubic solid phases,

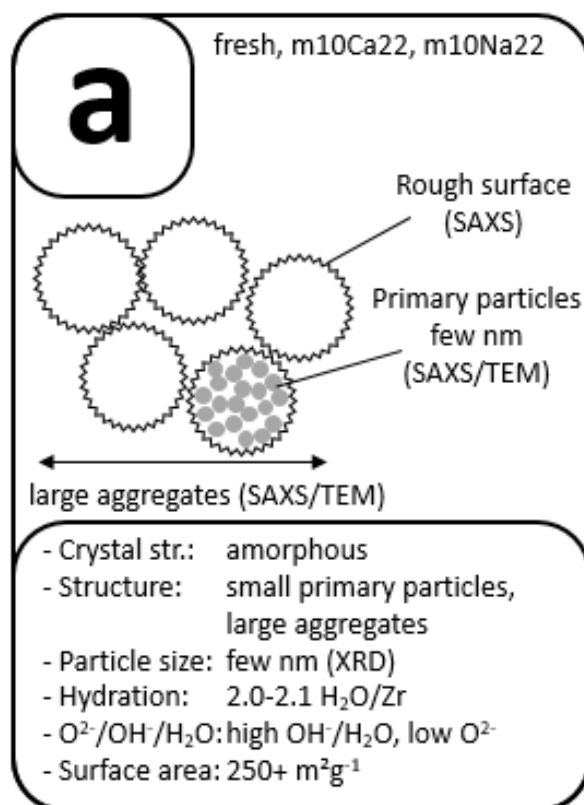


Figure 5.2: Solid phase characterization details of the amorphous solid phases (group a).

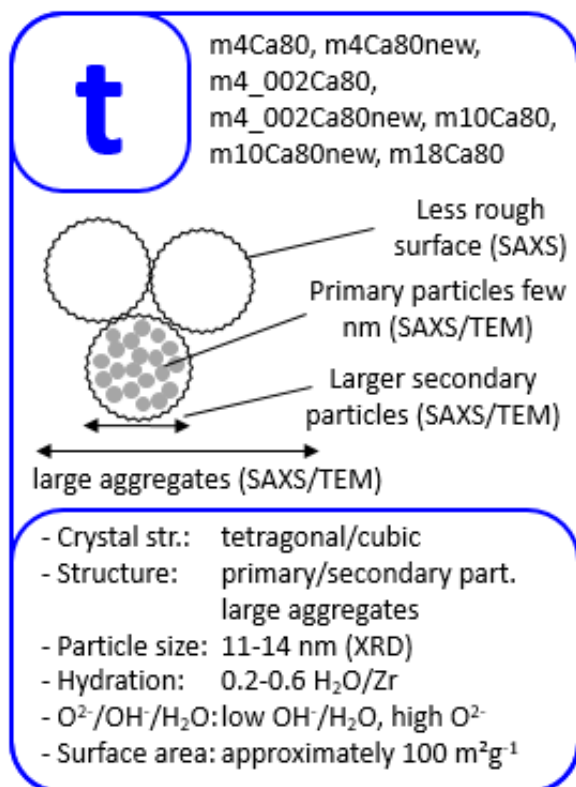


Figure 5.3: Solid phase characterization details of the tetragonal/cubic solid phases (group t).

summarized in group t. In contrast to the amorphous solids, the diffractograms of the solid phases of group t (m4Ca80, m10Ca80, m18Ca80, m4Ca80new, m10Ca80new, m4_002Ca80, and m4_002Ca80new) show broad reflexes agreeing well with either tetragonal or cubic ZrO_2 references. With Scherrer analysis of the reflexes, a particle size (more accurate size of crystal domains) of 11 to 14 nm can be determined. TEM and SAXS show again large aggregates and small primary particles, but additionally larger secondary particles and a less rough surface compared to the amorphous solids. The water contents determined by TG-DTA are between 0.2 and 0.6 water molecules and thus significantly lower as for group a solids. The estimated surface area is with approximately $100 \text{ m}^2\text{g}^{-1}$ also lower. The

m4Ca80 solid phase is in this context special, since it shows a water content of 1.2 water molecules and a surface area of $199 \text{ m}^2\text{g}^{-1}$. This behavior can hypothetically be explained by the simultaneous presence of a tetragonal/cubic and an amorphous phase in this sample, caused by incomplete solid phase transformation. Details of group t solid phases are summarized in Figure 5.3.

The ageing at $T = 80^\circ\text{C}$ in 0.001 M NaOH solutions or without liquid phase leads to a transformation into monoclinic solid phases, summarized in group m. The diffractograms of this group of solid phases (m4Ca80, m10Ca80, m18Ca80, m10noH2O80) show broad reflexes in contrast to the amorphous samples. Most of the reflexes agree well with references of monoclinic ZrO_2 . Additionally, the most intense reflexes of tetragonal/cubic ZrO_2 are also observed in these samples, but less pronounced as the reflexes corresponding to monoclinic ZrO_2 . Applying Scherrer analysis, delivered particle sizes of 23 to 27 nm corresponding to the monoclinic reflexes and approximately 12 nm belonging to the cubic/tetragonal reflexes. These results indicate, that the group m samples are not pure monoclinic ZrO_2 , but contain smaller contributions of tetragonal/cubic ZrO_2 . As for the group t solids, TEM and SAXS show small primary particles and larger secondary particles. Additionally large rods up to a length of 300 nm are visible on the TEM images of the samples and SAXS measurements indicate a rather smooth surface. A water content of 0.3 molecules is determined by TG-DTA and the measured surface area of $37 \text{ m}^2\text{g}^{-1}$ (m10noH2O80) agrees well with the estimated value of approximately $40 \text{ m}^2\text{g}^{-1}$. Details of group m solid phases are summarized in Figure 5.4.

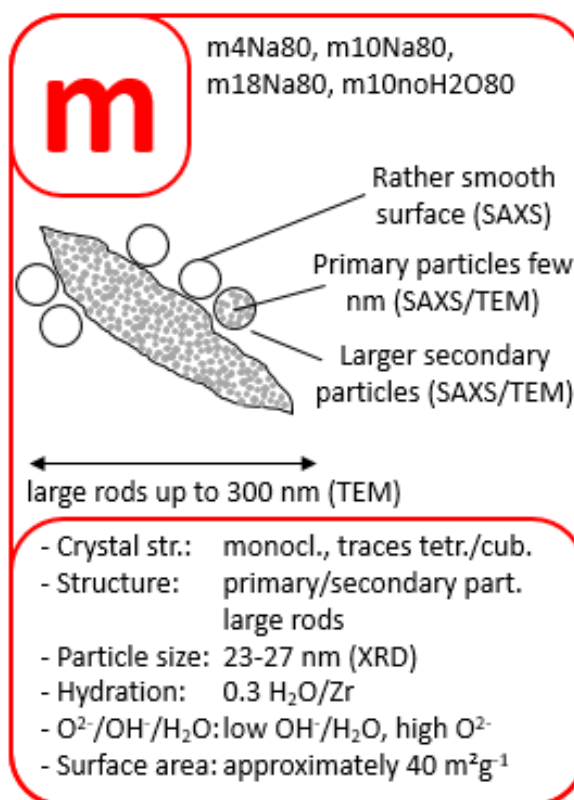


Figure 5.4: Solid phase characterization details of the monoclinic solid phases (group m).

As for the group t solids, TEM and SAXS show small primary particles and larger secondary particles. Additionally large rods up to a length of 300 nm are visible on the TEM images of the samples and SAXS measurements indicate a rather smooth surface. A water content of 0.3 molecules is determined by TG-DTA and the measured surface area of $37 \text{ m}^2\text{g}^{-1}$ (m10noH2O80) agrees well with the estimated value of approximately $40 \text{ m}^2\text{g}^{-1}$. Details of group m solid phases are summarized in Figure 5.4.

Finally, the commercial crystalline ZrO_2 which was used as reference material builds its own group cr. The diffractogram shows pure monoclinic ZrO_2 . The reflexes are also broad, what is explainable by the particle size of 26 nm determined with Scherrer analysis. TEM images show homogenous spherical particles with approximately the size evaluated from XRD. SAXS measurements indicate also for this sample the presence of smaller primary particles and show a smooth surface. The weight loss observed by TG-DTA was very small and corresponds to only 0.1 water molecule. The measured surface area of $24 \text{ m}^2\text{g}^{-1}$ is in the same order of

magnitude as the expected value of approximately $40 \text{ m}^2\text{g}^{-1}$. Following the observations for the aged solids, a however slightly different crystalline solid phase is expected to be present after sufficient ageing. The details of the commercial crystalline solid phase and the expected properties of an aged completely crystalline solid are summarized in Figure 5.5.

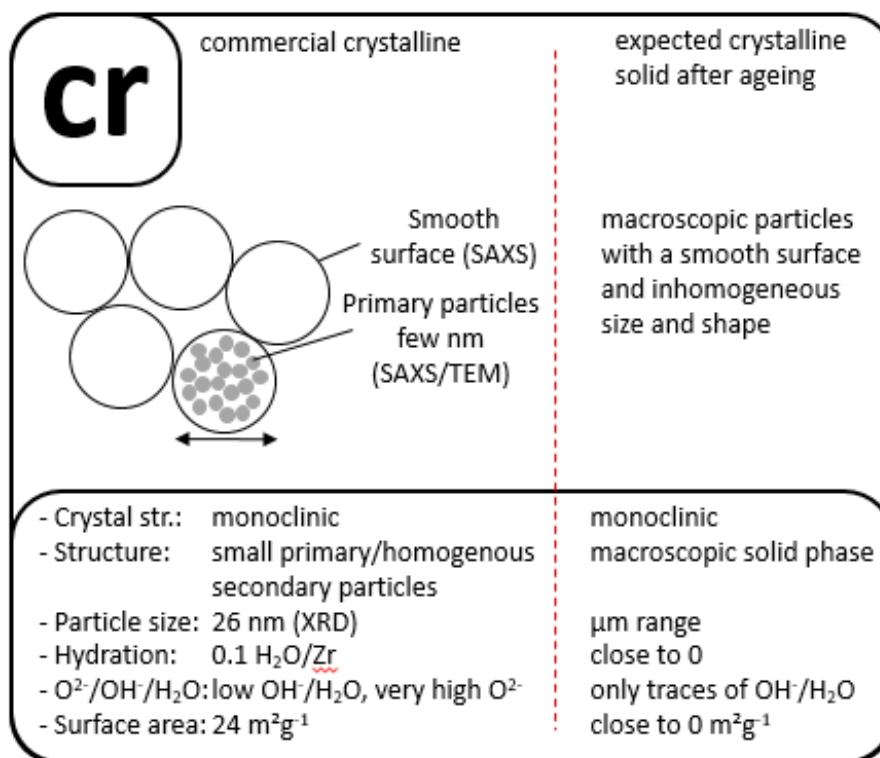


Figure 5.5: Solid phase characterization details of the commercial crystalline solid phase and the crystalline solid phases expected by ageing (group cr).

Summarizing these changes in solid phase properties: ageing of fresh, amorphous, hydrous $\text{ZrO}_2(\text{s})$ at 80°C induces a solid phase transformation process, which can be explained best by condensation reactions at the particle surfaces. Starting with small amorphous particles, the condensation reaction of two surface OH groups ($\text{Zr-OH} + \text{HO-Zr} \rightarrow \text{Zr-O-Zr} + \text{H}_2\text{O}$) leads to decreasing amount of water, decreasing surface area and increasing particle size as observed with TG-DTA, BET and XRD. Up to a certain particle size (9 nm according to ¹⁴, 3 nm according to ¹⁵) the amorphous phase remains stable, larger particles transform to cubic/tetragonal solid phases. For samples aged in CaCl_2 media the transformation stops at this point, probably due to incorporation of Ca and thus stabilization of the tetragonal phase ^{9,12,13}. In the case of samples aged in NaOH media, the particle increase continues and at a size of 48 nm ^{14,15} the solid transforms into the thermodynamically most stable monoclinic crystal structure, so that in these samples both the tetragonal and the monoclinic phase are present. With further ageing the complete transformation from remaining amorphous and tetragonal contributions in the solid phases towards the monoclinic structure as well as a further particle increase up to macroscopic scale are expected.

In contrast to solid phase characterization, where only changes in the solid properties were observable for solid phases equilibrated at $T = 80^\circ\text{C}$, but not for solid phases equilibrated at $T = 22^\circ\text{C}$ and also no effects of ageing time are visible, the solubility experiments show different behaviors for aged samples at both $T = 80^\circ\text{C}$ and $T = 22^\circ\text{C}$ as well as a decreasing solubility with increasing ageing time. The highest solubility, with a solubility constant of $\log^* K_{s,0}^\circ = -4.36 \pm 0.58$, is observed for the freshly precipitated amorphous hydrous $\text{ZrO}_2(\text{s})$. Even if the solid phases aged at 22°C , m10Ca22 and m10Na22, do not show any differences within the conducted solid phase characterization, their solubility constants of $\log^* K_{s,0}^\circ = -4.92 \pm 0.32$ and -4.68 ± 0.33 respectively, show a lower solubility, indicating that the transformation process occurring at 80°C also starts or takes place to a lesser extent at 22°C , but has not yet an observable effect on the solid phases. Therefore the amorphous solids of the group a are divided into a and a* as shown in Figure 5.1. Out of group t, the tetragonal/cubic solid phases aged at 80°C in CaCl_2 media, the m4Ca80 solid shows the highest solubility with a solubility constant of $\log^* K_{s,0}^\circ = -4.92 \pm 0.56$, indicating still the presence of amorphous contribution in this sample. For the other samples of this group solubility constants between -6.21 and -6.76 were determined although the determination of solubility products was more difficult since only a few data were above the detection limit. In the case of the monoclinic solids the sample with the shortest ageing time, m4Na80 shows higher solubility compared to the other samples, m10Na80, m18Na80, m10noH2O80 as well as the commercial crystalline ZrO_2 for which most data were below the detecting limit, indicating a very low solubility. These solubility results show that there are several factors that largely effect the solubility of a solid phase. The crystallinity of the solid phase plays a key role, the more crystalline the solid phase is, the lower is the solubility. The crystal structure is important since the different structures also show different solubility products. The tetragonal/cubic solids show a higher solubility compared to the monoclinic ones, but are still much lower compared to amorphous solids. This may be explained by the thermodynamically higher stability of monoclinic ZrO_2 , requiring more energy to dissolve the solid or by the different surface energetics as shown in DFT calculations. Another very important parameter effecting the solubility is the particle size or more precise the surface area. A lower particle size and thus higher surface area leads (as explained by the Schindler equation) to a higher reactivity and consequently a higher solubility, since solubility processes take mostly place in the surface layers of solid phases. Note that the collected data point to a lower surface energy as estimated with the Schindler equation. Therefore, the observed effect of particle size is also smaller compared to the expected effect. Since there are still solid phases with the same crystal structure and particle size showing significantly different solubility products, further surface properties, which are not observed in the present work, have also effects on the solubility.

6. Conclusion and perspectives

The ageing of freshly precipitated $\text{ZrO}_2(\text{am, hyd, fresh})$ at elevated temperatures and room temperature was systematically investigated with respect to changes in the solid phases and solubility. Ageing at $T = 22^\circ\text{C}$ leads to a decrease in solubility of $\text{ZrO}_2(\text{s})$ compared to the fresh solid, although no differences could be observed by solid phase characterization. This is also a starting point for further studies. Since the solid phase characterization methods in the present study focus more on the bulk solid characterization, it may be an option to study the surfaces of amorphous solids more extensively for example by contact angle measurements, calorimetric experiments or further theoretical calculations in order to explain the solubility decrease.

The ageing at $T = 80^\circ\text{C}$ leads to changes in solid phase properties and solubility. This behavior suggests that the elevated temperature is sufficient to overcome the kinetic hindrance and starts a solid phase transformation process from amorphous over cubic/tetragonal to monoclinic ZrO_2 , which is the thermodynamically most stable structure. The process is accompanied by increasing particle size, decreasing water content, decreasing surface area and decreasing solubility. However, samples aged in the presence of Ca form the cubic/tetragonal phase, their solubility remains higher and their particle sizes remain smaller compared to ageing without Ca (in NaOH), where the samples form the monoclinic phase with only small contributions of cubic/ tetragonal ZrO_2 . As reasons for the different crystal structures of these aged samples, among others the incorporation of Ca in the solid^{9,12,13} and thus the stabilization of cubic/tetragonal solid phase or effects of particle size/surface area leading to energy crossovers^{14,15} for small particles and also to the stabilization of the cubic/tetragonal solid phase are discussed. Since it is not completely determinable, if it is an effect of Ca incorporation, of particle size or of both, and since the way of Ca incorporation (presence in EDX) remains ill-defined, the formation of the different crystal structures in presence or absence of Ca could be a good starting point for future studies to investigate the effects of Ca during the ageing more systematically.

Besides the ageing temperature also the ageing time was investigated. With respect to solid phase characterization the ageing time seems to have only minor effects. Already after 4 months of ageing, the solid phases show the almost the same particle size, hydration amount and solid composition as after 10 or 18 months of ageing in the same background electrolyte. Therefore, samples with shorter ageing times in the range of days to months may also be investigated in future studies. On the other hand, the ageing time has a larger influence on the solubility of the samples. In this context, the samples aged for 4 months show significantly higher solubility compared longer aged samples. A difference in solubility between samples aged for 10 or 18 months was not observable, since most results of these solubility samples

were close to or below the detection limit of ICP-MS. In order to investigate, if the solubility still decreases with time for ageing times of more than 10 months, either a higher solubility or a determination of lower Zr(IV) concentrations is required. Therefore, different background electrolyte systems with higher solubility or other techniques with lower detection limits for the determination of Zr(IV) concentrations, could be used in future studies on zirconium solubility.

The combination of comprehensive solid phase characterization with a multimethod approach and manifold solubility experiments of solid phases systematically aged at elevated temperatures represents a relevant contribution to the thermodynamic description of Zr(IV) in alkaline aqueous systems. Since it is shown that solubility behavior is not always matching to solid phase properties, the surface properties of the solid phases are assumed to play a key role in solubility phenomena. Including surface properties into the thermodynamic description of aqueous systems of solid phases is therefore an important idea that could be considered for the future. In that sense, studies focusing even more on surface properties and their effect on solubility may be interesting.

The DFT calculations performed within this work showed interesting insights in the surface structures of the different crystal phases and their hydration behavior, despite the very limited time dedicated to the calculations. With future studies focusing only on DFT calculations, more details like other surfaces except the most stable ones, surface defects, the influence of dopants or complete surface hydration could be investigated and possibly improve the understanding of surface processes in solubility.

Appendix

A.1 Zr-⁹⁵Zr exchange experiments

For crystalline ZrO₂ solids, it was previously shown by means of isotope exchange experiments that the exchange kinetics are very slow. Only a few monolayers of the solids surface are involved in the solid/solution exchange, and thus equilibria between bulk solids and solutions cannot be reached⁷⁸. In order to assess also the exchange behavior of the fresh and aged ZrO₂ solids with Zr in solution, isotope exchange experiments with ⁹⁵Zr ($t_{1/2}$ = 64 d) were conducted. For this purpose, selected solubility samples (see 3.5.1) were spiked with a ⁹⁵Zr solution after enough solubility data were obtained. Aliquots of the liquid phases of the samples were then analyzed by γ -counting in several time intervals, to determine the activity of ⁹⁵Zr still present in the solution or exchanged into the solid phase. As samples for the isotope exchange experiments, solubility samples of the freshly precipitated solid (in 0.5 M NaCl-NaOH and 0.2 M CaCl₂-Ca(OH)₂, 4 pHs each) and the solids aged for 4 months at T = 80°C either in 0.001 M NaOH (m4Na80, solubility samples in 0.5 M NaCl-NaOH, 4 pHs) or in 0.2 M CaCl₂ (m4Ca80, solubility samples in 0.2 M CaCl₂-Ca(OH)₂, 4 pHs) were selected. Each of these samples was spiked with 20 μ l of a ⁹⁵Zr solution (5 μ l of ⁹⁵Zr stock solution, 10 μ l MilliQ and 5 μ l NaOH to neutralize the stock solution) containing 7.4 kBq of ⁹⁵Zr per sample. This amount of spiking solution was selected to firstly have a measurable amount of ⁹⁵Zr before and after exchange and secondly to not affect the solid/solution equilibrium by adding a too large amount of Zr to the solution (spiked [⁹⁵Zr] 2-3 orders of magnitude lower compared to measured solubility). After several days of equilibration aliquots of the samples were taken and analyzed by γ -counting after a phase separation step (ultrafiltration or ultracentrifugation). The measured activity in the solutions was even for blank samples (background electrolyte spiked with ⁹⁵Zr, without solid phase) much lower than expected, suggesting that no or almost no ⁹⁵Zr was left in solution. For most samples more than 99.9% of ⁹⁵Zr was lost, so that the remaining activity in solution was not determinable. For the blank samples with the highest solubility limit (0.5 M NaCl-NaOH, pH 13 and 13.4) up to 10% of activity remained in solution, for the samples with the highest solubility up to 2%. A quantitative evaluation is therefore difficult. Comparing the few samples with measurable activity, shows qualitatively lower remaining activities for the amorphous samples (comparison of fresh and m4Na80 in 0.5 M NaCl-NaOH, pH 13.4, and fresh and m4Ca80 in 0.2 M CaCl₂-Ca(OH)₂, pH 12) indicating a qualitatively higher exchange for these solids. The most reasonable cause for the low amount of remaining activity was the subsequently determined presence of inactive Zr carrier in the ⁹⁵Zr stock solution. The high concentration of the carrier exceeded the solubility limit for most samples by several orders of magnitude and probably led to an immediate precipitation of almost the complete amount of ⁹⁵Zr which was spiked.

A.2 TG-DTA data

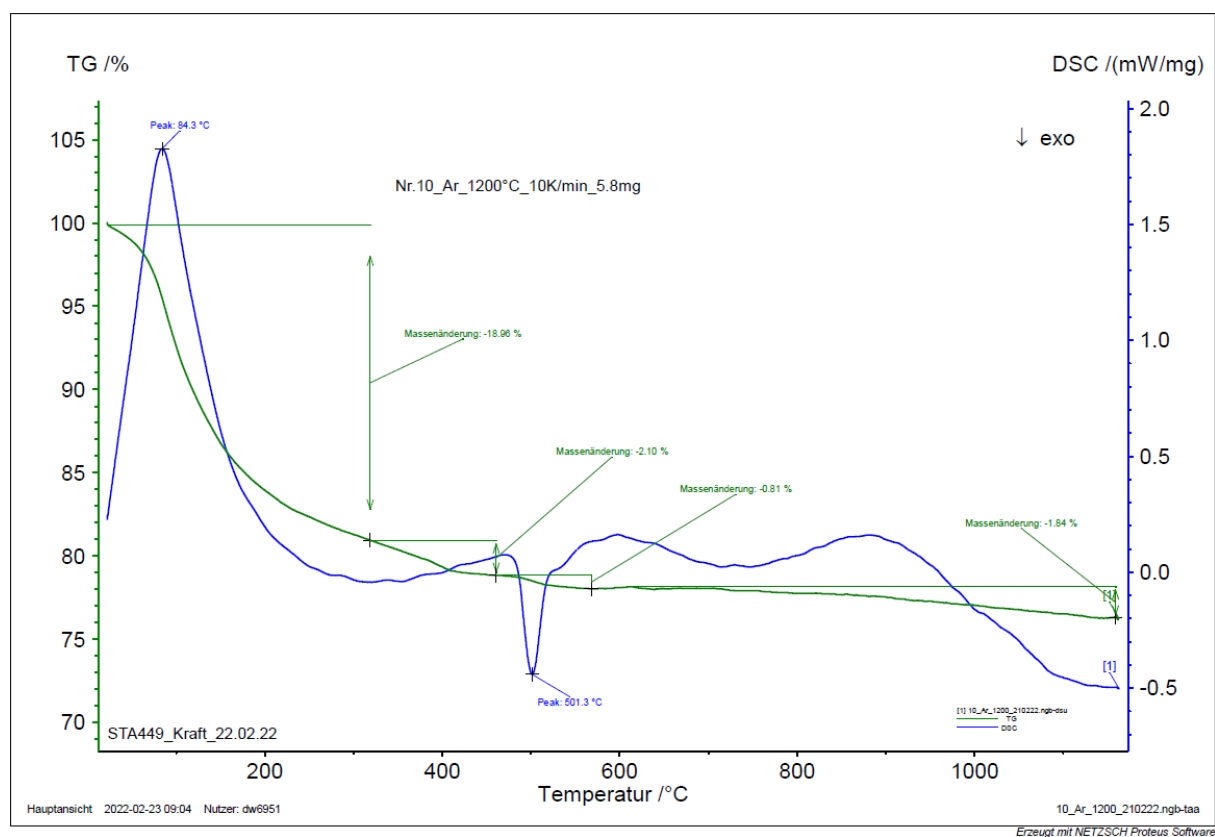
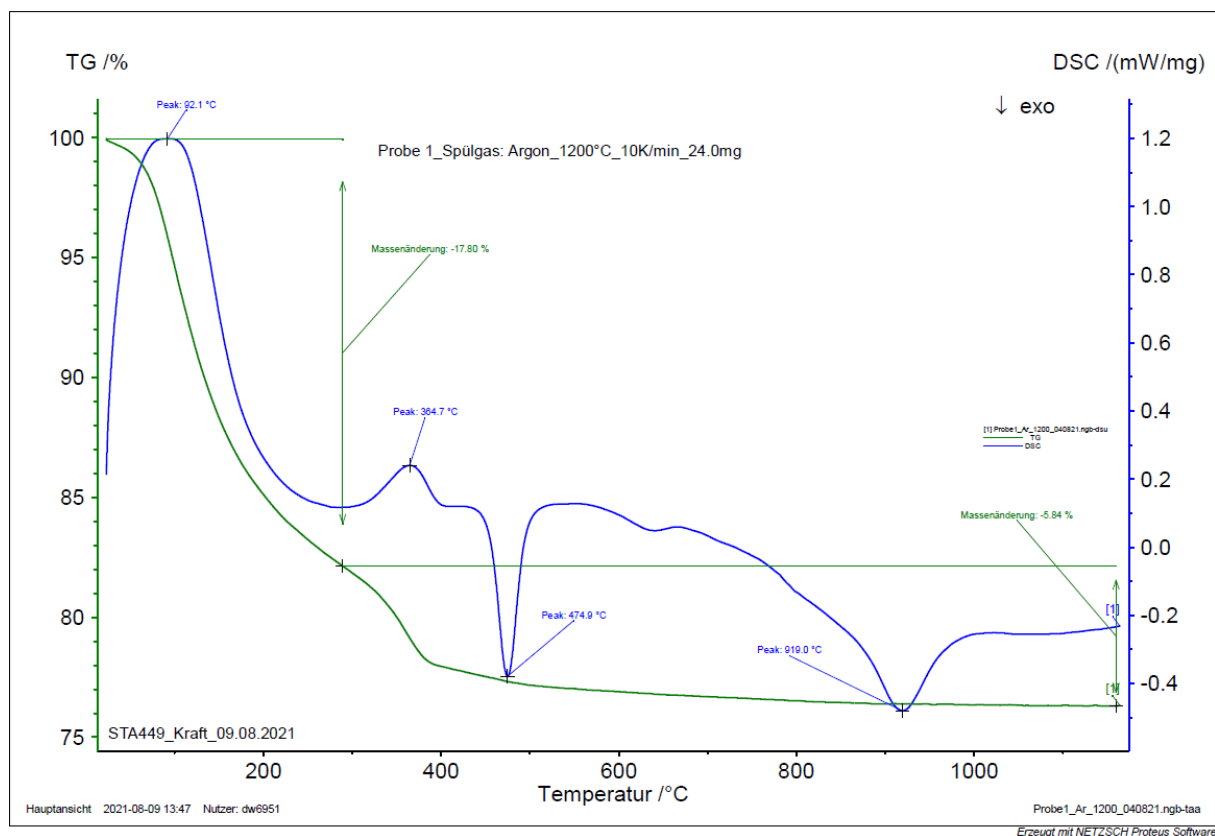


Figure A.1: TG-DTA results of the fresh (above) and m10Ca22 (below) $ZrO_2(s)$ solid phases.

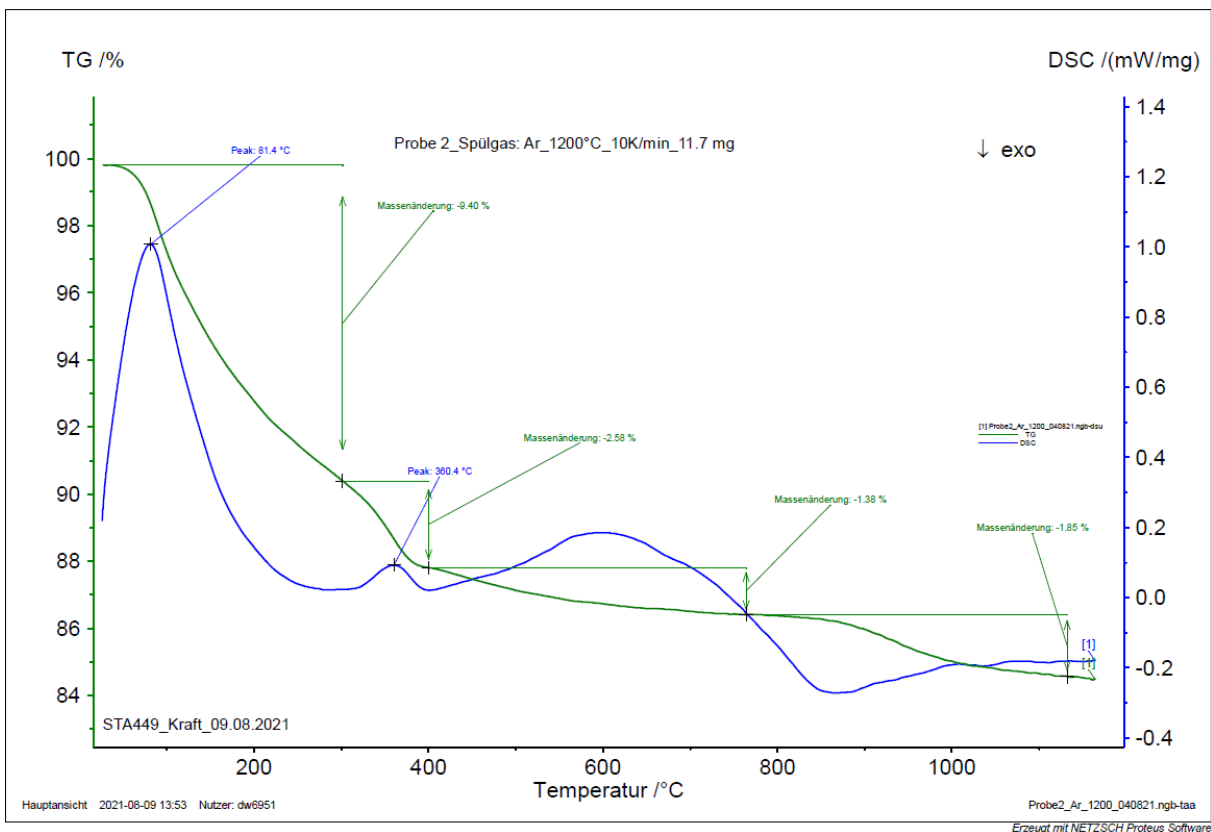
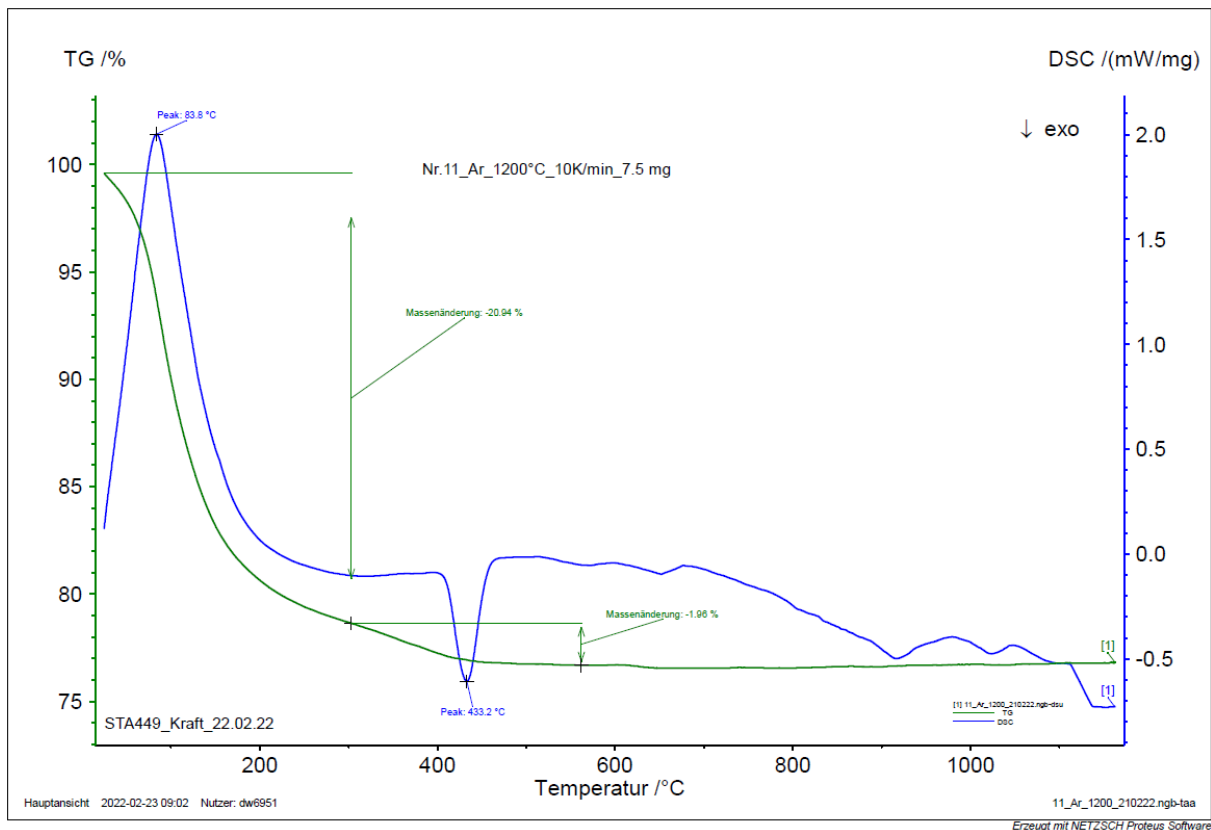


Figure A.2: TG-DTA results of the m10Na22 (above) and m4Ca80 (below) ZrO₂(s) solid phases.

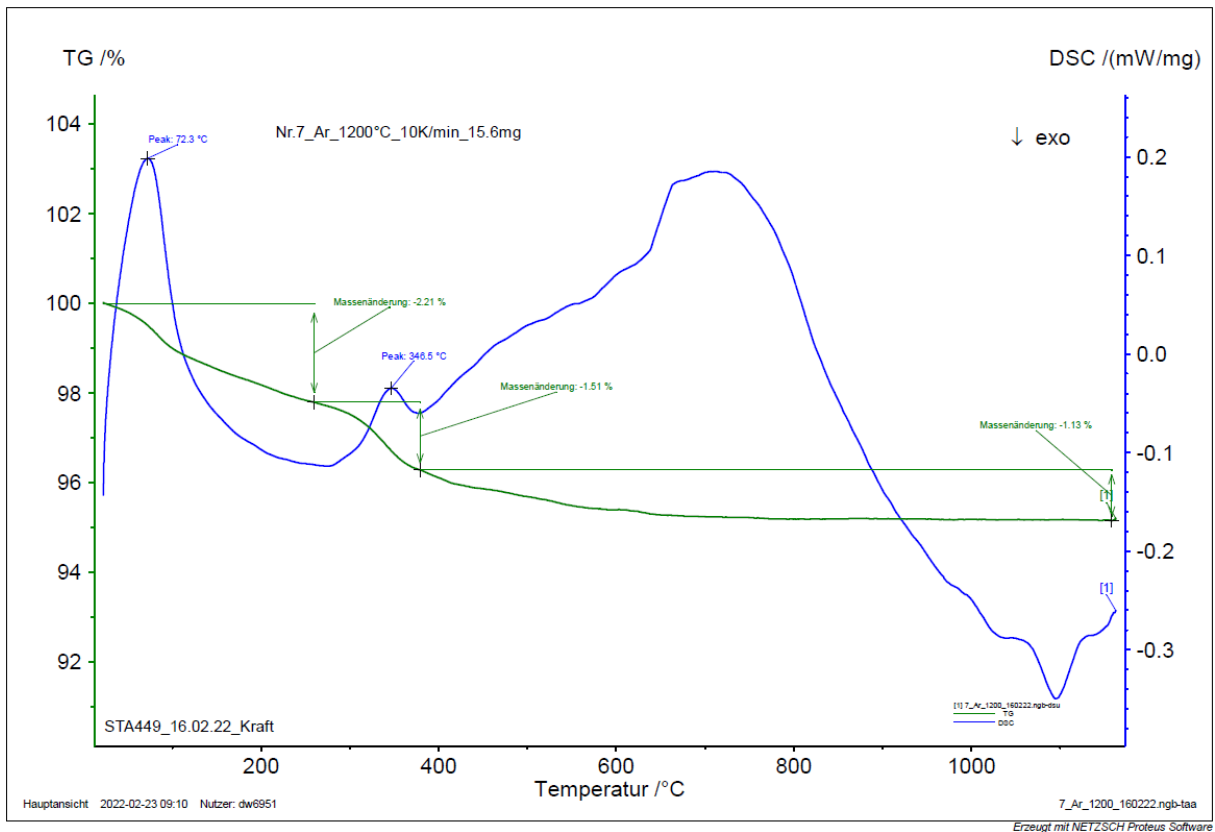
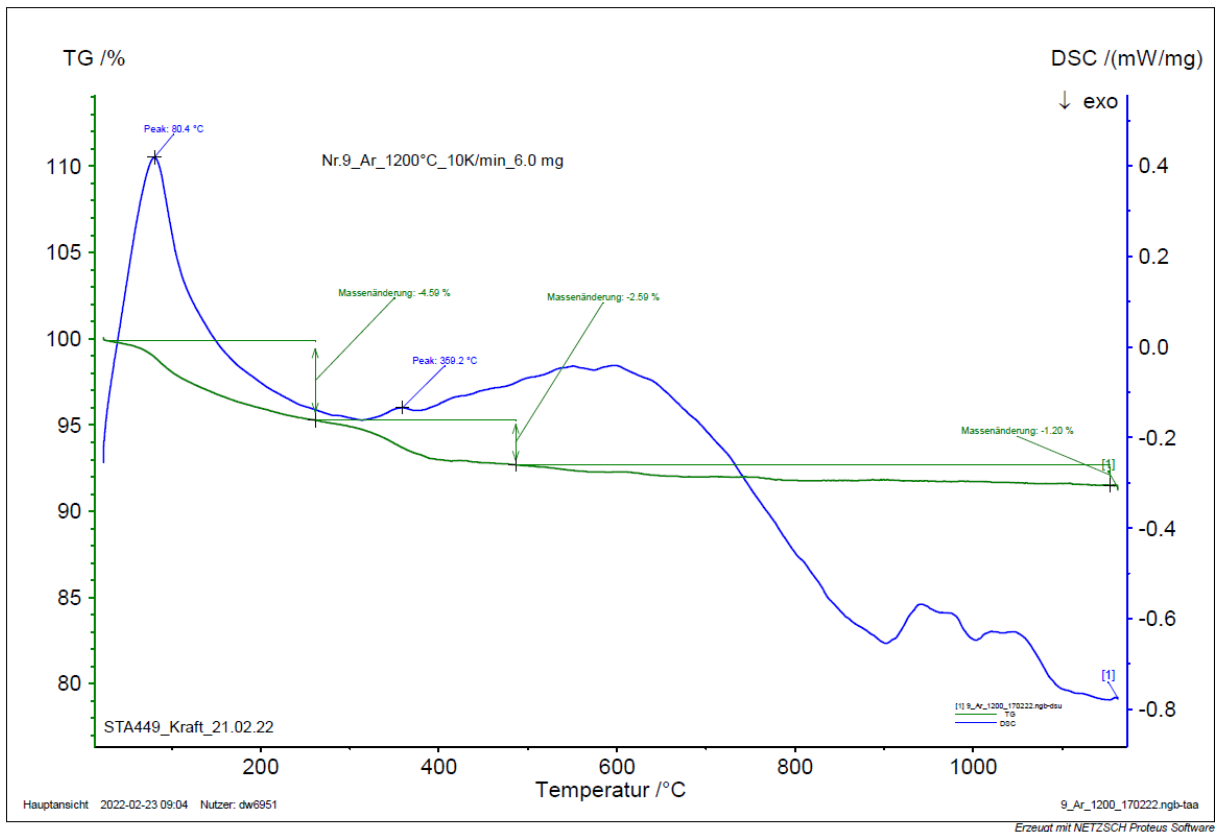


Figure A.3: TG-DTA results of the m4Ca80new (above) and m4_002Ca80 (below) ZrO₂(s) solid phases.

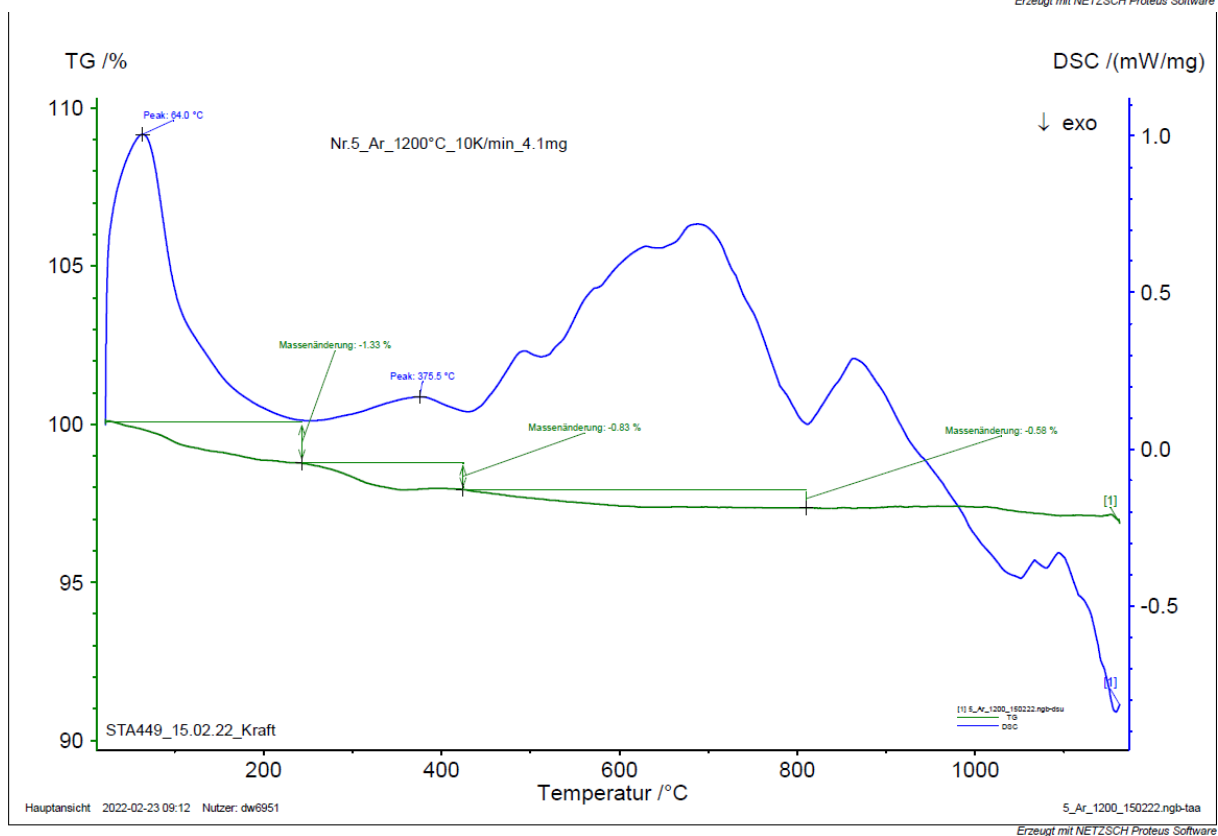
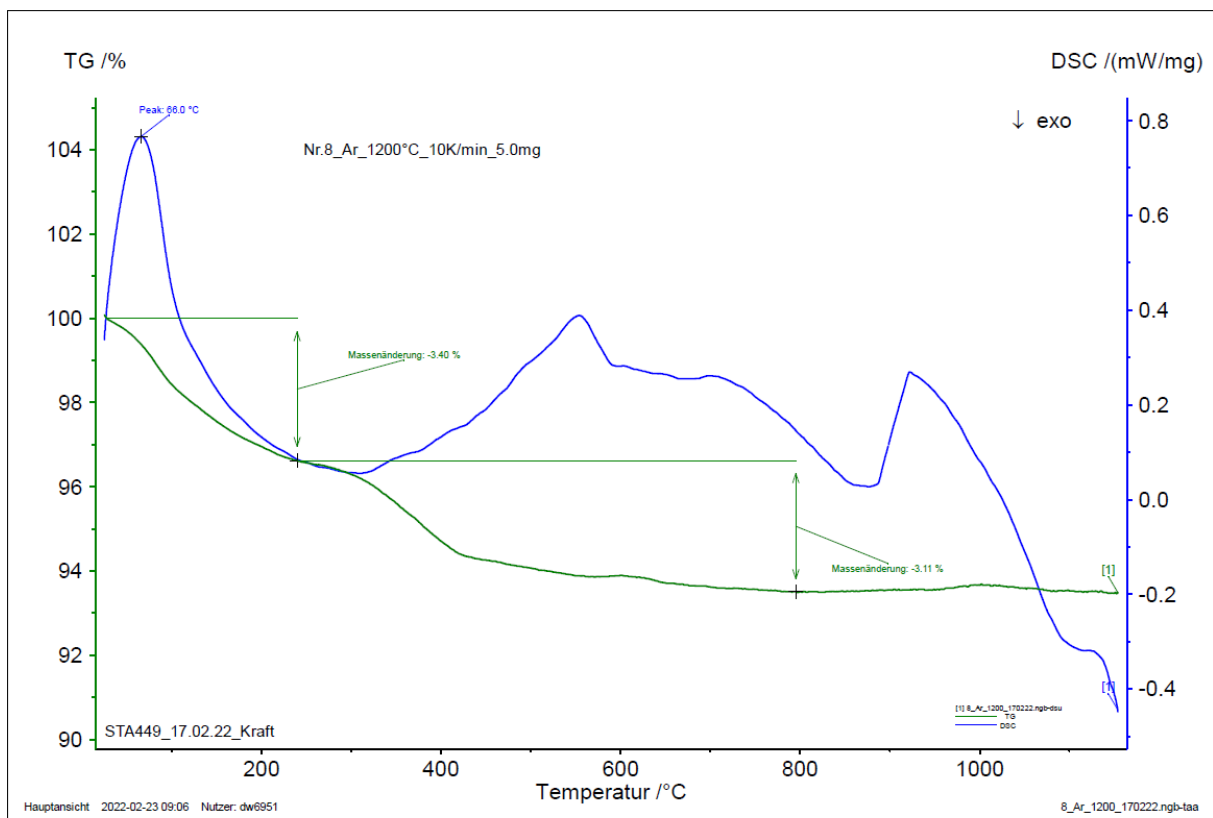


Figure A.4: TG-DTA results of the m4_002Ca80new (above) and m10Ca80 (below) ZrO₂(s) solid phases.

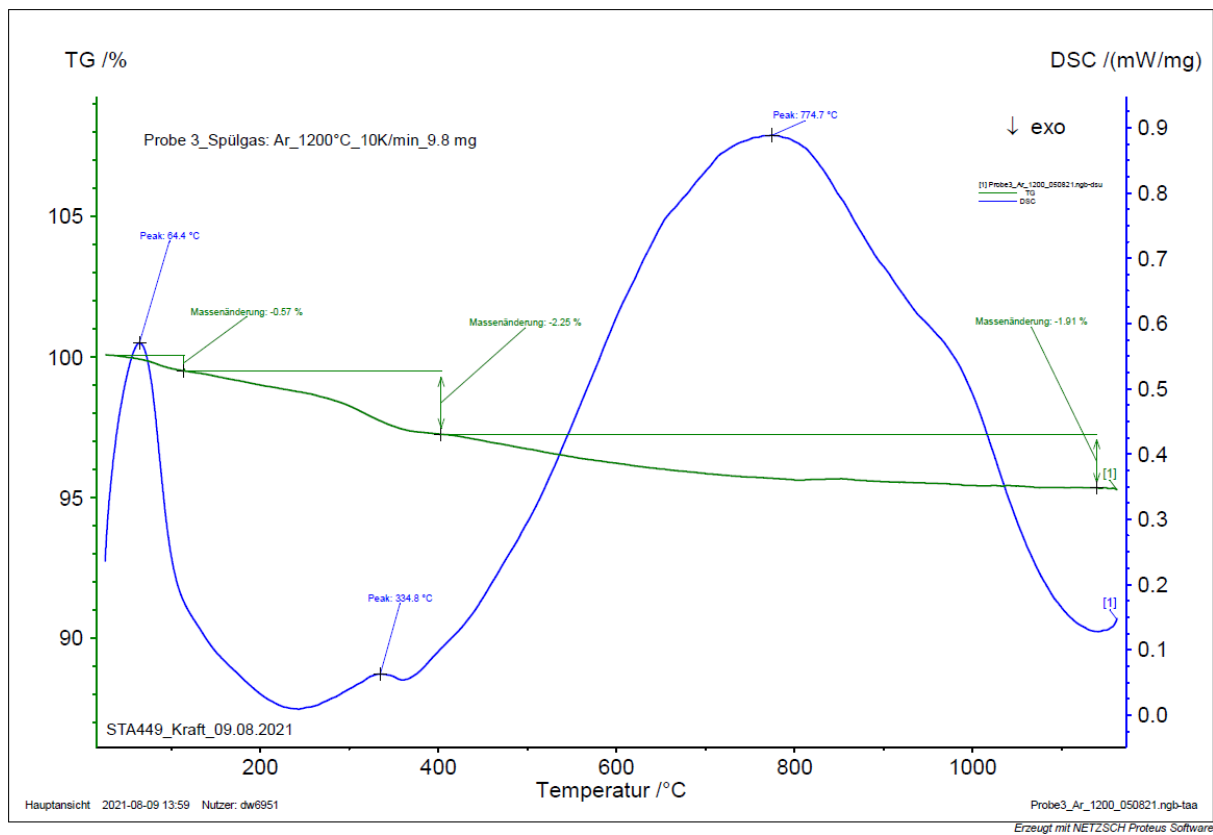
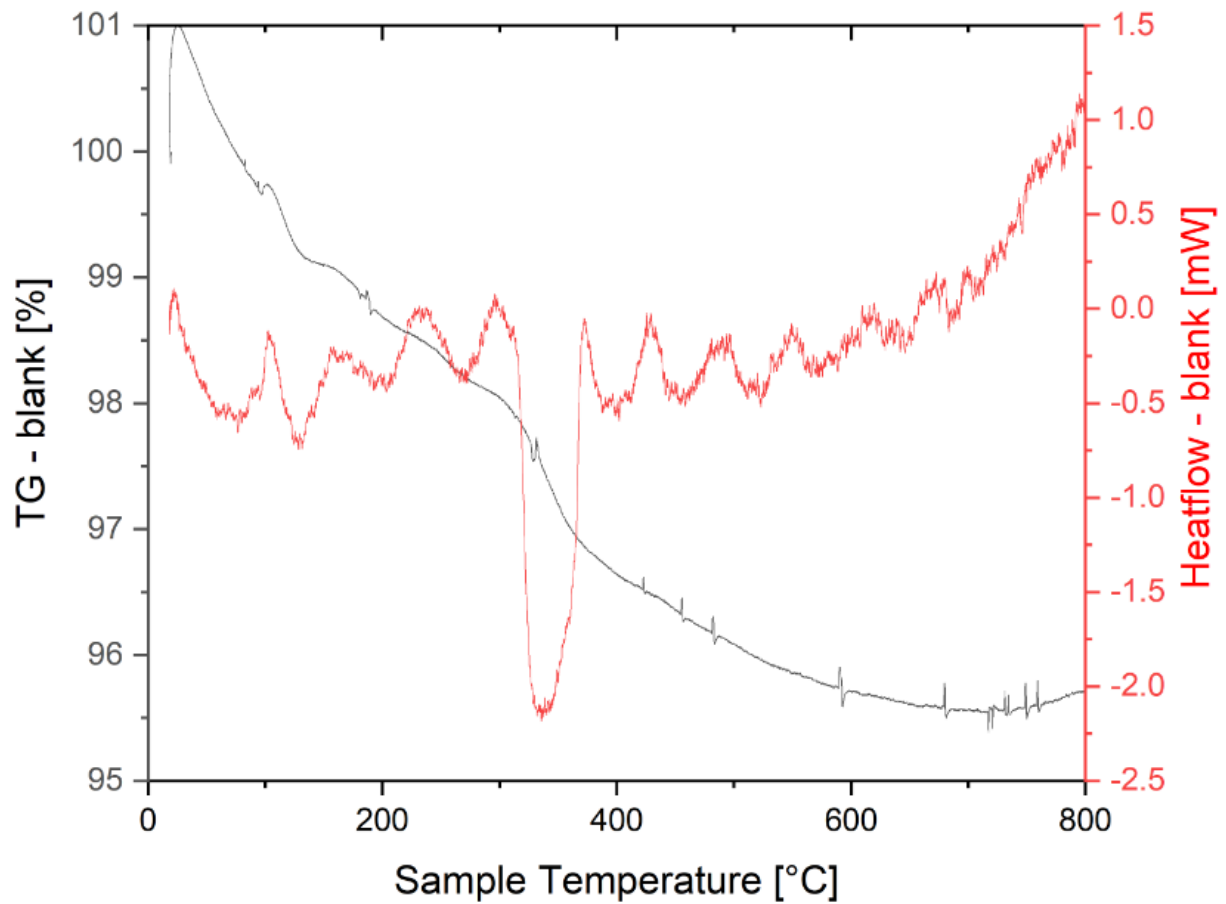


Figure A.5: TG-DTA results of the m18Ca80 (above) and m4Na80 (below) ZrO₂(s) solid phases.

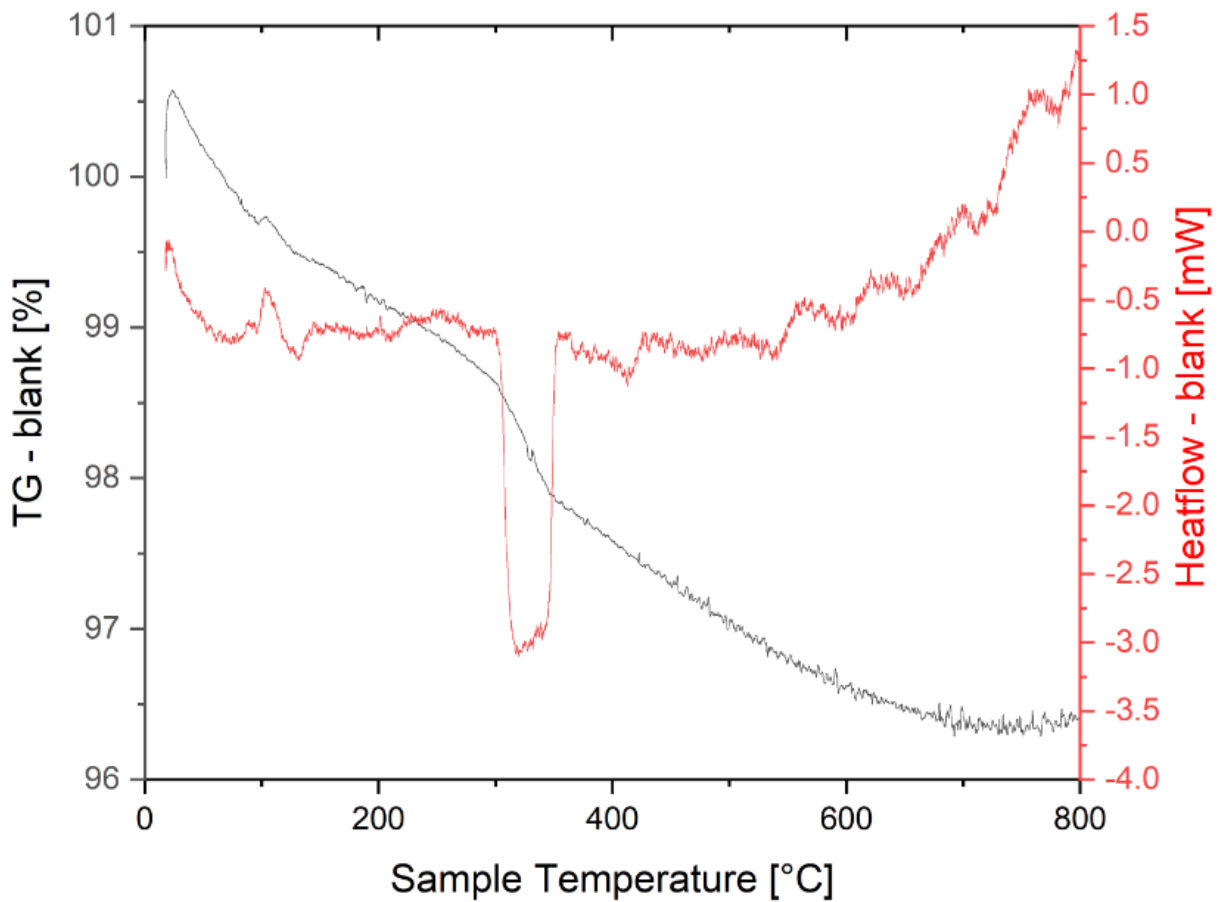
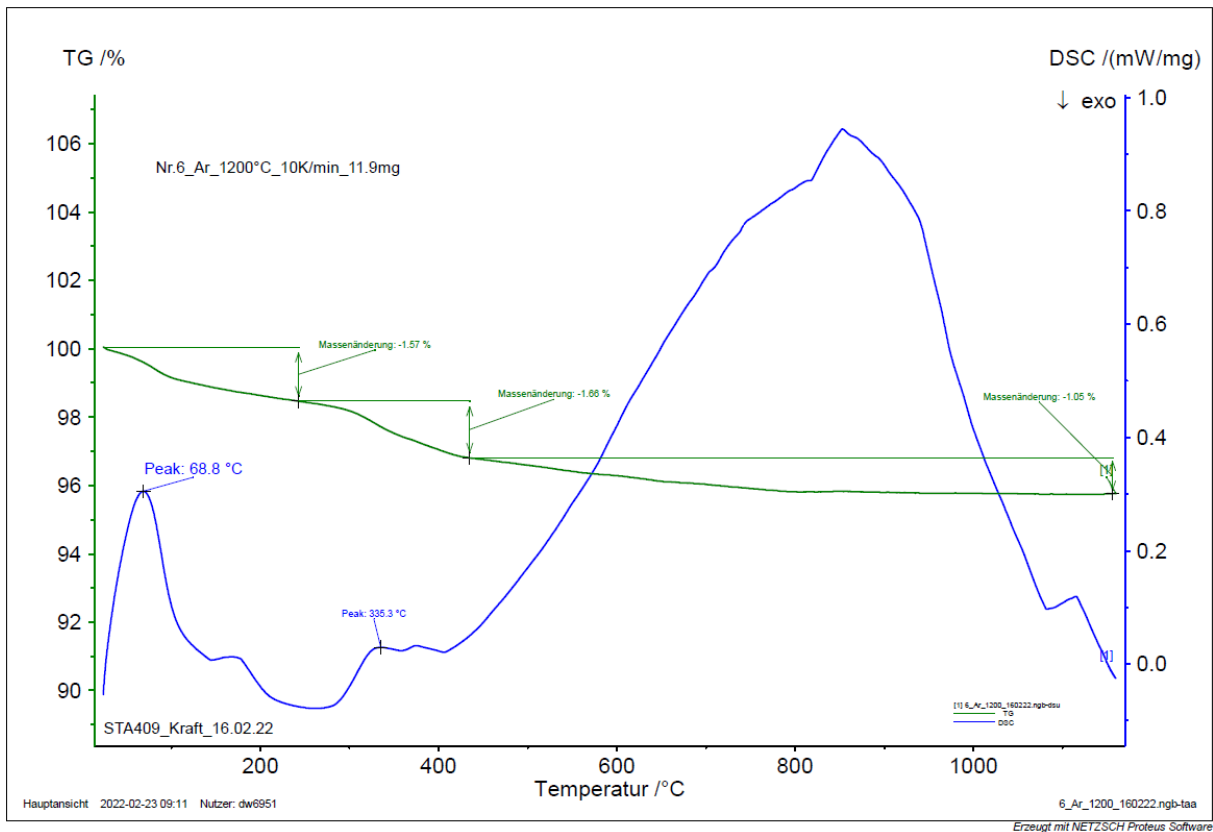


Figure A.6: TG-DTA results of the m10Na80 (above) and m18Na80 (below) $ZrO_2(s)$ solid phases.

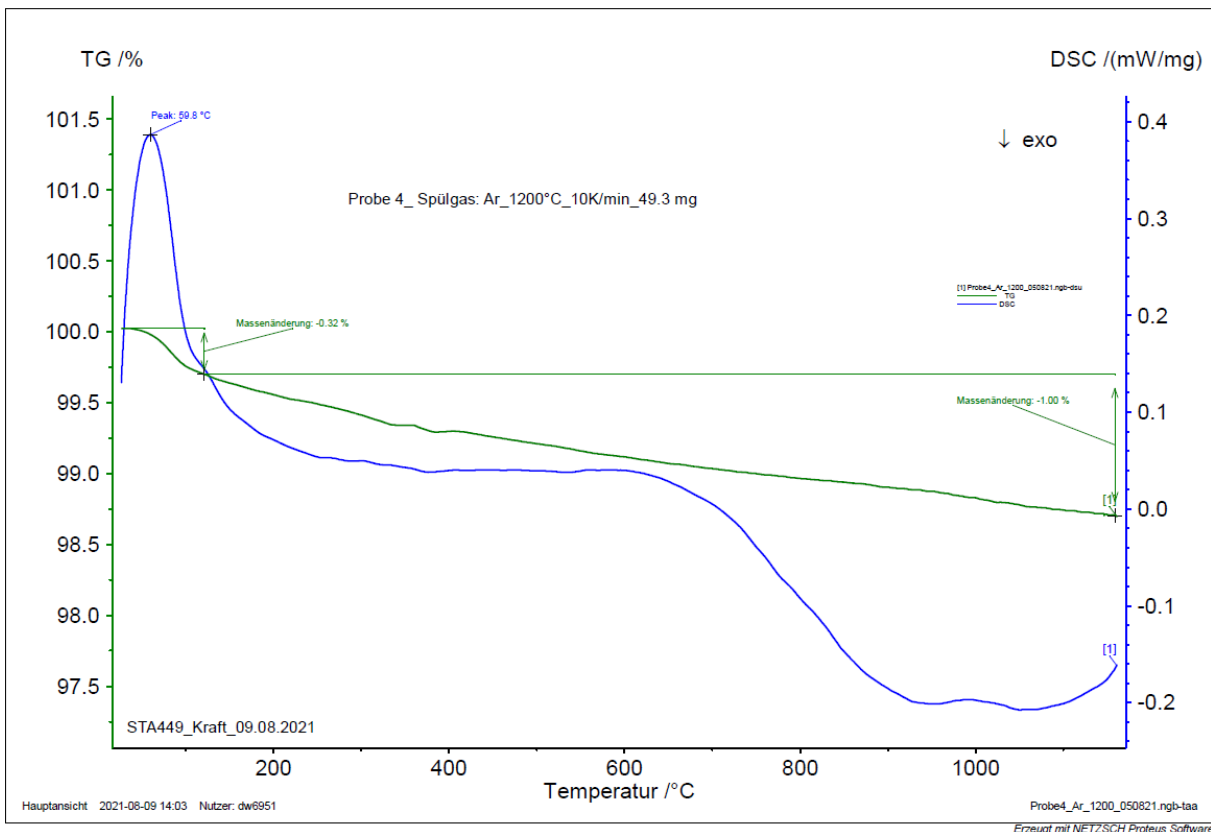
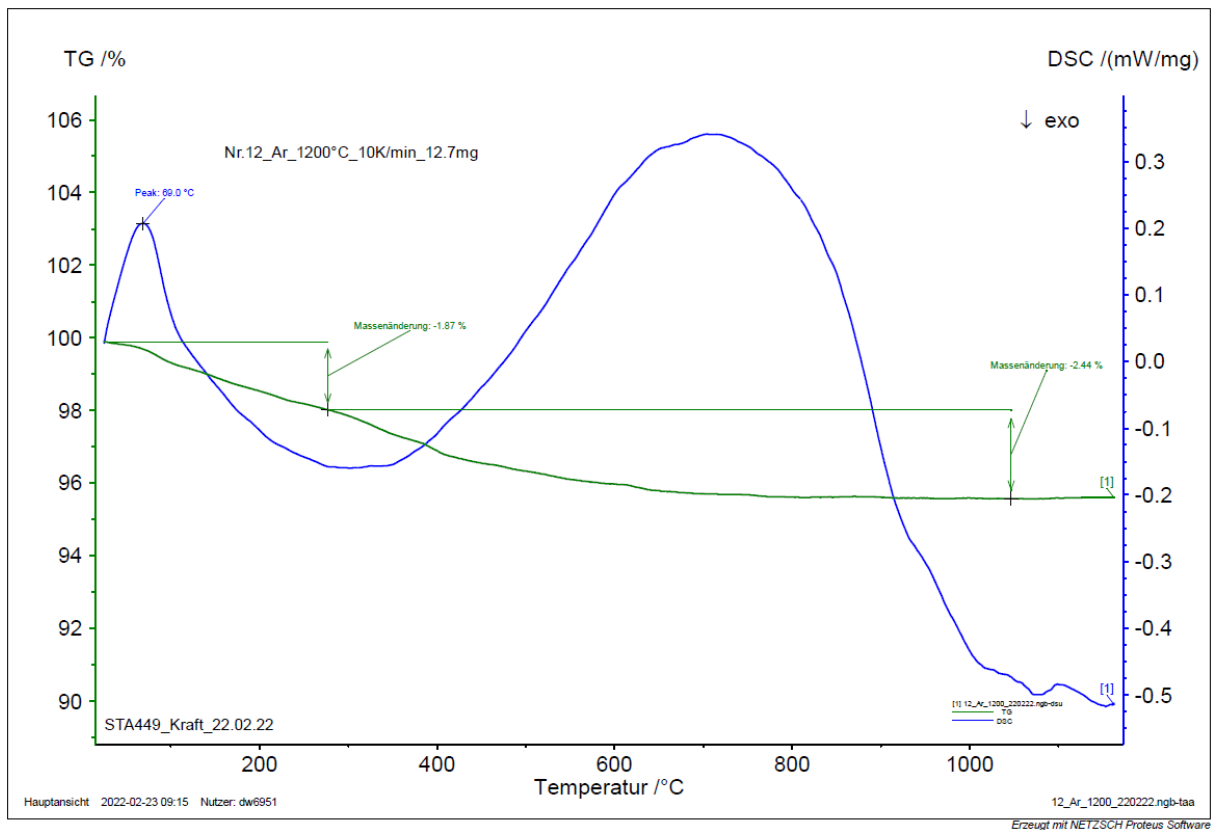


Figure A.7: TG-DTA results of the m10noH2O80 (above) and commercial crystalline (below) $ZrO_2(s)$ solid phases.

List of figures

Figure 1: XRD patterns (Résumé).	6
Figure 2: Amount of hydration (Résumé).	7
Figure 3: Solubility data in 0.5 M NaCl-NaOH (Résumé).	10
Figure 2.1: Electricity mix in France (2021).	15
Figure 2.2: Schematic overview of the nuclear waste types.	17
Figure 2.3: ZrO ₂ crystal structures.	24
Figure 2.4: Calculated solubility curve and species fraction based on NEA-TDB.	34
Figure 2.5: Calculated solubility curve and species fraction based on Altmaier et al.	35
Figure 3.1: K points and energy cutoff convergence tests.	58
Figure 4.1: XRD patterns, monoclinic.	60
Figure 4.2: XRD patterns, cubic/tetragonal.	61
Figure 4.3: TEM images, fresh, m4Ca80, m4Na80, commercial crystalline.	62
Figure 4.4: TEM images, m10Ca80, m10Na80, m4_002Ca80, m4_002Ca80new, m4Ca80new, m10Ca22.	63
Figure 4.5: TEM images, m10Na22, m10noH2O80.	64
Figure 4.6: Raman spectra of the ZrO ₂ (s) solid phases.	66
Figure 4.7: SEM images of the ZrO ₂ (s) solid phases.	68
Figure 4.8: Fourier transform EXAFS spectra.	71
Figure 4.9: SAXS spectra.	73
Figure 4.10: Amount of hydration water.	78
Figure 4.11: TG-DTA results of fresh rehydrated solid without heating.	79
Figure 4.12: TG-DTA results of fresh rehydrated solid heated at 200 and 400°C.	80
Figure 4.13: XRD patterns of the fresh rehydrated solids.	82
Figure 4.14: XPS spectra of the ZrO ₂ (s) solid phases.	84
Figure 4.15: FTIR spectra of the ZrO ₂ (s) solid phases.	85
Figure 4.16: TG-DTA and TG-MS data of fresh solid after D ₂ O exchange.	87
Figure 4.17: TG-DTA and TG-MS data of m10Ca80new solid after D ₂ O exchange.	88
Figure 4.18: TG-DTA and TG-MS data of m18Ca80 solid after D ₂ O exchange.	89
Figure 4.19: TG-DTA and TG-MS data of m18Na80 solid after D ₂ O exchange.	90
Figure 4.20: TG-DTA and TG-MS data of crystalline solid after D ₂ O exchange.	91
Figure 4.21: FTIR spectra of the solids after D ₂ O exchange.	92
Figure 4.22: Scheme of condensation reactions.	94
Figure 4.23: Zeta potentials of fresh, m4Ca80 and m4Na80 solids.	96
Figure 4.24: Zeta potentials m4Na80, m10Na80, m10noH2O80 and crystalline solids.	97
Figure 4.25: Zeta potentials m4Ca80 and m10Ca80 solids.	98
Figure 4.26: Solubility data of fresh solid in 0.5 M NaCl-NaOH.	104
Figure 4.27: Solubility data of m10Ca22, m10Na22, m4Ca80 and m4Na80 solids in 0.5 M NaCl-NaOH.	105
Figure 4.28: Solubility data of m10Ca80, m18Ca80, m4Ca80new, m4_002Ca80 m4_002Ca80new, m10noH2O80 and crystalline solids in 0.5 M NaCl-NaOH.	106
Figure 4.29: Modelled solubility curve of fresh solid in 0.5 M NaCl-NaOH.	107

Figure 4.30: Modelled solubility curve of m10Ca22, m10Na22, m4Ca80 and m4Na80 solids in 0.5 M NaCl-NaOH.	108
Figure 4.31: Application of the Schindler equation on the solubility data in 0.5 M NaCl-NaOH.	111
Figure 4.32: Solubility data in 0.02 M CaCl ₂ -Ca(OH) ₂ .	113
Figure 4.33: Solubility data of fresh solid in 0.2 M CaCl ₂ -Ca(OH) ₂ .	115
Figure 4.34: Solubility data of m10Ca22, m10Na22, m4Ca80 and m4Na80 solids in 0.2 M CaCl ₂ -Ca(OH) ₂ .	116
Figure 4.35: Solubility data of m18Ca80, m4Ca80new, m4_002Ca80 and m10noH2O80 solids in 0.5 M NaCl-NaOH.	117
Figure 4.36: Modelled solubility curve of fresh solid in 0.2 M CaCl ₂ -Ca(OH) ₂ .	119
Figure 4.37: Modelled solubility curve of m10Ca22, m10Na22 and m4Ca80 solids in 0.2 M CaCl ₂ -Ca(OH) ₂ .	120
Figure 4.38: Application of the Schindler equation on the solubility data in 0.2 M CaCl ₂ -Ca(OH) ₂ .	122
Figure 4.39: Schematic overview on the DFT calculations.	124
Figure 4.40: Optimized ZrO ₂ unit cells.	124
Figure 4.41: Monoclinic (-1 1 1) and tetragonal (1 0 1) surfaces.	126
Figure 4.42: Coordination analysis of the monoclinic (-1 1 1) surface.	127
Figure 4.43: Coordination analysis of the tetragonal (1 0 1) surface.	128
Figure 4.44: Coordination analysis of the amorphous surface.	129
Figure 4.45: Water adsorption on the monoclinic (-1 1 1) surface.	135
Figure 4.46: Water adsorption on the tetragonal (1 0 1) surface.	138
Figure 4.47: Water adsorption on the amorphous surface.	141
Figure 4.48: Comparison of water adsorption energies.	142
Figure 5.1: Scheme of solid phase transformation.	146
Figure 5.2: Solid phase characteristics of amorphous solid phases.	147
Figure 5.3: Solid phase characteristics of tetragonal/cubic solid phases.	147
Figure 5.4: Solid phase characteristics of monoclinic solid phases.	148
Figure 5.5: Solid phase characteristics of crystalline solid phases.	149
Figure A.1: TG-DTA results of fresh and m10Ca22 solids (Appendix).	154
Figure A.2: TG-DTA results of m10Na22 and m4Ca80 solids (Appendix).	155
Figure A.3: TG-DTA results of m4Ca80new and m4_002Ca80 solids (Appendix).	156
Figure A.4: TG-DTA results of m4_002Ca80new and m10Ca80 solids (Appendix).	157
Figure A.5: TG-DTA results of m18Ca80 and m4Na80 solids (Appendix).	158
Figure A.6: TG-DTA results of m10Na80 and m18Na80 solids (Appendix).	159
Figure A.7: TG-DTA results of m10noH2O80 and crystalline solids (Appendix).	160

List of tables:

Table 2.1: Nuclear power plants in 1989.	14
Table 2.2: Nuclear power plants in 2022.	15
Table 2.3: Amount of nuclear waste in European Union.	17
Table 2.4: Properties of host rocks.	19
Table 2.5: Zr isotopes.	21
Table 2.6: Zircaloy compositions.	22
Table 2.7: Properties of ZrO ₂ crystal structures.	23
Table 2.8: Equilibrium and hydrolysis constants.	31
Table 2.9: Ion interaction coefficients.	32
Table 3.1: List of chemicals.	39
Table 3.2: Samples and ageing conditions.	43
Table 3.3: Conditions of the solubility samples.	49
Table 3.4: Conditions of ZrO ₂ (cr) solubility samples.	51
Table 4.1: Raman signals.	67
Table 4.2: EDX data.	69
Table 4.3: EXAFS fit data.	71
Table 4.4: Weight loss determined with TG-DTA.	77
Table 4.5: Weight loss of rehydrated fresh solid phases.	81
Table 4.6: Oxygen speciation determined with XPS.	83
Table 4.7: Mass spectroscopy results after D-H exchange.	93
Table 4.8: BET results and surface estimations.	95
Table 4.9: Solubility data in 0.5 M NaCl-NaOH.	102
Table 4.10: Solubility constants in 0.5 M NaCl-NaOH.	109
Table 4.11: Solubility data in 0.02 M CaCl ₂ -Ca(OH) ₂ .	114
Table 4.12: Solubility data in 0.2 M CaCl ₂ -Ca(OH) ₂ .	118
Table 4.13: Solubility constants in 0.2 M CaCl ₂ -Ca(OH) ₂ .	121
Table 4.14: Structural parameters of optimized structures.	125
Table 4.15: Coordination analysis of bulk solids and surfaces.	130
Table 4.16: Surface energies.	132
Table 4.17: Water adsorption energies and positions for the monoclinic surface.	133
Table 4.18: Water adsorption energies and positions for the tetragonal surface.	136
Table 4.19: Water adsorption energies and positions for the amorphous surface.	139
Table 4.20: Water adsorption energies.	143

References

- (1) Kobayashi, T.; Bach, D.; Altmaier, M.; Sasaki, T.; Moriyama, H. Effect of Temperature on the Solubility and Solid Phase Stability of Zirconium Hydroxide. *Radiochim Acta* **2013**, *101*, 645–651.
- (2) Rand, M. ; F. *Chemical Thermodynamics Volume 11, Chemical Thermodynamics of Thorium*; OECD Publishing: Paris, 2007.
- (3) Metz, V.; Geckeis, H.; Gonzalez-Robles, E.; Loida, A.; Bube, C.; Kienzler, B. Radionuclide Behaviour in the Near-Field of a Geological Repository for Spent Nuclear Fuel. *Radiochim. Acta* **2012**, *100* (8–9), 699–713. <https://doi.org/10.1524/ract.2012.1967>.
- (4) Guillaumont, R. ; F. *Update on the Chemical Thermodynamics of Uranium, Neptunium, Plutonium, Americium and Technetium*; OECD Nuclear Energy Agency, 2003.
- (5) Rai, D.; Moore, D. A.; Oakes, C. S.; Yui, M. Thermodynamic Model for the Solubility of Thorium Dioxide in the Na⁺-Cl⁻-OH⁻-H₂O System at 23 Degrees C and 90 Degrees C. *Radiochim. Acta* **2000**, *88* (5), 297–306. <https://doi.org/DOI 10.1524/ract.2000.88.5.297>.
- (6) Kobayashi, T.; Sasaki, T.; Takagi, I.; Moriyama, H. Effect of Solid Phase Transformation on the Solubility Product of Thorium Hydrous Oxide at 363 K. *J. Nucl. Sci. Technol.* **2016**, *53* (11), 1787–1793. <https://doi.org/10.1080/00223131.2016.1160004>.
- (7) Nishikawa, S. ; K. Solubilities and Solubility Products of Thorium Hydroxide under Moderate Temperature Conditions. *Radiochim. Acta* **2018**, *106* (8), 655–667.
- (8) Liu, T. Communication of Nuclear Data Progress No. 25 (2001) - Reference Fission Yield Data Evaluation of ⁷⁹Se Etc.17 Fission Product Nuclides from ²³⁵U Fission.
- (9) Dell’Agli, G.; Mascolo, G. Low Temperature Hydrothermal Synthesis of ZrO₂-CaO Solid Solutions. *J. Mater. Sci.* **2000**, *35*, 661–665.
- (10) Ushakov, S. V.; Brown, C. E.; Navrotsky, A. Effect of La and Y on Crystallization Temperatures of Hafnia and Zirconia. *J Mater Res* **2004**, *19* (3), 693–696.
- (11) del Monte, F.; Larsen, W.; Mackenzie, J. D. Stabilization of Tetragonal ZrO₂ in ZrO₂-SiO₂ Binary Oxides. *J Am Ceram Soc* **2000**, *83* (3), 628–634.
- (12) Li, Z.; Lee, W. E.; Zhang, S. Low-Temperature Synthesis of CaZrO₃ Powder from Molten Salts. *J Am Ceram Soc* **2007**, *90* (2), 364–368.
- (13) Stubican, V. S.; Ray, S. P. Phase Equilibria and Ordering in the System ZrO₂-CaO. *J Am Ceram Soc* **1977**, *60* (11–12), 534–537.
- (14) Pitcher, M. W.; Ushakov, S. V.; Navrotsky, A.; Woodfield, B. F.; Li, G.; Boerio-Goates, J.; Tissue, B. M. Energy Crossovers in Nanocrystalline Zirconia. *J Am Ceram Soc* **2005**, *88* (1), 160–167.
- (15) Sharma, G.; Ushakov, S. V.; Navrotsky, A. Size Driven Thermodynamic Crossovers in Phase Stability in Zirconia and Hafnia. *J Am Ceram Soc* **2018**, *101*, 31–35.
- (16) Altmaier, M.; Gaona, X.; Fanghanel, T. Recent Advances in Aqueous Actinide Chemistry and Thermodynamics. *Chem Rev* **2013**, *113* (2), 901–943.
- (17) Brown, P. L.; Curti, E.; Grambow, B. *Chemical Thermodynamics of Zirconium*; Elsevier, 2005.
- (18) Grenthe, I.; Gaona, X.; Plyasunov, A. V.; Rao, L.; Runde, W. H.; Grambow, B.; Konings, R. J. M.; Smith, A. L.; Moore, E. E. *Second Update on the Chemical Thermodynamics of Uranium, Neptunium, Plutonium, Americium and Technetium*; OECD Nuclear Energy Agency, 2020.
- (19) Altmaier, M.; Neck, V.; Fanghanel, T. Solubility of Zr(IV), Th(IV) and Pu(IV) Hydrous Oxides in CaCl₂ Solutions and the Formation of Ternary Ca-M(IV)-OH Complexes. *Radiochim Acta* **2008**, *96*, 541–550.
- (20) Alwaeli, M.; Mannheim, V. Investigation into the Current State of Nuclear Energy and Nuclear Waste Management—A State-of-the-Art Review. *Energies* **2022**, *15*, 4275–4296.
- (21) Cherry, S. R. ; S. *Physics in Nuclear Medicine*; Elsevier Saunders, 2012.
- (22) Schicha, H. ; S. *Nuklearmedizin: Basiswissen Und Klinische Anwendung*; Schattauer, 2013.
- (23) Yordanova, A.; Eppard, E.; Kürpig, S.; Bundschuh, R. A.; Schönberger, S.; Gonzalez-Carmona, M.; Feldmann, G.; Ahmadzadehfar, H.; Essler, M. Theranostics in Nuclear Medicine Practice. *OncoTargets Ther.* **2017**, *10*, 4821–4828.

- (24) Collin, J.-M.; Bouveret, P.; Cariou, E. Military Nuclear Wastes. The Hidden Side of the French Nuclear Bomb., 2021.
- (25) Cherp, A.; Vinichenko, V.; Jewell, J.; Suzuki, M.; Antal, M. Comparing Electricity Transitions: A Historical Analysis of Nuclear, Wind and Solar Power in Germany and Japan. *Energy Policy* **2017**, *101*, 612–628. <https://doi.org/10.1016/j.enpol.2016.10.044>.
- (26) Abu-Khader, M. M. Recent Advances in Nuclear Power: A Review. *Prog. Nucl. Energy* **2009**, *51* (2), 225–235. <https://doi.org/10.1016/j.pnucene.2008.05.001>.
- (27) Hafele, W. Energy from Nuclear-Power. *Sci. Am.* **1990**, *263* (3), 136-+.
- (28) Atomgesetz, 2002. Gesetz Über Die Friedliche Verwendung Der Kernenergie Und Den Schutz Gegen Ihre Gefahren. [Act on the Peaceful Use of Nuclear Energy and Protection against Its Risks]. German Federal Parliament. Act of 23.12.1959. Amendment of 27.04.2002.
- (29) Atomgesetz, 2010. Gesetz Über Die Friedliche Verwendung Der Kernenergie Und Den Schutz Gegen Ihre Gefahren [Act on the Peaceful Use of Nuclear Energy and Protection against Its Risks]. German Federal Parliament. Act of 23.12.1959. Amendment of 28. 10.2010.
- (30) Atomgesetz., 2011. Gesetz Über Die Friedliche Verwendung Der Kernenergie Und Den Schutz Gegen Ihre Gefahren [Act on the Peaceful Use of Nuclear Energy and Protection against Its Risks]. German Federal Parliament. Act of 23.12.1959. Amendment of 30.06.2011.
- (31) Atomgesetz., 2022. Gesetz Über Die Friedliche Verwendung Der Kernenergieund Den Schutz Gegen Ihre Gefahren [Act on the Peaceful Use of Nuclear Energy and Protection against Its Risks]. German Federal Parliament. Act of 23.12.1959. Amendment of 04.12.2022.
- (32) IAEA. International Atomic Energy Agency: General Safety Guide No. GSG-1, Classification of Radioactive Waste; 2009.
- (33) Ewing, R. C. Long-Term Storage of Spent Nuclear Fuel. *Nat. Mater.* **2015**, *14* (3), 252–257. <https://doi.org/10.1038/nmat4226>.
- (34) Rohlig, K. J.; Geckeis, H.; Mengel, K. Facts and Concepts Disposal of radioactive Waste. *Chem. Unserer Zeit* **2012**, *46* (3), 140–149. <https://doi.org/10.1002/ciuz.201200578>.
- (35) Demarsily, G.; Ledoux, E.; Barbreau, A.; Margat, J. Nuclear Waste-Disposal - Can Geologist Guarantee Isolation. *Science* **1977**, *197* (4303), 519–527. <https://doi.org/DOI.10.1126/science.197.4303.519>.
- (36) Vernaz, E.; Bruezière, J. History of Nuclear Waste Glass in France. *Procedia Mater. Sci.* **7**, 3–9.
- (37) Ewing, R. C.; Whittleston, R. A.; Yardley, B. W. D. Geological Disposal of Nuclear Waste: A Primer. *Elements* **2016**, *12* (4), 233–237. <https://doi.org/10.2113/gselements.12.4.233>.
- (38) Bundesanstalt für Geowissenschaften und Rohstoffe. Endlagerung Radioaktiver Abfälle, Standortauswahl.
- (39) Bundesanstalt für Geowissenschaften und Rohstoffe. Nuclear Waste Disposal in Germany, 2007.
- (40) Young, R. P.; Nasser, M. H. B.; Sehzadeh, M. Mechanical and Seismic Anisotropy of Rocks from the ONKALO Underground Rock Characterization Facility. *Int. J. Rock Mech. Min. Sci.* **2020**, *126*. <https://doi.org/ARTN.104190.10.1016/j.ijrmms.2019.104190>.
- (41) de Saillan, C. Disposal of Spent Nuclear Fuel in the United States and Europe: A Persistent Environmental Problem. *Harv. Environ. Law Rev.* **2010**, *34* (2), 461–519.
- (42) Hilding-Rydevik, T. Why This Hurry in Relation to Nuclear Waste? *Environ. Impact Assess. Rev.* **2023**, *98*.
- (43) Geckeis, H.; Rohlig, K. J.; Mengel, K. Chemistry in the Repository system Disposal of radioactive Waste. *Chem. Unserer Zeit* **2012**, *46* (5), 282–293. <https://doi.org/10.1002/ciuz.201200583>.
- (44) Van Geet, M. Belgium’s Supercontainer Concept.
- (45) Bundesgesellschaft für Endlagerung (BGE). Zwischenbericht Teilgebiete gemäß § 13 StandAG, 2020.
- (46) Hicks, T. W.; Baldwin, T. D.; Hooker, P. J.; Richardson, P. J.; Chapman, N. A.; McKinley, I. G.; Neall, F. B. Concepts for the Geological Disposal of Intermediate-Level Radioactive Waste, 2008.
- (47) Bundesgesellschaft für Endlagerung (BGE). <https://www.bge.de/de/konrad/>, 2023.
- (48) Northwood, D. O. The Development and Applications of Zirconium Alloys. *Mater. Des.* **1985**, *6* (2), 58–70.

- (49) Goldak, J.; Lloyd, L. T.; Barrett, C. S. Lattice Parameters, Thermal Expansions, and Grüneisen Coefficients of Zirconium, 4.2 to 1130°K. *Phys. Rev.* **1966**, *144* (2), 478–484.
- (50) Wyckoff, R. W. G. *The Structure of Crystals*, 2nd edition.; Interscience Publishers: New York, 1963.
- (51) Kondev, F. G.; Wang, M.; Huang, W. J.; Naimi, S.; Audi, G. The NUBASE2020 Evaluation of Nuclear Properties. *Chin. Phys. C* **2021**, *45* (3).
- (52) Pavetich, S.; Carey, A.; Fifield, L. K.; Froehlich, M. B.; Halfon, S.; Kinast, A.; Martschini, M.; Nelson, D.; Paul, M.; Shor, A.; Sterba, J. H.; Tessler, M.; Tims, S. G.; Weissman, L.; Wallner, A. 93Zr Developments at the Heavy Ion Accelerator Facility at ANU. *Nucl. Inst Methods Phys. Res. B* **2019**, *438*, 77–83.
- (53) Deri, M. A.; Zeglis, B. M.; Francesconi, L. C.; Lewis, J. S. PET Imaging with 89Zr: From Radiochemistry to the Clinic. *Nucl Med Biol* **2013**, *40* (1), 3–14.
- (54) Yoon, J.-K.; Park, B.-N.; Ryu, E.-K.; An, Y.-S.; Lee, S.-J. Current Perspectives on 89Zr-PET Imaging. *Int J Mol Sci* **2020**, *21*.
- (55) Suman, S.; Khan, M. K.; Pathak, M.; Singh, R. N.; Chakravartty, J. K. Hydrogen in Zircaloy: Mechanism and Its Impacts. *Int. J. Hydrog. Energy* **2015**, *40*, 5976–5994.
- (56) Rudling, P.; Strasser, A.; Garzarolli, F. *Welding of Zirconium Alloys*; Advanced Nuclear Technology International: Sweden, 2007.
- (57) Thakare, V. Progress in Synthesis and Applications of Zirconia. *Int. J. Eng. Res. Dev.* **2012**, *5* (1), 25–28.
- (58) Wang, D.-N.; Guo, Y.-Q.; Liang, K.-M.; Tao, K. Crystal Structure of Zirconia by Rietveld Refinement. *Sci. China* **1999**, *42*, 80–86.
- (59) Lutterotti, L.; Scardi, P. Simultaneous Structure and Size-Strain Refinement by the Rietveld Method. *J. Appl. Crystallogr.* **1990**, *23*, 246–252.
- (60) Martin, U.; Boysen, H.; Frey, F. Neutron Powder Investigation of Tetragonal and Cubic Stabilized Zirconia, TZP and CSZ, at Temperatures up to 1400 K. *Acta Cryst* **1993**, *49*, 403–413.
- (61) Hannink, R. H.; Kelly, P. M.; Muddle, B. C. Transformation Toughening in Zirconia-Containing Ceramics. *J Am Ceram Soc* **2000**, *83* (3), 461–487.
- (62) Thomas, A. W.; Owens, H. S. Basic Zirconium Chloride Hydrosols. *J Am Chem Soc* **1935**, *57*, 1825–1828.
- (63) Fryer, J. R.; Hutchison, J. L.; Paterson, R. An Electron Microscopic Study of the Hydrolysis Products of Zirconyl Chloride. *J Colloid Interface Sci* **1970**, *34*, 238–248.
- (64) Keramidias, V. G.; White, W. B. Raman Scattering Study of the Crystallization and Phase Transformations of ZrO₂. *J. Am. Ceram. Soc.* **1974**, *57* (1), 22–24.
- (65) Li, P.; Chen, I.-W.; Penner-Hahn, J. E. X-Ray-Absorption Studies of Zirconia Polymorphs. I. Characteristic Local Structures. *Phys. Rev. B* **1993**, *48* (14), 10063–10073.
- (66) Li, P.; Chen, I.-W.; Penner-Hahn, J. E. X-Ray-Absorption Studies of Zirconia Polymorphs. II. Effect of Y₂O₃ Dopant on ZrO₂ Structure. *Phys. Rev. B* **1993**, *48* (14), 10074–10081.
- (67) Li, P.; Chen, I.-W.; Penner-Hahn, J. E. Effect of Dopants on Zirconia Stabilization-An X-Ray Absorption Study: I, Trivalent Dopants. *J Am Ceram Soc* **1994**, *77* (1), 118–128.
- (68) Li, P.; Chen, I.-W.; Penner-Hahn, J. E. Effect of Dopants on Zirconia Stabilization-An X-Ray Absorption Study: II, Tetravalent Dopants. *J Am Ceram Soc* **1994**, *77* (5), 1281–1288.
- (69) Kobayashi, T.; Uemura, T.; Sasaki, T.; Takagi, I.; Moriyama, H. The Solubilities and Solubility Products of Zirconium Hydroxide and Oxide after Aging at 278, 313, and 333 K. *Radiochim Acta* **2016**, *104* (3), 183–193.
- (70) Kobayashi, T.; Nakashima, S.; Motokawa, R.; Matsumura, D.; Saito, T.; Sasaki, T. Structural Approach to Understanding the Solubility of Metal Hydroxides. *Langmuir* **2019**, *35*, 7995–8006.
- (71) Connick, R. E.; McVey, W. H. The Aqueous Chemistry of Zirconium. *J Am Chem Soc* **1949**, *71*, 3182–3191.
- (72) Peshkova, V. M.; Mel'chakova, N. V.; Zhemchuzhin, S. G. Complex Formation in the Benzoyl-Acetone [1-Phenylbutane-1,3-Dione]-Zirconium-Benzene-Water System and the Hydrolysis of Zirconium Ions. *Russ J Inorg Chem* **1961**, *6*, 630–634.

- (73) Davydov, Y. P.; Zabrodskii, V. N. Hydrolysis of Zirconium(IV) with the Formation of Mono- and Polynuclear Hydroxy Complexes in Solutions. *Vestsi Akad Navuk BSSR Ser Khim Navuk* **1987**, *2*, 3–8.
- (74) Ekberg, C.; Källvenius, G.; Albinsson, Y.; Brown, P. L. Studies on the Hydrolytic Behavior of Zirconium(IV). *J Solut. Chem* **2004**, *33*, 47–79.
- (75) Sasaki, T.; Kobayashi, T.; Takagi, I.; Moriyama, H. Solubility Measurement of Zirconium(IV) Hydrous Oxide. *Radiochim Acta* **2006**, *94*, 489–494.
- (76) Kobayashi, T.; Sasaki, T.; Takagi, I.; Moriyama, H. Solubility of Zirconium(IV) Hydrous Oxides. *J. Nucl. Sci. Technol.* **2007**, *44* (1), 90–94.
- (77) Zouari, W. Étude de La Solubilité de l'oxyde de Zirconium et de Sa Réactivité de Surface En Milieux Aqueux. PhD Thesis, IMT-Atlantique, France, 2018.
- (78) Grambow, B.; Vandenborre, J.; Suzuki-Muresan, T.; Philippini, V.; Abdelouas, A.; Deniard, P.; Jobic, S. Solubility Equilibrium and Surface Reactivity at Solid/Liquid Interfaces of Relevance to Disposal of Nuclear Waste. *J Chem Thermodyn.* **2017**, *114*, 172–181.
- (79) Koch, W.; Holthausen, M. C. *A Chemist's Guide to Density Functional Theory*; Wiley-VCH, 2001.
- (80) Jansen, H. J. F. Electronic Structure of Cubic and Tetragonal Zirconia. *Phys. Rev. B* **1991**, *43* (9), 7267–7278.
- (81) Christensen, A.; Carter, E. A. First-Principle Studies of the Surfaces of Zirconia. *Phys. Rev. B* **1998**, *58* (12), 8050–8064.
- (82) Hofmann, A.; Clark, S. J.; Opper, M.; Hahndorf, I. Hydrogen Adsorption on the Tetragonal ZrO₂(101) Surface: A Theoretical Study of an Important Catalytic Reactant. *Phys Chem Chem Phys* **2002**, *4*, 3500–3508.
- (83) Haase, F.; Sauer, J. The Surface Structure of Sulfated Zirconia: Periodic Ab Initio Study of Sulfuric Acid Adsorbed on ZrO₂(101) and ZrO₂(001). *J Am Chem Soc* **1998**, *2*, 13503–13512.
- (84) Iskandarova, I. M.; Knizhnik, A. A.; Rykova, E. A.; Potapkin, B. V.; Korkin, A. A. First-Principle Investigation of the Hydroxylation of Zirconia and Hafnia Surfaces. *Microelectron Eng* **2003**, *69*, 587–593.
- (85) Korhonen, S. T.; Calatayud, M.; Krause, A. O. I. Stability of Hydroxylated (-111) and (-101) Surfaces of Monoclinic Zirconia: A Combined Study by DFT and Infrared Spectroscopy. *J Phys Chem C* **2008**, *112*, 6469–6476.
- (86) Piskorz, W.; Grybo, J.; Zasada, F.; Cristol, S.; Adamski, A. Periodic DFT and Atomistic Thermodynamic Modeling of the Surface Hydration Equilibria and Morphology of Monoclinic ZrO₂ Nanocrystals. *J Phys Chem C* **2011**, *115*, 24274–24286.
- (87) Syzgantseva, O. A.; Calatayud, M.; Minot, C. Revealing the Surface Reactivity of Zirconia by Periodic DFT Calculations. *J Phys Chem C* **2012**, *116*, 6636–6644.
- (88) Ricca, C.; Ringuédé, A.; Cassir, M.; Adamo, C.; Labat, F. A Comprehensive DFT Investigation of Bulk and Low-Index Surfaces of ZrO₂ Polymorphs. *J Comput Chem* **2015**, *36*, 9–21.
- (89) Puigdollers, A. R.; Illas, F.; Pacchioni, G. Structure and Properties of Zirconia Nanoparticles from DensityFunctional Theory Calculations. *J Phys Chem C* **2016**, *120*, 4392_4402.
- (90) Joutsuka, T.; Tada, S. Adsorption of CO₂ on Amorphous and Crystalline Zirconia: A DFT and Experimental Study. *J Phys Chem C* **2023**, *127*, 6998–7008.
- (91) Altmaier, M.; Metz, V.; Neck, V.; Muller, R.; Fanghanel, T. Solid-Liquid Equilibria of Mg(OH)₂(Cr) and Mg-2(OH)(3)Cl · 4H(2)O(Cr) in the System Mg-Na-H-OH-O-Cl-H₂O at 25 Degrees C. *Geochim. Cosmochim. Acta* **2003**, *67* (19), 3595–3601. [https://doi.org/10.1016/S0016-7037\(03\)00165-0](https://doi.org/10.1016/S0016-7037(03)00165-0).
- (92) Powder Diffraction Files, 2001.
- (93) Merkys, A.; Vaitkus, A.; Grybauskas, A.; Konovalovas, A.; Quirós, M. & Gražulis, S. Graph Isomorphism-Based Algorithm for Cross-Checking Chemical and Crystallographic Descriptions. *J. Cheminformatics* **2023**, *15*.
- (94) Vaitkus, A., Merkys, A. & Gražulis, S. Validation of the Crystallography Open Database Using the Crystallographic Information Framework. *J. Appl. Crystallogr.* **2021**, *54* (2), 661–672.

- (95) Quirós, M., Gražulis, S., Girdzijauskaitė, S., Merkys, A. & Vaitkus, A. Using SMILES Strings for the Description of Chemical Connectivity in the Crystallography Open Database. *J. Cheminformatics* **2018**, *10*.
- (96) Merkys, A., Vaitkus, A., Butkus, J., Okulič-Kazarinas, M., Kairys, V. & Gražulis, S. COD::CIF::Parser: An Error-Correcting CIF Parser for the Perl Language. *J. Appl. Crystallogr.* **2016**, *49*.
- (97) Gražulis, S., Merkys, A., Vaitkus, A. & Okulič-Kazarinas, M. Computing Stoichiometric Molecular Composition from Crystal Structures. *J. Appl. Crystallogr.* **2015**, *48*, 85–91.
- (98) Gražulis, S., Daškevič, A., Merkys, A., Chateigner, D., Lutterotti, L., Quirós, M., Serebryanaya, N. R., Moeck, P., Downs, R. T. & LeBail, A. Crystallography Open Database (COD): An Open-Access Collection of Crystal Structures and Platform for World-Wide Collaboration. *Nucleic Acids Res.* **2012**, *40*.
- (99) Gražulis, S., Chateigner, D., Downs, R. T., Yokochi, A. T., Quiros, M., Lutterotti, L., Manakova, E., Butkus, J., Moeck, P. & Le Bail, A. Crystallography Open Database – an Open-Access Collection of Crystal Structures. *J. Appl. Crystallogr.* **2009**, *42*, 726–729.
- (100) Downs, R. T. & Hall-Wallace, M. The American Mineralogist Crystal Structure Database. *Am. Mineral.* **2003**, *88*, 247–250.
- (101) Scherrer, P. *Gött. Nachrichten* **1918**.
- (102) Lábár, J. L. Electron Diffraction Based Analysis of Phase Fractions and Texture in Nanocrystalline Thin Films, Part I: Principles. *Microsc Microanal* **2008**, *14* (4), 287–295.
- (103) Rothe, J.; Butorin, S.; Dardenne, K.; Denecke, M. A.; Kienzler, B.; Loble, M.; Metz, V.; Seibert, A.; Steppert, M.; Vitova, T.; Walther, C.; Geckeis, H. The INE-Beamline for Actinide Science at ANKA. *Rev. Sci. Instrum.* **2012**, *83* (4). [https://doi.org/Artn 043105](https://doi.org/Artn%20043105) 10.1063/1.3700813.
- (104) Zimina, A.; Dardenne, K.; Denecke, M. A.; Doronkin, D. E.; Huttel, E.; Lichtenberg, H.; Mangold, S.; Pruessmann, T.; Rothe, J.; Spangenberg, T.; Steininger, R.; Vitova, T.; Geckeis, H.; Grunwaldt, J. D. CAT-ACT-A New Highly Versatile x-Ray Spectroscopy Beamline for Catalysis and Radionuclide Science at the KIT Synchrotron Light Facility ANKA. *Rev. Sci. Instrum.* **2017**, *88* (11). [https://doi.org/Artn 113113](https://doi.org/Artn%20113113) 10.1063/1.4999928.
- (105) Rothe, J.; Altmaier, M.; Dagan, R.; Dardenne, K.; Fellhauer, D.; Gaona, X.; Corrales, E. G. R.; Herm, M.; Kvashnina, K. O.; Metz, V.; Pidchenko, I.; Schild, D.; Vitova, T.; Geckeis, H. Fifteen Years of Radionuclide Research at the KIT Synchrotron Source in the Context of the Nuclear Waste Disposal Safety Case. *Geosciences* **2019**, *9* (2). [https://doi.org/ARTN 91](https://doi.org/ARTN%2091) 10.3390/geosciences9020091.
- (106) Ravel, B.; Newville, M. ATHENA, ARTEMIS, HEPHAESTUS: Data Analysis for X-Ray Absorption Spectroscopy Using IFEFFIT. *J Synchrotron Radiat* **2005**, *12*, 537–541.
- (107) Brunauer, S.; Emmett, P. H.; Teller, E. Adsorption of Gases in Multimolecular Layers. *J. Am. Chem. Soc.* **1938**, *60* (2), 309–319.
- (108) Kuila, U.; Prasad, M. Specific Surface Area and Pore-Size Distribution in Clays and Shales. *Geophys. Prospect.* **2013**, *61*, 341–362.
- (109) Hohenberg, P.; Kohn, W. Inhomogeneous Electron Gas. *Phys. Rev.* **1964**, *136* (3B), 864–871.
- (110) Kohn, W.; Sham, L. J. Self-Consistent Equations Including Exchange and Correlation Effects. *Phys. Rev.* **1965**, *140* (4A), 1133–1138.
- (111) Perdew, J. P.; Wang, Y. Accurate and Simple Analytic Representation of the Electron-Gas Correlation Energy. *Phys. Rev. B* **1992**, *45* (23), 13244–13249.
- (112) Perdew, J. P.; Burke, K.; Ernzerhof, M. Generalized Gradient Approximation Made Simple. *Phys. Rev. Lett.* **1996**, *77* (18), 3865–3868.
- (113) Klimes, J.; Bowler, D. R.; Michaelidis, A. Chemical Accuracy for the van Der Waals Density Functional. *J Phys Condens Matter* **2010**, *22*.
- (114) Grimme, S.; Antony, J.; Ehrlich, S.; Krieg, H. A Consistent and Accurate Ab Initio Parametrization of Density Functional Dispersion Correction (DFT-D) for the 94 Elements H-Pu. *J. Chem. Phys.* **2010**, *132*.
- (115) Becke, A. D. A New Mixing of Hartree-Fock and Local Density-Functional Theories. *J. Chem. Phys.* **1993**, *98*.

- (116) Adamo, C.; Barone, V. Physically Motivated Density Functionals with Improved Performances: The Modified Perdew–Burke–Ernzerhof Model. *J Chem Phys* **2002**, *116*, 5933–5940.
- (117) Kresse, G.; Hafner, J. Ab Initio Molecular Dynamics for Liquid Metals. *Phys. Rev. B* **1993**, *47*, 558–561.
- (118) Kresse, G.; Hafner, J. Ab Initio Molecular-Dynamics Simulation of the Liquid-Metal-Amorphous-Semiconductor Transition in Germanium. *Phys. Rev. B* **1994**, *49*, 14251–14269.
- (119) Kresse, G.; Furthmüller, J. Efficiency of Ab-Initio Total Energy Calculations for Metals and Semiconductors Using a Plane-Wave Basis Set. *Comput. Mater. Sci.* **1996**, *6*, 15–50.
- (120) Kresse, G.; Furthmüller, J. Efficient Iterative Schemes for Ab Initio Total-Energy Calculations Using a Plane-Wave Basis Set. *Phys. Rev. B* **1996**, *54*, 11169–11186.
- (121) Bouvier, P.; Djurado, E.; Ritter, C.; Dianoux, A. J.; Lucazeau, G. Low Temperature Phase Transformation of Nanocrystalline Tetragonal ZrO₂ by Neutron and Raman Scattering Studies. *Int. J. Inorg. Mater.* **2001**, *3*, 647–654.
- (122) Garg, N.; Mittal, V. K.; Bera, S.; Dasgupta, A.; Sankaralingam, V. Preparation and Characterization of Tetragonal Dominant Nanocrystalline ZrO₂ Obtained via Direct Precipitation. *Ceram. Int.* **2012**, *38*, 2507–2512.
- (123) Trugler, A.; Tinguely, J.-C.; Krenn, J. R.; Hohenau, A.; Hohenester, U. Influence of Surface Roughness on the Optical Properties of Plasmonic Nanoparticles. *Phys. Rev. B* **2011**, *83*.
- (124) Sheikhattar, M.; Attar, H.; Sharafi, S.; Carty, W. M. Influence of Surface Crystallinity on the Surface Roughness of Different Ceramic Glazes. *Mater. Charact.* **2016**, *118*, 570–574.
- (125) Hausmann, D. M.; Gordon, R. G. Surface Morphology and Crystallinity Control in the Atomic Layer Deposition (ALD) of Hafnium and Zirconium Oxide Thin Films. *J. Cryst. Growth* **2003**, *249*, 251–261.
- (126) Mechiakh, R.; Ben Sedrine, N.; Chtourou, R.; Bensaha, R. Correlation between Microstructure and Optical Properties of Nano-Crystalline TiO₂ Thin Films Prepared by Sol–Gel Dip Coating. *Appl. Surf. Sci.* **2010**, *257*, 670–676.
- (127) Kobayashi, T.; Fushimi, T.; Mizukoshi, H.; Motokawa, R.; Sasaki, T. Structural Approach to Understanding the Formation of Amorphous Metal Hydroxides. *Langmuir* **2022**, *38*, 14656–14665.
- (128) Picquart, M.; López, T.; Gómez, R.; Torres, E.; Moreno, A.; Garcia, J. DEHYDRATION AND CRYSTALLIZATION PROCESS IN SOL–GEL ZIRCONIA Thermal and Spectroscopic Study. *J. Therm. Anal. Calorim.* **2004**, *76*, 755–761.
- (129) Coblenz Society. *The Coblenz Society Desk Book of Infrared Spectra*, 2nd ed.; 1982.
- (130) Cui, H.; Li, Q.; Gao, S.; Shang, J. K. Strong Adsorption of Arsenic Species by Amorphous Zirconium Oxide Nanoparticles. *J. Ind. Eng. Chem.* **2012**, *18*, 1418–1427.
- (131) Su, Y.; Cui, H.; Li, Q.; Gao, S.; Shang, J. K. Strong Adsorption of Phosphate by Amorphous Zirconium Oxide Nanoparticles. *Water Res.* **2013**, *47*, 5018–5026.
- (132) Yamaguchi, T.; Nakano, Y.; Tanabe, K. Infrared Study of Surface Hydroxyl Groups on Zirconium Oxide. *Bull. Chem. Soc. Jpn.* **1978**, *51* (9), 2482–2487.
- (133) Meija, J.; Mester, Z.; D’Ulivo, A. Mass Spectrometric Separation and Quantitation of Overlapping Isotopologues. H₂O/HOD/D₂O and H₂Se/HDS_e/D₂Se Mixtures. *J Am Soc Mass Spectrom* **2006**, *17*, 1028–1036.
- (134) Kosmulski, M. *Surface Charging and Points of Zero Charge*; CRC press, 2009.
- (135) Neck, V.; Altmaier, M.; Seibert, A.; Yun, J. I.; Marquardt, C. M.; Fanghanel, T. Solubility and Redox Reactions of Pu(IV) Hydrous Oxide: Evidence for the Formation of PuO₂+x(s, Hyd). *Radiochim. Acta* **2007**, *95* (4), 193–207. <https://doi.org/10.1524/ract.2007.95.4.193>.
- (136) Schindler, P. W. Heterogeneous Equilibria Involving Oxides Hydroxides Carbonates and Hydroxide Carbonates. *Adv. Chem. Ser.* **1967**, No. 67, 196+.
- (137) Kiefer, C. Impact of Temperature on Th(IV) Solid Phases and Solubility. Master thesis, KIT, Karlsruhe, 2020.

- (138) Kiefer, C.; Neill, T.; Cevirim-Papaioannou, N.; Schild, D.; Gaona, X.; Vitova, T.; Dardenne, K.; Rothe, J.; Altmaier, M.; Geckeis, H. Interlink between Solubility, Structure, Surface and Thermodynamics in the ThO₂(s, Hyd)–H₂O(l) System. *Front Chem* **2022**.
- (139) Zhao, X.; Ceresoli, D.; Vanderbilt, D. Structural, Electronic, and Dielectric Properties of Amorphous ZrO₂ from Ab Initio Molecular Dynamics. *Phys. Rev. B* **2005**, *71*.
- (140) Whittle, K. R.; Ashbrook, S. E.; Lumpkin, G. R. Neutron Diffraction and MAS NMR of Cesium Tungstate Defect Pyrochlores. *J. Solid State Chem.* **2006**, *179*, 512–521.
- (141) Bondars, B. Ya.; Frey, F.; Heidemane, G.; Grabis, J.; Schneider, J.; Laschke, K.; Boysen, H. Powder Diffraction Investigations of Plasma Sprayed Zirconia. *J. Mater. Sci.* **1995**, *30*, 1621–1625.

Title: Fundamental investigation of Zr(IV) solubility and surface processes in alkaline systems: a combined solubility, spectroscopic and theoretical study.

Keywords: zirconium, crystallinity, solubility, thermodynamics, structure, surface

Abstract: Zirconium is an element of interest in the context of nuclear waste management and forms sparingly soluble $ZrO_2(am, hyd)$. The ageing or exposure to elevated temperatures expectedly results in a transition of amorphous $ZrO_2(am, hyd)$ into the thermodynamically stable crystalline phase $ZrO_2(cr)$ and thus in a decreased solubility in aqueous systems. The main objective of this study is to investigate this expected phase transformation process. Amorphous $ZrO_2(am, hyd)$ was precipitated, aged at $80^\circ C$ and investigated with solid phase characterization methods (XRD, TEM, TG-DTA,...), undersaturation solubility

experiments in alkaline 0.5 M NaCl-NaOH, 0.02 and 0.2 M $CaCl_2-Ca(OH)_2$ solutions and supporting theoretical calculations. The solid phase characterization results indicate, that a transformation process from amorphous towards crystalline $ZrO_2(s)$, accompanied by increasing particle size, decreasing water content and decreasing surface area is induced by ageing at $80^\circ C$. The solubility experiments show that this process also leads to a decreasing solubility, but additionally a decreasing solubility with ageing time and also for ageing at $22^\circ C$ was observed and attributed to changes in the surface properties.

Titre: Étude fondamentale de la solubilité du Zr(IV) et des processus de surface dans les systèmes alcalins : une étude combinée sur la solubilité, la spectroscopie et la théorie.

Mots clés: zirconium, cristallinité, solubilité, thermodynamique, structure, surface

Résumé: Le zirconium est un élément intéressant dans le contexte de la gestion des déchets nucléaires et forme du $ZrO_2(am, hyd)$ peu soluble. Le vieillissement ou l'exposition à des températures élevées devrait entraîner une transition du $ZrO_2(am, hyd)$ amorphe vers la phase cristalline thermodynamiquement stable $ZrO_2(cr)$ et donc une diminution de la solubilité dans les systèmes aqueux. L'objectif principal de cette étude est d'étudier ce processus de transformation de phase attendu. Du ZrO_2 amorphe (am, hyd) a été précipité, vieilli à $80^\circ C$ et étudié par des méthodes de caractérisation de la phase solide (XRD, TEM, TG-DTA,...), des expériences de solubilité par sous-saturation dans des solutions alcalines de 0,5 M NaCl-

NaOH, 0,02 et 0,2 M $CaCl_2-Ca(OH)_2$, ainsi que des calculs théoriques. Les résultats de la caractérisation de la phase solide indiquent qu'un processus de transformation de $ZrO_2(s)$ amorphe en $ZrO_2(s)$ cristallin, accompagné d'une augmentation de la taille des particules, d'une diminution de la teneur en eau et d'une diminution de la surface, est induit par le vieillissement à $80^\circ C$. Les expériences de solubilité montrent que ce processus conduit également à une diminution de la solubilité, mais une diminution de la solubilité avec le temps de vieillissement et également pour le vieillissement à $22^\circ C$ a été observée et attribuée à des changements dans les propriétés de surface.